CARDIFF UNIVERSITY

SCHOOL OF CHEMISTRY

Re(I), Ir(III) and Au(I) Luminescent Complexes for Imaging, Sensing and Therapy

A thesis submitted for the degree of Doctor of Philosophy by:

Emily Elizabeth Langdon–Jones

October 2015

CARDIFF UNIVERSITY
SCHOOL OF CHEMISTRY

Abstract

Doctor of Philosophy

Re(I), Ir(III) and Au(I) Luminescent Complexes for Imaging, Sensing and Therapy

By Emily Elizabeth Langdon-Jones

This thesis further developed several fluorescent ligand systems and their coordination to transition metals. Their synthesis and coordination chemistry to Re(I), Ir(III) or Au(I) is described, with detailed discussions on the photophysical properties and their potential towards imaging, sensing and therapeutic applications.

In Chapters 2–3, *N*–substituted–1,8–naphthalimide fluorophores were synthesised and their coordination to Re(I) was investigated. Chapter 2 describes a series of *fac*–$[Re(CO)_3(N^N)(LX)]BF_4$ complexes, axially substituted with naphthalimide fluorophores. Chapter 3 builds on work in Chapter 2 by investigating dipicolylamine–appended naphthalimide ligands and corresponding *fac*–$[Re(CO)_3(L)]BF_4$ complexes. The core investigations of both chapters centre on the photophysical properties where subtle changes of the substituents were observed to have profound effects on both the photophysical and physical properties. The feasibility of these compounds as cellular imaging agents, and also for photodynamic therapy in Chapter 2, was assessed.

Chapter 4 expands Au(I) coordination chemistry of alkynyl–derived 1,8–naphthalimide fluorophores. Seven new fluorophores, together with their Au(I) phosphine complexes, are described. These compounds were evaluated for imaging capabilities, *via* the fluorescent ligand and the inherent toxicity from the Au(I) core was assessed. Selected examples showed outstanding characteristics as potential optical/therapeutic agents.

Chapter 5 involved the further conjugated anthracene–1,9–dicarboximide core, possessing an additional ring compared to naphthalimide species in Chapters 2–4. The synthesis and characterisation of two novel anthracene based fluorophores, together with their Re(I) complexes, is described. These new compounds were again assessed as cellular probes and the results gave insight into the possible localisation of structurally related anticancer drugs.

Chapter 6 describes the synthesis of three novel cyclometalated Ir(III) complexes of the general form $[Ir(C^N)_2(N^N)]BF_4$, where N^N represents a novel, fluorescent phenylimidazo–phenanthroline ligand, capable of binding to NO. All precursors, ligands and complexes were extensively characterised and the response to NO was determined. The complexes in particular show great promise as effective NO probes.

Acknowledgements

I am lucky enough to be able to say that my PhD has been an incredible experience, one not possible without the support of my family, academics and friends.

Firstly I would like to express my immeasurable appreciation for my supervisor, Dr Simon Pope. Not only did you first spark my interest in research but you also endeavoured to materialise my position as a PhD student. Thank you for encouraging my research, giving me confidence and motivation and also for being a tremendous mentor and friend over the years. In the end "**IT** was well worth it" and I was very lucky to have you as a supervisor.

My sincere thanks also goes to Dr Anthony Hayes, Prof David Lloyd, Huw Mottram, Dr Shane Wainwright and Dr Catrin Williams, who together conducted confocal fluorescence microscopy and toxicity studies on many of my compounds. Furthermore, I am immensely grateful to Dr Benjamin Ward who was kind enough to dedicate his precious time to execute DFT for some of my compounds. I'd like to thank you all for sharing your expertise and time so willingly. On a similar note I am very grateful to all of the technical support staff in the chemistry department. Especially Dr Rob Jenkins, Robin Hicks and Simon Waller… none of this would have been possible without you, especially with the frequency of my mass spec submission and the amount of difficult carbon NMRs that you ran for me.

Importantly I need to thank my fellow labmates…Andy, Brendan, Gez, Lara, Mark, Mauro and Stokesy!!! I could pretend that the appreciation is for stimulating discussions but I'd be fibbing! I have been very fortunate to develop very special and close friendships with you throughout my PhD and our lunch time and pub gatherings have really made it such an entertaining period. You are the main reason why I have such fond memories of my time here. Thank you for making me laugh every day, listening to my moans and for letting me whistle while I beavered away, albeit with a little groaning! Also thank you to the other members of the inorganic section who have helped in more ways than one: Andy, Ariana, Ollie, Nadine and Sara. Also to Adam, Ali, Becky, Corey, Dayna, Jay, Jenn, Kate, Lenali, Lewis, Mohammed, Mohammed B., Owen, Seni, Smithy, Stacey, Tom H., TMob, Tracy and Woody.

Most significantly a special thanks goes to my family for encouraging me in all of my pursuits and inspiring me to follow my dreams. Words cannot express how eternally grateful I am to my parents and grandparents for encouraging my academic side all of those years ago and for all of the sacrifices that you've made on my behalf. I am very lucky to have such a close family and it is to you who I dedicate this thesis. Without your precious and unfaltering emotional and financial support it would not have been possible to conduct this research. I always knew that you believed in me and thank you for teaching me that my most important job in life is to learn, be happy and confident about myself.

Finally thanks to my husband–to–be, Alex, who I was lucky enough to meet during my studies at Cardiff. Our fun evenings and weekends have made difficult days in the lab bearable. As a non–chemist thank you for embracing my research, listening to me drone on about chemistry and for encouraging me towards my goal. I know that I have been very difficult to live with in the last few months but you have supported me in writing and calmed me when I've worked myself up. Mainly just thank you for being there whenever I needed you and I look forward to building a very happy life together.

Contents

List of Figures

List of Schemes

List of Tables

List of Abbreviations

Spectroscopy and Techniques	
NMR	Nuclear magnetic resonance
FT	Fourier transformation
UV–vis	Ultraviolet-Visible
IR	Infra–red
ATR	Attenuated total reflectance
MS	Mass spectrometry
ES	Electrospray
EI	Electron Ionisation
ICP	Inductively coupled plasma
APCI	Atmospheric Pressure Chemical Ionisation
LR	Low resolution
HR	High resolution
SR–XRF	Synchrotron radiation–induced X–ray fluorescence
TLC	Thin layer chromatography
CV	Cyclic voltammetry
EPR	Electron paramagnetic resonance
TD	Time dependent
DFT	Density functional theory
CFM	Confocal fluorescence microscopy
FLIM	Fluorescence lifetime imaging mapping
MTT assay	Microculture Tetrazolium assay
STED	Stimulated emission depletion
MRI	Magnetic resonance imaging
CT	Computed tomography
PET	Positron emission tomography
SPECT	Single photon emission computed tomography
PDT	Photodynamic therapy
SOG	Singlet oxygen generation
2D	Two dimensional
3D	Three dimensional
m/z	Mass/charge ratio
δ	Chemical shift
ppm	Parts per million
s	Singlet
d	Doublet
t	Triplet
q	Quartet
quin	Quintet
m	Multiplet
$\{^1H\}$	Proton decoupled
λ	Wavelength
υ	Frequency
IC_{50}	Concentration of drug where 50 % of cells are viable
Photophysical and chemical properties	
IC	Internal conversion

ISC	Intersystem crossing
SOC	Spin orbit coupling
ES	Excited state
GS	Ground state
LED	Light–emitting diode
OLED	Organic light–emitting diode
OLEC	Organic light–emitting electrochemical cell
ESIPT	Excited state intramolecular proton transfer
TBET	Through bond electron transfer
MC	Metal centred
IL	Intra–ligand
ICT	Intra–ligand charge transfer
MLCT	Metal–to–ligand charge transfer
MMLCT	Metal-metal-ligand charge transfer
LMMCT	Ligand-metal-metal charge transfer
HOMO	Highest occupied molecular orbital
LUMO	Lowest unoccupied molecular orbital
^{1}IL/LLCT/MLCT	Singlet excited state
^{3}IL/LLCT/MLCT	Triplet excited state
PeT	Photoinduced electron transfer
abs	Absorption
em	Emission
exc	Excitation
fluor	Fluorescence
phos	Phosphorescence
PS	Photosensitiser
τ	Lifetime
ϕ	Quantum yield
ECP	Effective core potential
Solvents, compounds, chemicals and biological substances	
DCE	Dichloroethane
DCM	Dichloromethane
DMF	Dimethylformamide
DMSO	Dimethylsulfoxide
MeCN	Acetonitrile
MeOH	Methanol
EtOH	Ethanol
TFA	Trifluoroacetic acid
PBS	Phosphate buffer solution
TMS	Trimethylsilyleacetyline
fac–	Facial
^{t}Bu	Tert–butyl
TM	Transition metal
Bpy	2,2'–bipyridine
Phen	1,10–phenanthroline
BOC	Tert–butyloxycarbonyl
Me	Methyl
Et	Ethyl

Ph	Phenyl
PPh_3	Triphenylphosphine
2–DPA	2–dipicolyl amine
NI / nap	Naphthalimide
An	Anthracene
ppy	Phenylpyridine
emptz	Ethyl–4–methylphenylthiazole–5–carboxylate
Cp	Cyclopentadiene
pyr	Pyridyl
EDTA	Ethylenediaminetetraacetic acid
DMEM	Dulbecco's modified Eagle's medium
$Pd_2(dba)_3$	[(dibenzylideneacetone)dipalladium(0)].
MTT	3-(4,5-dimethylthiazol-2-yl)-2,5-diphenyltetrazolium
CTC	5–cyano–2,3 ditolyl tetrazolium chloride
TrxR	Thioredoxin reductase
DO3A	1,4,7,10–tetraazacyclododecane–1,4,7–triacetic acid
NHC	N–heterocylic carbene
N^N	Di-imine ligand
L	Ligand
C^N	Cyclometalating ligand
PyX	Substituted pyridine ligand
Re–CDI	Re carbonyl di–imine complex
NADPH(+)	Nicotinamide adenine dinucleotide phosphate
DAN	Diaminonaphthalene
DAF	Diaminofluroscein
BODIPY	Boron–dipyrromethene
DNA	Deoxyribonucleic acid
rRNA	Ribosomal ribonucleic acid
HIV	Human immunodeficiency virus
TEMPO	2,2,6,6–tetramethyl–1–piperidinyloxy
DPA	9,10–diphenyl anthracene
BPEA	9,10–Bis(phenylethynyl)anthracene
TMRE	Tetramethylrhodamine ethyl ester
ROS	Reactive oxygen species
HEK	Human Embryonic Kidney
PC3	Human prostate cancer cell line
S. vortens	Spironucleus vortens
S. Pombe	Schizosaccharomyces pombe, or fission yeast
HeLa	Human cervical cancer cell line
ES2	Human ovarian cancer cell line
HepG	Human liver cancer cell line
LOVO	Human colon cancer cell line
MCF7	Human breast cancer cell line
HT29	Human colon cancer cell line
A549	Human lung cancer cell line
B16	Mouse melanoma cell line
P388	Mouse leukaemia cell line
RAW264.8	Macrophage cell line

Chapter 1

Introduction

1.1 Introduction

Recently there has been ever growing interest in the refinement of luminescent transition metal (TM) complexes. The ability to tune the electronic and photophysical properties through careful ligand design has led to the potential utilisation of luminescent TM complexes in a diverse range of applications. These include: i) photocatalysts; ii) luminescent probes or sensors; iii) sensitisers; iv) therapeutics; and v) lumophores in cellular imaging.[1]

1.2 Luminescence

Luminescence is effectively the emission of quantised energy packets (photons) by a molecule as it relaxes from its excited state (ES) to a ground state (GS).[2] This can be achieved *via* a number of pathways (Figure 1.1). Many different types of luminescence exist, each requiring diverse energy inputs to access the ES (electroluminescence, chemiluminescence, bioluminescence, radioluminescence and photoluminescence).[3,4] The work described herein focuses on photoluminescence.

1.2.1 Photoluminescence

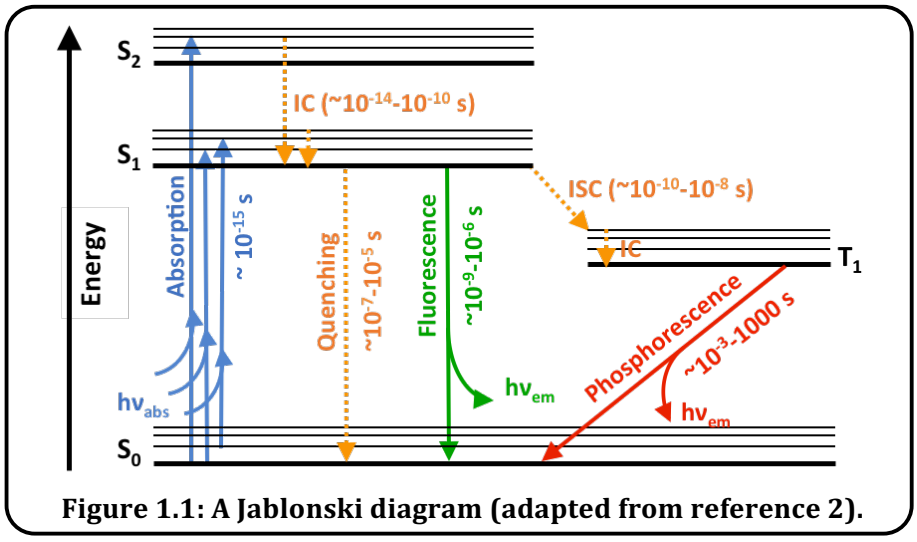

Figure 1.1: A Jablonski diagram (adapted from reference 2).

All types of luminescence require the promotion of an electron to excited energy levels.[5] For photoluminescence this process requires absorption of light[6,7] by the molecule because the energy gap is too large to be achieved thermally. The most likely excitation is from the ground singlet state (S_0) to vibronically excited states of the excited singlet energy level (S_1). This is described by the Franck–Condon Principle (Figure 1.2) and arises because; i) nuclei are much larger than electrons; and ii) a shift of internuclear separation

occurs if the bonding character is different in the ground and excited states (*i.e.* increased antibonding character).[8] Therefore the principle dictates that electronic transitions must be vertical[2] because the electronic transition is so rapid (10^{-15} s) that the nuclei do not have time to react and instead remain in a stationary framework.[2,8] The resultant state, and corresponding vertical transition, is called a Franck–Condon state.[9]

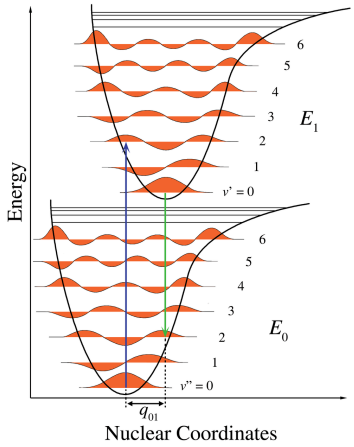

Figure 1.2: Illustration of the Franck–Condon Principle.[8]

After excitation by absorption of a photon, the high energy ES is relatively unstable and therefore must somehow lose excess energy.[3] This deactivation can occur *via* several processes. Firstly a molecule undergoes radiationless internal conversion (IC) that involves excess energy being lost in the form of heat,[4] caused by the molecule vibrating (Figure 1.1).[7,10] IC is essentially the rapid relaxation of a molecule as the electron drops down the vibrational sublevels and is the cause for the vibrational structure of emission spectra. This process generally occurs within 10^{-12} s and therefore has generally always occurred before emission and emission usually occurs from the lowest vibrational state of S_1, *i.e.* after reaching thermal equilibrium.[2,6]

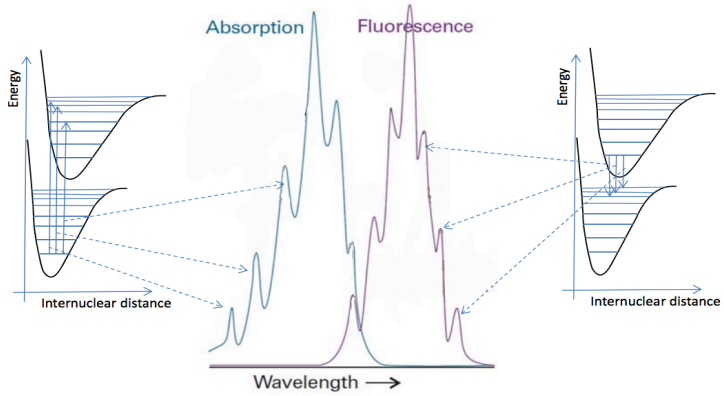

Figure 1.3: Illustration of the mirror image rule (adapted from reference 7).

IC also inevitably leads to the mirror image rule (emission spectra is generally a mirror image of the $S_0 \rightarrow S_1$ absorption profile) and the independent nature of the emission energy to the excitation wavelength (Kasha's rule). Exceptions to this include: i) pH sensitive systems that can result in ES proton transfer; ii) when ES reactions occur; or iii) if two ionisation states are available.

After IC the electron can undergo one of two processes. Relaxation back down to the ground singlet state, S_0, from the excited singlet state, S_1, is a process known as fluorescence,[7] and occurs for most organic fluorophores (Figure 1.1 and Figure 1.4). During fluorescence spin is conserved[5] and is thus allowed by the Laporte rules. Consequently this results in a very efficient process with decay rates in the region of 10^{-8} s,[2,3,10] leading to lifetimes below 10 ns.[2] The intensity of both the absorption and emission is proportional to the overlap of the vibrational wavefunctions of the GS and ES (Figure 1.2).[6]

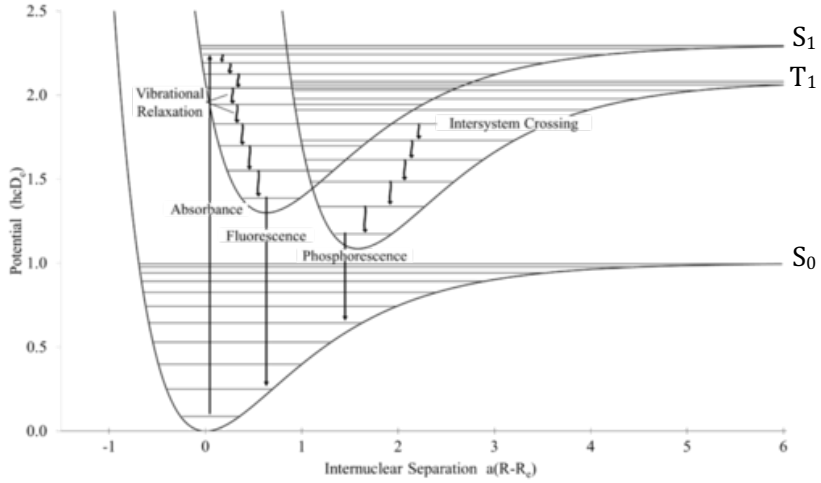

Figure 1.4: Potential energy wells showing vibrational relaxation, fluorescent and phosphorescent processes.[11]

Another possibility to fluorescence after IC is spin conversion involving extra energy loss *via* intersystem crossing (ISC). This is a non–radiative loss of energy allowing the electron to access the excited triplet state (T_1) (Figure 1.1). In the absence of spin–orbit coupling or an external magnetic field the singlet and triplet states are degenerate, however the triplet state is normally lower in energy than the singlet state (Figure 1.4).[6] ISC only occurs when two excited states of different spin have similar energies (Figure 1.4).[10] This process is spectroscopically spin forbidden[2] but facilitated by heavy atoms[2] and can occur because ISC is a kinetic process occurring *via* collisions.[10] Subsequently most transition metal complexes undergo spin change and exhibit phosphorescence.[5] Following ISC a small

amount of energy has been lost so the molecule cannot transfer back to S_1.[10] Further energy can again be lost by the emission of a photon to allow the electron to relax back down to S_0 (Figure 1.1 and Figure 1.4). This process is known as phosphorescence, also a spin forbidden process.[6,8] Therefore phosphorescent lifetimes are longer than fluorescence, generally ms–seconds,[6] and the additional energy loss means that the energy of phosphorescent emission is lower than that of fluorescent emission.[2,6]

1.2.2 Photophysical Characteristics and Considerations

Measuring the photophysical properties of luminescent compounds can allow determination of important photophysical features. Luminescent properties are measured using two techniques; steady state and time–resolved measurements.[2] Steady state measurements are the most common and are simply performed with constant illumination of the sample. This allows a steady excited state to be reached and therefore results in constant emission. Time–resolved measurements require sophisticated equipment due to the exceptionally short timeframes involved. This technique requires exposure of the sample to a pulse of light that needs to be shorter than the decay time to allow the decay profile to be recorded.[2] The nature of these different techniques renders steady state measurements an average of time–resolved measurements for the period of the decay. Combining these techniques can inform on several key parameters.

1.2.2.1 Quantum Yield (Φ)

The Φ is possibly the most important photophysical parameter because it represents the brightness of emission. Essentially the Φ is the ratio of the number of emitted photons relative to the number of absorbed photons.[2,6,7] High Φ values result in the brightest emission and values approaching unity can be seen in rhodamine species, for example. The quantum yield can be defined by Equation 1[2,6,7] where Γ = the radiative decay rate of the lumophore and k_{nr} = non–radiative decay rate. As the equation suggests both Γ and k_{nr} depopulate the ES and a good Φ is observed when $\Gamma > k_{nr}$.

$$Equation\ 1 \qquad Q = \frac{\Gamma}{\Gamma + k_{nr}}$$

1.2.2.2 Lifetime (τ)

The lifetime of the emission is a key parameter because, aside from allowing distinction between fluorescent and phosphorescent emission, it determines the time available for the ES to interact with the environment. The τ (Equation 2)[7] of a luminescent compound is the averaged time that a molecule spends in the ES before returning to the GS.[2,7]

$$Equation\ 2 \qquad \tau = \frac{1}{\Gamma + k_{nr}}$$

Species with longer lifetimes are useful for probes, however a long lifetime can be a downfall because the ES is more accessible to deactivation pathways such as quenching. Importantly lifetimes can offer an additional contrast parameter for cellular imaging techniques *e.g*. fluorescence lifetime imaging microscopy (FLIM).[7]

1.2.2.3 Quenching

Fluorescence quenching is effectively a decrease of fluorescence emission intensity and occurs from a variety of processes. Quenching processes are most prevalent for lumophores in solution. The most common is collisional, or dynamic, quenching whereby the ES is deactivated after contact with another molecule.[7] This type of quenching is greatly affected by diffusion effects in solution.[6] No permanent change occurs to the molecule however the quenching species must be in contact with the lumophore for quenching to occur.[12] One of the most well known quenching species is molecular oxygen and it is quite common practice to remove dissolved oxygen to obtain luminescent data. The specific mechanism of O_2 quenching is often debated however it is most likely due to the paramagnetic O_2 causing ISC.[12] Other quenching species that facilitate ISC include halogens. Once ISC has occurred the long–lived triplet state is completely quenched before phosphorescent emission can occur. Collisional quenching is described by the Stern–Volmer equation[12]:

$$Stern–Volmer\ equation \qquad \frac{F_0}{F} = 1 + K[Q] = 1 + k_q\tau_0[Q]$$

K, the Stern–Volmer quenching constant, indicates the sensitivity of the fluorophore to collisional quenching. F and F_0 are the fluorescence intensity with and without the quenching species, respectively. [Q] represents the quencher concentration, τ_0 = the unquenched lifetime and k_q = the bimolecular quenching constant.

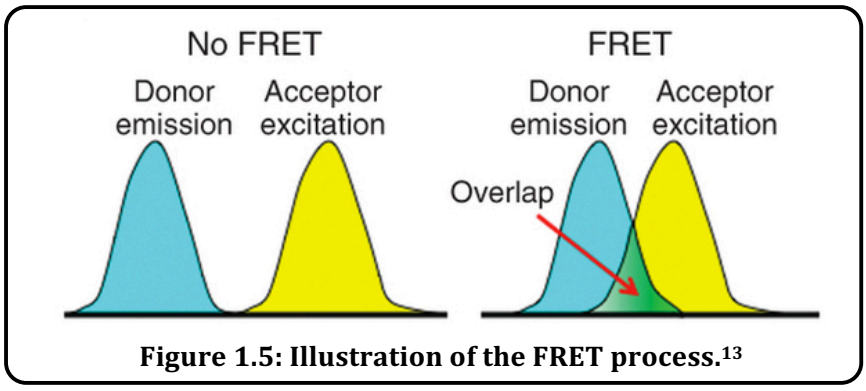

Figure 1.5: Illustration of the FRET process.[13]

Aside from collisional quenching several other quenching mechanisms are known. Static quenching involves the formation of non–emissive complexes of lumophores with quenching species.[7,12] Examples of this type of quenching species are amines that form ES charge transfer complexes for which the exciplex is quenched in polar solvents. Amines can also undergo photoinduced electron transfer (PeT) to quench fluorophores.

Furthermore, Resonance Energy Transfer (RET), sometimes called Förster RET (FRET), is a non–radiative transfer of energy between an excited donor and acceptor molecule.[7] Therefore efficient FRET only occurs when there is a high degree of overlap between the donor emission profile and acceptor absorption profile.[13] If the acceptor molecule is emissive then large Stokes' shift values are witnessed however full quenching is also possible with energy transfer to non–emissive acceptors. Furthermore FRET can be also be an example of self-quenching and occurs in species with very small Stokes' shifts.

Although quenching mechanisms can be troublesome to luminescent systems, the principle also leads to multiple applications,[7,12] such as 'on–off' fluorescent probes or use in photodynamic therapy. These are used for a number of purposes including:[12] i) DNA and protein binding probes; ii) diffusion membrane probes; and iii) quenching of fluorescence due to specific binding events, *e.g*. to metal ions.

1.2.2.4 Stokes' Shift

In 1852, Sir G. G. Stokes was the first to note that the emission wavelength is always longer than that of the excitation. The Stokes' shift value is the difference between the wavelength/frequency of the absorbed and emitted photons.[5] It is a critical property when considering the application of a ligand as a fluorophore. The emission energy is always lower than the excitation due to the energy lost by IC and thermalisation of excess vibrational energy,[2] however large Stokes' shifts can prevent self–quenching. Due to the tendency of spin conservation for organic fluorophores their Stokes' shifts tend to be small to moderate, however sometimes geometry changes in the ES can cause large Stokes' shift values.[5] Furthermore a large Stokes' shift allows distinction between fluorophore fluorescence and autofluorescence in cellular imaging applications. Autofluorescence is the intrinsic fluorescence of natural cellular objects. It tends to have a small Stokes' shift < 50 nm combined with short fluorescent lifetimes.[5] Therefore if a lumophore possesses a large Stokes' shift, an optical filter or FLIM techniques can be used to selectively filter out the autofluorescence.[7]

1.2.2.5 Environmental influences

Shifts in emission wavelength can be described as either bathochromic or hypsochromic, and changes to the intensity are referred to as either hyperchromic or hypochromic (Figure 1.6). Therefore careful ligand design is often involved with applications such as cell imaging, for which hyperchromic and bathochromic shifts are desirable. A bathochromic shift of the emission towards the near infra–red region is ideal for biological systems.[14]

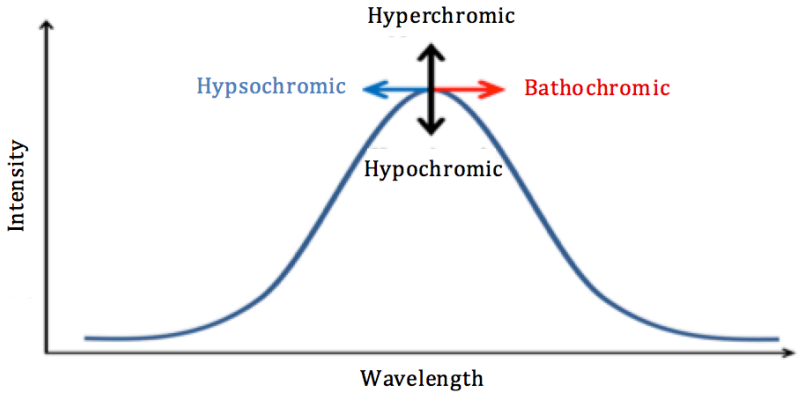

Figure 1.6: Terminology for shifts of absorption and emission spectra.

Environmental factors such as other fluorophores, solvent molecules, ions and pH can all greatly shift the emission.[7] For example, solution phase emission can be highly dependent upon the solvent present. This arises because the dipole moment of the lumophore can change during excitation. The ES tends to be more polar in nature and can therefore be stabilised by solvent reorientation around the molecule. The reorientation lowers the energy of the ES, resulting in a bathochromic shift. This is known as positive solvatochromism and can be quite a substantial contribution to the Stokes' shift. Negative solvatochromism also exists when the GS is more polar than the ES.

Aside from the aforementioned environmental influences, photobleaching can also vastly reduce the emission intensity. This is a common issue for fluorescence imaging techniques and occurs when an irreversible chemical change is induced after excitation.[7] Photobleaching can be reduced by increasing the sensitivity of an imaging technique and designing the fluorophore so that a low illumination level can be applied.[7,15]

1.2.2.6 Luminescence of Organic Species and Substituent Effects

Organic lumophores by definition must have the ability to absorb light, and an energy gap comparable to that of visible light. Common organic lumophores are based on aromatic species; which can be conjugated, substituted and functionalised. Unsaturated compounds

possess strong π→π* absorptions,[6] and often exhibit fluorescence from the lowest lying π* ES, and/or intra–ligand charge transfer (ICT).

Highly conjugated molecules result in larger bathochromic shifts and emission intensities[6] and furthermore often introduce vibronic structure due to their rigid nature.[16] Organic lumophores usually undergo fluorescence; triplet emission is possible in rare examples, however organic triplets are readily quenched by triplet oxygen and intersystem crossing is not always effective in organic species.

Substitution of aromatics can greatly affect the luminescent behaviour of a lumophore by affecting the electron density.[6,17] Substitution with an electron donating group, such as OH and amines, causes a shift in both the absorption and emission spectra, as well as an increase in the molar absorption coefficients. Electron donating groups can also cause spectra to become pH sensitive and broad, due to a significant l→π* contribution – essentially an intramolecular charge transfer process. Substitution with electron withdrawing groups, such as carbonyls or imides, causes a low lying[6] n→π* ES, giving lower extinction coefficients and quantum yields.[6] If the n→π* ES lies close in energy to the π→π* ES, the quantum yield will be highly solvent dependent.[18]

In addition, some organic compounds are known to aggregate together and form excimers (see Sections 5.1.4 and 5.3.5). Such excimers, known as J–aggregates, often exhibit a bathochromic and hyperchromic shift,[19] combined with a broadening of the emission profile.[20]

1.2.3 Luminescent Probes

Optical sensors are extensively applied in biochemical and medicinal studies,[21] for example to sense either: i) specific species of biological interest (such as Zn(II),[22] Cu(II)[23,24] and sugars[25]); ii) biological conditions (pH,[23] O_2 levels[21]) or to track biological processes.[20] The attributes of an effective luminescent probe include; i) an obvious change in the photophysical properties upon the sensing event; ii) a high affinity and selectivity for the chosen analyte; and iii) easy delivery to the subject matter.[26,27] Fluorescent probes are very advantageous because, with appropriate design, they can have high sensitivity, acquisition time, resolution and only need to be used in relatively low concentrations.[28] Biologically they are also capable of imaging at an intracellular level, in real time, with excellent spatial resolution.[26,29]

Luminescence based sensors report changes in the output of the emission: intensity changes including ratiometric dual–output and/or lifetime–based outputs are most

desirable. Many luminescent probes' downfall is that the results obtained cannot be verified by a standard. Ratiometric probes overcome this because the ratio of the emission/excitation intensity at two specific wavelengths allows calculation of analyte concentration.[30] This acts as an internal reference, improving the sensitivity and quantification of the probe.[28] One example of this type of sensor is based on a NI-rhodamine dyad[31] where the binding of Hg(II) affects the fluorescence resonance energy transfer (FRET) (Figure 1.7).

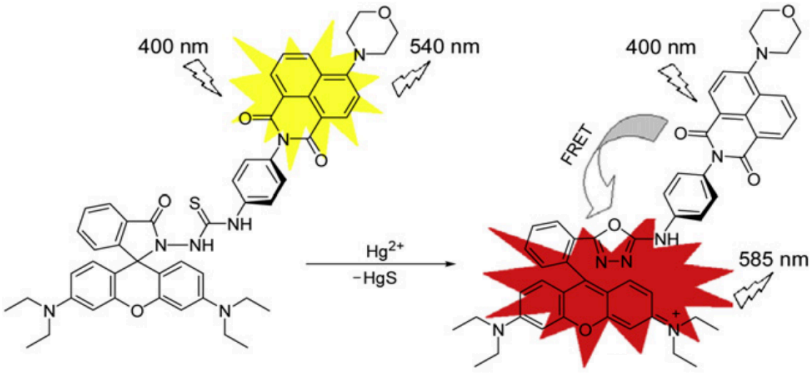

Figure 1.7: Example of a NI ratiometric probe by Liu *et al.*[31]

In addition, ratiometric probes can be designed around a number of approaches including; internal charge transfer (ICT), excited-state intramolecular proton transfer (ESIPT), through bond energy transfer (TBET) and monomer-excimer formation.[28] Another sensing technique uses the lifetime of the probes and allows changes in the local concentration of the analyte to be detected.

1.3 *d*–Block Metal Complexes

Most organic fluorophores possess a singlet excited state that is short lived and therefore tend to have small Stokes' shifts. In comparison luminescent *d*–block metal complexes, which typically emit from triplet excited states, are applicable to sensing and imaging applications due to a number of inherent properties.

1.3.1 Crystal Field Theory

Metal complexes are comprised of a number of ligands (ions or neutral molecules) forming coordinative dative bonds to a metal ion.[32] This is possible through donation of a lone pair of electrons[32] for σ–and π–donors, which can be complemented by a π–acceptor (*e.g.* carbonyl) component.[32] Polydentate ligands, such as bipyridine (bpy) and 1,10–phenanthroline (phen), that donate electron density from several sites[32] are often

preferred because they enhance the thermodynamic stability of a metal complex; this is known as the chelate effect. Other properties of the ligands and metal ion also affect the stability of the metal complex, such as the crystal field splitting energy (CFSE). CFSE is dependent upon the principle quantum number, charge of the metal, and the nature of the ligand.[9] The dependant nature of the CFSE on the nature of the ligands can lead to a high degree of tuning over photophysical properties with careful ligand design. The effect of different ligands is represented by the Spectrochemical Series (Figure 1.8) that ranks ligands in order of their coordination strength. The series cannot simply be explained by electrostatic effects but primarily depends upon the size and electronegativity of the donor atom.[32] The trend in general follows:

$Br^- < Cl^- < NO_3^- < F^- < H_2O < \underline{N}CS^- <$ Pyr $< NH_3 <$ Bpy $<$ Phen $< NO_2^- < PPh_3 < \underline{C}O/\underline{C}N^-$

Poor σ donor	Good σ donor
Good π donor	Good π acceptor
Low field	High Field
Δ_o	Δ_o

Figure 1.8: The Spectrochemical Series, adapted from reference 32.

1.3.2 Excited States of TM Complexes

The interesting photophysical nature of TM complexes, in the absence of ligands with such properties, is caused by charge transfer and *d–d* transitions (Figure 1.9), redistributing electron density over partially filled orbitals.[9,33] *d–d* transitions are formally disallowed by the Laporte rule and only occur due to small vibrations breaking symmetry in the molecule.[32] Therefore *d–d* transitions have a low probability and are typically weak (ε= 100–1000 $M^{-1}cm^{-1}$).

With respect to luminescence, intraligand (IL) or ligand–centered (LC) excited states originate from electronic transitions between ligand π orbitals (Figure 1.9).[34] Therefore if little perturbation to the metal occurs upon coordination, the luminescent properties of the complex may closely resemble those of the free ligand.[33] Furthermore, ligand–to–ligand charge transfer (LLCT) can occur when a complex possesses two very different types of ligand, one oxidising, the other reducing.[35] This becomes classified as ILCT when the oxidising and reducing moieties are on the same ligand.[35] TM complexes can show

luminescence from ligand–to–metal charge transfer (LMCT). This is more common for early TMs in high oxidation states,[36] such as Ta(V) complexes, but has also been observed in polynuclear d^{10} complexes involving Au(I) and Cu(I) complexes.[33]

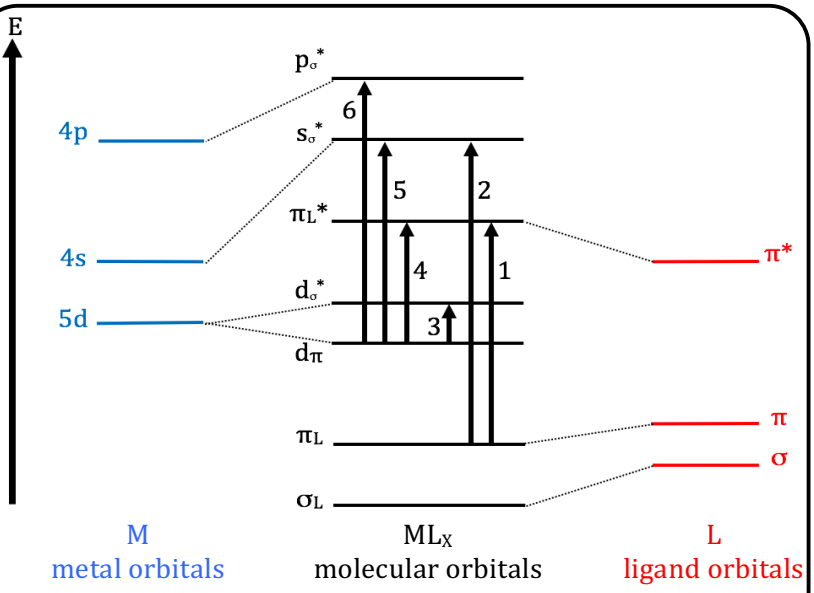

Figure 1.9: Possible electronic transitions of organometallic complexes. 1) π–π*, 2) LMCT, 3) *d–d* transition, 4) MLCT, 5) *d–s* transitions and 6) *d–p* transitions. Reproduced from reference 34.

Metal–to–ligand charge transfer (MLCT) transitions (Figure 1.9) are also possible and most studies into luminescent TM complexes focus around phosphorescent emission from the ^{3}MLCT excited state due to several key advantages. MLCT occurs if the metal is in a low oxidation state, between the *d*–orbitals and low lying, empty ligand π* orbitals.[9,33,35] MLCT is more common for highly conjugated, easily reduced chromophores that possess lower lying orbitals. Finally metal centred transitions can occur between $d \rightarrow p$ and $d \rightarrow s$ orbitals. Metal–to–metal charge transfer (MMCT) can also occur for ligand bridged polynuclear systems containing an oxidising and reducing metal, resulting in very low energy emission.[35]

Tuning of TM complexes' photophysical properties can be achieved by modulation of the lowest excited state. The most effective tuning method comprises structural variations of the coordinated ligands, such as altering the degree of π–conjugation, varying substituents, and adding heterocycles.[33,37]

1.3.3 Properties of Low Spin d^6 Complexes

Octahedral, transition metal d^6 complexes continue to be of significant interest due to their kinetic inertness.[32] The spin–paired filling of the t_{2g} orbitals results in slow ligand exchange rates; association or dissociation of ligands causes a large destabilisation of the complex *via* population of the e_g (formally antibonding) orbital, or decreasing ligand field stabilisation.

Many d^6 complexes possess long lived ^{3}MLCT excited states[38] and the first luminescent metal complex of ^{3}MLCT character, $[Ru(bpy)_3]^{2+}$, was reported in 1959 by Paris and Brandt.[39] The triplet state is excited when the *d*–orbitals of the metal lie close in energy to the ligand π* orbitals.[9,33,35] PeT occurs between the t_{2g} orbital to a ligand π* orbital (called MLCT) to form a ^{1}MLCT excited state. Emission from the ^{3}MLCT state is often observed for d^6 metal complexes because intersystem crossing is facilitated by the large spin–orbit coupling of heavy atoms. This spin–forbidden process results in: i) long lived emission with lifetimes up to the microsecond range; and ii) large Stokes' shifts, which in the context of fluorescence microscopy can allow detection away from autofluorescence, reduce the susceptibility to quenching, and also shift the emission to more tissue compatible wavelengths.[5,40] The ^{3}MLCT emission properties can be tuned with structural variations of the ligand systems.

To facilitate MLCT it is required to lower the π* orbital energy close to the t_{2g} orbital so that they are close enough for a transition to occur. Therefore strong field ligands are selected to increase the e_g orbital energy, ensuring that no population of the formally antibonding metal orbital occurs during excitation. Metals with low oxidation states are selected (*e.g.* Re(I),[41] Ir(III),[42] Ru(II)[43,44] and Os(II)[44]) because they tend to have higher energy *d*–orbitals. This combined with highly conjugated ligands, that help lower the level of the π* orbital, minimise the energy difference between the t_{2g} and π* orbitals. Although many phosphorescent d^6 metal complexes exist, not all d^6 metal complexes exhibit metal–based luminescence because this requires the ^3d–*d* orbitals to be higher in energy than the MLCT band. The strength of the luminescence is then dependent on the energy gap between the MLCT energy level and the ground state because the rate of non–radiative processes increases as the energy gap decreases (energy gap law).

1.3.4 Properties of d^{10} Metal Complexes

Most d^{10} metal complexes are Group 11 (Cu(I), Ag(I), Au(I)) examples of the form ML_2. In d^{10} complexes the *d* orbitals are full and therefore these complexes are 'spectroscopically

quiet'[45] and only possess 14 valence electrons. The electron deficient nature of the metal, alongside the low coordination number, often makes such species highly reactive.[46]

With regards to Cu(I), the most common class of complex has the general formula $[Cu(N\hat{}N)_2]^+$, where N^N is typically a functionalised phen ligand. Photoexcitation causes these tetrahedral compounds to undergo molecular rearrangement to a square planar geometry.[47] This is because photoexcitation results in the oxidisation of Cu(I) to Cu(II),[48] for which the d^9 configuration strongly encourages Jahn–Teller distortions. It is thought that this flattening rearrangement may be accompanied by the addition of external nucleophiles (*e.g.* solvent molecules or ions) to the 'open' structure to form a five–coordinate exciplex.[48,49] The weak emission of $[Cu(N\hat{}N)_2]^+$ species is observed at *ca*. 700 nm, corresponding to emission from the ^{3}MLCT state.[50] Consequently phosphorescent lifetimes of tens to hundreds of nanoseconds are observed.[48] Heteroleptic $[Cu(N\hat{}N)(P\hat{}P)]^+$ compounds (Figure 1.10) show much more interesting photophysical properties. Suitably tuning the di–imine and phosphine ligands can result in strong green emission,[51] again ascribed to ^{3}MLCT emission.

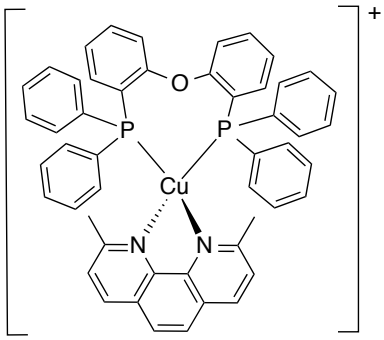

Figure 1.10: Luminescent Cu(I) complex by Cuttell *et al*.[51]

Schiele and Senebier first discovered light sensitive silver compounds in the late 1700s. Consequently experiments with silver halide layers on metal plates by J. Herschel *et al*. led to one of the most widely known TM applications: photography.[47] Ag(I) forms stable, often clustered, d^{10} complexes with varied photophysical properties. MC, LMCT and LC transitions can all be observed depending on the number of metal centres and the photophysical properties of the ligand.[47]

Au(I) complexes (see Section 4.1.2) are known for their aurophilic interactions (*ca*. 10 kcalmol^{-1})[47] which result in a tendency to form weak metal–metal bonds. This is attributed to a stabilisation of the filled *5d* orbitals *via* interaction with empty *6s*/*6p* molecular orbitals. These are only close in energy due to the strong relativistic effect of

gold.[52] Mononuclear Au(I) complexes (see Section 4.1.5) commonly form linear and trigonal planar geometries and therefore possess very different properties to Cu(I) and Ag(I) complexes. Dori *et al*. first reported the luminescence of Au(I) phosphine complexes,[53] dominated by LMCT and IL transitions. Phosphine alkynyl derivatives are an exception to this. For these species the presence of low energy π* orbitals of the alkynyl ligand introduces metal perturbed ^{3}IL character, with some contribution from metal–to–alkynyl ^{3}MLCT excited states.[54] In addition gold possesses the highest spin–orbit coupling constant (ζ Au = 5104 cm^{-1})[47] of metals which provides effective facilitation of ISC as a route to phosphorescent Au(I) complexes.

1.4 Diagnostic Medicine - Medical Imaging

Coordination compounds are widely used in a variety of medical imaging techniques.[1] Medical imaging has been extensively used as a diagnostic and monitoring tool for many years, with the field ever advancing and evolving since the turn of the twentieth century.[55] Medical imaging is reliant upon detecting the differences between the composition of different tissues within the body, using an external source.[56] This can be further broken down into two classes: anatomical and molecular imaging which involve the detection of internal structural consequences and biochemical/physiological abnormalities respectively, from outside the body.[57] Medical imaging is important because it can lead to the early treatment of conditions that could otherwise be fatal. Many imaging modalities are available to the clinician (PET, CT, MRI, X-Ray, fluorescence microscopy *etc*.) all with distinct advantages and disadvantages.

1.4.1 Bimodal imaging

Many diagnostic techniques are available to the clinician however each has their individual strengths and weaknesses in terms of: i) cost; ii) penetration; iii) resolution; iv) applicability; v) equipment requirements; vi) the need for external agents; and vii) sensitivity to the environment.[58] Due to these respective strengths and weaknesses it has become increasingly desired to combine different modalities in order the exploit the different strengths, simultaneously.[45,59-61] Common collections involve modalities with high penetration and relatively low resolution (*e.g*. MRI, PET) combined with a poor penetration but high sensitivity technique (*e.g*. fluorescence microscopy).[45,57,60,61] Imaging probes are often used in medical imaging to increase the quality/sensitivity of the image. Ideally, for a bimodal application, the two external probes would be combined into a single entity – a single molecule bimodal probe.[58] This allows simplification of design and reduces both the administration (toxicology, licensing etc.) and cost associated with the

diagnostic technique. However most importantly a single molecule approach assures single biodistribution,[58] hopefully preventing false negatives or mis-diagnosis.[57] Nevertheless, integrating two modalities into a single–molecule for effective bimodal capabilities can be difficult due to the large differences of contrast agent dose required by different modalities.

In the past most research has focused on MR/optical imaging probes, centred on gadolinium chelates, quantum dots and iron oxide nanoparticles.[59] Several examples of such bimodal probes have been reported by Long *et al.* with remarkable success. One example (Figure 1.11) featured a luminescent rhodamine–DO3A conjugate (λ_{em} = 580 nm) whereby water solubility was achieved *via* the introduction of an amide linker. The gadolinium complex possessed a relaxivity of 3.8 $mM^{-1}s^{-1}$ and confocal fluorescence microscopy with human embryonic kidney cells revealed good uptake in cells. Interestingly fluorescence was only visible from cells with reduced mitochondrial potential due to the suppression of the luminescent character below pH 6.5.

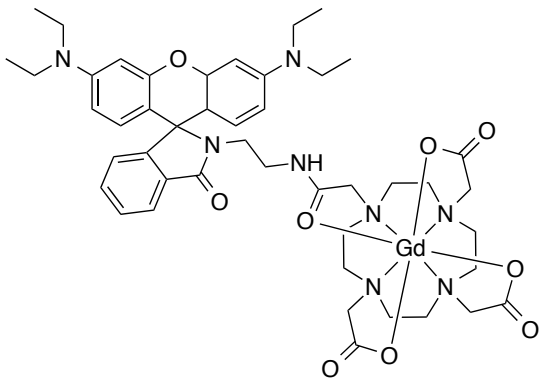

Figure 1.11: Example of a bimodal MR/optical imaging probe based on a rhodamine–DO3A conjugate by Long *et al.*[60]

More recently an investigation on multimodal imaging probes combining radionuclear and optical imaging techniques has been reported (see Section 3.1.4).[59] Furthermore other related research has led to diagnostic techniques being coupled with therapeutic action. If these modalities were successfully combined it would mean that detection and treatment could be undertaken simultaneously, in one appointment, thus reducing resources and increasing convenience for both patient and clinician.

1.5 Fluorescence microscopy

Fluorescence microscopy is a powerful, highly sensitive technique[40] that is commonly used in biological or medicinal applications.[7,62] The practice is essentially a microscopic

imaging technique, reliant upon the use of fluorescent probes, or in rare cases the intrinsic fluorescence upon excitation of the biological sample.[5,63] Fluorescent probes illuminate non–emissive cells and importantly provide enhanced contrast[63,64] and signal–to–noise ratios compared to standard microscopy techniques,[5,23] thus allowing fine detail to be observed. Consequently fluorescence microscopy is a highly favourable technique, especially when considering its high nanometer resolution (*ca*. half of the emission wavelength),[3,7,64] non–invasive character and relatively small concentrations of probes required. Furthermore, detecting emitted light, *versus* reflected light as for normal microscopy, leads to a greater level of sensitivity.[64] Therefore it can allow visualisation at a molecular level for a relatively low cost. In industry the technique allows inspection of surfaces and coatings[62] but in a biological context fluorescence imaging dynamically informs on the localisation and uptake of molecules within cells.[40,65]

Unfortunately fluorescence microscopy is inherently limited due to the requirement for the excitation wavelength to be close to an available laser and for both excitation and emission wavelengths to be tissue compatible. Furthermore tissue compatible wavelengths are typically in the near IR to red region of the spectrum and have poor penetration[5] through tissue. Therefore this technique is not a whole body method and is instead generally limited to imaging at a cellular or thin tissue level.[40]

1.5.1 Confocal Fluorescence Microscopy

In the last 15 years the field of fluorescence microscopy has been quickly advancing due to improvements in methods, equipment and fluorescent probe design. Most notably there have been large developments in two relatively modern techniques,[62] both of which display vastly improved resolution. One technique, confocal fluorescence microscopy (CFM), limits photon detection to light that is emitted from a singular focal point and plane and therefore out–of–focus information is rejected for improved contrast.[62] The other is two–photon microscopy that involves the excitation of a chromophore by two photons, simultaneously. For this to occur the concentration of photons needs to be very high, fortunately a property that only occurs at the focal point, thus automatically generating focused, sectioned images.[66] Additional developments have most recently been centred towards fluorescent nano–crystals and quantum dots.[63] It is CFM that is the primary focus of the work described herein.

The confocal principle was first discovered by Martin Minsky in 1957 and the first commercial instrument was developed in 1982.[62] By the 1990s CFM was widely recognised as a more refined technique[5] and possessed several key advantages due to the

nature of the image collection process (Figure 1.12). In CFM firstly the excitation photons pass through a pinhole before focusing through the objective lens onto a precise location in one focal plane.[5,63] The emission is then passed through a second pinhole aperture to reject any out–of–focus (reflected/diffracted) light[40,62,64] so that only a small area is imaged with incredibly high contrast.[63] Consequently this technique allows two–dimensional (2D) optical slices (*z*–stacks) to be collected to ensure that the fluorophore has entered the cell interior. These can then be reconstructed to form a false–colour,[64] three–dimensional (3D) image of a 'thick' object.[5,7,40,62-64]

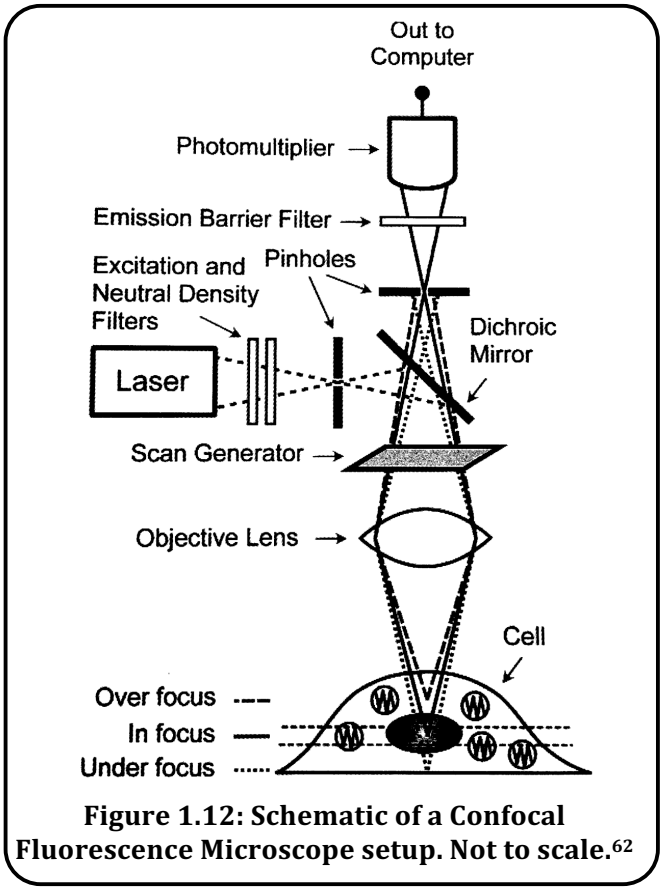

Figure 1.12: Schematic of a Confocal Fluorescence Microscope setup. Not to scale.[62]

Furthermore CFM can perform multi channel/colour detection, forced *via* a master beam splitter, which only reflects selected wavelengths. These selected wavelengths are split using dichroic mirrors (Figure 1.12) and detected over various detectors. This multi–channel detection allows specific staining to be observed and for co–localisation experiments to be conducted. This technique involves the simultaneous administration of two fluorescent probes; one postulated to locate in a certain cellular substructure, and the other of different emissive properties that is known to target the same substructure, *e.g.* a specific organelle.[7] Overlaying the corresponding images allows the degree of co–localisation to be deduced and consequently conclude the target of the new probe.[64]

A further, more recently developed technique is super–resolution fluorescence microscopy. This encompasses a whole range of subtechniques mainly focused on tailored illumination, non–linear optical (NLO) devices and the accurate localisation of single molecule probes.[67] E. Betzig, W. E. Moerner and S. Hell won the Nobel Prize in 2014 for developing some of the specific techniques. These included stimulated emission depletion (STED) microscopy and single molecule microscopy. STED microscopy utilises two laser beams, simultaneously; one to excite a lumophore and a second depletion beam to deactivate it.[67,68] Only lumophores slightly off–centre are illuminated with the depletion beam, which has a node at its centre, resulting in incredibly high resolution.[67] The second technique, single molecule microscopy, relies upon photoswitchable dyes. Multiple images are then collected with only several of the lumophores activated which almost precludes the possibility of overlapping signals; superimposing the images then results in incredibly high resolution images.[67,68] This technique is very good at overcoming photobleaching.[68]

1.5.2 Luminescent Probes for Cell Imaging

Fluorophores were first used in cellular imaging in the early 1900s.[69] For example S. Bommer published the first report of fluorescent imaging of a fixed tissue sample in 1929, in this case using an acriflavine dye.[69] By the 1950s preferential accumulation into certain organelles was well documented[69] and the broad scope of cellular imaging using fluorophores became apparent.

One of the benefits of CFM is that it gives real–time data and therefore probes can be synthesised to give information on species active and present in biological systems. For such biological applications fluorescent probes possess a number of basic requirements. Photophysical requirements include: i) bright emission (high Φ) at tissue compatible wavelengths (preferably low energy, near infra–red); ii) tissue and laser compatible excitation wavelengths; iii) a low tendency of photobleaching; and iv) a method of differentiating from autofluorescence, *i.e.* with large Stokes' shifts or long lifetimes.[1,7,40,64,69,70] Furthermore, biocompatibility and uptake characteristics need to be considered. For example, a luminescent probe for cell imaging by definition needs good membrane permeability (lipophilic, charged), solubility in aqueous media and low toxicity. Furthermore it is desirable for the probe to specifically concentrate in certain cellular substructures with low levels of leaching from the cell.[1,7,64,70,71] Each cell substructure has different probe requirements for targeted localisation.[70] For example preferential staining of the golgi apparatus and endoplasmic reticulum tend to require lipids or inhibitors of protein movement whereas the nucleus (Figure 1.13) often requires DNA binding properties.[7]

Currently most probes used in biological imaging applications are organic structures, stereotypically containing fused aromatic or heterocylic rings (Figure 1.13), however fluorescent proteins have also been applied to cell imaging studies.[5,40] Such organic fluorophores possess large extinction coefficients and quantum yields, however their small Stokes' shift and lifetime values can make detection away from autofluorescence problematic. Furthermore organic fluorophores tend to have a high degree of photobleaching which limits experiment timescales.[40]

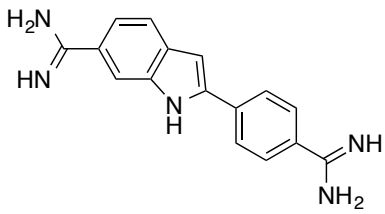

Figure 1.13: Structure of DAPI, a well known nuclear fluorescent stain.

Quantum dot fluorophores overcome many of these photophysical limitations and are also tuneable by varying their constitution and size. However the semi–conductor materials (*e.g.* Cd, Se) used in their synthesis renders quantum dots highly toxic. Therefore quantum dots used for biological imaging require an organic coating which is laborious and expensive.[40,72] In addition, inorganic species have more recently been applied to cell imaging due to their favorable photophysical properties and tuneable nature. Transition metal cellular probes are more common, however lanthanide complexes have also been applied[73] due to their visible to near infra–red emission that is highly tissue compatible and sensitive to the environment (Figure 1.14). Unfortunately the free lanthanide ions are highly toxic and therefore macrocyclic ligands are required, often with a pendant antenna due to the poor direct excitation of lanthanide *4f-4f* electronic transitions.[40,73]

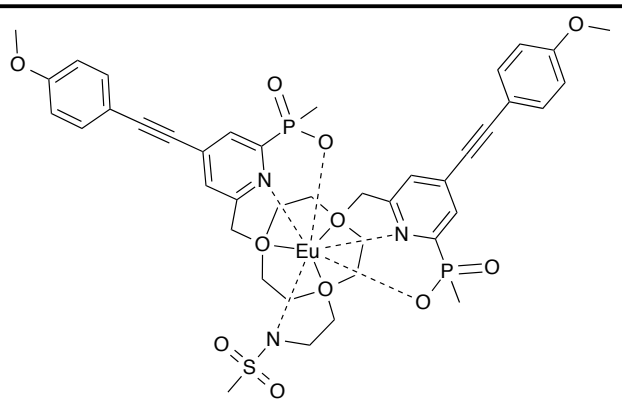

Figure 1.14: A luminescent, pH responsive probe that localises in the endoplasmic reticulum, by Heffern *et al.*[73]

1.5.3 Transition Metal Complexes in Cell Imaging

In the past decade it has become of increasing interest to study the cellular uptake, localisation, toxicity and metabolic fate of luminescent transition metal complexes. These factors are heavily influenced by the lipophilic nature and charge of the species. TM complexes offer a high degree of tuning over both the physical and photophysical characteristics by varying the metal and oxidation state, and furthermore by the stepwise addition of ligands of varying nature.[1,63,70] The presence of a metal is also advantageous because often TM complexes offer long–lived triplet emission that can be exploited to overcome many of the limitations of commercially available organic cellular imaging probes.[1,5] Most commonly, *d*–block cellular imaging agents utilise second or third row TMs with low spin d^6 electronic configurations (Ir(III), Re(I), Ru(II) and Rh(II)) for improved kinetic stability which helps to reduce the toxicity of the metal ion (Figure 1.15).[5,40] Reports of cell imaging with d^8 (Pt(II) and Ir(I)) and d^{10} (Au(I)) TM complexes also exist but are fewer in number.[5,40,63,64]

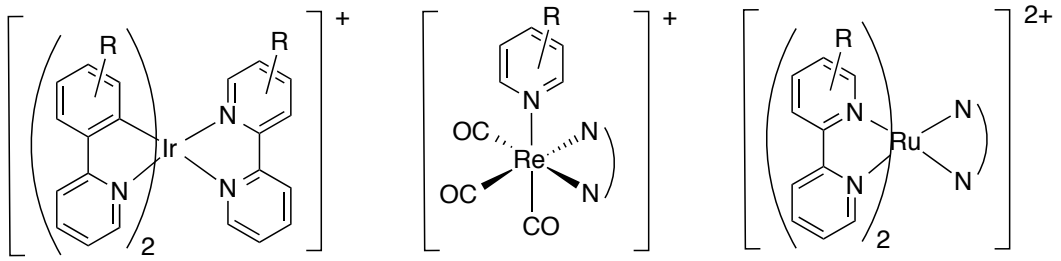

Figure 1.15: Common d^6 cores investigated as CFM probes.

The field of luminescent TM cellular probes centres around iridium(III) cyclometalates of the form $[Ir(C^N)_2(N^N)]^+$ (Figure 1.16) but neutral $[Ir(C^N)_3]$ complexes have also been investigated.[1,5] As expected the cationic nature of the $[Ir(C^N)_2(N^N)]^+$ species is preferred for enhanced uptake *via* active transport[5,64] but both species show application in time–gated methods.[5] Luminescent Ir(III) based compounds (see Section 6.1.4) are largely based around bidentate ligands. Bis–cyclometalated iridium complexes allow modification of the cyclometalating ligand to tune the luminescence and ancillary ligand to tune the uptake within biological systems.[1] Cell imaging using an Ir(III) species was first reported by Lo *et al*. in 2008.[74] The experiments only yielded unspecific cytoplasmic staining. Many examples of non–specific staining with Ir(III) have since been reported[75-78] due to their highly lipophilic nature when compared to other TM metal cores. On the other hand a few later examples have shown localisation in specific organelles such as the nucleolus.[5,79] Rh(III) based imaging probes offer similar behaviour to Ir complexes. Rh(III)

cyclometalates offer shorter wavelength and less intense emission but improved localisation.[5] Two examples in the literature with 4–formyl–2–ppy ligands and varying di–imine ligands showed localisation in both the perinuclear region and nucleus.[80]

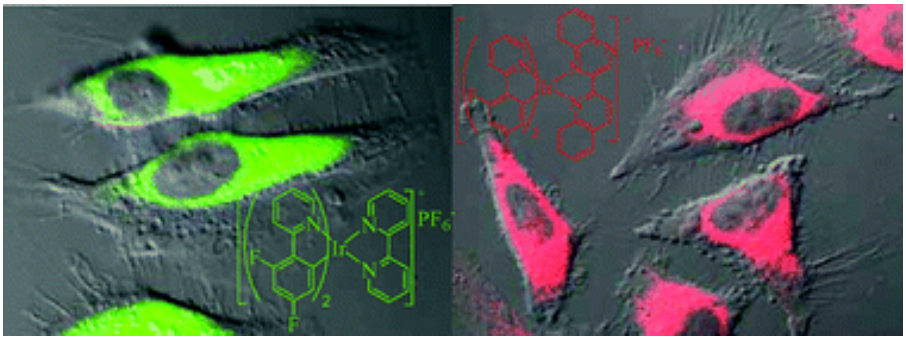

Figure 1.16: Phosphorescent Ir(III) based dyes for CFM by Yu *et al*.[74]

The second most common class of d^6 TM cellular probes are those based around the Re(I) *fac*–tricarbonyl core, with polypyridyl or heterocylic ligands (see Section 2.1.4).[63,64] These compounds again offer a route to ^{3}MLCT emission[5] but with a greater degree of tuning than for Ir(III) complexes.[63] Luminescent Re(I) based compounds are commonly based around a $[Re(N\hat{}N)(CO)_3X]^{0/+}$ model, where X = an interchangeable axial ligand. The axial ligand allows modification of physical properties and the photophysics are generally tuned *via* the bidentate ligand. Importantly varying the axial ligand on Re(I) has a large effect on the biological properties, whereas varying the ancillary ligand on Ir(III) is unpredictable. Furthermore Re(I) often shows improved uptake when compared to Ir(III) due to the smaller size of the Re(I) ion. The charged species are preferred due to the improved uptake however neutral species often possess superior photophysical properties, *i.e.* longer lifetimes and higher quantum yields.[5] In addition the ^{1}MLCT absorption of the neutral species means that excitation with the 405 nm laser is very effective.[5] The first example of a Re(I) *fac*–tricarbonyl species applied in cell imaging was reported in 2007 and revealed that the charge and lipophilicity greatly affected uptake and localisation.[81] These properties can be tuned more effectively than for Ir(III) due to the less lipophilic nature of the Re(I) ion,[5] resulting in the specific staining nature of Re(I) cellular probes. For research purposes such Re(I) imaging agents are used to identify the metabolic fate of ^{99m}Tc radiopharmaceutical drugs that are used in single photon emission computer tomography (SPECT) imaging (Section 3.1.1–3.1.3).[64]

Ru(II) complexes are of interest in cellular imaging studies due to their anticancer properties. $[Ru(N\hat{}N)_3]$ species are the most common class and offer ^{3}MLCT *via* a transition from the $t_{2g} \rightarrow \pi^*$ states.[40] Ru(II) species have shown little control over their

cellular localisation and tend to concentrate in the nucleus due to strong DNA binding affinities.[40] They do however show great promise towards FLIM and O_2 sensing applications.[40]

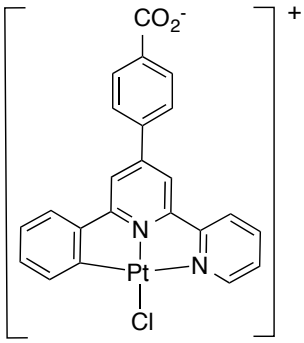

Figure 1.17: 'Switch on' Pt(II) probe for proteins and other analytes that was utilised in CFM.[82]

Although d^6 complexes dominate the field of TM ceullar probes, a few examples of d^8 and d^{10} probes have also been reported. Most d^8 species contain a Pt(II) ion, offering MLCT through a $d_z^2 \rightarrow \pi^*$ transition, often after two–photon excitation techniques.[64] Pt(II) species generally show low toxicities and good uptake, both crucial for biological applications. They commonly form 'turn–on' probes where binding to an analyte within a cell reveals strong emission (Figure 1.17).[64,82]

Recently, d^{10} Au(I) complexes have also been applied to cell imaging (see Section 4.1.6) and, as for Ru(II), are of interest due to their therapeutic nature. Reports of discrete Au(I) complexes are rarer than bimetallic or clustered species that in addition to strong LMCT character, possess aurophillic interactions[5] and LMMCT transitions.[63,64] N–heterocyclic carbene (NHC) species are the most common because they can possess intense emission, long lifetimes and large Stokes' shift values,[63] however they tend to absorb in the UV region which is not ideal for biological applications.[64] Localisation of Au(I) species is varied. Au(I) NHC complexes have shown preferential accumulation in the mitochondria and lysosomes[83] whereas a gold phosphine thionaphthalimide complex was seen to penetrate the nucleus.[84]

1.6 Transition Metals in Therapeutics

TMs play an important role in many biological processes,[85] for example the presence of iron in haemoglobin and other metal ions in redox transfer roles.[86] Consequently many metal ions are found as trace elements (*e.g.* Cu(II), Zn(II)) within the body.[61,87] A deficiency

of these elements can lead to illness, but metal ions can also be toxic to the body.[88,89] Furthermore TM complexes offer a range of different oxidation states that can therefore interact with an array of negatively charged species.[85,90]As a result of the rich biochemistry of TMs, inorganic medicine is a rapidly growing and varied area.[91] New metal based drugs are sought to compliment current organic pharmaceuticals that work *via* a different mode of action.[86,90]

The sudden increase of interest in TMs as therapeutic agents arose after the antiproliferative effects of Cisplatin were first recognised in 1965 by Rosenburg *et al*.[89] Cisplatin is still one of the leading anticancer drugs and is administered to 50–70 % of cancer patients.[90] However, as with all pharmaceuticals, Cisplatin possesses drawbacks such as: i) non–specific toxicity, *i.e.* kills healthy cells;[85] ii) does not treat all cancers;[89] and iii) drug resistance issues.[85] This actively led to the investigation of other TMs as therapeutics[89] that could potentially offer less side–effects.[86] As a result many radiation–based and small molecule therapeutic TM agents[89] have since been reported. These have been discovered to treat a range of illnesses, such as carcinomas, infections, inflammatory diseases, diabetes and neurological disorders.[85,90]

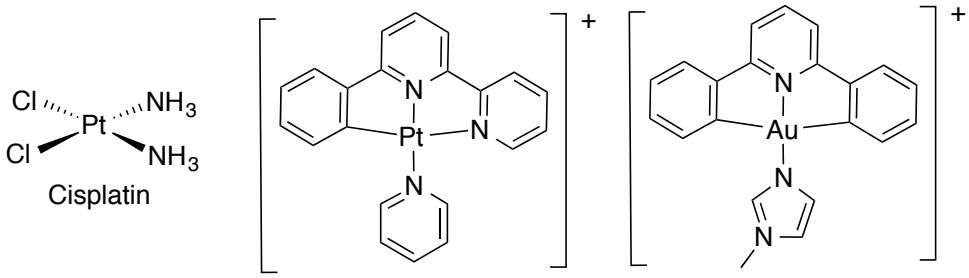

Figure 1.18: Examples of Pt(II) and Au(III) anticancer compounds.

Antiproliferative drugs have received the most attention due to cancer being the current leading cause of human death. Cisplatin (Figure 1.18), the 'flagship' anticancer drug,[86,91] contains a Pt(II) ion and is in fact a pro–drug that is only active upon hydrolysis.[86,88] Binding of Pt(II) to DNA then causes intra-strand cross–links[88,89] that ultimately results in cell death. Many titanium, vanadium, copper, gold, gallium, germanium, tin, chromium, manganese, iron and ruthenium complexes based around Cisplatin have also reported antiproliferative effects with copper, ruthenium and gold being particularly effective.[90] Some Ru(II) compounds have completed Phase I clinical trials[86] and Ru(II) complexes of quinonedi–imine ligands have displayed anticancer properties[85] *via* DNA binding.[86] Studies have also been extended to Ru(II) imidazole and Ru(III) indazole complexes with

great success.[85,87] Au(III) anticancer compounds have a different mode of action to Pt(II) and Ru(II) drugs. Instead of DNA binding, Au(III) anticancer agents target the mitochondria to induce apoptosis.[85,86] Discrete Au(I) based anticancer agents (see Section 4.1.4) typically show poor stability in solution and therefore are synthesised with strong σ–donors within a rigid scaffold (*e.g*. porphyrin and cyclometallates) to improve the stability.[86] Nevertheless, cytotoxicity values comparable to Cisplatin have been reported[86] and the combination of gold nanoparticles to radio– or chemotherapy techniques has also been shown to enhance and improve selectivity of DNA damage.[85]

Aside from the potential anticancer properties of Au(III), Au(I) has been successfully used to treat anti–inflammatory diseases such as rheumatoid arthritis (see Section 4.1.3).[85,91,92] Other less well–known TM therapeutic agents include anti–infective drugs. For example colloidal silver and silver(I) sulfadiazine (Figure 1.19) are commonly used to treat burns and infections.[85] In addition, Ag(I),[86] Cu(II) and Co(II) complexes of pyrimethamine ligands as well as Mn(II) quinolone[93] (Figure 1.19) and N–macrocyclic species also possess antimicrobial and antibacterial properties, with Ag(I) showing enhanced activity.[90] Anti–human immunodeficiency virus (HIV) drugs, targeting HIV reverse transcriptase, is also a rapidly expanding area with rare examples of Ru(II) compounds and oxovanadium thiourea complexes showing promising anti–HIV properties without killing the host cell.[86] Interestingly vanadium salts have also been shown to assist the regulation of glucose within the body through the activation of insulin signalling pathways.[85] Zn(II) ions, aside from their role in neuron signalling pathways (and hence neurological drugs) have also shown this anti–diabetic behaviour.[85]

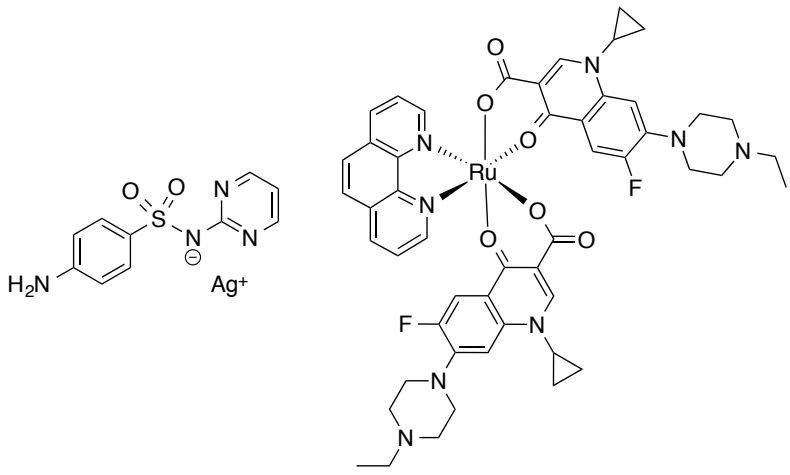

Figure 1.19: Silver sulfadiazine (left) and [Ru(enrofloxacin)$_2$(phen)][93] (right) as examples of antimicrobial agents.

1.7 Project Aims

The work within this thesis aims to develop a range of tuneable luminescent ligands and their corresponding transition metal complexes. Thorough exploration of their photophysical properties would assess their application as biological probes, particularly for use in confocal fluorescence microscopy. This technique allows further understanding of the cellular uptake and localisation of these species to be obtained. In addition, cytotoxicity studies, combined with knowledge of their cellular fate, would allow reveal any therapeutic potential of the species, with a view creating bimodal, cellular imaging and/or therapeutic agents. Careful structural consideration of both the ligand and metal complex should allow for multiple modalities to be utilised, while offering a breadth of physical and localisation characteristics.

1.8 References

1. E. Baggaley, J. Weinstein and J. A. G. Williams, *Coord. Chem. Rev.*, 2012, **256**, 1762-1785.
2. J. R. Lakowicz, in *Principles of Fluorescence Spectroscopy*, Springer, Singapore, 3rd edn., 2006, ch. 1, pp. 1-26.
3. S. Ploem, in *Fluorescent and Luminescent Probes for Biological Activity: A Practical Guide to Technology for Quantitative Real-Time Analysis*, ed. W. T. Mason, Elsevier Ltd., @nd edn., 1999, ch. 1, pp. 3-13.
4. G. F. Imbush, in *Luminescence Spectroscopy*, ed. M. D. Lumb, Academic Press, London, 1st edn., 1978, ch. 1, pp. 1-92.
5. M. P. Coogan and S. J. A. Pope, in *The Chemistry of Molecular Imaging*, eds. N. Long and W. T. Wong, John Wiley and Sons Inc., New Jersey, 1st edn., 2015, ch. 12, pp. 275-298.
6. M. D. Lumb, in *Luminescence Spectroscopy*, ed. M. B. Lumb, Academic Press, London, 1st edn., 1978, ch. 2, pp. 93-148.
7. A. Periasamy, in *Methods in Cellular Imaging*, Oxford University Press, New York, 2001, ch. 1, pp. 5-19.
8. Linköping University Physics Department, Molecular spectroscopy II: Electronic transitions, http://webstaff.itn.liu.se/~igozo/Molecular_Physics/Notes/Lectures12.pdf, Accessed 29th September 2015.
9. A. K. Brisdon, in *Inorganic Spectroscopic Methods*, Oxford University Press, New York, 1998, ch. 4.
10. C. N. Banwell and E. M. McCash, in *Fundamentals of Molecular Spectroscopy*, McGraw-Hill, Maidenhead, UK, 4th edn., 1994, ch. 6, pp. 162-198.
11. P. Atkins, J. de Paula and R. Froedman, *Physical Chemistry: Quanta, Matter and Change*, W. H. Freeman, New York, 2nd edn., 2009.
12. J. R. Lakowicz, in *Principles of Fluorescence Spectroscopy*, Springer, Singapore, 3rd edn., 2006, ch. 8, pp. 278-330.
13. J. A. Broussard, B. Rappaz, D. J. Webb and C. M. Brown, *Nat. Protoc.*, 2013, **8**, 265-281.
14. W. S. Li Dangjuan, Lu Jinjun, *International Conference on Thin Film Physics and Applications*, 2010, **7995**, 799531-799534.
15. J. Hoyland, in *Fluorescent and Luminescent Probes for Biological Activity - A Practical Guide to Technology for Quantitative Real-Time Analysis*, Academic Press, 2nd edn., 1999, ch. 8, pp. 108-113.
16. S. O. S. Barlow, K Lancaster et al., *Journal of Physical Chemistry B*, 2010, **114**, 14397-14407.
17. X. Z. Dong Chen, Jingying Zhang, Yue Wang, *Supramolecular Structure and Materials*, 2015, **36**, 484-488.
18. P. G. B. Saiki, S. Sharmah, S. Dolui, *Polymer International*, 2015, **64**, 437-445.
19. D. W. G. Haridas Kar, Frederic Laquai, Suhrit Ghodh, *Nanoscale*, 2015, **7**, 6729-6736.
20. Z. Liu, W. He and Z. Guo, *Chem. Soc. Rev.*, 2013, **42**, 1568-1600.
21. T. Kálai, E. Hideg, F. Ayaydin and K. Hideg, *Photochem. Photobiol. Sci.*, 2013, **12**, 432-438.
22. M. Kumar, N. Kumar and V. Bhalla, *Chem. Commun.*, 2013, **49**, 877-879.
23. V. Bojinov, N. Georgiev and P. Bosch, *J. Fluoresc.*, 2009, **19**, 127-139.
24. Z. Chen, L. Wang, G. Zou, J. Tang, X. Cai, M. Teng and L. Chen, *Spectrochim. Acta, Part A*, 2013, **015**, 57-61.
25. T. Gunnlaugsson, C. McCoy, R. Morrow, C. Phelan and F. Stomeo, *Arkivoc*, 2003, 216-228.

26. E. Kimura and S. Aoki, *BioMetals*, 2001, **14**, 191-204.
27. J. R. Lakowicz, *Principles of Fluoresence Spectroscopy*, Kluwer/Plenum, New York, 2 edn., 1999.
28. M. H. Lee, J. Kim and J. L. Sessler, *Chem. Soc. Rev.*, 2015, **44**, 4185-4191.
29. H. Woo, Y. You, T. Kim, G. Jhon and W. Nam, *J. Mater. Chem.*, 2012, **22**, 17100-17112.
30. Y. Li, H. Yang, Q. Zhao, W. Song, J. Han and X. Bu, *Inorg. Chem.*, 2012, **51**, 9642-9648.
31. Y. Liu, X. Lv, Y. Zhao, M. Chen, J. Liu, P. Wang and W. Guo, *Dyes Pigm.*, 2012, **92**, 909-915.
32. D. M. P. Mingos, *Essentials of Inorganic Chemistry*, Oxford University Press, New York, 2nd edn., 2007.
33. H. Xiang, J. Cheng, X. Ma, X. Zhou and J. J. Chruma, *Chem. Soc. Rev.*, 2013, **42**, 6128-6185.
34. A. Vogler and H. Kunkely, *Coord. Chem. Rev.*, 2000, **200-202**, 991–1008.
35. A. Vogler, in *Photoinduced Electron Transfer, Part D*, eds. M. A. Fox and M. Chanon, Elsevier, Amsterdam, 1988, ch. 5.5, pp. 179-199.
36. J. Heine and K. Müller-Buschbaum, *Chem. Soc. Rev.*, 2013, **42**, 9232-9242.
37. E. E. Langdon-Jones, A. J. Hallett, J. D. Routledge, D. A. Crole, B. D. Ward, J. A. Platts and S. J. A. Pope, *Inorg. Chem.*, 2013, **52**, 448-456.
38. J. Yarnell, J. Deaton, C. McCusker and F. Castellano, *Inorg. Chem.*, 2011, **50**, 7820-7830.
39. W. W. B. J. P. Paris, *Journal of the American Chemical Society*, 1959, **81**, 5001-5002.
40. V. Fernández-Moreira, F. L. Thorp-Greenwood and M. P. Coogan, *Chem. Commun.*, 2010, **46**, 186-202.
41. L. Bracco, M. Feliz and E. Wolcan, *J. Photochem. Photobiol., A*, 2010, **210**, 23-30.
42. F. Nastasi, F. Puntoriero, S. Campagna, S. Schergna, M. Maggini, F. Cardinali, B. Delavaux-Nicot and J.-F. Nierengarten, *Chem. Commun.*, 2007, **34**, 3556-3558.
43. M. Semeraro, A. Secchi, S. Silvi, M. Venturi, A. Arfuini and A. Credi, *Inorg. Chem.*, 2014, **417**, 258-262.
44. F. Puntoriero, S. Serroni, A. Licciardello, M. Venturi, A. Juris, V. Ricevutoa and S. Campagna, *Dalton. Trans.*, 2001, **7**, 1035-1042.
45. C. Rivas, G. J. Stasiuk, M. Sae-Heng and N. J. Long, *Dalton Trans.*, 2015, **44**, 4976-4985.
46. Y. Jean, in *Molecular Orbitals of Transition Metal Complexes*, Oxford University Press, New York, 1st edn., 2005, ch. 2, pp. 32-96.
47. A. Barbieri, G. Accorsi and N. Armaroli, *Chem. Commun.*, 2008, 2185-2193.
48. N. Armaroli, *Chem. Soc. Rev.*, 2001, **30**, 113-124.
49. N. Armaroli, G. Accorsi, F. Cardinali and A. Listorti, *Top. Curr. Chem.*, 2007, **280**, 69-115.
50. M. Iwamura, S. Takeuchi and T. Tahara, *J. Am. Chem. Soc.*, 2007, **129**, 5248-5256.
51. D. G. Cuttell, S. M. Kuang, P. E. Fanwick, D. R. McMillin and R. A. Walton, *J. Am. Chem. Soc.*, 2002, **124**, 6-7.
52. N. Kaltsoyannis, *J. Chem. Soc., Dalton Trans.*, 1997, 1-12.
53. R. F. Ziolo, S. Lipton and Z. Dori, *J. Chem. Soc.* , 1970, 1124-1125.
54. V. W.-W. Yam, K. L. Cheung, S. K. Yip and K. K. Cheung, *J. Organomet. Chem.*, 2003, **681**, 196-209.
55. Wilhelm Conrad Röntgen - Nobel Diploma; Nobel Prize, http://www.nobelprize.org/nobel_prizes/physics/laureates/1901/rontgen-diploma.html.
56. C. Jones, J. Thornback, P. Sadler, J. Dilworth, D. Williams and D. Taylor, *Medicinal Applications of Coordination Chemistry (RSC Paperbacks)*, Royal Society of Chemistry, 2007.
57. E. Toth, *C. R. Chimie*, 2010, **13**, 700-714.
58. F. L. Thorp-Greenwood and M. P. Coogan, *Dalton Trans.*, 2011, 6129-6143.

59. L. E. Jennings and N. J. Long, *Chem. Commun.*, 2009, 3511-3524.
60. C. Rivas, G. J. Stasiuk, F. Minuzzi, G. A. Rutter and N. J. Long, *Inorg. Chem.*, 2013, **52**, 14284-14293.
61. G. J. Stasiuk, F. Minuzzi, M. Sae-Heng, C. Rivas, H.-P. Juretschke, L. Piemonti, P. R. Allegrini, D. Laurent, A. R. Duckworth, A. Beeby, G. A. Rutter and N. J. Long, *Chem. Eur. J.*, 2015, **21**, 5023-5033.
62. C. J. R. Sheppard, in *Fluorescent and Luminescent Probes for Biological Activity - A Practical Guide to Technology for Quantitative Real-Time Analysis*, Academic Press, 2nd edn., 1999, ch. 21, pp. 303-309.
63. F. L. Thorp-Greenwood, *Organometallics*, 2012, **31**, 5686-5692.
64. F. L. Thorp-Greenwood, R. G. Balasingham and M. P. Coogan, *J. Organomet. Chem.*, 2012, **714**, 12-21.
65. T. Terai and T. Nagano, *Curr. Opin. Chem. Biol.*, 2008, **12**, 515-521.
66. R. Yuste, *Nat. Methods*, 2005, **2**, 902-904.
67. L. Schermelleh, R. Heintzmann and H. Leonhardt, *J. Cell Biol.*, 2010, **190**, 165-175.
68. E. Betzig, S. W. Hell and W. E. Moerner, Nobel Media 2014.
69. F. H. Kasten, in *Fluorescent and Luminescent Probes for Biological Activity - A Practical Guide to Technology for Quantitative Real-Time Analysis*, Academic Press, 2nd edn., 1999, ch. 2, pp. 17-39.
70. K. K.-W. Lo, A. W.-T. Choi and W. H.-T. Law, *Dalton Trans.*, 2012, **41**, 6021-6047.
71. V. Fernández-Moreira, M. L. Ortego, C. F. Williams, M. P. Coogan, M. D. Villacampa and M. C. Gimeno, *Organometallics*, 2012, **31**, 5950-5957.
72. J. K. Jaiswal, E. R. Goldman, H. Mattoussi and S. M. Simon, *Nat. Methods*, 2004, **1**, 73-78.
73. M. C. Heffern, L. M. Matosziuk and T. J. Meade, *Chem. Rev.*, 2014, **114**, 4496-4539.
74. K. K. Lo, P. K. Lee and J. S. Y. Lau, *Organometallics*, 2008, **27**, 2998-3006.
75. M. Yu, Q. Zhao, L. Shi, F. Li, Z. Zhou, H. Yang, T. Yia and C. Huanga, *Chem. Commun.*, 2008, 2115-2117.
76. D. L. Ma , H.-J. Zhong, W.-C. Fu, D. S.-H. Chan, H.-Y. Kwan, W.-F. Fong, L.-H. Chung, C.-Y. Wong and C.-H. Leung, *J. Photochem. Photobiol., B*, 2013, **8**, 551-557.
77. X. Wang, J. Jia, Z. Huang, M. Zhou and H. Fei, *Chem. Eur. J.*, 2011, **17**, 8028-2032.
78. L. Murphy, A. Congreve, L.-O. Palsson and G. Williams, *Chem. Commun.*, 2010, **46**, 8743-8745.
79. Y. H. S. Moromizato, T. Suzuki, Y. Matsuo, R. Abe, S. Aoki, *Inorg. Chem.*, 2012, **51**, 12697-12706.
80. S. K. Leung, K. Y. Kwok, K. Y. Zhang and K. K.-W. Lo, *Inorg. Chem.*, 2010, **49**, 4984-4995.
81. A. J. Amoroso, M. P. Coogan, J. Dunne, E., V. Fernández-Moreira, J. B. Hess, A. J. Hayes, D. Lloyd, C. Millet, S. J. A. Pope and C. Williams, *Chem. Commun.*, 2007, 3066-2068.
82. P. Wu, E. L.-M. Wong, D.-L. Ma, G. S. M. Tong, K. M. Ng and C. M. Che, *Chem. Eur. J.*, 2009, **15**, 3652-3656.
83. P. J. Barnard, M. V. Baker, S. J. Berners-Price and D. A. Day, *J. Inorg. Biochem.*, 2004, **98**, 1642-1647.
84. C. P. Bagowski, Y. You, H. Scheffler, D. H. Vlecken, D. J. Schmitz and I. Ott, *Dalton Trans.*, 2009, 10799-10805.
85. S. Rafique, M. Idrees, A. Nasim, H. Akbar and A. Athar, *Biotechnol. Mol. Biol. Rev.*, 2010, **5**, 38-45.
86. R. W.-Y. Sun, D.-L. Ma, E. L.-M. Wong and C.-M. Che, *Dalton Trans.*, 2007, 4884-4892.
87. N. Farrell, *Transition Metal Complexes as Drugs and Chemotherapeutic Agents*, Kluwer Academic Publishers, Netherlands, 1989.
88. S. J. Lippard, in *Bioinorganic Chemistry*, University Science Books, USA, 1st edn., 1994, ch. 9, pp. 505-593.

89. Y.-J. Ho, presented in part at the Chem 535 Fall, Illinois University, 2010.
90. A. A. Warra, *J. Chem. Pharm. Res.*, 2011, **3**, 951-958.
91. P. Sadler and Z. Guo, *Pure & Appl. Chem.*, 1998, **70**, 863-871.
92. O. M. N. Dhubhghaill and P. J. Sadler, in *Metal complexes in cancer chemotherapy*, ed. B. K. Keppler, VCH, Weinheim, 1993, pp. 221-248.
93. M. Zampakou, M. Akrivou and E. G. Andreadou, *J. Inorg. Biochem.*, 2013, **121** 88-99.

Chapter 2

Synthesis and Characterisation of Rhenium Tricarbonyl Di–imine Complexes, Axially Functionalised with Naphthalimide Ligands

2.1 Introduction

This chapter reports a series of *fac*–$Re(CO)_3(N^N)(LX)]BF_4$ complexes (where N^N = a di–imine donor), axially substituted with functionalised naphthalimide ligands. The core investigations centre on both the free ligands' and complexes' photophysical properties. The feasibility of these compounds towards use in cellular imaging and photodynamic therapy (PDT) techniques is explored herein.

2.1.1 Properties of Functionalised Naphthalimide (NI) Ligands

1,8–Naphthalimide derivatives have been of great interest due to a number of highly favorable properties. These derivatives are straightforwardly synthesised (with excellent purity and on large scales) with a high degree of stepwise functionalisation.[1] Firstly the NI derivatives are synthesised from a commercially available anhydride species by reaction with an amine and similarly the 3– or 4–positions of the ring are commonly substituted for amino or nitro groups (Figure 2.1).[2] The high degree of functionalisation of NI ligands has led to a breadth of applications including: cell imaging, DNA binding, small molecule probes, anticancer drugs[2] and antiviral agents towards HIV.[3]

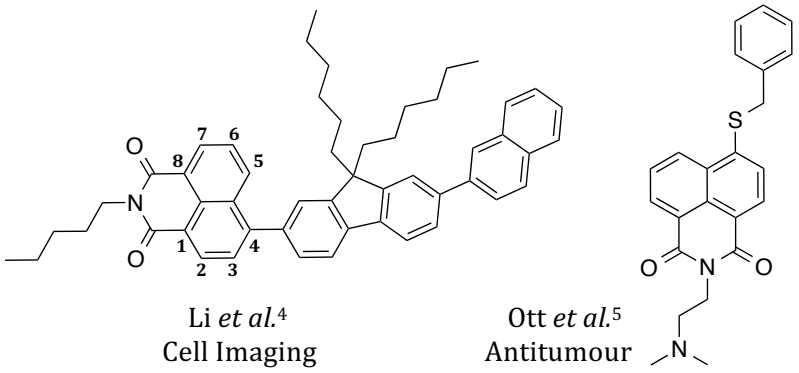

Li *et al.*[4] Cell Imaging

Ott *et al.*[5] Antitumour

Figure 2.1: Examples of functionalised NI ligands.

NI ligands are known to possess very high luminescence efficiency[1] in the visible region[6] when an electron donating group is substituted at the 4-position,[7] often exhibiting yellow-green fluorescence.[8] Further desirable properties include high photostability[8,9] and large Stokes' shifts[1] (which allows the filtering of autofluorescence and a reduction of fluorescence quenching). These photophysical attributes arise due to the fact that NI ligands are intramolecular charge transfer (CT) fluorophores,[6] also often resulting in solvatochromic behaviour.[10]

Importantly, highly functionalised 1,8–NI derivatives can de designed according to utilisation by modulating both physical and photophysical properties. With regards to photophysical properties the CT, that is very sensitive to the nature of the substituent and environmental conditions,[2,9,11,12] is induced upon placing an amine on the ring: increasing the electron donating ability of this group leads to a bathochromic shift of the emission wavelengths.[11] A further advantage of placing an amine at a ring position for these photoinduced electron transfer (PeT) active systems is that the basicity is affected and therefore NI probes are often highly pH dependant.[13,14] Aside from photophysical characteristics, the imide and amino/nitro substituents can also be used to tune properties such as solubility,[15] targeting and cell localisation making NI ligands suitable to a range of biological[2,10] and sensing systems.

2.1.2 Naphthalimide (NI) Ligands as Fluorescent Probes

1,8–NI derivatives are currently being utilised in a range of areas[8] including: i) colouration of polymers;[7] ii) laser active media; iii) fluorescent markers; iv) analgesics; v) light emitting diodes (LEDs)/ liquid crystal displays; and vi) fluorescence switches/ion probes. Recently the latter has been widely investigated due to the CT nature of the fluorophores[6] where a 'switch' of fluorescence properties occurs upon binding of the analyte. This feature is aided by the capability of the NI ligand unit to be designed into the very popular 'fluorophore–(spacer)–receptor' framework; akin to those first developed by De Silva *et al*. in 1992.[16]

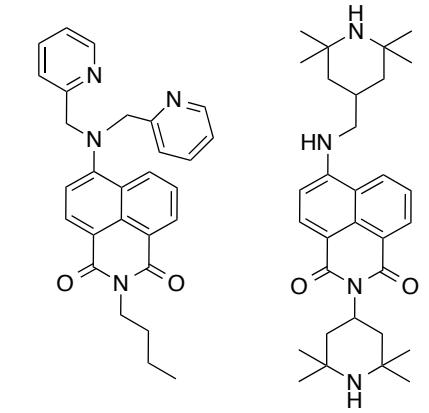

Wang *et al*.[1] 'turn–off' sensor

Bojinov *et al*.[17] 'turn–on' sensor

Figure 2.2: Examples of fluorescence NI probes.

Previous examples by Wang *et al.*[1] (Figure 2.2) show incredible 'turn off' changes to absorption and emission spectra upon coordination to copper and zinc. The signals were

blue and red shifted respectively, with a significant hypochromic shift, proposedly due to PeT[17] activation. This leads to quenching of the triplet state[8] that sits on the NI unit. The existence of this triplet state means that these molecules also have a potential use for O_2 sensing[9] or singlet oxygen generation for photodynamic therapy.

On the other hand, examples of 'turn on' sensors by Bojinov *et al*.[8,17] (Figure 2.2) exhibit an increase in emission intensity upon binding to a cation because this event inhibits PeT.[8] Most 'turn–on' structures contain an amino substituent that quenches the fluorescence *via* PeT from the unbound amino group to the fluorophore. In the presence of the sensing species, for example Zn(II), the lone pair of the amine group is no longer (energetically) available to undertake PeT.[18,19]

2.1.3 *fac*–[Re(CO)$_3$(N^N)(X)] Complexes

Many reports involving d^6 Re(I) species have focused on *fac*–[Re(CO)$_3$(N^N)(X)] species due to their stability in a range of media, photophysical properties and the ability to add ligands in a stepwise fashion. The latter property allows both the physical (*e.g*. solubility, lipophilicity, uptake) and photophysical properties to be tuned.[20-22] Bipyridine (bpy) and 1,10–phenanthroline (phen) di–imine species are the most common with neutral complexes containing anionic ligands at the axial position (X = Cl, Br).[23] Cationic Re(I) complexes, where commonly X = a pyridine derivative, are more desirable due to enhanced photophysical properties[23] including: i) large Stokes' shifts (150–200 nm); ii) visible emission (500–600 nm);[24] iii) lifetimes from hundreds of nanoseconds up to microseconds;[20,24] iv) favourable quantum yields commonly between 1–10 %;[25] and v) solvent dependent emission (due to CT character). It is these numerous, favourable photophysical properties that have led to *fac*–[Re(CO)$_3$(N^N)(X)]$^+$ species being utilised in a range of applications[22,26] (organic light emitting diodes (OLEDs), fluorescence imaging, biological sensing and DNA binding).

For *fac*–[Re(CO)$_3$(N^N)(X)]$^+$ species the ^{3}MLCT state is known to localise on the di–imine ligand[27] and properties can therefore be tuned *via* the ligand system.[28] For photophysical properties this is particularly evident when varying the di–imine ligand. For example, a phenanthroline–NI conjugate has been reported to give a 3000 fold increase in the lifetime of such a species due to a "bidirectional 'ping–pong' energy transfer"[29] and non–labile ligands reduce toxicity.[23] In addition tuning the axial ligand can be useful for properties such as solubility.

2.1.4 Re(I) Carbonyl Di–imine (Re–CDI) Complexes for Sensing and Imaging

Re(I)–CDI complexes have been extensively applied as fluorescent probes and imaging agents due to the phosphorescent nature exhibited when Re(I) forms complexes with di–imine species.[30] Re–CDI conjugates have been used to sense a range of analytes such as anions/cations, pH, O_2 and even volatile organics.[21] Furthermore Re(I)–CDI complexes offer a very elegant design of ratiometric sensors whereby the equatorial di–imine ligand provides the ^{3}MLCT reference signal that is incapable of the sensing event; the axial position can be exploited as the fluorescent chromophore dependent on the sensing event.

Re–CDI polypyridyl complexes are a very common choice for fluorescence imaging.[27] $[Re(CO)_3(bpy)(PyX)]$ species, where PyX is a substituted pyridine, are synthesised with ease and varying PyX can majorly vary both physical and photophysical properties. The first example of these species applied in imaging was reported by Amoroso *et al*. in 2007,[31] employing a pyridine substituted with a simple ester moiety (Figure 2.3).

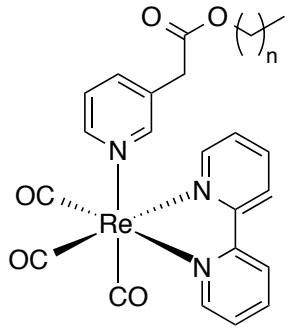

Figure 2.3: First Re polypyridyl species applied to fluorescence imaging.[31]

Since then the field has opened up to more elegant and complexly substituted pyridine groups that can offer additional benefits and functionality towards bimodal techniques, such as combinations with metal ion detection[32] and DNA sensing probes.[33] Aside from steady–state imaging an alternative technique is fluorescence lifetime imaging microscopy (FLIM) that can be used to detect other analytes, such as O_2, and calculate their concentration.

The fluorescence cell imaging applications of Re complexes are only possible because they can readily be taken into cells. Uptake of Re(I) complexes into cells is enhanced by the cationic nature and the lipophilicity associated with the metal core. Providing lipophilic or hydrophilic substituents on the ligands can furthermore modulate the uptake (and

localisation). In addition, modulation of the ligand systems can help overcome common issues of Re(I) probes. For example one drawback of Re(I) polypyridyl species is that the excitation profiles, although broad, still sit in the UV region of the spectrum; appending fluorophores as light harvesters can allow compatible wavelengths and lasers to be used.

2.1.5 Singlet Oxygen Generation (SOG) and Photodynamic Therapy (PDT)

Probes that can sense reactive oxygen species (ROS) or ground state $^3O_2$ are of increased interest due to their scope for use in SOG and therefore PDT. Light has been used for decades to treat many skin–related diseases[34-37] and more recently PDT has been shown to stimulate cell damage or death, towards potential anticancer treatments.[34,35,38]

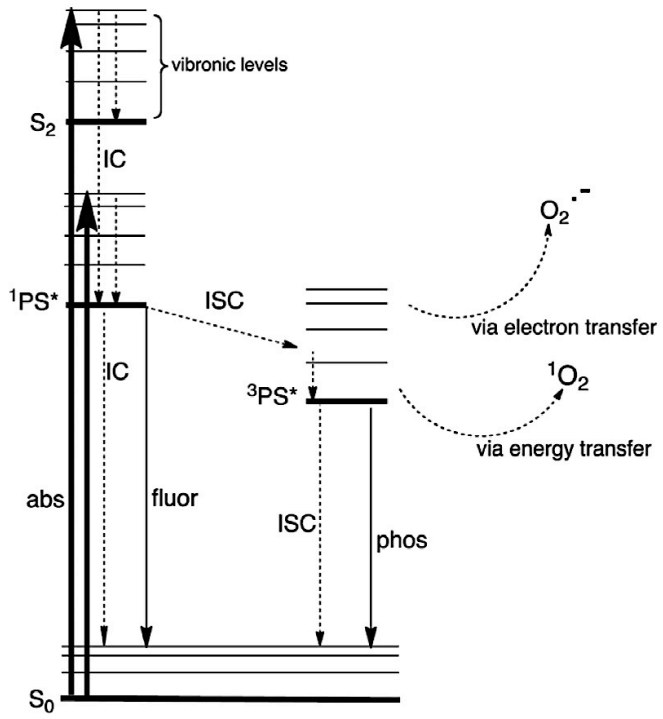

Figure 2.4[38]: Simplified energy level diagram for SOG (abs = absorption; fluor = fluorescence; phos = phosphorescence, ISC = intersystem crossing, IC = internal conversion).

PDT begins with irradiation of a photosensitiser (PS) that reacts with $^3O_2$ to form $^1O_2$ radicals *via* electron or energy transfer (Figure 2.4). It is key that the PS does not react with $^3O_2$ if no radiation is applied. *Via* the electron transfer mechanism, radical cascades ultimately lead to the formation of hydrogen peroxide and hydroxyl radicals which, being highly reactive, are cytotoxic species. *Via* energy transfer to produce $^1O_2$ it is the $^1O_2$ itself that delivers the cytotoxic effects.[38]

Due to the mechanism for SOG a long–lived excited triplet state is desired in the PS which had led to phosphorescent metal complexes being the focus of study.[38,39] However a few examples of NI based systems have been reported in the literature[9] due to their PeT properties that could induce electron transfer to form $^1O_2$. The capability of NI species towards such applications can be probed. Analysing the response of NI species' photophysical properties to oxygen can determine their capability to such applications. Oxygen is a known quenching mechanism of triplet states[40] and therefore changes in luminescence intensity, wavelengths, quantum yields and lifetimes can be expected.

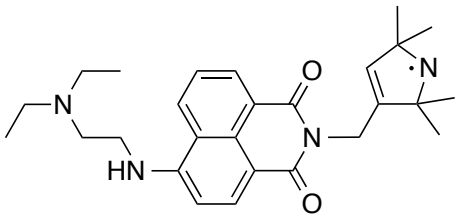

Figure 2.5: Example of NI based ROS species by Kálai *et al.*[9]

The example reported by Kálai *et al.*[9] (Figure 2.5) contained a paramagnetic amine substituent on the NI ring and therefore the response to ROS species was determined by measured decreases in the electron paramagnetic resonance (EPR) TEMPO signal (TEMPO = 2,2,6,6–tetramethyl–1–piperidinyloxyl).

2.2 Aims

$[Re(CO)_3(N^N)(L)]$ complexes are widely utilised in a range of applications for which the desired properties greatly differ. Tuning the properties of $[Re(CO)_3(N^N)(L)]$ complexes is possible through varying the ligand system and therefore investigation towards alternative ligand types is key.

This chapter aimed to develop the synthetic chemistry of a range of novel, fluorescent, functionalised naphthalimide ligands containing a pyridine binding site. Therefore investigations were completed into the coordination chemistry of these ligands with Re(I) for which many $[Re(CO)_3(N^N)(PyX)]$ species are known.

Once synthesised it was intended for both ligands and complexes to be spectroscopically and analytically characterised. This provided data indicating their synthesis, with spectroscopic studies being particularly important for characterising the complexes and their electronic properties. Assessing their photophysical properties furthermore revealed the feasibility of these ligands and complexes for use within and towards single–molecule, bimodal, cell imaging and therapeutic agents.

2.3 Results and Discussion

2.3.1 Ligand Synthesis and Characterisation

Ligands (**L1–7**) were isolated from up to two steps (Scheme 2.1) from commercially available (4–chloro–)1,8–naphthalic anhydride, whereas many literature examples are formed from either the 4–bromo[10,41] or 4–nitro[8,17] derivatives. The first step involved conversion to the (4–chloro–) naphthalimide (NI) species (**L1–3**) which functionalised the imide position with a pyridine group capable of binding to a range of metals. These condensation reactions were facile (yields > 80 %) and conducted by heating the appropriate amine with (4–chloro–)1,8–naphthalic anhydride, in ethanol.[42] Reaction progression was indicated by a darkening of the reaction mixture from pale yellow to brown. In addition it could be followed more accurately by thin layer chromatography (TLC). Most products were found to be spectroscopically pure after filtering from the cooled reaction mixture and washing with an appropriate solvent. Any intermediate products formed (*i.e.* non ring closed) could be separated by dissolving the desired product (**L1–3**) in chloroform and removing any insoluble species by filtration.

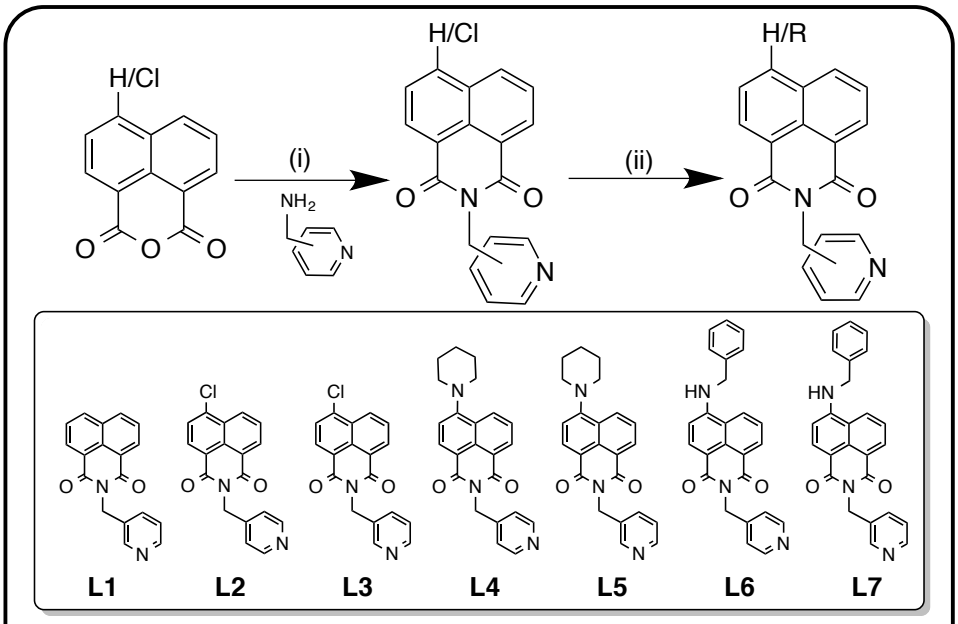

[a](i) 3– or 4–picolylamine, EtOH; (ii) appropriate amine, DMSO

Scheme 2.1: Synthetic route to the ligands[a].

Successful formation of the (4–chloro) NI species (**L1–3**) was evident in the ^{1}H NMR spectra. A common, identifiable feature when forming the imide species was the peak for N–CH_2 with a noticeable singlet at 5.4–4.9 ppm (Figure 2.6).

Upon forming the NI species the 4–chloro position of **L2–3** becomes susceptible to aromatic nucleophilic attack due to the electron withdrawing nature of the imide group. Hence **L2–3** were further functionalised by substitution with a simple amine at the 4–position. Successful aromatic nucleophilic substitution (S_NAr) reactions proceeded for both **L2** and **L3** with piperidine, however with benzylamine it became apparent that the reactivity of **L2** was enhanced. For these simple amines reaction completion was observed by TLC (dichloromethane) after 2 hours of heating in DMSO at 70 °C with 4 equivalents of amine.[7] However longer reaction times can be required for more sterically encumbered or less electronically activated amines (see Chapters Three and Four). The literature based work up involved precipitation of the product from the reaction mixture, induced by the addition of water and neutralisation with 1 M HCl. For **L4–7** improved yields (70–95 %) and cleaner products were observed from an extraction and aqueous work up, followed by precipitation of the product using petroleum ether and minimal chloroform.

Successful formation of **L4–7** was easily determined by ^{1}H and ^{13}C{^{1}H} NMR spectroscopy. Upon functionalisation at the 4–position of the NI, there was a significant change of the resonance for the NI C3–proton which tends to shift from being part of a NI–aromatic multiplet (7.8–8.4 ppm depending on the R groups) to a distinctive doublet at *ca.* 6.4 ppm; shielded more greatly by nitrogen compared to chlorine (Figure 2.6). For **L6–7** (that comprise a secondary amine at the 4–position) there was also a broad triplet (N*H*) at *ca.* 5.7 ppm. In addition the ^{13}C{^{1}H} NMR spectra showed a shift of two of the C=C resonances to below 115 ppm whereas in **L2–3** all C=C resonances were above 120 ppm.

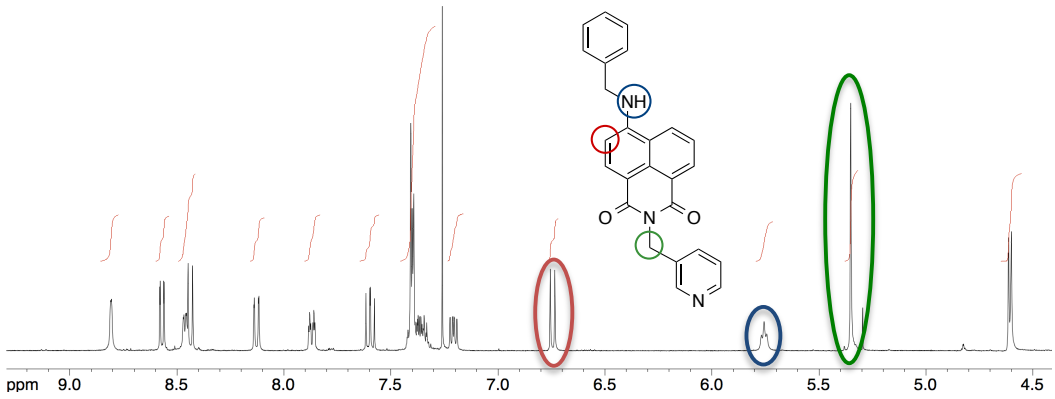

Figure 2.6: ^{1}H NMR spectra ($CDCl_3$, 400 MHz) of L7 highlighting common identifiable resonances of NI ligands.

L2 and **L4** had previously been reported in a patent[43] however all products formed from **L3** were novel. All novel ligands were characterised by high resolution mass spectrometry

(HRMS) (ES^+), showing the $[M+H]^+$ cation peak in all cases. IR spectroscopy showed two C=O bands at *ca.* 1690 and 1650 cm^{-1}, with **L2–3** having an additional strong peak at *ca*. 780 cm^{-1} (C–Cl) and **L6–7**, with a secondary amine, showing the expected peaks for the N–H bend and stretch modes *ca.* 3300 and 1560 cm^{-1}.

Due to the relative ease of formation of **L4–7**, variations with more complex amines, such as cyclen derivatives and 1–aminoanthraquinone were attempted. It became apparent that the sterics and nucleophilicity of the amine have a large role to play in the ease of formation. Due to the lack of success using the same conditions for these more complex amines, different reaction conditions were investigated. Firstly the addition of a little organic base (NEt_3) was employed, followed by using 2–methoxyethanol[1,44] as an alternative solvent for DMSO. These reactions were again unsuccessful and showed no reaction *via* ^1H NMR spectroscopy or mass spectrometry.

As a final effort cross–coupling with Pd catalysts was attempted requiring the synthesis of a $Pd(dba)_2$ catalyst,[45-48] however the reaction was again unsuccessful. This was not helped by a number of deviations from the stated method[49] having to be employed *e.g*. a different phosphine co–ligand. These variants with more complex amines were not pursued any further.

2.3.2 Complex Synthesis and Characterisation

A rhenium precursor complex was first synthesised so that it would then be correctly designed for facile coordination to the set of NI ligands. The precursors were made by well–known literature methods.[21,50,51] Once the precursors had been synthesised, **L1–7** could then substitute the labile acetonitrile ligand at the axial position. This was achieved with refluxing the $[Re(CO)_3(N\text{^}N)(MeCN)]BF_4$ precursors and the appropriate ligand (in slight excess) in chloroform, under a dinitrogen atmosphere for 12 hours[26] (Scheme 2.2). Purification of the yellow powders was very straightforward; reprecipitation yielded spectroscopically pure products in high yields (mostly > 80 %) by exploiting the high solubility of the free ligand in diethyl ether. Interestingly **L2/4/6,** that contain *N*–4–picolylamine, seemed to form with more ease comparative to the *N*–3–picolylamine variants, presumably on steric grounds. **L1–7** were successfully reacted with bpy and/or phen precursors of Re(I) to form thirteen novel complexes that were fully characterised by ^1H and $^{13}C\{^1H\}$ NMR spectroscopies and HRMS. **[Re(bpy)(L1)]** was not synthesised because **[Re(phen)(L1)]** was made purely for comparative reasons.

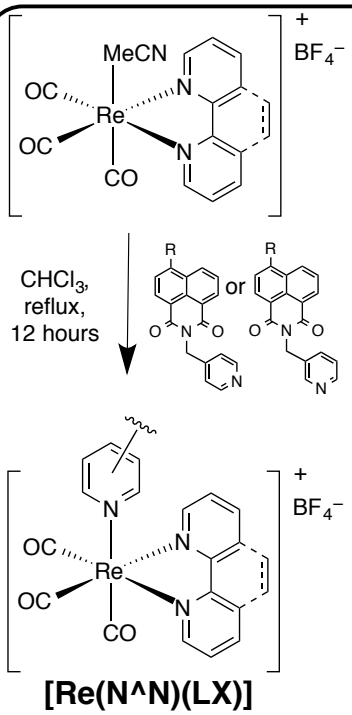

[Re(N^N)(LX)]

Complex	N^N	*N*–X–picolyl X =	R =
[Re(bpy)(L2)]	bpy	4	Chloro
[Re(bpy)(L4)]			Piperidine
[Re(bpy)(L6)]			Benzylamine
[Re(bpy)(L3)]		3	Chloro
[Re(bpy)(L5)]			Piperidine
[Re(bpy)(L7)]			Benzylamine
[Re(phen)(L2)]	phen	4	Chloro
[Re(phen)(L4)]			Piperidine
[Re(phen)(L6)]			Benzylamine
[Re(phen)(L1)]		3	H
[Re(phen)(L3)]			Chloro
[Re(phen)(L5)]			Piperidine
[Re(phen)(L7)]			Benzylamine

Scheme 2.2 Synthetic route to complexes [Re(N^N)(LX)] where N^N = bpy or phen.

Successful coordination was firstly identified through changes in the proton resonances of the ligands and the appearance of additional peaks associated with the bpy and phen co–ligands (Figure 2.7). ^{1}H NMR spectroscopy was used to compare the N_{imide}–CH_2 groups for the Re complexes to those in the corresponding free ligands. For this peak the values did not shift as significantly as expected upon coordination (*ca.* 0.2 ppm). Therefore other characterisation techniques became key in supporting coordination.

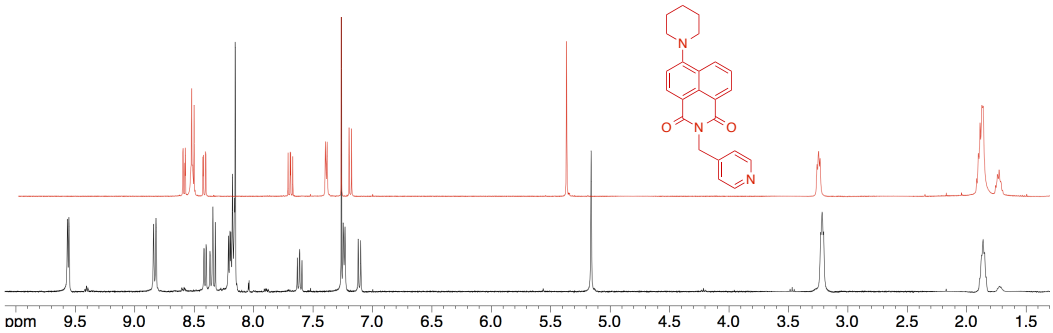

Figure 2.7: Comparison of the ^{1}H NMR spectra ($CDCl_3$, 400 MHz) of L4 (red) and [Re(phen)(L4)] (black).

^{13}C{^{1}H} NMR spectroscopy easily identified the metal bound and ligand based C=O resonances. The resonances for metal–carbonyls were typically higher (*ca.* 180 ppm) than that for imide–carbonyls (*ca.* 160 ppm).

HRMS (ES^+) was also employed and for each sample produced a cluster of peaks for the $[M]^+$ ion and also commonly $[M+MeCN]^+$. The presence of Re(I) was confirmed by the expected isotopic distribution (^{185}Re, 37.4%; ^{187}Re 62.6%).[52] Furthermore, IR spectroscopy confirmed the proposed geometry which, akin to the $^{13}C\{^1H\}$ NMR spectra, showed two metal carbonyl stretches at *ca*. 2030–1900 cm^{-1} and a slight shift in the organic carbonyl peaks. IR spectroscopy data supported the assignment of approximated C_{3v} symmetry, which predicts two carbonyl stretches for the $[Re(CO)_3(X)_3]$ complexes. All complexes possess an additional peak at *ca.* 1050 cm^{-1} when compared to the free ligands suggesting that this peak arises from a Re–N bond.

2.3.3 Single Crystal X–ray Diffraction Studies

As well as solution state characterisation a single crystal structure determination was obtained for **[Re(phen)(L4)]** (Figure 2.8). Data collection, refinement and structure solution was conducted by Dr Peter Horton at the UK National Crystallography Service, Southampton. The data collection parameters are shown in Appendix 2.7.1. The structural analysis confirmed the proposed structure with a distorted octahedral coordination geometry for rhenium, involving a *fac*–tricarbonyl arrangement combined with chelating di–imine donor and axially N–coordinated **L4**.

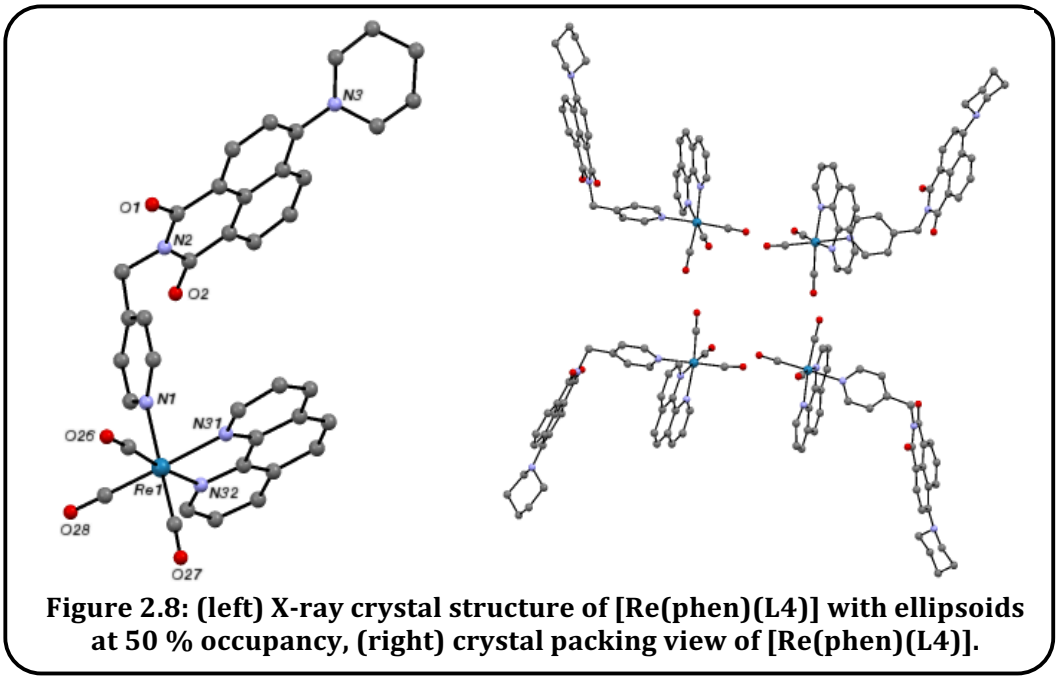

Figure 2.8: (left) X-ray crystal structure of [Re(phen)(L4)] with ellipsoids at 50 % occupancy, (right) crystal packing view of [Re(phen)(L4)].

The bond lengths (Table 2.1) associated with the coordination sphere are typical of related Re(I) complexes.[53-56] The Re–CO distances lie within the range 1.875–1.948 Å whilst the Re–N distances were typically longer at 2.173–2.221 Å.

Table 2.1: Selected bond lengths and bond angles for [Re(phen)(L4].

Bond Lengths / Å	
Re1–C28	1.095(18)
Re1–C27	1.921(13)
Re1–C26	1.945(11)
Re1–N31	2.178(13)
Re1–N1	2.189(10)
Re1–N32	2.190(9)
Bond Angles / °	
C28–Re1–C27	88.4(6)
C28–Re1–C26	85.6(6)
C27–Re1–C26	87.2(5)
C28–Re1–N31	172.9(5)
C27–Re1–N31	96.1(5)
C26–Re1–N31	100.0(5)
C28–Re1–N1	92.6(6)
C27–Re1–N1	179.1(5)
C26–Re1–N1	92.7(4)
N31–Re1–N1	83.0(4)
C28–Re1–N32	98.4(5)
C27–Re1–N32	95.9(4)
C26–Re1–N32	175.0(5)
N31–Re1–N32	75.7(4)
N1–Re1–N32	84.2(3)

Unlike similar examples in the literature[56] the Re–N bond lengths to the axial mono–dentate pyridine are very similar to those associated with the chelating di–imine. This could be explained by the lack of distortion along the axial plane (C_{ax}–Re–N_{ax} 179.1(5)°) compared to the equatorial plane (C_{eqt}–Re–N_{eqt} 172.9(5)° and 175.0(5)°), resulting in a marginal strengthening of the Re–N_{ax} bond and destabilisation of the Re–$N_{di–imine}$ bond. Aside from confirming the proposed coordination geometry several key parameters are worth mention. Firstly the Re(I)–bound carbonyl bond lengths (*ca.* 1.15 Å) were shorter than the ligand carbonyl bond lengths at *ca*. 1.23 Å which agree well with similar

ligands.[11,57,58] As expected there was a noticeable difference between the bond lengths of sp^2 and sp^3 hydridised C and N atoms. C=C bond lengths were found *ca*. 1.39 Å whilst C–C piperidine lengths were *ca*. 1.53 Å. Sp^2 hybridised nitrogen atoms (N1/31/32) had average C–N bond lengths *ca*. 1.33 Å, whilst the two sp^3 nitrogen atoms (N2/3) formed C–N bonds of *ca*. 1.44 Å.

Interestingly this example shows the NI core of **L4** positioned over and relatively co–planar to the phen co–ligand. Nevertheless, despite the high degree of planarity of both aromatic ligands, this arrangement does not appear to be intermolecular π–π stacking interactions (C_{naph}–C_{phen} 7.26–8.40 Å). For a true π–stacked conformation distances in the range of 3.3–3.8 Å[59,60] would have been expected and therefore it was concluded that this conformation was due to crystal packing effects.

2.3.4 UV–Vis Absorption Spectroscopy

Ligand Properties

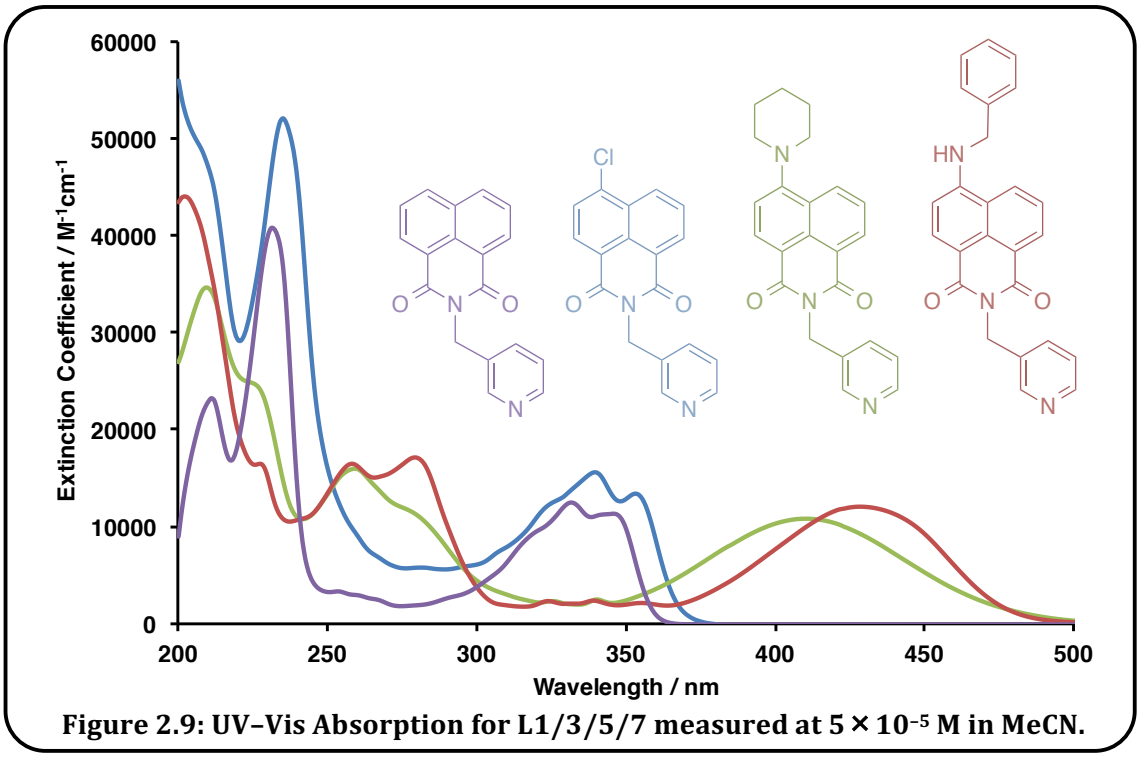

Figure 2.9: UV–Vis Absorption for L1/3/5/7 measured at 5×10^{-5} M in MeCN.

All ligands possessed strong π→π* bands below 350 nm (Figure 2.9). The structured peak observed at *ca.* 340 nm for **L1–3** shifts to *ca*. 270 nm in **L4–7**. Comparison with the unsubstituted ligands (**L1–3**) showed that the addition of a 4–amino substituent induced weaker but tuneable ICT bands[2,10,29,61] (formally of n→π* character), centred at 410–440 nm in **L4–7**. Wu *et al.*[12] suggested that the ICT band is weakened by a lack of planarity

between the NI ring and any 4–amino substituent, thus to some extent inhibiting CT and destabilising the excited state. The tuneablilty was dependent on the availability of the 4–amino lone pair, resulting in a red shift of the absorption profile (Figure 2.9 and Table 2.2).

Complex Properties

For all Re(I) complexes the UV–vis absorption properties were highly ligand dominated with the intense ICT transition dwarfing the MLCT peak expected at 340–400 nm.[56,62] Furthermore the Re(I) complexes π→π* absorption possessed higher extinction coefficients compared to the free ligands due to the additional chromophores of bpy and phen (Table 2.2).

Table 2.2: UV–vis absorption properties of the ligands and complexes.

Structure	λ_{max} / nm (ε / $M^{-1}cm^{-1}$)[a]		
	Free Ligand	**[Re(bpy)(LX)]**	**[Re(phen)(LX)]**
L1	344 (11300)	–	345 (14100)
L2	340 (12600)	341 (16600)	340 (19700)
L3	340 (15600)	341 (14100)	340 (19600)
L4	411 (10400)	411 (12500)	408 (19500)
L5	410 (10800)	411 (9544)	406 (7000)
L6	429 (8100)	430 (–[b])	431 (14600)
L7	428 (12000)	432 (13800)	431 (16500)

[a]2.5 or 5×10^{-5} M MeCN, [b]extinction coefficient could not be determined due to impure sample

Table 2.2 shows the UV–vis absorption properties of both the free ligands and complexes. The complexes' λ_{max} values show very little variation from the free ligands, presumably due to the lack of conjugation between the NI ring and the metal binding site. Promisingly all 4–amino NI species are seen to absorb within the visible region, hence their strong yellow–orange colour to the naked eye, also arising from the high extinction coefficient values of the overlapping n→π* and ^{1}MLCT peaks (*ca.* 10000 $M^{-1}cm^{-1}$).

2.3.5 Luminescence Spectroscopy

Ligand Properties

Solutions of all ligands and complexes were found to be highly luminescent and this was visible to the naked eye for **L4–7** and their corresponding complexes. Using λ_{exc} of 345–425 nm on aerated MeCN solutions of **L1–3** resulted in a slightly structured band centred at 380–390 nm, assigned to π–π* transitions. In addition, **L4–7** possessed a broad,

unstructured, visible emission band centred at 510—530 nm showing slight sensitivity to the nature of the amine situated at the 4–position (Figure 2.10 and Table 2.3). This band is typical of NI ligands and is consistent with a high degree of ICT character, agreeing well with examples from the literature.[8,10,11,17,63] This ICT band was dominant with the exception of **L6** (Figure 2.10) which showed an additional peak at 340 nm, the same as the structured emission of unsubstituted species, **L1–3**. The sensitivity of the ICT emission to the nature of the 4–amino substituent correlates well with the electron donating ability of the group, as found for similar examples.[11] In **L4–5**, the electron donating ability of piperidine helps to stabilise the charged ICT excited state, hence lowering the energy of the transition.

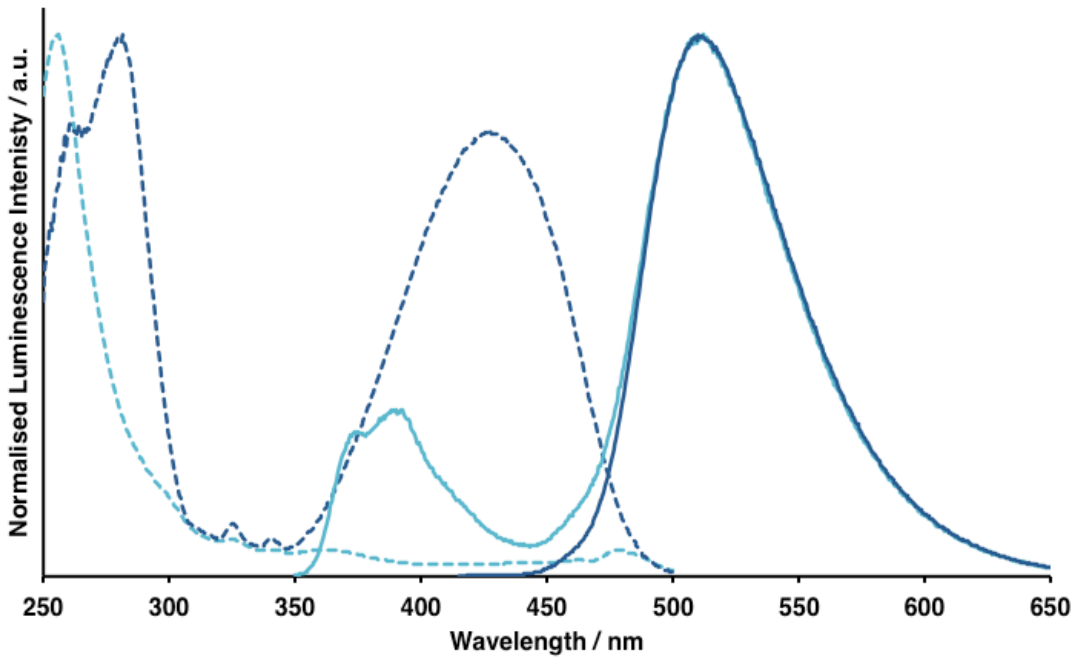

Figure 2.10:Excitation and emission spectra (dashed and solid respectively) for L6 and [Re(bpy)(L6)] (light and dark blue respectively).

The main ligand excitation profile (Figure 2.10) was observed at 260 nm with a low intensity plateau to 500 nm. Interestingly **L4–5,** containing the piperidine substituent, both had a much stronger peak centred at 425 nm. The large Stokes' shift associated with these excitation and emission wavelengths further supports an excited state of ICT character.

Lifetime measurements of **L1–7** show that the ligands were fluorescent in all cases (<10 ns). The emission was generally shown to be dual component (with the exception of **L4–5**) with the longer, dominant component *ca.* 10 ns. Hence it appears that, with the

exception of **L4–5,** the minor component is being quenched by PeT as observed for other species of this nature.[17]

Table 2.3: Fluorescence properties of the ligands and complexes in MeCN.

Structure	λ_{em} / nm[a]			τ / ns (% component)[b]		
	Ligand	[Re(N^N)(LX)]		Ligand	[Re(N^N)(LX)]	
		bpy	phen		bpy	phen
L1	381	–	528	0.2	–	0.1, 0.2 (76 %)
L2	392	521	515	1.6, 8.8 (91 %)	8.2, 104.7 (92 %)	4.2, 40.2 (60 %)
L3	392	518	515	1.29	5.5, 111.5 (96 %)	7.7, 72.6 (75 %)
L4	534	538	537	0.2, 0.9 (78 %)	1.3, 29.7 (94 %)	0.6, 6.5 (51 %)
L5	534	533	534	0.8	9.2	0.6, 16.1 (66 %)
L6	512	514	514	2.6, 9.8 (99 %)	4.7, 7.4 (90 %)	5.0, 10.4 (47%)
L7	511	511	511	6.6, 10.1	0.2, 9.6 (96 %)	0.3, 9.5 (79 %)

[a]λ_{exc} at 345 or 405 nm, [b]λ_{exc} at 295 nm

Complex Properties

For complexes of **L1–3**, that lack ICT character, evidence of spin forbidden ^{3}MLCT emission (*ca.* 520 nm), as expected for this class of polypyridyl Re(I) complexes,[32,56,62] was apparent and independent of λ_{exc}. The Re(I) centred luminescence originates from the ^{3}MLCT state positioned solely on the di–imine equatorial ligand[21] and therefore differences were observed between the bpy and phen containing complexes (Table 2.3). For example, the lifetimes of the bpy containing compounds were considerably longer than those containing phen. This was somewhat surprising considering the literature precedents longer lifetimes for complexes containing the highly rigid phen co–ligand[56] which limits vibrational deactivation pathways. The 40–110 ns dominant lifetime components of **[Re(N^N)(L2–3)]** were consistent with phosphorescent components that can only originate from a triplet excited state and agree well with literature examples of Re(I) di–imine ^{3}MLCT emission.[56,62]

The photophysical properties of **[Re(N^N)(L4–7)]** were found to be highly ligand dominated. Similar to **[Re(N^N)(L1–3)]**, **[Re(N^N)(L4–7)]** also possessed strong emission bands at *ca.* 520 nm. However, for these examples the bands were found at the same wavelengths as the ligand based emission. Hence it was concluded that the ligand emission was so intense that it was dwarfing or overlaying the ^{3}MLCT peak. Unlike **[Re(N^N)(L4–7)]** emission profiles, the excitation profiles were very different from the

free ligands. The intense excitation peak at 260 nm in the free ligands was shifted to *ca.* 300 nm and furthermore an equally strong peak was seen at 425 nm. Lifetimes of **[Re(N^N)(L4–7)]** were again dual component and generally extended compared to the free ligands, however much shorter than **[Re(N^N)(L1–3)]**. The longer, dominant component has a larger % component in the **[Re(bpy)(LX)]** species (>90 %) versus the **[Re(phen)(LX)]** species (50–80 %), again disagreeing with the literature.[56]

2.3.6 Oxygen Sensitivity

Collaboration with The Zhao Group (Dalian University of Technology, China) allowed us to assess the oxygen sensitivity of a selection of compounds. The selection allowed for comparison between ligand *versus* complex, bpy co–ligand *versus* phen, the 4–NI substituents and *N*–4–picolyl binding site *versus* N–3–picolyl binding site. The oxygen sensitivity was assessed by investigating the luminescence properties in N_2, air and O_2 in order to ultimately evaluate the feasibility of these compounds towards SOG and PDT. Oxygen sensitivity was tested in both acetonitrile and dichloromethane. Data for both solvents showed similar trends however the results were more apparent when using acetonitrile.

The free ligand tested, **L5**, showed very little sensitivity to oxygen with the luminescence emission intensity only slightly greater in a dinitrogen atmosphere, as expected for a singlet state emitter. This was the same for **[Re(bpy)(L5)]** which allows us to conclude that this species is ICT dominated, therefore complementing the luminescence observations previously discussed. Conversely the complexes tested containing the phen co–ligand mostly showed an extreme intensification of the emission at *ca.* 540 nm in an inert atmosphere (Figure 2.11).

All complexes containing ligands with the *N*–3–picolyl binding site (**L3/5/7**) showed greater sensitivity than the complex of **L4** that contains the 4–picolyl binding site. The most obvious sensitivity to O_2 was seen for **[Re(phen)(L3)]**, followed by **[Re(phen)(L5)]** which showed a five– and two–fold decrease in their emission intensity in an aerated atmosphere *versus* N_2. This was consistent with the literature precedent whereby species with long–lived excited states are usually more sensitive to oxygen.[64] It also indicated that the main quenching mechanism of the ^{3}MLCT state for **[Re(phen)(L3–5)]** is *via* ground state $^3O_2$ which produces excited state $^1O_2$.[38] The high sensitivity of the emissions to O_2 indicates the emitting triplet state was mainly ^{3}IL π–π* character.[64]

Furthermore the Zhao group also assessed the application of these compounds as photosensitisers for upconverion with 9,10–diphenylanthracene (DPA, triplet acceptor) however no obvious triplet–triplet annihilations were evident.

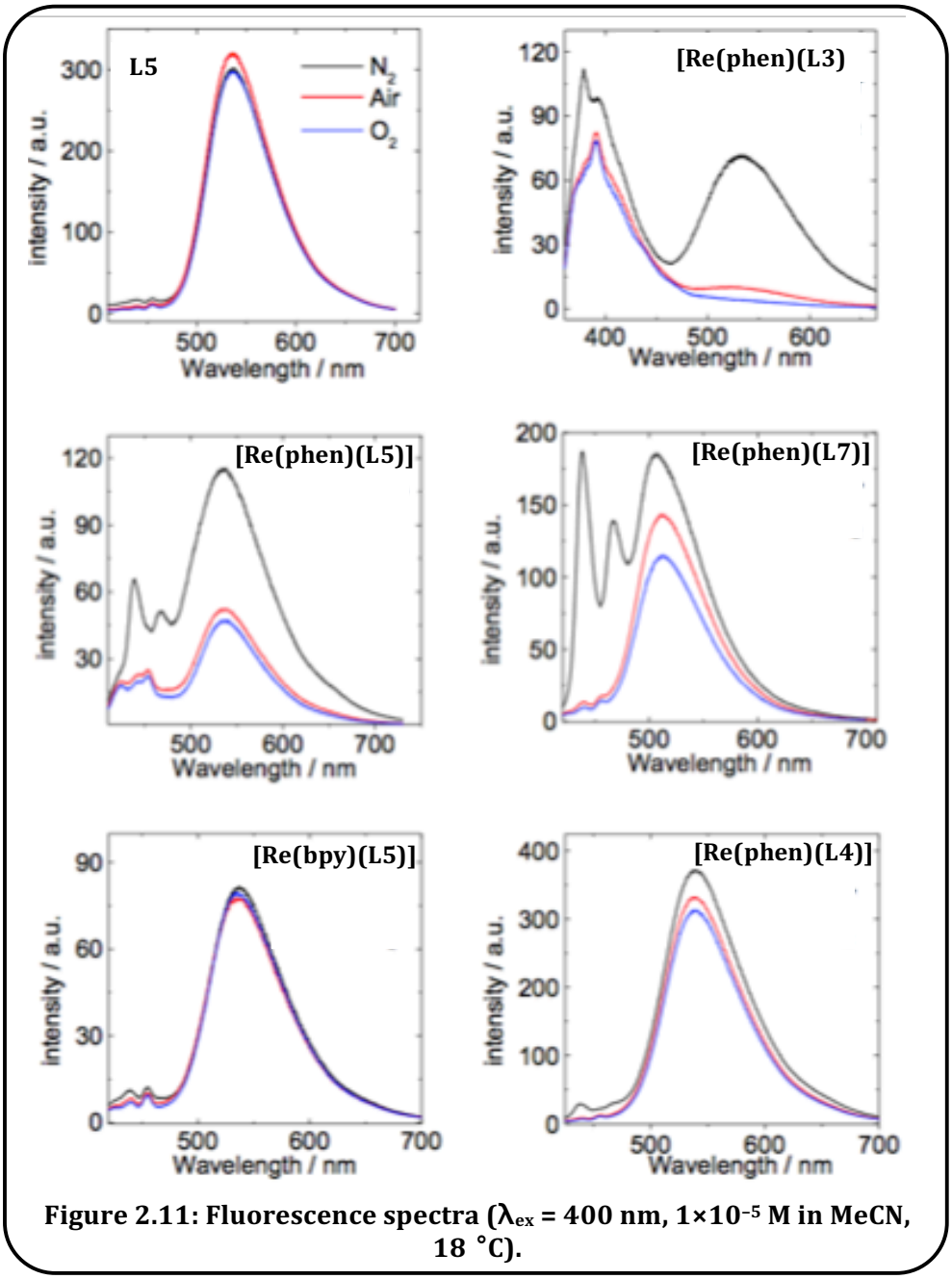

Figure 2.11: Fluorescence spectra (λ_{ex} = 400 nm, 1×10^{-5} M in MeCN, 18 °C).

2.3.7 Confocal Fluorescence Microscopy (CFM)

Having recognised that the Re(I) complexes possess favourable and attractive photophysical properties for fluorescence imaging (large Stokes' shifts, intense emission *etc.*), CFM was conducted to assess the imaging capability of a selection of the complexes.

The compounds were incubated with *Schizosaccharomyces pombe* (*S. Pombe*) (fission yeast cells) due to their ease of culture. Following washing to remove the compounds from the culture medium, cells were imaged with λ_{exc} = 405 nm and detection between 500–600 nm.

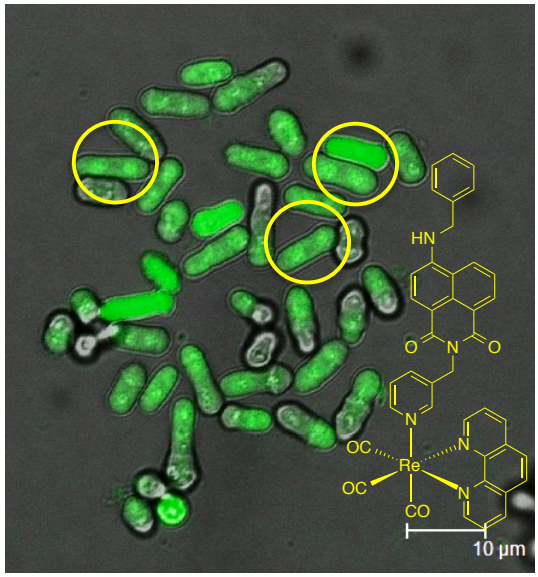

Figure 2.12: CFM of *S. Pombe* yeast cells imaged using [Re(phen)(L7)] (λ_{exc} = 405 nm; λ_{em} = 500–600 nm).

Imaging was initially conducted with the *N*–3–picolyl containing **[Re(phen)(LX)]** species (where X = 1, 3, 4, 5 and 7) due to similar examples in the literature proving non–toxic, as opposed to the corresponding toxic *N*–4–picolyl species.[65] Cell incubation with the compounds at a concentration of 10 µg mL^{-1} resulted in very poor uptake by the cells[65] however yeast cell walls are known to be relatively impermeable. To improve the cell uptake the concentration of the compounds was increased to 100 µg mL^{-1} which resulted in much better uptake of the 4–amino substituted complexes, however the uptake of **[Re(phen)(L1/3)]** still remained poor. The exception to this was **[Re(phen)(L4)]** which seemed to form precipitates at the higher concentration.

The compound with the best uptake, **[Re(phen)(L7)]**, was extensively imaged. At the lower incubation concentration **[Re(phen)(L7)]** showed some cytoplasmic staining and more concentrated mitochondrial accumulation; the typical staining pattern observed for Re(I) species.[65,66] At the higher incubation concentration, remarkably detailed images were collected that showed clear concentration of the compound in nuclei, particularly in dividing cells where two nuclei are present (Figure 2.12). This phenomenon has

previously been observed in the literature[65,67] and suggests that cell division weakens the wall and membranes, enhancing their permeability and allowing uptake of the compound. **[Re(phen)(L7)]** gave very bright images with very little background signal, even without washing with buffer solution. **[Re(phen)(L5)]** gave similar results and even though very little uptake of **[Re(phen)(L1)]** was observed, good quality images were still obtained, again showing distinct 'hot spots' of emission (Figure 2.13).

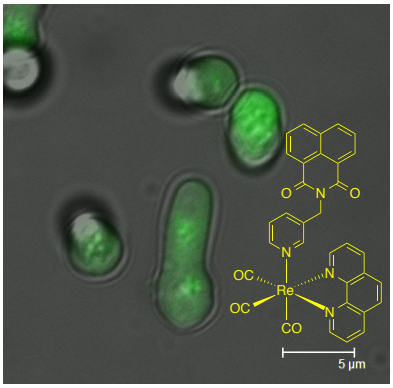

Figure 2.13: CFM of *S. Pombe* yeast cells imaged using [Re(phen)(L1)] (λ_{exc} = 405 nm; λ_{em} = 500–600 nm).

Although the Re(I) complexes were seen to concentrate in specific organelles, due to the poor uptake of the samples, further study was not pursued.

Throughout the duration of the experiments there was no reduction in the number of yeast cells when compared to the unstained control. Promisingly this indicates that these compounds were not toxic to yeast cells, as seen in the literature,[65] although this could simply be due to the low uptake levels. Unfortunately all of the samples tested showed a high degree of photobleaching[65] which is not ideal for applied CFM techniques.

2.4 Conclusion

To summarise, the naphthalimide core allows a high degree of functionality and tuneability of the NI's favourable photophysical properties. The ligands discussed herein are clearly interesting in their own right with the photophysical data displaying intense emission properties with favourable characteristics towards cell imaging applications.

The ligands clearly form stable Re(I) complexes which have scope to be further tuned *via* the di–imine ligand, for example towards solubility for biological media or to improve application feasibility. Surprisingly the steady–state luminescence data of the complexes do not obviously show dual–emission due to the very high intensity of the ligand based ICT emission of the 4–amino substituted ligands. On the other hand, strong evidence of ^{3}MLCT emission was seen for complexes of the unsubstituted ligands.

The complexes discussed herein showed great promise towards confocal fluorescence microscopy and varying the nature of the amine group at the 4–position greatly tuned the localisation and imaging capability. This was also true for the oxygen sensitivity of the complexes. **[Re(phen)(L5)]** displayed both excellent cell imaging capability and oxygen sensitivity. In addition **[Re(phen)(L3/5)]** seems a feasible option for use in PDT. This is particularly true when considering their tuneable photophysical properties that could be adjusted to absorb within more suitable wavelengths (650–850 nm) for this application.

2.5 Experimental Section

2.5.1 Diffraction Data Collection, Processing, Structure Analysis and Refinement

Data collection, refinement and structure solution was conducted by Dr Peter Horton at the UK National Crystallography Service, Southampton.

Suitable crystals were selected and measured following a standard method on a *Rigaku AFC12* goniometer equipped with an enhanced sensitivity (HG) *Saturn724+* detector mounted at the window of a *FR–E+ SuperBright* molybdenum rotating anode generator with VHF *Varimax* optics (100μm focus) at 100K. Cell determination, data collection, reduction, cell refinement and absorption correction were carried out using *CrystalClear–SM Expert 3.1b25* (Rigaku 2012). The structure was solved by direct methods using SHELXS–97[68] and refined in SHELXL–97.[68] It was not possible to accurately model the highly disodered solvent and thus PLATON SQUEEZE was used. Disorder was observed in most of the BF_4 anions resulting in using both geometrical (SAME) and thermal (SIMU) restraints. Also a general thermal restraint (DELU) was used. The figures were created using the ORTEP3 for Windows.[69]

2.5.2 Response to ROS *in vitro*

Undertaken by the Zhao group at Dalian University of Technology, China.

UV–Vis absorption spectra were measured with a HP8453 UV–vis spectrophotometer. Fluorescence spectra were recorded on Shimadzu 5301 PC spectrofluorometer. Upconversion was carried out on a customized Sanco 970 CRT spectrofluorometer. Phosphorescence quantum yields were measured with $[Ru(dmb)_3(PF_6)_2]$ as the standard (Φ = 7.3% in acetonitrile, dmb = 4,4′–dimethyl–2,2′–bipyridine).

A diode pumped solid state (DPSS) continuous laser (473 nm) was used as the excitation source for the upconversions. The diameter of the laser spot was *ca.* 3 mm. The power of the laser beam was measured with a VLP–2000 pyroelectric laser power meter. For the upconversion experiments, the mixed solution of the compound (triplet sensitiser) and 9,10–diphenylanthracene (DPA) was degassed with N_2 for at least 15 min (note the upconversion can be significantly quenched by O_2). Then the solution was excited with laser. The upconverted fluorescence of DPA was observed with a spectrofluorometer. In order to repress the scattered laser, a black box was put behind the fluorescent cuvette to trap the laser beam. The upconversion quantum yields (Φ_{UC}) were determined with the prompt fluorescence of coumarin–6 (Φ_F = 78% in C_2H_5OH). All these data were

independently measured three times (with different solutions samples). The CIE coordinates (x, y) of the emission of the sensitizers alone and the emission of the upconversion were derived from the emission spectra with the software of CIE color Matching Linear Algebra.

2.5.3 Cell Incubation and Confocal Microscopy

Undertaken by collaborators within the Lloyd and Hayes groups in BIOSCI at Cardiff University.

Cell imaging was executed using *Schizosaccharomyces pombe* (*S. Pombe*) – fission yeast. The preparation used homogenous overnight cell suspension aliquots (1 mL), each being subject to incubation with a different lumophore (10 μL). Lumophores were initially dissolved in dimethylsulfoxide (DMSO) (5 mg mL^{-1}) to yield a concentration of 10 μg mL^{-1}. *S. pombe* yeast cells were then incubated at 35 °C (under 5 % CO_2 and 95 % air) and 20 °C, respectively, for 30 minutes. Cells were then twice washed in phosphate buffer saline (PBS, pH 7.2) removing the lumophore from the medium and finally *S. Pombe* cells 1 mL of PBS for imaging. Preparations were viewed by epifluorescence and transmitted light (Nomarski differential interference contrast optics) using a Leica TCS SP2 AOBS confocal laser microscope (Leica, Germany) using ×63 or ×100 objectives, ×4 zoom factor and laser power of 20 %. Excitation of the lumophore was at 405 nm using a diode laser, with detection between 500 and 600 nm. Initial imaging yielded minimal fluorescence so the concentration of the lumophore was increased to 100 μgmL^{-1} final concentration, which was then incubated with the cells at room temperature for a further 30 minutes.

2.5.4 General

^{1}H NMR spectra were recorded on an NMR–FT Bruker 250 or 400 MHz spectrometer and $^{13}C\{^{1}H\}$ NMR spectra on a Jeol Eclipse 300 or 600 MHz spectrometer and recorded in $CDCl_3$, CD_3CN or CD_3OD. ^{1}H and $^{13}C\{^{1}H\}$ NMR chemical shifts (δ) were determined relative to residual solvent peaks with digital locking and are given in ppm. Low–resolution mass spectra were obtained by the staff at Cardiff University. High–resolution mass spectra were carried out at the EPSRC National Mass Spectrometry Facility at Swansea University. UV–Vis studies were performed on a Perkin Elmer UV/Vis/NIR Lambda 900 Spectrometer as MeCN solutions (2.5 or 5 × 10^{-5} M). IR spectra were recorded on a Thermo Scientific Nicolet iS5 spectrometer fitted with an iD3 ATR attachment. Photophysical data were obtained on a JobinYvon–Horiba Fluorolog spectrometer fitted with a JY TBX picoseconds photodetection module as MeCN solutions. Emission spectra were uncorrected and

excitation spectra were instrument corrected. The pulsed source was a Nano–LED configured for 295 nm output operating at 1 MHz. Luminescence lifetime profiles were obtained using the JobinYvon–Horiba FluoroHub single photon counting module and the data fits yielded the lifetime values using the provided DAS6 deconvolution software.

All reactions were performed with the use of vacuum line and Schlenk techniques. Reagents were of commercial grade and were used without further purification. The ($[Re(CO)_3(N^N)(MeCN)]BF_4$), precursors where (N^N) = either i) 2,2'–bipyridine (bpy) or ii) 1,10–phenanthroline (phen) were obtained using well established methods from the literature.[21,50,51,70]

2.5.5 Ligand Synthesis

Synthesis of 4–chloro–N–(4'–picolylamine)–1,8–naphthalimide ***(L1)***[42]

1,8–Napthalic anhydride (279 mg, 1.41 mmol) was added to a solution of 3–picolylamine (0.29 mL, 2.82 mmol) in ethanol (10 mL) and heated at reflux for 12 hours, under a dinitrogen atmosphere. Reaction progression was followed by thin layer chromatography. Upon reaction completion the solution was cooled during which heavy precipitation occurred. The solution was filtered under suction and the resultant solid washed with ethanol, followed by diethyl ether. The solid was then dried *in vacuo* to give **L1** as an off–white solid. Yield: 316 mg, 1.10 mmol, 78 %. ^{1}H NMR (400 MHz, $CDCl_3$): δ_H = 8.83 (s, 1H, NCH_2CCHN), 8.59 (d, 2H, $^3J_{HH}$ = 5.7 Hz), 8.52–8.40 (m, 1H), 8.19 (d, 2H, $^3J_{HH}$ = 8.2 Hz), 7.90–7.84 (m, 1H), 7.73 (t, 2H, $^3J_{HH}$ = 7.9 Hz), 7.23–7.18 (m, 1H), 5.36 (s, 2H, CH_2) ppm; UV–Vis (CH_3CN): λ_{max} ($\varepsilon/M^{-1}cm^{-1}$) = 344 (11300), 332 (12500), 321 (9700), 252 (3300), 232 (40600), 210 (22900) nm.

Synthesis of 4–chloro–N–(4'–picolylamine)–1,8–naphthalimide ***(L2)***

Prepared as for **L1** using 4–chloro–1,8–napthalic anhydride (1.997 g, 8.58 mmol) and 4–picolylamine (1.75 mL, 17.2 mmol) to give **L2** as a yellow solid. Yield: 2.216 g, 6.87 mmol, 80 %. ^{1}H NMR (250 MHz, $CDCl_3$): δ_H = 8.71–8.48 (m, 5H, nap), 7.93–7.78 (m, 2H, pyr), 7.39 (d, 2H, $^3J_{HH}$ = 5.7 Hz, pyr), 5.37 (s, 2H, CH_2) ppm; UV–Vis (CH_3CN): λ_{max} ($\varepsilon/M^{-1}cm^{-1}$) = 353 (10800), 340 (12600), 235 (36300), 210 (20100) nm.

Synthesis of 4–chloro–N–(3'–picolylamine)–1,8–naphthalimide ***(L3)***

Prepared as for **L1** using 4–chloro–1,8–napthalic anhydride (1.975 g, 8.49 mmol) and 3–picolylamine (1.75 mL, 17.2 mmol) to give **L3** as a yellow solid. Yield: 2.444 g, 7.57 mmol, 89 %. ^{1}H NMR (250 MHz, $CDCl_3$): δ_H = 8.76 (d, 1H, $^3J_{HH}$ = 1.4 Hz, $ClCCH$), 8.62–8.37 (m, 4H, nap), 7.86–7.70 (m, 3H, pyr), 7.21–7.13 (m, 1H, pyr–$CCHN$), 5.30 (s, 2H, CH_2)

ppm. $^{13}C\{^1H\}$ NMR (300 MHz, $CDCl_3$): δ_C = 163.7 (*C*O), 163.5 (*C*O), 150.7, 149.0, 139.5, 137.1, 132.8, 132.4, 131.5, 131.0, 129.4, 127.9, 127.5, 123.5, 122.8, 121.3, 41.3 (*C*H_2) ppm; LRMS (ES^+) found *m/z* 323.06 for $[M+H]^+$, calculated 323.73 for $[M+H]^+$; HRMS (ES^+) found *m/z* = 323.0583 for $[C_{18}\ H_{11}N_2O_2Cl+H]^+$, calculated 323.0582 for $[C_{18}\ H_{11}N_2O_2Cl+H]^+$; IR (solid) ν_{max} (±2 cm^{-1}) = 1697 (C=O), 1655 (C=O), 1616, 1590, 1570, 1505, 1478, 1462, 1400, 1373, 1339, 1316, 1234, 1225, 1173, 1159, 1117, 1094, 1053, 1028, 995, 955, 934, 912, 851, 793, 777 (C–Cl), 752, 733, 714, 667, 623 cm^{-1}; UV–Vis (CH_3CN): λ_{max} ($\varepsilon/M^{-1}cm^{-1}$) = 353 (13400), 340 (15600), 235 (52100) nm.

Synthesis of 4–piperidyl–N–(4'–picolylamine)–1,8–naphthalimide ***(L4)***[7]

L2 (104 mg, 0.32 mmol) and piperidine (0.13 mL, 1.29 mmol) were heated in DMSO (6 mL) under a dinitrogen atmosphere at 80 °C for 2 hours during which the reaction was followed by thin layer chromatography (TLC). The solution was allowed to cool and then water was added to induce precipitation of the product upon neutralisation with dilute HCl (1 M). The solution was then filtered and the solid washed with copious amounts of water, followed by petroleum ether, and subsequently dried *in vacuo* to give **L4** as a yellow solid. Yield: 86 mg, 0.23 mmol, 72 %. ^1H NMR (400 MHz, $CDCl_3$): δ_H = 8.52 (d, 1H, $^3J_{HH}$ = 7.3 Hz, pyr), 8.38–8.49 (m, 3H, nap), 8.34 (d, 1H, $^3J_{HH}$ = 8.4 Hz, pyr), 7.68 (app t, 2H, $^3J_{HH}$ = 7.3 Hz, $NCH_2CH_2CH_2$), 7.63 (dd, 1H, J_{HH} = 8.4 Hz, 8.5 Hz, nap), 7.32 (d, 2H, $^3J_{HH}$ = 5.9 Hz, NC*H*), 7.12 (d, 1H, $^3J_{HH}$ = 8.2 Hz, nap), 5.30 (s, 2H, CH_2–pyr), 3.18 (t, 4H, $^3J_{HH}$ = 5.0 Hz, NCH_2), 1.87–1.72 (m, 4H, NCH_2CH_2) ppm; UV–Vis (CH_3CN): λ_{max} ($\varepsilon/M^{-1}cm^{-1}$) = 411 (10400), 339 (2000), 326 (1900), 275 (16000), 260 (17900), 225 (25000), 207 (33100) nm.

Synthesis of 4–piperidyl–N–(3'–picolylamine)–1,8–naphthalimide ***(L5)***

Prepared as for **L4** using **L3** (100 mg, 0.31 mmol) and piperidine (0.06 mL, 0.62 mmol) however in this instance isolation of the pure product resulted from extraction of the neutralised reaction mixture into dichloromethane (2 x 20 mL). The organic layer was washed with water (3 x 20 mL), dried over $MgSO_4$ and reduced to minimal volume. Precipitation of the product was then induced *via* the slow addition of petroleum ether. Subsequent filtration and drying *in vacuo* gave **L5** as an orange solid. Yield: 111 mg, 0.30 mmol, 98 %. ^1H NMR (400 MHz, $CDCl_3$): δ_H = 8.81 (s, 1H, NC*H*C), 8.53–8.47 (m, 2H, pyr), 8.43 (d, 1H, $^3J_{HH}$ = 8.2 Hz), 8.34 (d, 1H, $^3J_{HH}$ = 8.4 Hz, nap), 8.19 (broad d, 1H, $^3J_{HH}$ = 7.9 Hz, pyr), 7.63 (dd, 1H, J_{HH} = 7.4 Hz, 7.3 Hz,nap), 7.49–7.42 (m, 1H, pyr), 7.12 (d, 1H, $^3J_{HH}$ = 8.2 Hz, NCC*H*), 5.37 (s, 1H, CH_2–pyr), 3.19 (t, 4H, $^3J_{HH}$ = 5.1 Hz, NCH_2), 1.88–1.79 (m, 4H, $NHCH_2CH_2$), 1.72–1.64 (m, 2H, $NCH_2CH_2CH_2$) ppm; $^{13}C\{^1H\}$ NMR (300 MHz, $CDCl_3$): δ_C = 164.6 (*C*O), 164.0 (*C*O), 157.7, 150.6, 148.8, 136.9, 133.3, 133.1, 131.4, 131.1, 130.0, 126.2,

125.4, 123.4, 122.8, 115.4, 114.8, 54.6, 41.0 (*C*H_2), 26.2, 24.3 ppm; LRMS (ES^+) found *m/z* = 372.17 for $[M+H]^+$; HRMS (ES^+) found *m/z* = 372.1706 for $[C_{23}H_{21}N_2O_2+H]^+$, calculated 372.1707 for $[C_{23}H_{21}N_2O_2+H]^+$; IR (solid) ν_{max} (±2 cm^{-1}) = 1688 (C=O), 1645 (C=O), 1584, 1570, 1512, 1481, 1449, 1429, 1414, 1377 (C–N), 1350, 1339, 1316, 1277, 1250, 1231, 1219, 1192, 1175, 1153, 1124, 1105, 1076, 1039, 1028, 985, 958, 939, 897, 864, 843, 814, 779, 758, 741, 712, 665 cm^{-1}; UV–Vis (CH_3CN): λ_{max} ($\varepsilon/M^{-1}cm^{-1}$) = 410 (10800), 340 (2500), 325 (2300), 259 (15900), 224 (24800), 209 (34600) nm.

Synthesis of 4–benzylamine–N–(4–picolylamine)–1,8–naphthalimide ***(L6)***

Prepared as for **L5** using **L2** (101 mg, 0.31 mmol) and benzylamine (0.10 mL, 0.62 mmol) in DMSO (4 mL), heating for 12 hours to give **L6** as a yellow–orange solid. Yield: 164 mg, 0.41 mmol, >100%. The product was then recrystallised from MeOH/ice cooled petroleum ether. Yield: 122 mg, 0. 31 mmol, 94.3 %. ^1H NMR (400 MHz, $CDCl_3$): δ_H = 8.62 (d, 1H, $^3J_{HH}$ = 7.3 Hz), 8.52 (d, 1H, $^3J_{HH}$ = 5.7 Hz), 8.48 (d, 1H, $^3J_{HH}$ = 8.4 Hz), 8.17 (d, 1H, $^3J_{HH}$ = 8.5 Hz), 7.66 (t, 1H, $^3J_{HH}$ = 7.9 Hz), 7.55–7.33 (m, 7H), 6.80 (d, 1H, $^3J_{HH}$ = 8.5 Hz, NHCC*H*), 5.68 (t, 1H, $^3J_{HH}$ = 5.2 Hz, N*H*), 5.38 (s, 2H, NCH_2), 4.64 (d, 2H, $^3J_{HH}$ = 5.1 Hz, NHCH_2) ppm; $^{13}C\{^1H\}$ NMR (300 MHz, $CDCl_3$): δ_C = 164.6 (*C*O), 164.0 (*C*O), 149.8, 149.6, 146.8, 137.0, 135.0, 131.7, 130.4, 130.0, 129.2, 128.2, 127.7, 126.6, 125.1, 123.3, 122.7, 120.4, 110.3, 105.2, 48.1 (NH*C*H_2), 42.5 (pyr–*C*H_2) ppm; LRMS (ES^+) found *m/z* = 394.11 for $[M+H]^+$; HRMS (ES^+) found *m/z* = 394.1548 for $[C_{25}H_{19}O_2N_3+H]^+$, calculated 394.1550 for $[C_{25}H_{19}O_2N_3+H]^+$; IR (solid) ν_{max} (±2 cm^{-1}) = *ca.* 3300 (N–H stretch), 1684 (C=O), 1643 (C=O), 1574 (N–H bend), 1539, 1495, 1451, 1416, 1387, 1370, 1341, 1314, 1295, 1242, 1182, 1163, 1130, 1098, 1067, 1028, 991, 979, 963, 939, 772, 758, 737, 696, 669, 652, 633 cm^{-1}; UV–Vis (CH_3CN): λ_{max} ($\varepsilon/M^{-1}cm^{-1}$) = 429 (8100), 353 (3300), 339 (3800), 325 (3200), 279 (11600), 256 (11600), 229 (16100), 202 (36900) nm.

Synthesis of 4–benzylamine–(N–3–picolylamine)–1,8–naphthalimide ***(L7)***

Prepared as for **L6** using **L3** (174 mg, 0.54 mmol) and benzylamine (0.24 mL, 2.16 mmol) to give **L7** as an orange solid. Yield: 90 mg, 0.23 mmol, 42 %; ^1H NMR (400 MHz, $CDCl_3$): δ_H = 8.74 (s, 1H, NCH_2CCH), 8.52 (d, 1H, $^3J_{HH}$ = 8.0 Hz), 8.36–8.42 (m, 2H), 8.06 (d, 1H, $^3J_{HH}$ = 8.5 Hz), 7.84–7.78 (m, 1H), 7.53 (dd, 1H, $^3J_{HH}$ = 7.5 Hz, $^3J_{HH}$ = 7.3 Hz), 7.39–7.24 (m, 5H), 7.18–7.11 (m, 1H), 6.68 (d, 1H, $^3J_{HH}$ = 8.5 Hz, nap), 5.69 (t, 1H, $^3J_{HH}$ = 4.8 Hz, N*H*), 5.29 (s, 2H, CH_2), 4.54 (d, 2H, $^3J_{HH}$ = 5.1 Hz, NHCH_2) ppm; $^{13}C\{^1H\}$ NMR (300 MHz, $CDCl_3$): δ_C = 164.7, 164.0, 150.6, 149.5, 148.7, 136.9, 136.9, 134.9, 133.6, 131.6, 129.8, 129.2, 128.2, 127.7, 126.5, 125.0, 123.5, 122.9, 120.4, 110.4, 105.1, 48.1 (NH*C*H_2), 41.0 (pyr–*C*H_2) ppm; LRMS (ES^+) found *m/z* = 394.16 for $[M+H]^+$; HRMS (ES^+) found *m/z* = 394.1150 for

$[C_{25}H_{19}N_3O_2+H]^+$, calculated 394.1150 for $[C_{25}H_{19}N_3O_2+H]^+$; IR (solid) ν_{max} (±2 cm^{-1}) = *ca.* 3350 (N–H stretch), 1734, 1674 (C=O), 1630 (C=O), 1614, 1576 (N–H bend), 1559, 1516, 1497, 1479, 1451, 1429, 1393, 1369, 1344, 1318, 1298, 1236, 1221, 1186, 1163, 1132, 1120, 1103, 1096, 1065, 1043, 1030, 988, 970, 932, 856, 843, 816, 801, 769, 754, 714, 702, 669, 663 cm^{-1}; UV–Vis (CH_3CN): λ_{max} ($\varepsilon/M^{-1}cm^{-1}$) = 428 (12000), 356 (2100), 339 (2400), 324 (2300), 279 (17100), 258 (16400), 227 (16400), 202 (44000) nm.

2.5.6 Re(I) complex synthesis

*Synthesis of fac–[Re(CO)$_3$(phen)**(L1)**]* ***[Re(phen)(L1)]***[26]

Fac–[*Re*(*phen*)(*CO*)$_3$(MeCN)]BF_4 (46.7 mg, 80.8 µmol) and **L1** (25.5 mg, 88.9 µmol) were dissolved in chloroform (3 mL) and heated at reflux, under a dinitrogen atmosphere, for 12 hrs. After cooling the solvent was reduced *in vacuo*. Precipitation of the product was then induced *via* the slow addition of diethyl ether. The product was subsequently filtered and dried *in vacuo* give **[Re(phen)(L1)]** as an off–white solid. Yield: 60.3 mg, 73.0 µmol, 90 %; ^{1}H NMR (400 MHz, CD_3CN): δ_H = 9.45 (dd, 2H, J_{HH} = 5.4 Hz, 5.1 Hz, phen), 8.92 (dd, 2H, J_{HH} = 8.3 Hz, 7.8 Hz, phen), 8.76–8.73 (m, 1H), 8.60 (d, 2H, $^3J_{HH}$ = 7.3 Hz, phen), 8.46 (d, 1H, $^3J_{HH}$ = 5.3 Hz), 8.40 (d, 2H, $^3J_{HH}$ = 8.2 Hz, phen), 8.28 (s, 2H, phen), 8.10 (dd, 2H, J_{HH} = 8.3 Hz, 5.1 Hz), 7.94–7.90 (m, 1H), 7.86 (t, 2H, $^3J_{HH}$ = 7.8 Hz), 7.38 (dd, 1H, J_{HH} = 8.2 Hz, 4.8 Hz), 5.36 (s, 2H, CH_2) ppm; ^{13}C{^{1}H} NMR (300 MHz, CD_3CN): very weak δ_C = 205.4 (M–*C*O), 161.5 (NC*C*O), 161.3 (NC*C*O), 154.6, 152.8, 150.2, 148.9, 140.1, 136.6, 134.5, 131.1, 128.0, 127.2, 125.6, 87.8 (*C*H_2) ppm; LRMS (ES^+) found *m/z* = 737.10 for $[M]^+$; HRMS (ES^+) found *m/z* = 737.0953 for $[C_{33}H_{20}N_4O_5Re]^+$, calculated 737.0598 for $[C_{33}H_{20}N_4O_5Re]^+$; IR (solid) ν_{max} (±2 cm^{-1}) = 2029 (M–C=O), 1950 (M–C=O), 1907, 1694 (C=O), 1655 (C=O), 1583, 1519, 1483, 1431, 1417, 1381, 1356, 1338, 1319, 1236, 1197, 1176, 1149, 1060(Re–N), 1026, 974, 955, 935, 850, 810, 783, 771 (C–Cl), 723, 710, 644, 624, 499, 420, 410 cm^{-1}; UV–Vis (CH_3CN): λ_{max} ($\varepsilon/M^{-1}cm^{-1}$) = 345 (14100), 332 (15900), 273 (43000), 230 (61600), 210 (46200), 202 (48200) nm.

*Synthesis of fac–[Re(CO)$_3$(bpy)**(L2)**]* ***[Re(bpy)(L2)]***

Prepared as for **[Re(phen)(L1)]** using *fac*–[*Re*(*bpy*)(*CO*)$_3$(MeCN)]BF_4 (36 mg, 64.9 µmol) and **L2** to give **[Re(bpy)(L2)]** as a yellow solid. Yield: 34 mg, 41.0 µmol, 63 %; ^{1}H NMR (400 MHz, CD_3CN): δ_H = 9.10 (dd, 2H, $^3J_{HH}$ = 5.8 Hz, $^3J_{HH}$ = 4.8 Hz, bpy), 8.54 (d, 1H, $^3J_{HH}$ = 8.5 Hz), 8.46 (d, 1H, $^3J_{HH}$ = 8.2 Hz), 8.32–8.23 (m, 3H), 8.15 (t, 2H, $^3J_{HH}$ = 7.9 Hz), 8.16 (d, 2H, $^3J_{HH}$ = 7.9 Hz), 7.84–7.78 (m, 2H), 7.70–7.63 (m, 2H), 7.22 (d, 2H, $^3J_{HH}$ = 6.6 Hz), 5.12 (s, 2H, CH_2) ppm; ^{13}C{^{1}H} NMR (300 MHz, CD_3CN): δ_C = 195.7 (M–*C*O), 191.5 (M–*C*O), 163.6 (NC*C*O), 163.3 (NC*C*O), 155.8, 153.9, 151.9, 150.9, 141.1, 132.0, 131.2, 130.9, 129.1, 129.0, 128.8,

128.4, 127.7, 125.5, 124.7, 124.7, 122.7, 121.4, 118.8, 42.2 (CH$_2$) ppm; LRMS (ES$^+$) found *m/z* = 749.21 for [M]$^+$; HRMS (ES$^+$) found *m/z* = 749.0572 for [$C_{31}H_{19}ClN_4O_5Re$]$^+$, calculated 749.0568 for [$C_{31}H_{19}ClN_4O_5Re$]$^+$; IR (solid) ν_{max} (±2 cm^{-1}) = 2029 (M–C=O), 1921 (M–C=O), 1705 (C=O), 1667 (C=O), 1620, 1602, 1589, 1572, 1506, 1473, 1445, 1431, 1400, 1379, 1350, 1342, 1311, 1224, 1178, 1166, 1130, 1091, 1076, 1051(Re–N), 1026, 974, 958, 850, 810, 783, 767 (C–Cl), 752, 733, 644, 624 cm^{-1}; UV–Vis (CH_3CN): λ_{max} (ε/M^{-1}cm^{-1}) = 353 (16600), 341 (19000), 319 (22500), 308 (18400), 265 (24200), 235 (57200), 211 (50800) nm.

*Synthesis of fac–[Re(CO)$_3$(phen)(**L2**)]* ***[Re(phen)(L2)]***

Prepared as for **[Re(phen)(L1)]** using *fac*–[*Re*(*phen*)(*CO*)$_3$(MeCN)]BF$_4$ (31 mg, 53.6 µmol) and **L2** (19 mg, 59.0 µmol) to give **[Re(phen)(L2)]** as a yellow solid. Yield: 31 mg, 36.3 µmol, 68 %; ^{1}H NMR (400 MHz, $CDCl_3$): δ_H = 9.46 (dd, 2H, J_{HH} = 5.1 Hz, 3.8 Hz, phen), 8.67 (d, 2H, $^3J_{HH}$ = 7.6 Hz), 8.43 (d, 1H, $^3J_{HH}$ = 8.5 Hz), 8.33 (d, 1H, $^3J_{HH}$ = 7.2 Hz), 8.17 (d, 1H, $^3J_{HH}$ = 7.9 Hz), 8.12–8.06 (m, 2H), 7.97 (s, 2H), 8.00–7.92 (m, 2H), 7.74–7.69 (m, 2H), 7.09 (d, 2H, $^3J_{HH}$ = 6.6 Hz), 4.99 (s, 2H, CH_2) ppm; ^{13}C{^{1}H} NMR (300 MHz, CD_3CN): δ_C = 163.4 (NCC=O), 163.2 (*NCC*=O), 154.5, 151.9, 150.8, 146.6, 140.3, 140.2, 138.8, 131.9, 131.3, 131.1, 130.8, 129.0, 128.8, 128.3, 128.1, 127.6, 127.1, 125.5, 122.6, 121.3, 118.2, 78.2, 42.1 (CH$_2$) ppm; LRMS (ES$^+$) found *m/z* = 773.21 for [M]$^+$; HRMS (FTMS) found *m/z* = 771.0567 for [$ReC_{33}H_{19}N_4O_5Cl$]$^+$, calculated 771.0568 for [$ReC_{33}H_{19}N_4O_5Cl$]$^+$; IR (solid) ν_{max} (±2 cm^{-1}) = 2023 (M–C=O), 1903 (M–C=O), 1697 (C=O), 1654 (C=O), 1618, 1589, 1572, 1560, 1519, 1506, 1464, 1427, 1373, 1350, 1327, 1309, 1224, 1174, 1161, 1149 (Re–N), 1091, 1047, 1033, 960, 856, 815, 781, 754, 748, 723, 675, 659, 644 cm^{-1}; UV–Vis (CH_3CN): λ_{max} (ε/M^{-1}cm^{-1}) = 353 (16600), 340 (19700), 327 (17200), 274 (37000), 231 (67200), 213 (66400) nm.

*Synthesis of fac–[Re(CO)$_3$(bpy)(**L3**)]* ***[Re(bpy)(L3)]***

Prepared as for **[Re(phen)(L1)]** using *fac*–[*Re*(*bpy*)(*CO*)$_3$(MeCN)]BF$_4$ (40 mg, 72.2 µmol) and **L3** (26 mg, 79.4 µmol) to give **[Re(bpy)(L3)]** as a yellow solid. Yield: 41 mg, 48.9 µmol, 63 %); ^{1}H NMR (400 MHz, $CDCl_3$): δ_H = 9.00 (dd, 2H, J_{HH} = 5.7 Hz, 4.6 Hz, bpy), 8.66 (d, 2H, $^3J_{HH}$ = 8.2 Hz), 8.63–8.55 (m, 2H), 8.44 (d, 2H, $^3J_{HH}$ = 7.8 Hz), 8.33–8.23 (m, 2H), 8.17 (d, 1H, $^3J_{HH}$ = 5.0 Hz), 8.10 (d, 1H, $^3J_{HH}$ = 6.0 Hz), 7.95–7.86 (m, 2H), 7.76 (t, 2H, $^3J_{HH}$ = 6.3 Hz), 7.33 (t, 1H, $^3J_{HH}$ = 6.8 Hz), 5.13 (s, 2H, CH_2) ppm; ^{13}C{^{1}H} NMR (300 MHz, $CDCl_3$): δ_C =183.7 (M–*C*=O), 183.7 (M–*C*=O), 163.6 (*C*=O), 163.3 (*C*=O), 155.9, 153.0, 152.8, 152.5, 151.1, 141.9, 141.5, 141.0, 136.3, 132.7, 131.8, 131.6, 129.5, 128.9, 128.1, 127,8, 127.0, 126.2, 125.5, 123.3, 122.4, 120.7, 40.4 (CH$_2$) ppm; LRMS (ES$^+$) found *m/z* = 749.19 for [M]$^+$; HRMS (ES$^+$) found *m/z* = 747.0571 for [$C_{31}H_{19}N_4O_5ClRe$]$^+$, calculated 747.0568 for [$C_{31}H_{19}N_4O_5ClRe$]$^+$;

IR (solid) ν_{max} (±2 cm^{-1}) = 2031 (M–C=O), 1922 (M–C=O), 1703 (C=O), 1662 (C=O), 1604, 1289, 1573, 1473, 1400, 1379, 1344, 1317, 1284, 1236, 1178, 1165, 1055 (Re–N), 1033, 972, 854, 771 (C–Cl), 752, 733, 706, 669, 646, 626 cm^{-1}; UV–Vis (CH_3CN): λ_{max} ($\varepsilon/M^{-1}cm^{-1}$) = 353 (12400), 340 (14100), 318 (18500), 307 (15900), 265 (20500), 236 (43800), 209 (44900) nm.

*Synthesis of fac–[Re(CO)$_3$(phen)(**L3**)]* ***[Re(phen)(L3)]***

Prepared as for **[Re(phen)(L1)]** using *fac*–[*Re*(*phen*)(*CO*)$_3$(MeCN)]BF_4 (38 mg, 65.9 µmol) and **L3** (25 mg, 73.2 µmol) to give **[Re(phen)(L3)]** as a yellow solid. Yield: 46 mg, 53.7 µmol, 82 %; ^{1}H NMR (400 MHz, CD_3CN): δ_H = 9.42 (d, 2H, $^3J_{HH}$ = 3.6 Hz, phen), 8.59–8.50 (m, 3H), 8.35 (dd, 1H, J_{HH} = 7.3 Hz, 1.0 Hz), 8.26 (d, 1H, $^3J_{HH}$ = 5.6 Hz), 8.20 (d, 2H, $^3J_{HH}$ = 7.9 Hz), 8.01 (d, 1H, $^3J_{HH}$ = 1.6 Hz), 7.92–7.81 (m, 7H), 7.07 (dd, 1H, J_{HH} = 7.8 Hz, 5.7 Hz), 4.83 (s, 2H, CH_2) ppm; ^{13}C{^{1}H} NMR (300 MHz, CD_3CN): δ_C = 195.7 (M–*C*=O), 191.2 (M–*C*=O), 163.2 (*C*=O), 163.0 (*C*=O), 154.5, 154.4, 152.0, 151.7, 146.5, 140.8, 140.2, 138.9, 136.0, 132.0, 131.2, 130.8, 129.1, 128.8, 128.4, 128.0, 127.7, 127.1, 126.2, 122.6, 121.3, 40.3 (*C*H_2) ppm; LRMS (ES^+) found *m/z* = 773.12 for $[M]^+$; HRMS (ES^+) found *m/z* = 771.0570 for $[C_{33}H_{19}O_5N_4ClRe]^+$, calculated 771.0568 for $[C_{33}H_{19}O_5N_4ClRe]^+$; IR (solid) ν_{max} (±2 cm^{-1}) = 2027 (M–C=O), 1928 (M–C=O), 1911, 1701 (C=O), 1666 (C=O), 1587, 1572, 1521, 1508, 1483, 1458, 1431, 1377, 1342, 1230, 1199, 1176, 1151, 1053 (Re–N), 1035, 850, 779 (C–Cl), 752, 723, 706, 648 cm^{-1}; UV–Vis (CH_3CN): λ_{max} ($\varepsilon/M^{-1}cm^{-1}$) = 354 (16700), 340 (19600), 326 (17100), 274 (32200), 233 (62300), 211 (61000) nm.

*Synthesis of fac–[Re(CO)$_3$(bpy)(**L4**)]* ***[Re(bpy)(L4)]***

Prepared as for **[Re(phen)(L1)]** using *fac*–[*Re*(*bpy*)(*CO*)$_3$(MeCN)]BF_4 (40 mg, 66.4 µmol) and **L4** (27 mg, 73.1 µmol) to give **[Re(bpy)(L4)]** as a yellow solid. Yield: 51 mg, 54.7 µmol, 82 %; ^{1}H NMR (400 MHz, CD_3CN): δ_H = 8.92 (d, 2H, $^3J_{HH}$ = 5.4 Hz, bpy), 8.19 (d, 2H, $^3J_{HH}$ = 7.6 Hz), 8.10 (d, 3H, $^3J_{HH}$ = 8.1 Hz), 7.98 (dd, 2H, J_{HH} = 7.9 Hz, 6.4 Hz), 7.87 (d, 2H, $^3J_{HH}$ = 6.6 Hz), 7.53–7.40 (m, 3H), 7.02 (d, 2H, $^3J_{HH}$ = 6.6 Hz), 6.96 (d, 1H, $^3J_{HH}$ = 8.2 Hz), 4.94 (s, 2H, NCH_2C), 2.98 (t, 4H, $^3J_{HH}$ = 5.0 Hz, NCH_2CH_2), 1.67–1.58 (m, 4H), 1.51–1.42 (m, 2H, NCH_2CH_2CH_2) ppm; ^{13}C{^{1}H} NMR (600 MHz, CD_3CN): δ_C =195.7 (M–*C*=O), 191.4 (M–*C*=O), 164.2 (*C*=O), 163.6 (*C*=O), 157.8, 155.8, 153.8, 1521.8, 151.6, 141.1, 132.7, 131.4, 131.0, 129.9, 128.8, 126.1, 125.6, 125.3, 124.7, 122.6, 114.9, 144.4, 54.3, 41.9, 25.9, 24.0 ppm; LRMS (ES^+) found *m/z* = 798.19 for $[M]^+$; HRMS (ES^+) found *m/z* = 796.1693 for $[C_{36}H_{29}N_5O_5Re]^+$, calculated 796.1693 for $[C_{36}H_{29}N_5O_5Re]^+$; IR (solid) ν_{max} (±2 cm^{-1}) = 2031 (M–C=O), 1919 (M–C=O), 1691 (C=O), 1654 (C=O), 1616, 1587, 1572, 1514, 1475, 1444, 1429, 1419, 1357, 1344, 1313, 1238, 1222, 1176, 1159, 1130, 1087, 1078, 1060, 1047,

1022, 985, 947, 898, 860, 835, 812, 796, 781, 767, 734, 677, 661, 644, 623 cm^{-1}; UV–Vis (CH_3CN): λ_{max} ($\varepsilon/M^{-1}cm^{-1}$) = 411 (12700), 339 (6400), 318 (16900), 257 (34500), 207 (64100) nm.

*Synthesis of fac–[Re(CO)$_3$(phen)(**L4**)]* ***[Re(phen)(L4)]***

Prepared as for **[Re(phen)(L1)]** using *fac*–[*Re*(*phen*)(*CO*)$_3$(MeCN)]BF_4 (40 mg, 69.2 µmol) and **L4** (28 mg, 76.1 µmol) to give **[Re(phen)(L4)]** as an orange–yellow solid. Yield: 42 mg, 46.1 µmol, 67 %; ^{1}H NMR (400 MHz, $CDCl_3$): δ_H = 9.50 (d, 2H, $^3J_{HH}$ = 4.6 Hz, phen), 8.77 (d, 2H, $^3J_{HH}$ = 8.1 Hz), 8.34 (d, 1H, $^3J_{HH}$ = 6.6 Hz), 8.28 (t, 2H, $^3J_{HH}$ = 8.3 Hz), 8.28–8.16 (m, 6H), 7.55 (t, 1H, $^3J_{HH}$ = 7.5 Hz), 7.17 (d, 2H, $^3J_{HH}$ = 6.3 Hz), 7.04 (d, 1H, $^3J_{HH}$ = 8.2 Hz), 5.09 (s, 2H, CH_2), 3.15 (t, 4h, $^3J_{HH}$ = 4.6 Hz, NCH_2CH$_2$), 1.86–1.78 (m, 4H, NCH$_2$CH_2), 1.71–1.60 (m, 2H, NCH$_2$CH$_2$CH_2) ppm; ^{13}C{^{1}H} NMR (300 MHz, $CDCl_3$): δ_C = 195.1 (M–*C*=O), 164.3 (*C*=O), 163.7 (*C*=O), 158.1, 154.3, 153.9, 152.0, 151.5, 151.3, 146.4, 140.6, 140.6, 133.4, 131.6, 131.4, 130.1, 128.6, 127.7, 126.1, 125,7, 125.4, 122.1, 114,8, 144.4, 52.5, 42.0, 26,1, 24.3 ppm; LRMS (ES$^+$) found *m/z* = 822.20 for [M]$^+$; HRMS (ES$^+$) found *m/z* = 820.1690 for [$C_{38}H_{29}N_5O_5Re$]$^+$, calculated 820.1693 for [$C_{38}H_{29}N_5O_5Re$]$^+$; IR (solid) ν_{max} (±2 cm^{-1}) = 2029 (M–C=O), 1911 (M–C=O), 1691, (C=O), 1654 (C=O), 1618, 1577, 1560, 1518, 1450, 1429, 1381, 1354, 1340, 1313, 1280, 1232, 1178, 1153, 1130, 1051, 1033, 989, 949, 914, 900, 848, 817, 760, 740, 723, 702, 671, 644, 624 cm^{-1}; UV–Vis (CH_3CN): λ_{max} ($\varepsilon/M^{-1}cm^{-1}$) = 408 (9700), 340 (5600), 326 (6600), 274 (36700) nm.

*Synthesis of fac–[Re(CO)$_3$(bpy)(**L5**)]* ***[Re(bpy)(L5)]***

Prepared as for **[Re(phen)(L1)]** using *fac*–[*Re*(*bpy*)(*CO*)$_3$(MeCN)]BF_4 (40 mg, 66.4 µmol) and **L5** (27 mg, 73.1 µmol) to give **[Re(bpy)(L5)]** as a yellow solid. Yield: 61 mg, 65.6 µmol, 99 %; ^{1}H NMR (400 MHz, $CDCl_3$): δ_H = 9.10 (d, 2H, $^3J_{HH}$ = 5.1 Hz), 8.66 (d, 2H, $^3J_{HH}$ = 8.1 Hz), 8.46 (d, 1H, $^3J_{HH}$ = 7.2 Hz), 8.46–8.35 (m, 3H), 8.23–8.16 (m, 2H), 8.10 (d, 1H, $^3J_{HH}$ = 7.9 Hz), 7.76–7.67 (m, 4H), 7.33–7.25 (m, 1H), 7.15 (d, 1H, $^3J_{HH}$ = 8.2 Hz), 5.12 (s, 2H, NCH$_2$C), 3.27 (broad t, 4H, NCH_2CH$_2$), 1.93–1.84 (m, 4H, NCH$_2$CH_2), 1.77–1.68(m, 2H, NCH$_2$CH$_2$CH_2) ppm; ^{13}C{^{1}H} NMR (300 MHz, $CDCl_3$): δ_C = 195.6 (M–*C*=O), 190.9 (M–*C*=O), 164.3 (*C*=O), 163.7 (*C*=O), 158.2, 155.8, 152.6, 151.0, 141.7, 141.3, 136.8, 133.4, 133.4, 131.8, 131.8, 130.0, 128.9, 126.9, 126.2, 126.0, 125.6, 122.2, 115.0, 114.4, 65.9 (*C*H$_2$), 54.5, 40.1, 26.2, 24.3, 15.3 ppm; LRMS (ES$^+$) found *m/z* = 798.08 for [M]$^+$; HRMS (FTMS) found: *m/z* 796.1696 for [$C_{36}H_{29}N_5O_5Re$]$^+$, calculated 796.1693 for [M]$^+$; IR (solid) ν_{max} (±2 cm^{-1}) = 2029 (M––C=O), 1903 (M–C=O), 1689 (C=O), 1651 (C=O), 1602, 1573, 1558, 1514, 1471, 1444, 1377, 1344, 1315, 1232, 1178, 1157, 1051, 1022, 983, 962, 945, 896, 860, 829, 812, 767, 760,

733, 704, 667, 644, 628 cm^{-1}; UV–Vis (CH_3CN): λ_{max} ($\varepsilon/M^{-1}cm^{-1}$) = 411 (9500), 340 (5200), 318 (12900), 261 (31200), 203 (60700) nm.

*Synthesis of fac–[Re(CO)$_3$(phen)(**L5**)]* ***[Re(phen)(L5)]***

Prepared as for **[Re(phen)(L1)]** using *fac––Re*(*phen*)(*CO*)$_3$(MeCN)]BF_4 (39 mg, 67.4 µmol) and **L5** (31 mg, 74.1 µmol) to give **[Re(phen)(L5)]** as an orange solid. Yield: 39 mg, 43.3 µmol, 64 %; ^{1}H NMR (400 MHz, $CDCl_3$): δ_H = 9.54 (d, 2H, $^3J_{HH}$ = 4.6 Hz), 8.82–8.76 (m, 2H), 8.42–8.36 (m, 3H), 8.33 (d, 2H, $^3J_{HH}$ = 7.9 Hz), 8.10–8.01 (m, 5H), 7.96 (d, 1H, $^3J_{HH}$ = 7.9 Hz), 7.73 (t, 1H, $^3J_{HH}$ = 8.1 Hz), 5.02 (s, 2H, CH_2), 3.27 (broad t, 4H, NCH_2CH_2), 1.94–1.86 (m, 4H, NCH_2CH_2), 1.80–1.79 (m, 2H, NCH_2CH_2CH_2) ppm; ^{13}C{^{1}H} NMR (300 MHz, $CDCl_3$): δ_C = 195.3 (M–*C*=O), 164.1 (*C*=O), 153.6, 153.1, 152.5, 152.3, 151.4, 146.3, 141.2, 140.6, 133.3, 131.8, 131.8, 131.4, 131.4, 128.6, 128.1, 127.5, 127.3, 126.9, 125.8, 125.7, 122.1, 54.8, 54.5, 40.0, 26.0, 24.1 ppm; LRMS (ES^+) found *m/z* = 822.24 for $[M]^+$; HRMS (ES^+) found *m/z* = 820.1691 for $[C_{38}H_{29}N_5O_5Re]^+$, calculated 820.1693 for M^+; IR (solid) ν_{max} (±2 cm^{-1}) = 2031 (M–C=O), 1911 (M–C=O), 1691 (C=O), 1651 (C=O), 1585, 1519, 1483, 1431, 1417, 1381, 1346, 1317, 1280, 1234, 1199, 1178, 1151, 1057, 1035, 989, 989, 964, 947, 900, 875, 848, 785, 760, 740, 723, 706, 646, 628 cm^{-1}; UV–Vis (CH_3CN): λ_{max} ($\varepsilon/M^{-1}cm^{-1}$) = 406 (7000), 274 (34500) nm.

*Synthesis of fac–[Re(CO)$_3$(bpy)(**L6**)]* ***[Re(bpy)(L6)]***

Prepared as for **[Re(phen)(L1)]** using *fac*–[*Re*(*bpy*)(*CO*)$_3$(MeCN)]BF_4 (40 mg, 66.4 µmol) and **L6** (29 mg, 73.1 µmol) to give **[Re(bpy)(L6)]** as an orange–yellow solid. Yield: 35.6 mg, 39.3 µmol, 50 %. ^{1}H NMR (400 MHz, $CDCl_3$): δ_H = aromatic– impure and overlapping, 6.61 (d, 1H, $^3J_{HH}$ = 8.6 Hz), 5.98 (broad t, 1H, N*H*), 5.19 (s, 2H, NCH_2), 4.55 (d, 2H, $^3J_{HH}$ = 5.0 Hz, NHCH_2) ppm; ^{13}C{^{1}H}NMR (300 MHz, $CDCl_3$): δ_C = 193.2 (M–*C*=O), 185.3 (M–*C*=O), 164.4 (*C*=O), 163.5 (*C*=O), 163.5, 154.0, 153.8, 151.9, 151.2, 141.1, 134.3, 128.5, 128.3, 127.9, 127.6, 125.1, 124.8, 124.6123.2, 120.4, 119.8, 104.9, 47.1, 42.2 ppm; LRMS (ES^+) found *m/z* = 820.16 for $[M]^+$, calculated 819.92 for $[M]^+$; HRMS found *m/z* = 818.1531 for $[C_{38}H_{27}N_5O_5Re]^+$, calculated 818.1536 for $[C_{38}H_{27}N_5O_5Re]^+$; IR (solid) ν_{max} (±2 cm^{-1}) = 2360, 2341, 2301 (M–C=O), 1913 (M–C=O), 1683, 1647, 1622, 1604, 1577, 1473, 1446, 1429, 1392, 1344, 1317, 1294, 1288, 1246, 1180, 1165, 1062, 1020, 902, 771, 733, 677, 648, 630 cm^{-1}; UV–Vis (CH_3CN): λ_{max} ($\varepsilon/M^{-1}cm^{-1}$) = 430, 355, 339, 319, 278, 254, 228 nm. Extinction coefficients could not be obtained due to impurity of sample.

*Synthesis of fac–[Re(CO)$_3$(phen)(**L6**)]* ***[Re(phen)(L6)]***

Prepared as for **[Re(phen)(L1)]** using *fac*–[*Re*(*phen*)(*CO*)$_3$(MeCN)]BF$_4$ (38 mg, 65.7 μmol) and **L6** (27 mg, 72.3 μmol) to give **[Re(phen)(L6)]** as a yellow solid. Yield: 42 mg, 45.1 μmol, 61 %; ^{1}H NMR (250 MHz, CD_3CN): δ_H = 9.60 (d, 2H, $^3J_{HH}$ = 5.13 Hz), 8.81 (dd, 2H, J_{HH} = 7.6 Hz, 7.9 Hz), 8.40 (t, 2H, $^3J_{HH}$ = 7.8 Hz), 8.24–8.06 (m, 8H), 7.65 (t, 1H, $^3J_{HH}$ = 8.1 Hz), 7.51–7.32 (m, 4H), 7.18 (d, 2H, $^3J_{HH}$ = 7.4 Hz), 6.98 (t, 1H, 5.3 Hz, N*H*), 6.62 (d, 1H, $^3J_{HH}$ = 8.0 Hz, NHCC*H*), 5.10 (s, 2H, NCH_2), 4.68 (d, 2H, $^3J_{HH}$ = 6.0 Hz, NHCH_2) ppm; ^{13}C{^{1}H} NMR (300 MHz, CD_3CN): δ_C = 195.5(M–*C*=O), 191.5 (M–*C*=O), 164.2 (*C*=O), 163.1 (*C*=O), 154.7, 151.7, 150.3, 146.6, 140.3, 138.2, 134.1, 131.3, 131.0, 128.7, 128.1, 127.9, 127.4, 127.2, 127.1, 125.4, 124.7, 122.1, 120.3, 108.8, 104.8, 46.43 (*C*H$_2$), 41.6 (NH*C*H$_2$) ppm; LRMS (ES$^+$) found *m/z* = 844.24 for [M]$^+$; HRMS found *m/z* = 842.1536 for [$C_{40}H_{27}N_5O_5Re$]$^+$, calculated 842.1536 for [$C_{40}H_{27}N_5O_5Re$]$^+$; IR (solid) ν_{max} (±2 cm^{-1}) = 2031 (M–C=O), 1913 (M–C=O), 1685 (C=O), 1647 (C=O), 1618, 1577, 1550, 1521, 1503, 1496, 1429, 1392, 1369, 1356, 1344, 1315, 1296, 1246, 1184, 1166, 1136, 1057, 1053, 993, 943, 918, 877, 848, 817, 802, 775, 758, 742, 723, 698, 645, 628 cm^{-1}; UV–Vis (CH_3CN): λ_{max} (ε/M^{-1}cm^{-1}) = 431 (14600), 354 (6900), 337 (9300), 323 (9600), 275 (47300), 256 (39800), 226 (58400) nm.

*Synthesis of fac–[Re(CO)$_3$(bpy)(**L7**)]* ***[Re(bpy)(L7)]***

Prepared as for **[Re(phen)(L1)]** using *fac*–[*Re*(*bpy*)(*CO*)$_3$(MeCN)]BF$_4$ (18 mg, 31.5 μmol) and **L7** (14 mg, 34.6 μmol) to give **[Re(bpy)(L7)]** as a yellow solid. Yield: 24 mg, 25.5 μmol, 81 %; ^{1}H NMR (400 MHz, $CDCl_3$): δ_H = 8.93 (d, 2H, $^3J_{HH}$ = 4.4 Hz), 8.33 (app s, 4H), 8.24 (t, 1H, $^3J_{HH}$ = 9.5 Hz), 8.16 (d, 1H, $^3J_{HH}$ = 8.2 Hz), 8.06–7.92 (m, 4H), 7.60 (t, 1H), 7.49 (app s, 2H), 7.38 (d, 2H, $^3J_{HH}$ = 7.3 Hz), 7.32–7.18 (m, 4H), 6.66 (d, 1H, $^3J_{HH}$ = 8.3 Hz), 6.46 (app s, 1H, N*H*), 5.23 (s, 2H, CH_2), 4.63 (app s, 2H, NHCH_2) ppm; ^{13}C{^{1}H} NMR (300 MHz, $CDCl_3$): δ_C = 190.7 (M–*C*=O), 169.6 (*C*=O), 167.1 (*C*=O), 155.6, 153.4, 152.4, 151.1, 148.6, 147.9, 142.0, 141.7, 137.3, 135.0, 131.7, 129.0, 128.6, 128.2, 127.9, 127.7, 126.7, 126.1, 125.8, 125.3, 123.1, 108.7, 47.9 (*C*H$_2$), 42.4 (NH*C*H$_2$) ppm; LRMS (ES$^+$) found *m/z* = 820.16 for [M]$^+$; HRMS (FTMS) found *m/z* 818.1549 for [$C_{38}H_{27}N_5O_5Re$]$^+$, calculated 818.1536 for [$C_{38}H_{27}N_5O_5Re$]$^+$; IR (solid) ν_{max} (±2 cm^{-1}) = 2031 (M–C=O), 1915 (M–C=O), 1683 (C=O), 1645 (C=O), 1602, 1577, 1548, 1494, 1471.7, 1446, 1419, 1390, 1369, 1346, 1317, 1296, 1246, 1182, 1165, 1136, 1060, 1033, 939, 908, 898, 802, 771, 734, 702, 661, 646, 628 cm^{-1}; UV–Vis (CH_3CN): λ_{max} (ε/M^{-1}cm^{-1}) = 432 (13800), 319 (12800), 277 (32600, 256 (31200), 227 (30300) nm.

*Synthesis of fac–[Re(CO)$_3$(phen)(**L7**)]* ***[Re(phen)(L7)]***

Prepared as for **[Re(phen)(L1)]** using *fac*–[*Re*(*phen*)(*CO*)$_3$(MeCN)]BF$_4$ (42 mg, 72.1 μmol) and **L7** (31 mg, 79.3 μmol) to give **[Re(phen)(L7)]** as a yellow solid. Yield: 43 mg,

46.2 μmol, 64 %; ^{1}H NMR (400 MHz, CD_3CN): δ_H = 9.39 (d, 2H, $^{3}J_{HH}$ = 3.8 Hz), 8.44 (m, 2H), 8.32 (d, 2H, $^{3}J_{HH}$ = 4.9 Hz), 8.29 (d, 2H, $^{3}J_{HH}$ = 8.2 Hz), 8.02 (d, 1H, $^{3}J_{HH}$ = 8.6 Hz), 7.83 (s, 1H), 7.82–7.71 (m, 5H), 7.66 (t, 1H, $^{3}J_{HH}$ = 7.9 Hz), 7.51 (s, 1H), 7.41 (d, 2H, $^{3}J_{HH}$ = 7.5 Hz), 7.31 (t, 2H, $^{3}J_{HH}$ = 7.5 Hz), 7.11 (dd, 1H, J_{HH} = 7.7 Hz, 5.6 Hz), 7.02 (app s, 1H, N*H*), 6.66 (d, 1H, $^{3}J_{HH}$ = 8.6 Hz), 4.83 (s, 2H, CH_2), 4.66 (d, 2H, $^{3}J_{HH}$ = 6.0 Hz, NHCH_2) ppm; ^{13}C{^{1}H} NMR (300 MHz, CD_3CN): δ_C = 195.7 (M–C=O), 191.5 (M–C=O), 163.8 (C=O), 162.9 (C=O), 154.3, 151.7, 150.5, 146.3, 140.3, 139.9, 140.0, 138.3, 137.0, 134.3, 131.2, 131.0, 129.7, 128.7, 128.0, 127.8, 127.4, 127.3, 126.9, 126.1, 124.9, 122.1, 120.7, 120.6, 119.9, 119.1, 105.0, 46.5 (CH_2), 39.9 ($NHCH_2$) ppm; LRMS (ES^+) found *m/z* = 844.16 for $[M]^+$; HRMS (FTMS) found *m/z* 842.1543 for $[C_{40}H_{27}N_5O_5Re]^+$, calculated 842.1536 for $[C_{40}H_{27}N_5O_5Re]^+$; IR (solid) ν_{max} (±2 cm^{-1}) = 2031 (M–C=O), 1915 (M–C=O), 1683 (C=O), 1645, 1602, 1577, 1548, 1494, 1471, 1446, 1419, 1390, 1369, 1346, 1317, 1296, 1246, 1182, 1165, 1136, 1060, 1033, 939, 908, 898, 802, 771, 734, 702, 646, 628 cm^{-1}; UV–Vis (CH_3CN): λ_{max} ($\varepsilon/M^{-1}cm^{-1}$) = 431 (16500), 323 (8300), 275 (47800), 257 (40800), 226 (53500) nm.

2.6 References

1. H. Wang, L. Yang, W. Zhang, Y. Zhou, B. Zhao and X. Li, *Inorg. Chim. Acta*, 2012, **381**, 111-116.
2. S. Banerjee, E. B. Veale, C. M. Phelan, S. A. Murphy, G. M. Tocci, L. J. Gillespie, D. O. Frimannsson, J. M. Kelly and T. Gunnlaugsson, *Chem. Soc. Rev.*, 2013, **42**, 1601-1618.
3. D. Rideout, R. Schinazi, C. D. Pauza, K. Lovelace, L. C. Chiang, T. Calogeropoulou, M. McCarthy and J. H. Elder, *J. Cell. Biochem.*, 1993, **51**, 446-457.
4. Y. Li, Y. Wu, C. J., M. Chen, R. Liu and F. Li, *Chem. Commun.*, 2013, 11335-11337.
5. I. Ott, Y. Xu, J. Liu, M. Kokoschka, M. Harlos, W. S. Sheldrick and X. H. Qian, *Bioorg. Med. Chem.*, 2008, **16**, 7107-7116.
6. L. Chen, W. Sun, W. Li, J. Li, L. Du, W. Xu, H. Fang and M. Li, *Analytical Methods*, 2012, **4**, 2661-2663.
7. R. Stolarski, *Fibres & Textiles in Eastern Europe*, 2009, **17**, 91-95.
8. V. Bojinov and I. Panova, *Dyes Pigm.*, 2009, **80**, 61-66.
9. T. Kálai, E. Hideg, F. Ayaydin and K. Hideg, *Photochem. Photobiol. Sci.*, 2013, **12**, 432-438.
10. S. S. Bag, M. K. Pradhan, R. Kundu and S. Jana, *Bioorg. Med. Chem.*, 2013, **23**, 96-101.
11. E. E. Langdon-Jones, N. O. Symonds, S. E. Yates, A. J. Hayes, D. Lloyd, R. Williams, S. J. Coles, P. N. Horton and S. J. A. Pope, *Inorg. Chem.*, 2014, **53**, 3788-3797.
12. Z. Y. Wu, J. N. Cui, X. H. Qian and T. Y. Liu, *Chin. Chem. Lett.*, 2013, **24**, 359-361.
13. Z. Liu, W. He and Z. Guo, *Chem. Soc. Rev.*, 2013, **42**, 1568-1600.
14. D. Staneva, E. Vasileva-Tonkova, M. S. I. Makki, A. M. Asiri and I. Grabchev, *J. Mol. Struct.*, 2014, 88-94.
15. Y. Li, H. Yang, Q. Zhao, W. Song, J. Han and X. Bu, *Inorg. Chem.*, 2012, **51**, 9642-9648.
16. R. Bissell, A. De Silva, H. Gunartane, P. Lynch, G. Maguire and K. Sandanayake, *Chem. Soc. Rev.*, 1992, **21**, 187-195.
17. V. Bojinov, N. Georgiev and P. Bosch, *J. Fluoresc.*, 2009, **19**, 127-139.
18. M. Pluth, E. Tomat, S. Lippard, R. Kornberg, C. Raetz, J. Rothman and J. Thorner, *Annual Review of Biochemistry, Vol 80*, 2011, **80**, 333-355.
19. E. Hao, T. Meng, M. Zhang, W. Pang, Y. Zhou and L. Jiao, *J. Phys. Chem. A*, 2011, **115**, 8234-8241.
20. E. Baggaley, J. Weinstein and J. A. G. Williams, *Coord. Chem. Rev.*, 2012, **256**, 1762-1785.
21. B. Yeo, A. Hallett, B. Kariuki and S. Pope, *Polyhedron*, 2010, **29**, 1088-1094.
22. M. Cattaneo, F. Fagalde and N. E. Katz, *Inorg. Chem.*, 2006, **45**, 6884-6891.
23. V. Fernández-Moreira, F. L. Thorp-Greenwood and M. P. Coogan, *Chem. Commun.*, 2010, **46**, 186-202.
24. F. L. Thorp-Greenwood, R. G. Balasingham and M. P. Coogan, *J. Organomet. Chem.*, 2012, **714**, 12-21.
25. D. J. Stufkens and A. Vlcek Jr., *Coord. Chem. Rev.*, 1998, **177**, 127-179.
26. L. Mullice and S. Pope, *Dalton Trans.*, 2010, **39**, 5908-5917.
27. M. P. Coogan and S. J. A. Pope, in *The Chemistry of Molecular Imaging*, eds. N. Long and W. T. Wong, John Wiley and Sons Inc., New Jersey, 1st edn., 2015, ch. 12, pp. 275-298.
28. D. Tyson, C. Luman, X. Zhou and F. Castellano, *Inorg. Chem.*, 2001, **40**, 4063-4071.
29. J. Yarnell, J. Deaton, C. McCusker and F. Castellano, *Inorg. Chem.*, 2011, **50**, 7820-7830.
30. L. Sacksteder, A. Zipp, E. Brown, J. Streich, J. Demas and B. Degraff, *Inorg. Chem.*, 1990, **29**, 4335-4340.

31. A. J. Amoroso, M. P. Coogan, J. Dunne, E., V. Fernández-Moreira, J. B. Hess, A. J. Hayes, D. Lloyd, C. Millet, S. J. A. Pope and C. Williams, *Chem. Commun.*, 2007, 3066-2068.
32. M.-W. Louie, H.-W. Liu, M. Ho-Chuen Lam, T.-C. Lau and K. K.-W. Lo, *Organometallics*, 2009, **28**, 4297-4307.
33. F. L. Thorp-Greenwood, M. P. Coogan, L. Mishra, N. Kumari, G. Rai and S. Saripella, *New J. Chem.*, 2012, **36**, 64-72.
34. S. Anand, B. J. Ortel, S. P. Pereira, T. Hasan and E. V. Matytin, *Cancer Lett. (Amsterdam, Neth.)*, 2012, **326**, 8-16.
35. D. E. J. G. J. Dolmans, F. D. and R. K. Jain, *Nat. Rev. Cancer*, 2003, **3**, 380-387.
36. J. MacDonald and T. J. Dougherty, *J. Porphyrins Phthalocyanines*, 2001, **5**, 105-129.
37. W. M. Sharman, C. M. Allen and J. E. van Lier, *Drug Discovery Today*, 1999, **4**, 507-517.
38. S. J. A. Pope and O. J. Stacey, *RSC Adv.*, 2013, **3**, 25550-25564.
39. X. Yi, J. Zhao, W. Wu, D. Huang, S. Ji and J. Sun, *Dalton Trans.*, 2012, **41**, 8931-8940.
40. J. Kollár, P. Hrdlovic, S. Chemela and G. Guyot, *J. Photochem. Photobiol., A*, 2005, **170**, 151-159.
41. Z. Chen, L. Wang, G. Zou, J. Tang, X. Cai, M. Teng and L. Chen, *Spectrochim. Acta, Part A*, 2013, **015**, 57-61.
42. K. de Oliveira, P. Costa, J. Santin, L. Mazzambani, C. Burger, C. Mora, R. Nunes and M. de Souza, *Bioorg. Med. Chem.*, 2011, **19**, 4295-4306.
43. *Germany Pat.,* W. Mederski, R. Devant, G. Barnickel, S. Bernotat-Danielowski, G. Melzer, P. Raddatz, Z. Wu, D. Dhanoa, R. Soll, J. Rinker and T. Graybill, WO 2000031039, 2000.
44. J. Zhang, M. Park, W. Ren, Y. Kim, S. Kim, J. Jung and J. Kim, *Chem. Commun.*, 2011, **47**, 3568-3570.
45. C. Conrad and M. Dolliver, *Org. Synth.*, 1932, **12**, 22-24.
46. T. Ukai, H. Kawazura, Y. Ishii, J. Bonnet and J. Ibers, *J. Organomet. Chem.*, 1974, **65**, 253-266.
47. Y. Takahashi, T. Ito, S. Sakai and Y. Ishii, *Chem. Commun.*, 1970.
48. L. Titcomb, *ChemSpider Synthetic Pages*, 2001.
49. J. Hartwig, M. Kawatsura, S. Hauck, K. Shaughnessy and L. Alcazar-Roman, *J. Org. Chem.*, 1999, **64**, 5575-5580.
50. R. H. Reimann and E. Singleton, *J. Organomet. Chem.*, 1973, **59**, C24-C26.
51. S. P. Schmidt, W. C. Trogler, F. Basolo, M. A. Urbancic and J. R. Shapley, *Inorg. Synth.*, 2007, **28**, 160.
52. N. N. Greenwood and A. Earnshaw, in *Chemistry of the Elements* ed. B.-H. Ltd, Butterworth-Heinemann Ltd, Oxford, UK, 2nd edn., 1997, ch. 24, pp. 1040-1062.
53. N. M. Shavaleev, A. Barbieri, Z. R. Bell, M. D. Ward and F. Barigelletti, *New J. Chem.*, 2004, **28**, 398-405.
54. S. Belanger, M. Gilbertson, D. I. Yoon, C. L. Stern, D. Dang and J. T. Hupp, *Dalton Trans.*, 1999, 3407-3411.
55. L. A. Mullice, R. H. Laye, L. P. Harding, N. J. Buurma and S. J. A. Pope, *New J. Chem.*, 2008, **32**, 2140-2149.
56. F. L. Thorp-Greenwood, M. P. Coogan, A. Hallett, R. Laye and S. J. A. Pope, *J. Organomet. Chem.*, 2009, **694**, 1400-1406.
57. D. E. Lewis, *Organic Biomolecular Chemistry*, 2013, **11**, 4390-4396.
58. H. Xia and F. Zhao, *Applied Mechanics and Materials*, 2013, **252**, 306-309.
59. C. Janiack, *Dalton Trans.*, 2000, 3885-3896.
60. S. Alvarez, *Dalton Trans.*, 2013, **42**, 8617-8636.
61. M. Shahid, P. Srivastava and A. Misra, *New J. Chem.*, 2011, **35**, 1690-1700.

62. L. Sacksteder, A. P. Zipp, E. A. Brown, J. Streich, J. N. Demas and B. A. DeGraff, 1990, **29**, 4335-4340.
63. J. Gan, K. Chen, C. Chang and H. Tian, *Dyes Pigm.*, 2003, **57**, 21-38.
64. H. Guo, J. Shaomin, W. Wu, W. Wu, J. Shao and J. Zhao, *Analyst (Cambridge, U. K.)*, 2010, **135**, 2832-2840.
65. V. Fernández-Moreira, M. L. Ortego, C. F. Williams, M. P. Coogan, M. D. Villacampa and M. C. Gimeno, *Organometallics*, 2012, **31**, 5950-5957.
66. M.-W. Louie, A. W.-T. Choi, H.-W. Liu, B. T.-N. Chan and K. K.-W. Lo, *Organometallics*, 2012, **31**, 5844-5855.
67. V. Fernández-Moreira, F. L. Thorp-Greenwood, A. J. Amoroso, J. Cable, J. B. Court, V. Gray, A. J. Hayes, R. L. Jenkins, B. M. Kariuki, D. Lloyd, C. O. Millet, C. F. Williams and M. P. Coogan, *Org. Biomol. Chem.*, 2010, **8**, 3888-3901.
68. G. M. Sheldrick, *Acta crystallographica. Section A, Foundations of crystallography*, 2008, **64**, 112-122.
69. L. J. Farrugia, *J. Appl. Crystallogr.*, 1997, 565.
70. J. Smieja and C. Kubiak, *Inorg. Chem.*, 2010, **49**, 9283-9289.

2.7 Appendix

2.7.1 Crystallographic data for [Re(phen)(L4)]

Table S2.1: Crystal Data and Structure Determination Refinement for [Re(phen)(L4)]

Identification code	**2013ncs0110 / EL*J*172**	
Empirical formula	$C_{38}H_{29}BF_4N_5O_5Re$	
Formula weight	908.67	
Temperature	100(2) K	
Wavelength	0.71075 Å	
Crystal system	Orthorhombic	
Space group	*Fdd*2	
Unit cell dimensions	a = 22.9167(16) Å	α = 90°
	b = 51.006(4) Å	β = 90°
	c = 56.261(4) Å	γ = 90°
Volume	65763(8) Å^3	
Z	64	
Density (calculated)	1.468 Mg / m^3	
Absorption coefficient	3.020 mm^{-1}	
F(000)	28672	
Crystal	Plate; Orange	
Crystal size	0.090 × 0.080 × 0.030 mm^3	
θ range for data collection	2.919 – 27.481°	
Index ranges	$-28 \le h \le 29$, $-66 \le k \le 64$, $-72 \le l \le 72$	
Reflections collected	134955	
Independent reflections	37115 [R_{int} = ?]	
Completeness to θ = 25.242°	99.8 %	
Absorption correction	Semi–empirical from equivalents	
Max. and min. transmission	1.000 and 0.760	
Refinement method	Full–matrix least–squares on F^2	
Data / restraints / parameters	37115 / 2131 / 2128	
Goodness–of–fit on F^2	0.982	
Final R indices [$F^2 > 2\sigma(F^2)$]	*R1* = 0.0538, *wR2* = 0.1225	
R indices (all data)	*R1* = 0.0915, *wR2* = 0.1353	
Extinction coefficient	n/a	
Largest diff. peak and hole	2.458 and –1.255 e Å^{-3}	

Diffractometer: *Rigaku AFC12* goniometer equipped with an enhanced sensitivity (HG) *Saturn724+* detector mounted at the window of an *FR–E+ SuperBright* molybdenum rotating anode generator with HF *Varimax* optics (100μm focus). **Cell determination and data collection**: *CrystalClear–SM Expert 3.1 b25* (Rigaku, 2012). **Data reduction, cell refinement and absorption correction**: *CrystalClear–SM Expert 3.1 b25* (Rigaku, 2012). **Structure solution**: *SHELXS97* (Sheldrick, G.M. (2008). Acta Cryst. A64, 112–122). **Structure refinement**: *SHELXL97* (Sheldrick, G.M. (2008). Acta Cryst. A64, 112–122). **Graphics:** *ORTEP3 for Windows* (L. *J*. Farrugia, *J*. Appl. Crystallogr. 1997, 30, 565

Table S 2.2: Selected Bond Lengths (Å) and Bond Angles (°) for [Re(phen)(L4)]

Bond Lengths / Å	
Re1–C28	1.095(18)
Re1–C27	1.921(13)
Re1–C26	1.945(11)
Re1–N31	2.178(13)
Re1–N1	2.189(10)
Re1–N32	2.190(9)
C11–O2	1.217(16)
C7–O1	1.254(16)
C26–O26	1.131(13)
C27–O27	1.140(14)
C28–O28	1.18(2)
Bond Angles / º	
C28–Re1–C27	88.4(6)
C28–Re1–C26	85.6(6)
C27–Re1–C26	87.2(5)
C28–Re1–N31	172.9(5)
C27–Re1–N31	96.1(5)
C26–Re1–N31	100.0(5)
C28–Re1–N1	92.6(6)
C27–Re1–N1	179.1(5)
C26–Re1–N1	92.7(4)
N31–Re1–N1	83.0(4)
C28–Re1–N32	98.4(5)
C27–Re1–N32	95.9(4)
C26–Re1–N32	175.0(5)
N31–Re1–N32	75.7(4)
N1–Re1–N32	84.2(3)
N2–C6–C3	112.0(11)

Chapter 3

Fluorescent Rhenium–Naphthalimide Conjugates as Cellular Imaging Agents

3.1 Introduction

This chapter discusses the development of some new dipicolyl amine ligands, which are appended with a N–substituted 1,8–naphthalimide fluorophore, together with their corresponding Re(I) complexes. These four new complexes are highly fluorescent, kinetically inert, and biologically compatible and have been successfully applied for cellular imaging using confocal fluorescence microscopy. They also have potential towards SPECT imaging.

3.1.1 Single Photon Emission Computed Tomography (SPECT) Imaging

SPECT is a very powerful, diagnostic, *in vivo*,[1] whole body[2] molecular imaging technique. It is used worldwide with *ca.* 40 million scans being performed each year.[3] SPECT imaging utilises gamma emissions from a radioisotope to act as a contrast agent[1] for the technique. A gamma radiation source is administered to the patient, either by inhalation, ingestion or injection.[4] The radiopharmaceutical normally comprises of an organometallic species where the metal provides the gamma source while the ligand acts as a targeting vector (certain tissues, biochemical events).[1,5,6] Within the body the radioactive metal decays, emitting gamma rays that each produce a single, high energy photon.[6] These are subsequently passed through a collimator towards a gamma camera that is step rotated around the patient.[6] The camera contains thallium activated NaI crystals that convert the high energy photons to visible light.[6] The images can then be reconstructed to form a 3D image of the gamma source within the body.[4] The collimator comprises of a pattern of holes in a gamma absorbent material (such as lead or tungsten).[6] This feature ensures that the detected photons have travelled along parallel paths and is vital for accurately determining the source of the photon (Figure 3.1).[4]

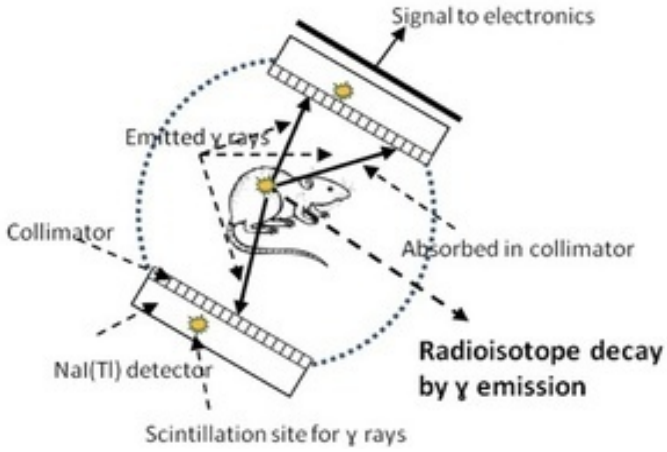

Figure 3.1: Schematic of SPECT equipment.

SPECT has become a favoured technique due to a number of key advantages. Firstly it has a high sensitivity[1,6] allowing very low doses (nM–pM range)[7,8] of the radiopharmaceuticals to be used, limiting the potential toxicity. However this sensitivity is a couple of orders of magnitude lower than positron emission tomography (PET) due to the use of the collimator in SPECT.[6] SPECT is also readily available, providing a good field of view (cm–sub m range) with good temporal resolution (secs–minutes).[3,6] Furthermore the technique has unlimited depth penetration[2] and the breadth of contrast agents available provides specificity for a range of protocols.

On the other hand SPECT has many limitations that often require the use of multiple techniques for full diagnosis. Most significantly the spacial resolution (cm range),[1,6,7,9] although better than PET,[3] is very poor. This is somewhat caused by the requirement for the collimator which also results in the low detection efficiency of SPECT ($<10^{-4}$).[4] In addition SPECT also requires relatively long acquisition times (min–hr) and the signal is insensitive to the environment,[2] rendering detection of biochemical events very difficult.

3.1.2 Technetium SPECT Contrast Agents

SPECT is inherently a contrast agent technique. ^{99m}Tc is the 'work horse' of nuclear medicine and is used in *ca.* 80%[10] of scans worldwide.[5,8,10] Other less common heavy isotopes used in contrast agents include ^{133}Xe ($t_{½}$= 125 hrs), ^{111}In ($t_{½}$= 67 hrs) and ^{123}I ($t_{½}$= 13 hrs).[7,10] The range of radioisotopes available also means that simultaneous two tracer imaging can be conducted by separating photons of different energy.[6]

Table 3.1: Radioisotopes of Tc and Re used in imaging or therapy.[3]

Isotope	Half life	Decay Products	Production
^{99m}Tc	6 hrs	γ = 140 KeV (98.6 %) γ = 142.7 KeV (1.4 %) Auger = 2.1 KeV	^{99}Mo/^{99m}Tc generator
^{94m}Tc	52 mins	β^+ = 2.4 MeV (72 %) β = 1.07 MeV (71 %)	Cyclotron from ^{94}M Reactor
^{186}Re	90 hrs	β = 1.07 MeV (71 %) γ = 137 MeV (9 %)	
^{188}Re	17 hrs	β = 2.1 MeV (100 %) γ = 155 MeV (15 %)	^{188}W/^{188}Re generator

^{99m}Tc is an artificial element but has become the isotope of choice due to a number of advantages. Firstly ^{99m}Tc is the main component of nuclear waste[8,10] and conveniently synthesised from ^{99m}Tc/^{99m}Mo generators at a reasonable cost.[10] Therefore SPECT contrast agents are more readily available than those for PET. Crucially ^{99m}Tc possess good decay characteristics (Table 3.1).[3,9-11] The half-life is long enough to provide a good imaging

window with no major radioactive hazard while being short enough to provide a good signal with no prolonged exposure. There are also several available oxidation states to offer different chemical properties.[3,5]

In recent years the focus has been on *fac*–[^{99m}Tc(I)(CO)$_3$] complexes[5,10] (Figure 3.2) since the development of the chemistry of [^{99m}Tc(CO)$_3$(H$_2$O)$_3$]$^+$ by Alberto and Schible *et al.* in 1998.[12] Subsequently numerous tridentate *N*–, *S*– and *O*– ligands, and also η^5–cyclopentdienide and carborane ligands, have been investigated with the [M(CO)$_3$)]$^+$ core and found to be stable and suitable towards *in vivo* SPECT imaging using a conjugate approach.[8,10]

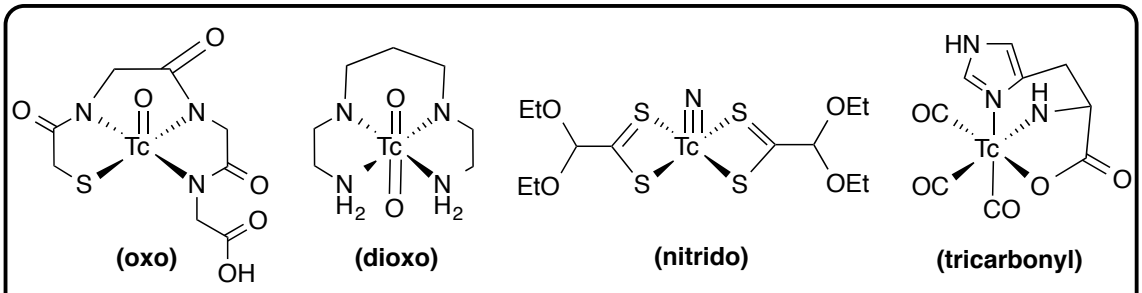

Figure 3.2: Different Tc cores explored for radiopharmaceutical applications.

The [M(CO)$_3$)]$^+$ core became popular due to the ease of preparation from [M(VII)O$_4$]$^-$ *via* commercial kits using aqueous solvents.[10] The aqua ligands could then be easily exchanged for functionalised organic ligands offering targeting vectors. The d^6, low spin[3] metal core is chemically and kinetically inert and its lipophilic and organometallic nature further leads to stable complexes due to the more covalent nature.[5,10] Stable complexes are required so that the metal ion is not liberated. This reduces the toxicity in the body and ensures that the metal can be safely excreted to reduce prolonged exposure. The metal stability is also assisted by the strong π–acceptor ability of the carbonyl ligands which expands the HOMO/LUMO gap, making oxidation/reduction more difficult. Also the polydentate ligands help to prevent ligand exchange.[3]

3.1.3 Rhenium as an Analogue for ^{99m}Tc

Re(I) is a well known analogue for ^{99m}Tc[3,11] and they form isostructural complexes[3] due to their shared electron configuration, stereochemistry and thermodynamics. Therefore characterisation of potential SPECT agents is often carried out using Re(I) as a cold isotope in order to avoid the use of radioactive ^{99m}Tc at high concentrations.[5] Using this method the biological characteristics and binding can be assessed without risk. On the other hand Re(I) possesses radionuclides in its own right. (Table 3.1). ^{186}Re is formed in a nuclear

reactor *via* neutron bombardment of elemental Re. The ^{188}Re is then removed by decay or the levels can be significantly reduced by using a ^{185}Re rich source.

$^{186/188}$Re radioisotopes do not have such favourable decay characteristics as ^{99m}Tc. This means that complexes of $^{186/188}$Re need much stricter stability constraints.[3] Re(I) is also much more expensive. These are two key reasons why ^{99m}Tc SPECT agents dominate. Nevertheless there is always a need to investigate new ligand systems and metals towards imaging applications. Favourably Re(I) is more inert than ^{99m}Tc and also offers the potential for combined/matched pair constellation diagnosis due to the two beta emitting isotopes.[5,10] The possibility of combined diagnosis (γ/^{99m}Tc) and radiotherapy (β/Re) is also being explored (theranostics). [7,13]

3.1.4 Dual Entity Bimodal Re/Tc Radio– and Fluorescent Imaging Agents

SPECT is known to have very high sensitivity and penetration, yet poor spatial resolution. Therefore combination with fluorescence imaging (high sensitivity, poor penetration, high resolution) can help to overcome the limitations of both techniques and cross validate results.[7] Recent research has focused on investigating bimodal fluorescent radiotracers,[5] ideally in a single molecule so that complementary data can be collected from the same device.[1] The single molecule approach is required for cross validation however issues can arise with the different dosages required for each technique.[2] Using combined nuclear and fluorescence techniques essentially allows SPECT to image the whole body (for example to locate a tumour) and then for the more highly resolved fluorescence technique to provide subcellular information (highlight the tumour boundaries for biopsy and validate tissue samples).[1,2] This approach can also reveal the cellular outcome of radiopharmaceuticals which is key in new drug design.[9]

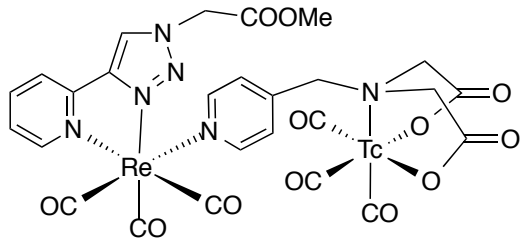

Figure 3.3: Example of a heterobimetallic bimodal SPECT/optical imaging agent.[7]

Bimodal agents are in their infancy however several examples have been reported in the literature for which two approaches are taken: i) mononuclear 'organic–inorganic' systems, and ii) heterobimetallic systems. The latter is at proof of principle stage and mostly investigated for MRI/optical techniques at present.[7] However several

nuclear/optical examples have been reported. Older examples possess one chelation site where half of the sample is bound to ^{99m}Tc (nuclear) and Re (fluorescent).[14-16] More recent examples contain two distinct chelation sites to hold Re/Tc simultaneously (Figure 3.3).[7,13]

'Organic–inorganic' examples are more common due to the breadth of chromphores and chelator sites available. In 2014 Davies *et al.*[9] synthesised a fluorescent bidentate phosphine capable of coordination to Re/Tc. The Re complex was highly fluorescent and resistant to degradation. Epifluorescence microscopy studies on PC–3 cells, using λ_{exc} = 460–500 and λ_{em} = 570 nm, allowed visualisation of organelles and the compound was seen to be non toxic. Other examples append a fluorescent unit to the metal chelation site. An example by Agorastos *et al.*[17] comprised an acridine/Tc conjugate, based around the cell receptor targeting protein Bombesin (Figure 3.4). Confocal fluorescence microscopy experiments showed very good uptake of the complexes with nuclear targeting and significant accumulation in nucleoli. In addition strong DNA binding was witnessed showing potential for auger therapy. Another example suitable for ^{99m}Tc by Mullice *et al.*[11] appended a pyrene or quinoline core to a 2–dipicolyl amine binding site (Figure 3.4).

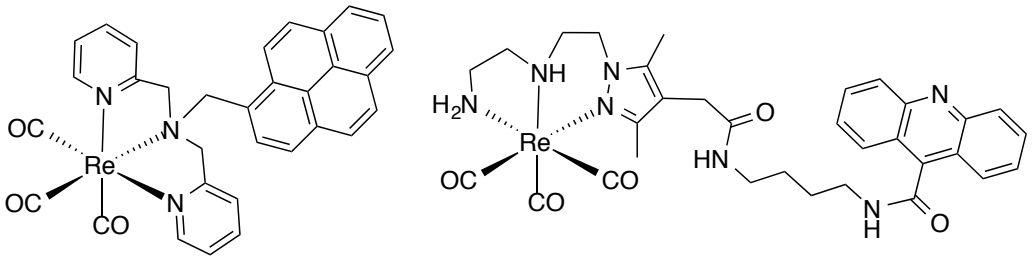

Figure 3.4: Example 'organic–inorganic' potential SPECT/optical agents.[11,17]

Other examples use fluorescent units that are inherently biologically active.[18] For example Tzanapoulou *et al.*[16] in 2010 reported series of 2–(4–aminophenyl)benzothiazoles with a N,N,O chelation site suitable for Re/Tc. Benzothiazoles are of interest due to anticancer properties and confocal fluorescence microscopy showed preferential cytoplasmic uptake of the compounds in tumorous cells. More recently Spagnul *et al.*[5] prepared two water soluble porphyrins with a peripheral chelator for Re/Tc. These examples showed preferential uptake and retention by tumours whereas other related porphyrin examples have shown poor uptake in Hep–2 tumour cells.[19]

3.2 Aims

Re(I) is a well known analogue to ^{99m}Tc and has radionuclides in its own right. Tuning the properties of such complexes is possible through varying the ligand system to optimise the properties and potentially introduce other imaging modalities. As single–molecule bimodal imaging agents these species would potentially overcome the limitations of each separate imaging technique.

This chapter describes the synthetic chemistry of a range of functionalised naphthalimide ligands towards cellular imaging probes. These examples will contain a 2–dipicolyl amine moiety suited to coordination chemistry of these ligands to Re(I).

Once synthesised both ligands and complexes were spectroscopically and analytically characterised to provide data indicating their synthesis, with spectroscopic studies being particularly important for assessing their feasibility towards cell imaging. Ultimately the aim was to develop a range of imaging agents highly suited to confocal fluorescence microscopy with the potential for dual use with SPECT. The ease at which the NI ligand can be tuned gave excellent control over the physical and photophysical properties. Therefore CFM studies assessed the imaging capability across the series to determine the feasibility of these compounds towards such a technique.

3.3 Results and Discussion

3.3.1 Ligand Synthesis and Characterisation

Ligands (**L1–4**) were isolated from a four step synthetic approach. As in Chapters Two and Four, the first step involved conversion to the 4–chloro–NI species (**Cl1–4**) by heating 4–chloro–1,8–naphthalic anhydride with the appropriate amine in ethanol (Scheme 3.1).[20]

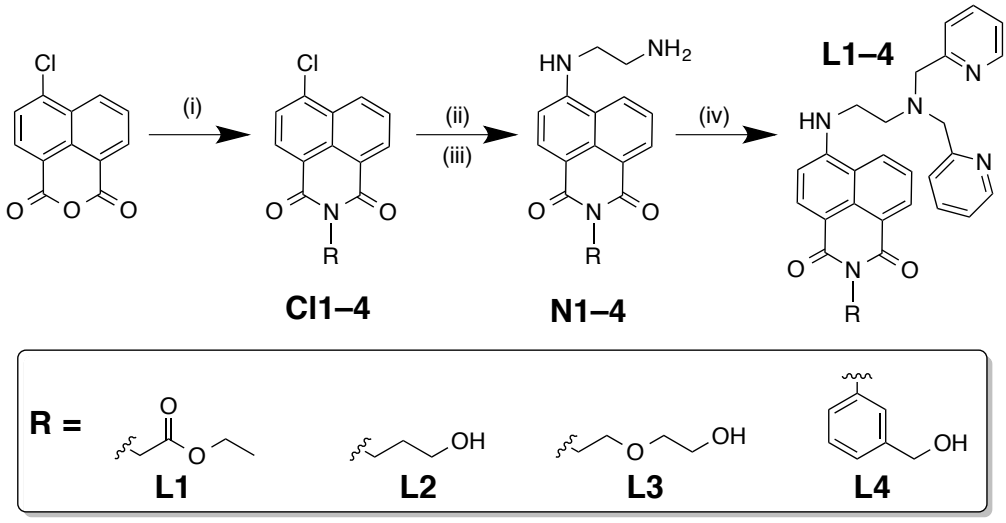

[a](i) RNH_2, EtOH; (ii) Boc–$NH(CH_2)_2NH_2$, (NEt_3), DMSO; (iii) TFA, dichloromethane; (iv) 2–pyridinecarboxaldehyde, $Na[BH(OAc)_3]$, 1,2–dichloroethane.

Scheme 3.1: Synthetic route to the ligands[a].

During this step it became apparent that the nucleophilicity and sterics of the amine had a large role to play. Initial reactions for the benzyl alcohol reagent, that lacks a $NH_2\underline{CH_2}$ group, resulted in highly insoluble, black solids. This suggested that the second step of the reaction was very slow and the product had not cyclised to form the imide. In order to activate this reaction several conditions were investigated including; higher boiling point solvents (DMF, *iso*–butyl alcohol[21], pyridine[22]), longer reaction times and mechanical techniques (grinding the solids together and heating crude). All of these attempts either resulted in no indication of reaction *via* TLC or still gave the amide intermediate (Figure 3.5).

An attempt to deprotonate the amide intermediate was made to assist reaction completion. The initial DMSO conditions were trialled with the addition of organic base; NEt_3 was selected (pKa = 10.78 at 25 ºC).[23] NEt_3 was strong enough to deprotonate the NH group (predicted pKa = 4.4)[24] to activate cyclisation, however not strong enough to deprotonate the OH group (predicted pKa = 14.5).[24,25] The addition of 1.5 equivalents of NEt_3 finally yielded the desired product.

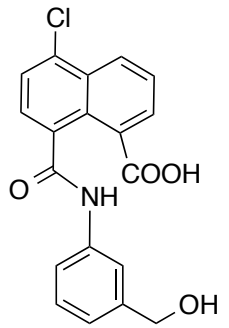

Figure 3.5: Structure of the proposed non–cyclised intermediate of Cl4.

Cl1–4 were found to be spectroscopically pure after extracting into dichloromethane, removing insoluble intermediates and washing away any excess amine with water. Successful formation of the 4–chloro substituted NI species (**Cl1-4**) was evident in the ^{1}H NMR spectra. A common, identifiable feature of the **Cl1-4** precursors when forming the imide species, with the exception of **Cl4**, was a noticeable singlet or triplet present at 4.8–3.5 ppm[26] assigned to the N–CH_2 resonance.

To successfully incorporate the 2–dipicolylamine (2–DPA) moiety into the NI chromophore a 2–aminoethyl linker was adopted (Scheme 3.1). To introduce this to the intermediate compounds, **Cl1–4**, *N*–*tert*–Boc–ethylenediamine was reacted with the 4–chloro species in DMSO[27] *via* a S_NAr mechanism with good yields (mostly *ca.* 90 %). This S_NAr reaction was less activated than those in the literature and Chapter Two, requiring longer reaction times of 12–16 hours. This step greatly improved the solubility of the compounds. Subsequent trifluoroacetic acid (TFA)–mediated deprotection of the Boc group yielded the amino–derived proligands **N1–4**. For this step the yields are not reported due to their hygroscopic nature and presence of TFA salts.

All of the Boc–protected intermediates were charactrised by ^{1}H NMR spectroscopy. Upon amine functionalisation at the 4–position there was a significant change in the resonance of the NI C3–proton. This shifted from being part of an aromatic multiplet (7.8–8.4 ppm depending on the R groups) to a distinctive doublet at *ca.* 6.4 ppm; shielded more greatly by nitrogen compared to chlorine (Figure 3.6). The *tert*–butyl group of Boc was also seen as a large peak at *ca.* 1.4 ppm. The resonances of the ethylene CH_2 protons shifted significantly upon substitution onto the NI core. After deprotection of the Boc group the ethylenediamine functionality of **N1–4** was witnessed as multiplets at 3.7–3.3 ppm in the ^{1}H NMR spectra, due to coupling with both the neighbouring CH_2 and NH or NH_2 group. The CH_2 protons' resonance shifted according to the specific nature of the imide

substituent. A corresponding disappearance of the resonance for the butyl group was also key in identifying deprotection of the bulk sample.

The final step to form **L1–4** used a one pot reductive amination method using 2–pyridinecarboxaldehyde, yielding the desired 2–DPA binding site.[28] All final ligands were novel with the exception of **L2** which was published during the course of this study using a different synthetic route.[29] Zhang *et al*. synthesised **L2** using the 4–bromo NI reagent and 9,10–bis(phenylethynyl)anthracene (BPEA) in 2–methoxyethanol with NEt_3. Therefore all **L1–4** were fully characterised *via* NMR and IR studies which agreed well with the proposed structures.

The ^1H NMR spectra of **L1–4** (Figure 3.6) showed the ethyl linker shift by *ca.* 0.5 ppm when compared to the **N1–4** precursors. An additional resonance for the CH_2 linker to the pyridine functional groups was also witnessed at *ca.* 4.0 ppm for each ligand.[30] These peaks always appeared as a noticeable singlet, indicating free rotation of the pyridine rings in solution and therefore equivalence of the CH_2 linker protons. The ^1H NMR spectra of **L1–4** also indicated free rotation of the imide substituents in solution. $^{13}C\{^1H\}$ NMR spectroscopy was used to determine the differences in the carbonyl environments, caused by the unsymmetrical substitution of the NI core. Two peaks at *ca.* 165 ppm[29-31] were observed for all ligands. IR spectroscopy was also used to distinguish differences in the carbonyl regions and spectra showed two distinct carbonyl peaks at *ca.* 1680 and 1640 cm^{-1}.[26,32] High resolution mass spectrometry (HRMS) (ES^+), showed the $[M+H]^+$ cation peak in all cases, and also commonly peaks for $[M+Na]^+$ and $[M+MeCN+Na]^+$.

3.3.2 Complex Synthesis and Characterisation

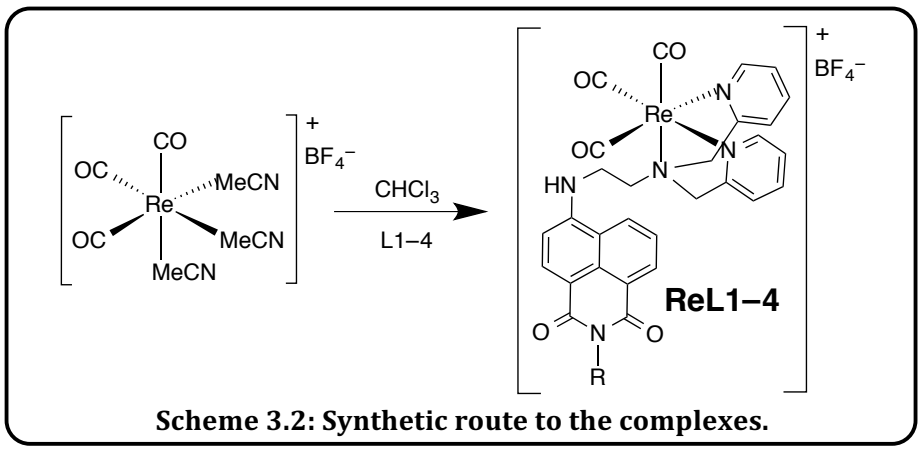

Scheme 3.2: Synthetic route to the complexes.

The preordered rhenium precursor complex *fac*–$[Re(CO)_3(MeCN)_3]BF_4$ was first synthesised to be correctly designed for facile coordination to the set of NI ligands. The precursor was made by well-known literature methods.[33] Once the precursor had been

synthesised the four ligands were each reacted with the precursor complex in chloroform[34] to give the desired *fac*–[Re(CO)$_3$(**LX**)]BF$_4$ complexes, **ReLX** (Scheme 3.2). In the *fac*-Re(I) coordination mode rhenium acts as a very close chemical analogue for ^{99m}Tc radioagents, for which it is key to add the metal as the last synthetic step. The yellow powders were isolated through precipitation with diethyl ether resulting in yields between 17–50 %. The range of the yields could have been due to the very small scale that these reactions were completed on.

In order to confirm the proposed N$_3$ facially capped Re(I) complexes, **ReL1–4** were fully characterised *via* NMR and IR spectroscopy.

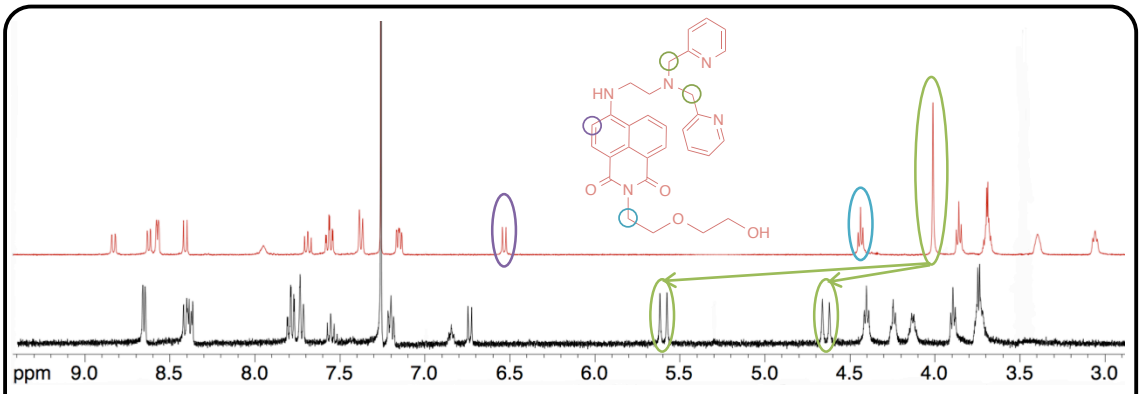

Figure 3.6: Comparison of the ^{1}H NMR spectra ($CDCl_3$, 400 MHz) of L3 (red) and ReL3 (black) highlighting significant resonances.

Firstly ^{1}H NMR spectroscopy was used to confirm coordination of the ligand to Re(I) by comparison of the CH_2 groups (Figure 3.6). For the imide–CH_2 the values did not shift significantly upon coordination however both the methylene and ethylene linkers were significantly shifted when compared to the ligands. In addition the complexes showed a splitting of the singlet resonance for the CH_2–pyr linker seen for the ligands. The asymmetry of the molecule and fixed position of the Re(I) bound ligand created a pair of diastereotopic protons with the resultant $^2J_{HH}$ geminal coupling[11] (16–18 Hz) observed in all of the complexes' ^{1}H NMR spectra. The observation of diastereotopic protons provided incredibly strong support of the proposed facial binding mode, thus rendering coordinative involvement of the NI nitrogen donor improbable.[29]

^{13}C{^{1}H} NMR spectroscopy was also used to characterise the carbonyls on both the naphthalimide unit and the carbonyl ligands directly bound to the Re(I) centre. The resonances for metal bound carbonyls were typically higher (*ca*. 180 ppm) than that for imide–carbonyls (*ca*. 160 ppm). IR spectroscopy further supported the facially capped Re(I) geometry (pseudo C_s), showing three metal bound CO stretching frequencies[11] at

2030–1890 cm^{-1} as well as the ligand carbonyls at *ca*. 1640 and 1690 cm^{-1}. In addition the presence of the metal was confirmed *via* HRMS that showed the parent ion peak with the correct $^{185/187}$Re isotopic pattern[8] in all cases (Figure 3.7).

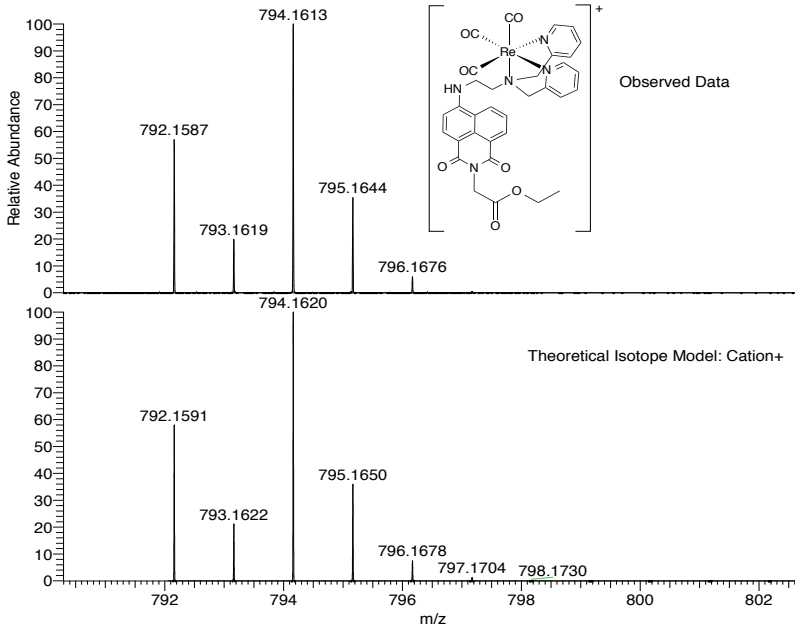

Figure 3.7: Example HRMS of ReL1 displaying the expected isotope pattern of $^{185/187}$Re.

3.3.3 Single Crystal X-ray Diffraction Studies

As well as solution state characterisation, a single crystal structure determination was obtained for **L1** (Figure 3.8). The crystal was grown *via* room temperature slow vapour diffusion of diethyl ether into a chloroform solution of **L1**. Data collection, refinement and structure solution was conducted by Dr Peter Horton at the UK National Crystallography Service, Southampton. The data collection parameters are shown in Appendix 3.7.1. The structure confirmed the proposed ligand framework.

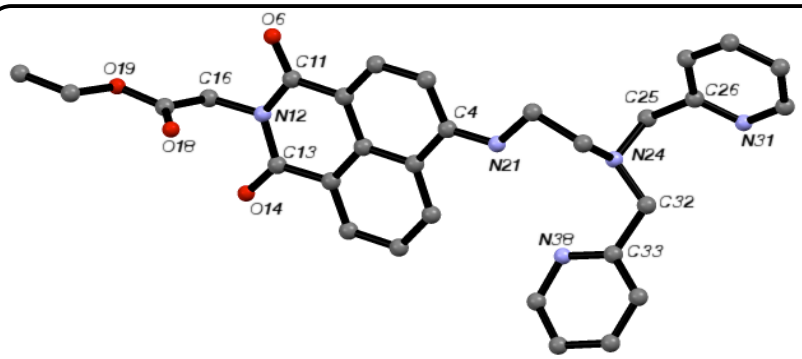

Figure 3.8: X-ray crystal structure of L1 with ellipsoids at 50 % occupancy. Hydrogen atoms omitted for clarity.

The structure revealed an intramolecular hydrogen bonding interaction (Table 3.2) between N21–H21···N38 atoms which correlates with the lack of disorder of the 2–DPA moiety. The donor(D)–acceptor(A) length was 3.451(17) Å and therefore this interaction was classed as weak and electrostatically driven,[35] and therefore should be easily overcome when forming the metal complex.

Table 3.2: Table of selected bond lengths and bond angles for L1

Bond Lengths / Å	
C4–N21	1.3488(16)
C11–O6	1.2278(15)
C11–N12	1.4024(17)
C13–N12	1.3981(16)
C13–O14	1.2196(16)
C16–N12	1.4534(16)
C17–O18	1.1997(16)
N21–H21 (*D*–H)	0.88
H21···N38 (H···*A*)	2.50
Bond Angles / º	
C1–C11–N12	116.54(11)
C4–N21–C22	124.01(11)
C12–C13–O14	120.00(12)
N24–C25–C26	115.34(11)
N24–C32–C33	114.66(11)
N21–H21···N38 (*D*–H···*A)*	161.7

The ligand carbonyl bond lengths were calculated at *ca*. 1.22 Å and agreed well with similar ligands.[36-38] Furthermore the imide bond (C16–N12 = 1.45 Å) was seen to be much weaker than the 4–amino bond (C4–N21 = 1.35 Å) as indicated by the difference in reaction conditions employed for functionalising these groups. The imide moiety was observed sitting orthogonally to the NI core.

3.3.4 UV–Vis Absorption Spectroscopy

Ligand Properties

The solution state absorption spectra of **L1–4** (Table 3.3), recorded in both MeCN and MeOH, showed three main absorption peaks and were dominated by two transitions below 300 nm (Figure 3.9). The highest energy peak (*ca.* 265 nm) can be assigned to the pyridyl units[11] whereas the slightly lower energy peak witnessed at *ca.* 280 nm is likely to originate from the NI core. The ligands were coloured due to the broad, low energy ICT transition observed at *ca.* 440 nm.[30,39,40] The ICT nature is induced upon placing an amine at the 4–position as with other examples from the literature.[30,41-44]

The solubility of **L3** allowed further measurements in aqueous solvents and revealed a further bathochromic shift to 447 nm. Effects on the molar absorption coefficient were also evident.[45] The high sensitivity of this peak to solvent polarity was consistent with significant ICT (n–π*) character, arising from the donating amino substituent and accepting imide moiety.

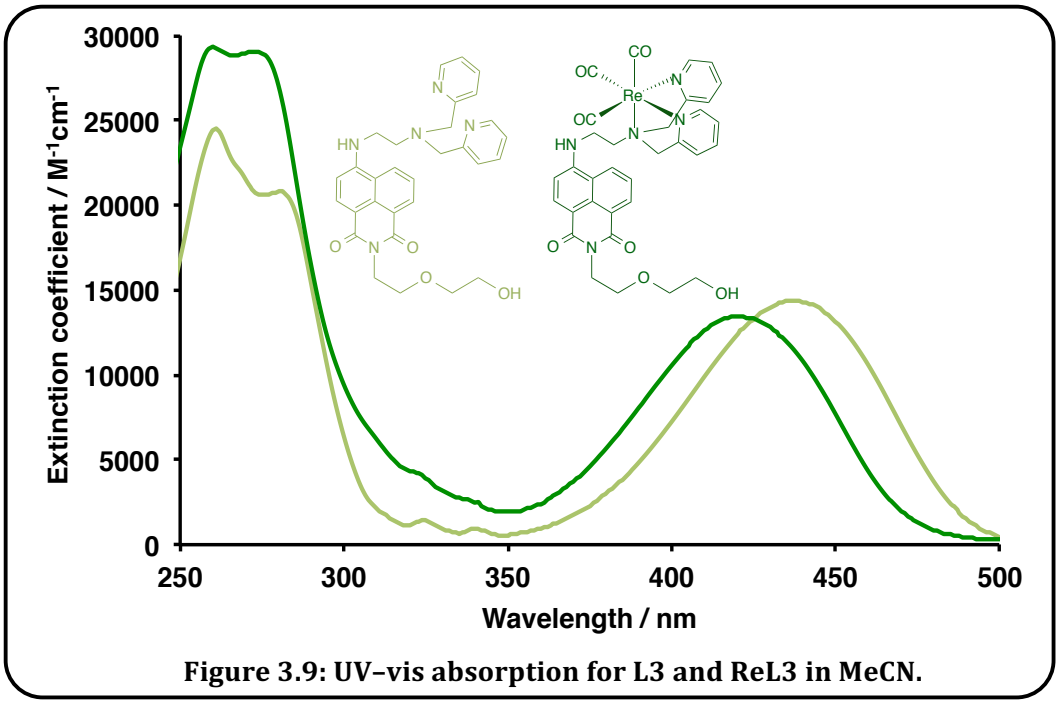

Figure 3.9: UV–vis absorption for L3 and ReL3 in MeCN.

Complex Properties

The absorption spectra of **ReL1–4** closely resembled those of the free ligands (Figure 3.9). A slight hypsochromic shift (*ca.* 15 nm) of the ICT band was observed for the complexes when compared to **L1–4**, consistent with electron density being donated from the ligand to the metal. Thus the absorption profiles were found to be highly compatible with confocal fluorescence microscopy. Contrary to Re(I) di–imine complexes no MLCT

transitions *ca*. 360–420 nm were observed as the lowest energy transition.[46] Therefore the absorption properties of **ReL1–4** can be described as highly ligand dominated.

Table 3.3: Absorption Properties of the Ligands and Complexes

Structure	λ_{max} / nm (ε / $M^{-1}cm^{-1}$)[a]	
	MeCN	MeOH
L1	439 (13500)	445 (13800)
L2	437 (13100)	431 (12900)
L3	437 (14400)	442 (13900)
L4	436 (14900)	445 (14200)
ReL1	421 (12800)	427 (13100)
ReL2	421 (13800)	427 (13000)
ReL3	421 (12800)	427 (15200)
ReL4	420 (15200)	427 (17900)

[a]2.5 or 5 × 10^{-5} M in MeCN.

3.3.5 Luminescence Spectroscopy

Ligand Properties

Solutions of **L1–4** were found to be highly luminescent as for most 4–amino NI species (Figure 3.10 and Table 3.4).[42,45,47,48] Using an excitation wavelength of 345–425 nm on **L1–4** in aerated MeCN and MeOH solutions revealed a visible emission band centred at 520 nm, typical of ICT NI species.[37,42,47-49] This was mostly insensitive to the nature of the imide group. Comparisons with work described in Chapters Two and Four show that photophysical properties of 4-amino NI species are tuned more profoundly *via* the 4–amino substituent.

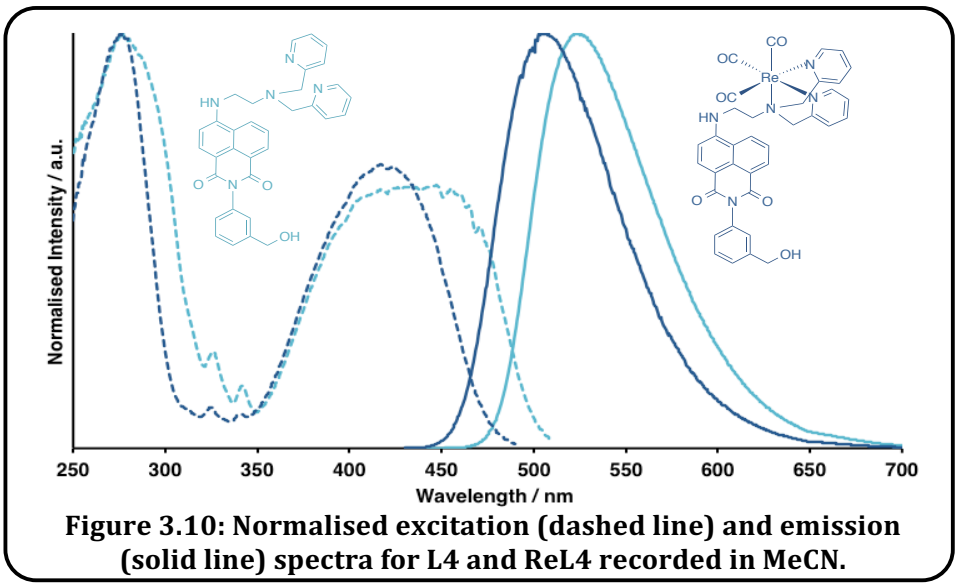

Figure 3.10: Normalised excitation (dashed line) and emission (solid line) spectra for L4 and ReL4 recorded in MeCN.

Again the solubility of **L3** allowed fluorescence measurements to be conducted in water, resulting in a bathochromic shift of the emission to 537 nm. When λ_{em} of **L1–4** were compared to the excitation profiles (270 nm and 400–500 nm) a moderate Stokes' shift was apparent (*ca*. 125 nm). This combined with the emission sensitivity to solvent polarity suggests an excited state of ICT character,[37,42,47-49] agreeing well with UV-vis studies.

Time resolved lifetime measurements (Table 3.4) showed that the ligands were fluorescent in all cases with lifetimes shorter than 10 ns. In the majority of cases the decay profiles fit best to a biexponential with the longer component dominating (> 80 %). The dual component lifetimes suggests a minor, quenched species akin to Chapter Two.

Complex Properties

Upon coordination of **L1–4** to Re(I) the ligands preserved their distinctive visible emission properties with a slight hypsochromic shift observed for **ReL1–4** when compared to the free ligands. In addition the lifetimes were generally extended, possibly as a result of the overall cationic charge of the complexes modulating the ICT excited state.[50,51] This was opposite to what is seen for Re(I) complexes of related pyrene appended 2–DPA ligands.[11]

Table 3.4: Fluorescence Properties of the Ligands and Complexes.

	λ_{em} / nm[a]	λ_{em} / nm[b]	τ / ns[c]	τ / ns[d]	Φ[e]
L1	523	534	2.6, 7.6 (97 %)	2.8, 8.7 (83 %)	–
L2	529	537	2.6, 6.4 (89 %)	1.7, 5.4 (92 %)	–
L3	523	530	3.7, 8.2 (90 %)	2.9, 7.1 (80 %)	–
L4	524	533	4.5, 8.5 (93 %)	1.8, 5.1 (90 %)	–
ReL1	505	518	3.1, 9.8 (98 %)	3.8, 8.8 (98 %)	0.83
ReL2	510	514	3.2, 9.7 (96 %)	3.3, 8.8 (95 %)	0.57
ReL3	505	516	4.1, 9.8 (95 %)	2.2, 8.4 (97 %)	0.58
ReL4	506	520	9.1	8.1	0.89

[a]MeCN, λ_{exc} = 425 nm, [b]MeOH, λ_{exc} = 425 nm, [c]MeCN, λ_{exc} = 425 nm, [d]MeOH, λ_{exc} = 425 nm, [e]Aerated MeCN.

ReL1–4 all possessed excellent quantum yields (> 50 %) (Table 3.4) in aerated solution suggesting that oxygen is not a major quenching species for these compounds. The uniformly high quantum yields further suggested that other deactivation pathways were suppressed to some extent. For example the occupancy of the 2–DPA binding site by Re(I) increases the rigidity of the compound and hence reduces vibrational relaxation. Furthermore the binding to Re(I) could inhibit PeT that has been shown as a significant

quenching pathway in many 4–amino substituted NI species.[48,52,53] This correlated well with other examples of 2–DPA NI species in the literature that have been used for metal ion sensing. **L3** has also been synthesised and tested as a metal ion probe by Zhang *et al.*[29] and showed strong emission enhancement upon binding to Zn(II). Conversely the N_{imide}–butyl analogue[30,40] showed almost complete quenching in the presence of Cu(II), however little effect for other metal ions.

3.3.6 Confocal Fluorescence Microscopy

The photophysical properties of both the free ligands and Re(I) complexes were highly suited to confocal fluorescence microscopy (visible emission, appropriate absorption wavelengths, large Stokes' shifts, *etc.*). Therefore CFM was conducted to assess the imaging capability of the series. The compounds were initially incubated with a human osteoarthritic cells due to their large size and thus ease of imaging. Following washing to remove the compounds from the culture medium, cells were imaged with λ_{exc} = 405 or 488 nm and detection between 515–685 nm. (See for Appendix 3.6.2 for autofluorescence assessments).

Ligand Properties

Comparison of the imaging capabilities of the free ligands showed profound differences in their behaviour in terms of uptake and localisation (Figure 3.11).

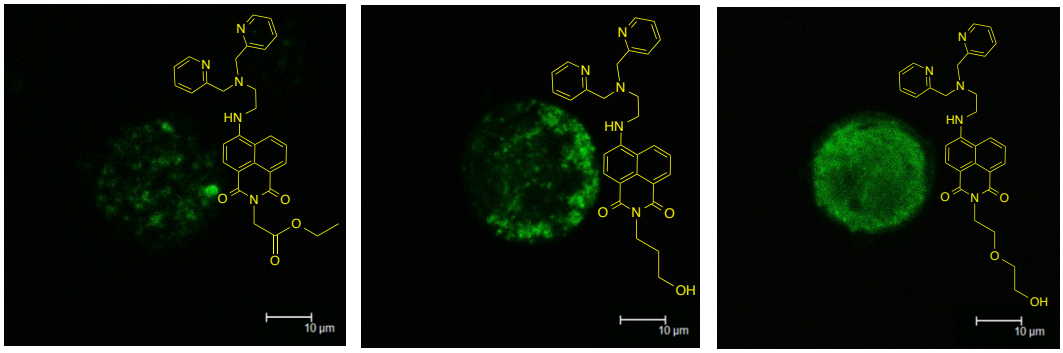

Figure 3.11: CFM of osteoarthritic cells imaged using (left to right): L1 (poor uptake), L2 (excellent uptake, mitochondrial localisation) and L3 (good uptake, cytoplasmic binding). All images obtained using λ_{exc} = 405 nm and λ_{em} = 535 nm.

Firstly **L4**, containing the benzyl alcohol substituent, showed the most disappointing result with no uptake into the cells. **L1** showed reasonable uptake resulting in a bright, distinct, granular staining pattern. This suggested that **L1** was being concentrated in certain organelles, most likely mitochondria due to the circular dispersed appearance and literature precedent (Figure 3.11).[54] The alkyl alcohol containing compounds, **L2** and **L3**, showed the best uptake into cells indicating that introducing a hydrophilic moiety may

assist. **L2** again showed a distinct staining pattern representative of mitochondria however **L3** had no specific hot spots of fluorescence. The diffuse emission of **L3** throughout the cell suggested binding of this imaging agent to the cytoplasm. No nuclear uptake was observed for any of the free ligands in this study. This behaviour contrasts to imaging work undertaken on HepG2 (liver cancer) and HeLa cells by Zhang *et al.*[29] during the course of our studies where **L3** was seen to penetrate the nuclear envelope, possibly indicative of unhealthy or dead cells.[55] It is apparent that these results were not replicated on the osteoarthritic cell line. Other studies on ES–2 cells by Chen *et al*. were seen to bridge both behaviours, showing blue emission of the NI probe in the nucleus and intense green emission in the cytoplasm.[39] Other recent literature examples of imaging with organic NI agents have revealed lysosomal[56] and mitochondrial[54] localisation in HeLa cells.

Complex Properties

Upon coordination of the ligands into cationic Re(I) complexes the imaging capability of the different variants was greatly affected. Again a vast range of uptake and localisation behaviour was witnessed across the series (Figure 3.12). With the exception of **ReL3** the cellular uptake was improved by the cationic and enhanced lipophilic nature of the complexes compared to the free ligands.[57] The charged species allow active uptake through the cell membrane instead of relying on passive diffusion. As for the free ligands none of the Re(I) complexes showed nuclear penetrability.

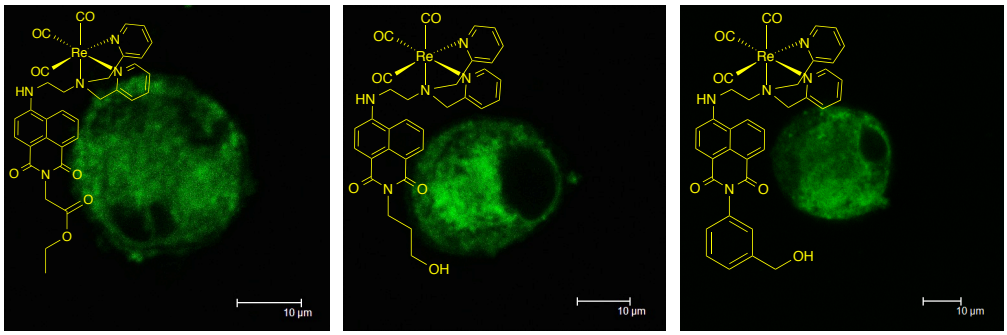

Figure 3.12: CFM of osteoarthritic cells imaged using (left to right): ReL1, ReL2 and ReL4. All images obtained using λ_{exc} = 405 nm and λ_{em} = 535 nm.

Considering the favourable uptake of **L3**, unexpectedly **ReL3** possessed the poorest uptake of all the complexes and could not be used as an effective imaging fluorophore. In contrast **ReL4**, for which the free ligand showed almost no uptake, showed very good uptake into the osteoarthritic cells. **ReL4** gave very bright emission with clear evidence of cytoplasmic staining. **ReL1** showed similar properties to **ReL4**, however in addition to the background cytoplasmic staining, foci of emission were visible. The specific staining

pattern of **ReL1** suggests that specific organelles were targeted (possibly mitochondria and vacuoles). **ReL2** showed the greatest capability towards CFM, possessing impressive uptake resulting in incredibly bright, high quality images, even at reduced laser power. The foci of emission near the nucleus (Figure 3.12) indicated labelling of the smooth endoplasmic reticulum, including those of the Golgi apparatus.[57] Throughout the duration of the study no loss of cell viability was witnessed indicating that at this concentration (110–190 μM), all complexes were non-toxic to this cell line.

The high capability of **ReL2** as an imaging agent led to studies conducted at higher concentrations (4 times greater) of the probe. This yielded incredibly detailed images of osteoarthritic cells with clear evidence of rapid binding to mitochondrial membranes and other cellular ultrastructures (Figure 3.13). This was particularly true in cells undergoing apoptosis, indicated by the widespread membrane blebbing (zeiosis), cytoplasmic vacuolation, loss of cell integrity, and, in some cases, nuclear fragmentation. Therefore it seems likely that the increased concentration of probe may have induced cell death, presumably due to membrane perturbation as seen for other examples with MCF–7 cells.[57]

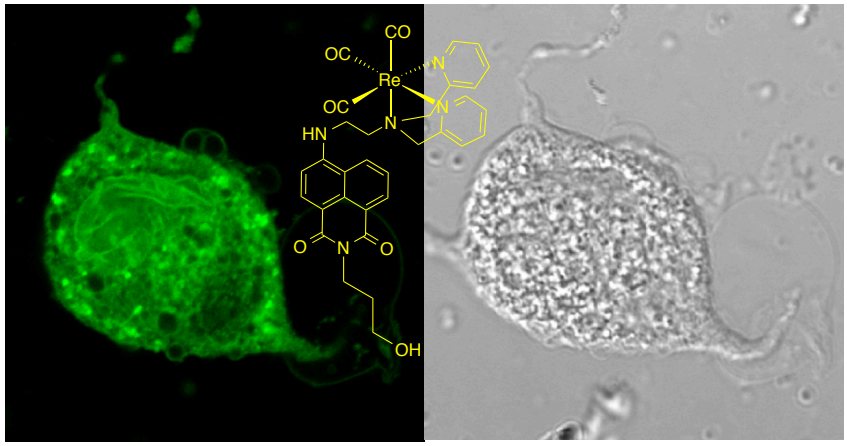

Figure 3.13: CFM images of an osteoarthritic cell undergoing apoptosis. (left) Imaged using fluorescence from ReL2 (λ_{exc} = 405 nm; λ_{em} = 515 nm). (Right) Imaged using transmitted light.

Knowing the outstanding imaging capability of **ReL2** it was also selected for imaging *Spironucleus Vortens*; an aerotolerant fish parasite grown anaerobically. *S. vortens* possess rapid flagellar driven motility and therefore 280 mM of 2,2,2–trichloroethane–1,1–diol (chloral hydrate) was required to anaesthetise the cells immediately before imaging in order to obtain sharp images. Good uptake of **ReL2** was again witnessed for *S. vortens* and foci of emission were observed. These spots were characteristic of hydrogenosomes; the redox–active organelle equivalent to the mitochondria in aerobic eukaryotic cells. In order

to prove localisation in hydrogenosomes a co–localisation experiment was conducted using **ReL2** and a well known hydrogenosomal stain, tetramethylrhodamine ethyl ester (TMRE) (Figure 3.14). It is important to note that there was no bleedthrough of the different $\lambda_{exc/em}$ channels used for this study that resulted in clear co–localisation in the hydrogenosomes. Importantly **ReL2** was not evidently toxic to *S. vortens* throughout the duration of the imaging experiment (4 hours), akin to other literature examples.[57] The cell motility was maintained throughout the whole population with the lack of chloral hydrate.

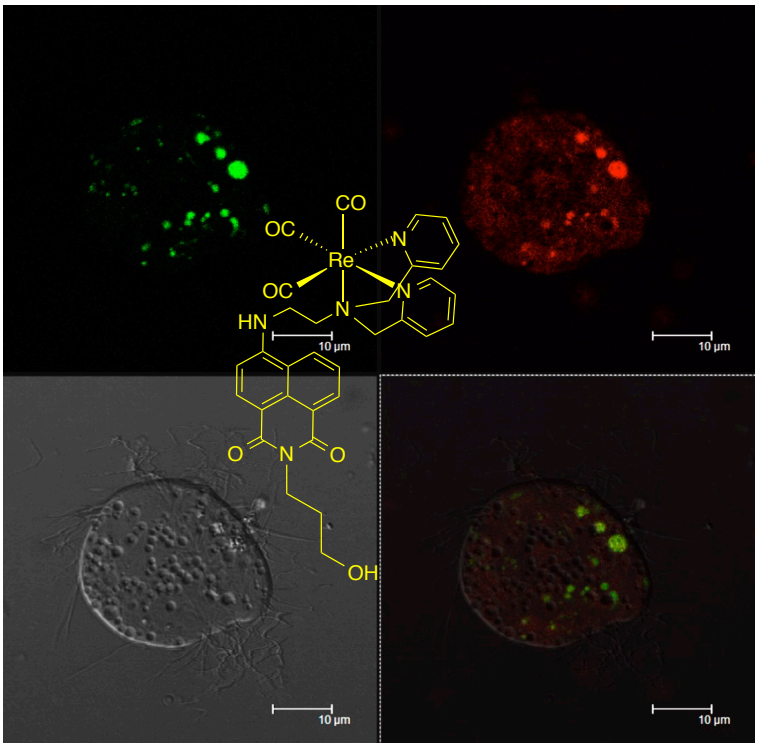

Figure 3.14: CFM images of *S. vortens* incubated with ReL2 and TMRE showing (clockwise from top left): green fluorescence from ReL2 (λ_{exc} = 488 nm; λ_{em} = 515 nm); red fluorescence from TMRE (λ_{exc} = 543 nm; λ_{em} = 600 nm); overlaid images showing co–localisation; transmitted light image.

The imaging results for both cell types provide strong evidence for the use of these compounds as biocompatible imaging agents. Importantly the nature of the imide moiety had a profound effect on the imaging capability of the probe, modulating both the uptake and localisation. The amphiphilic nature of the propyl alcohol moiety of **L2** appeared to offer the best balance, resulting in excellent image collection, especially when incorporated into the cationic complex **ReL2**. This complements other cases in the literature. For example extensive cellular imaging studies with emissive lanthanide complexes have also shown that the nature of a fluorophore substituent can influence their intracellular uptake, distributions, and cytotoxicity, perhaps through varied affinities for proteins.[58]

3.4 Conclusion

In conclusion a series of 4–amino substituted NI fluorophores have been synthesised *via* a multistep synthesis. When incorporated into the cationic tricarbonyl rhenium complexes the metal ion was added at the final step as required for potential SPECT agents. The structures vary by the amphiphilic nature of the imide group.

The optical properties were dictated by ligand centered ICT, dominated by transitions that facilitate visible absorption and efficient emission characteristics. Both are properties highly compatible with CFM. Cellular imaging studies were conducted on both human osteoarthritic cells and *S. vortens* and revealed the excellent imaging capabilities of both the free ligands and complexes. Crucially, the cellular uptake and localisation characteristics can be controlled by the structure of the ligand that is highly tuneable in these examples due to the stepwise functionalisation of the NI core. For the series of compounds studied herein, the 3-propanol moiety of **L2** offered the most favorable uptake and mitochondrial localisation.

To summarise, these NI based ligands provide a chelating site that is ideally suited to radioimaging nuclides such as ^{99m}Tc(I), while simultaneously offering the desirable physical and photophysical characteristics that are biocompatible with optical cellular imaging techniques such as confocal fluorescence microscopy. Therefore **ReL2** in particular offers great potential towards a bimodal SPECT–fluorescence probe.

3.5 Experimental Section

3.5.1 Diffraction Data Collection, Processing, Structure Analysis and Refinement

Data collection, refinement and structure solution was conducted by Dr Peter Horton at the UK National Crystallography Service, Southampton. Suitable crystals were selected and measured following a standard method[59] on a Rigaku AFC12 goniometer equipped with an enhanced sensitivity (HG) Saturn724+ detector mounted at the window of an FR–E+ SuperBright molybdenum rotating anode generator with HF Varimax optics (100 μm focus) at 100 K. Data collection, data reduction, cell refinement, and absorption correction using CrystalClear–SM Expert 3.1 b26 (Rigaku, 2013). The structure was solved by direct methods using SHELXS-9723[60] and was completed by iterative cycles of ΔF syntheses and full-matrix least-squares refinement in SHELKX-2013.[60] All non-H atoms were refined anisotropically, and difference Fourier syntheses were employed in positioning idealized hydrogen atoms, which were allowed to ride on their parent C–atoms. CCDC reference number 981267 contains the supplementary crystallographic data (see Appendix 3.7.1). The figures were created using the Mercury for Windows.[61]

3.5.2 Human Cell Incubation and Confocal Microscopy

Undertaken by collaborators within the Lloyd and Hayes groups in BIOSCI at Cardiff University.

An osteoporetic cell line was maintained in *N*-(2-hydroxyethyl)-piperazine-*N*′-ethanesulfonic acid (Hepes)–modified minimum essential medium (HMEM) supplemented with 10% fetal bovine serum, penicillin, and streptomycin. Cells were detached from the plastic flask using a trypsin–ethylenediaminetetraacetic acid (EDTA) solution and suspended in an excess volume of growth medium. The homogeneous cell suspension was then distributed into 1 mL aliquots, with each aliquot being subject to incubation with a different imaging probe. These luminescent probes were initially dissolved in dimethyl sulfoxide (DMSO) (5 mg mL^{-1}) before being added to the cell suspensions, with a final concentration of 100 μg ml^{-1} (corresponding to about 110–190 μM) before incubation at 20 °C for 30 min. Cells were finally washed in phosphate buffer saline (PBS, pH 7.2), removing agent from the medium, then harvested by centrifugation (5 min, 800 g) and mounted on a slide for imaging. Preparations were viewed using a Leica TCS SP2 AOBS confocal laser microscope using ×63 or ×100 objective, with excitation at 405, 488, or 543 nm and detection at 515–600 nm.

3.5.3 General

^{1}H and $^{13}C\{^{1}H\}$ NMR spectra were recorded on an NMR-Fourier transform (FT) Bruker 400 and 250 MHz or Jeol Eclipse 300 MHz spectrometer and recorded in $CDCl_3$, CD_3CN, CD_3OD, or $(CD_3)_2CO$. ^{1}H and $^{13}C\{^{1}H\}$ NMR chemical shifts (δ) were determined relative to residual solvent peaks with digital locking and are given in ppm. Low–resolution mass spectra were obtained by the staff at Cardiff University. High–resolution mass spectra were carried out at the EPSRC National Mass Spectrometry Service at Swansea University. UV–visible (UV–vis) studies were performed on a Jasco V–570 spectrophotometer as MeCN and MeOH solutions (2.5 or 5 × 10^{-5} M). Photophysical data were obtained on a JobinYvon–Horiba Fluorolog spectrometer fitted with a JY TBX picosecond photodetection module as MeCN solutions. Emission spectra were uncorrected, and excitation spectra were instrument-corrected. The pulsed source was a Nano-LED configured for 295 nm output operating at 1 MHz. Luminescence lifetime profiles were obtained using the JobinYvon–Horiba FluoroHub single photon counting module, and the data fits yielded the lifetime values using the provided DAS6 deconvolution software. Quantum yield measurements were obtained on aerated MeCN solutions of the complexes using $[Ru(bpy)_3](PF_6)_2$ in aerated MeCN as a standard (Φ = 0.016).[62,63]

All reactions were performed with the use of vacuum line and Schlenk techniques. Reagents were commercial grade and used without further purification. *fac*–$[Re(CO)_3(MeCN)_3]BF_4$[33] and *N*–*tert*–Boc–ethylenediamine[64] were prepared according to the literature.

3.5.4 Proligand Synthesis

*Synthesis of 4–chloro–N'–(glycine ethyl ester)–1,8–naphthalimide (**Cl1**)*[20]

Triethylamine (1 mL, 7.16 mmol) and 4–chloro–1,8–naphthalic anhydride (1.110 g, 4.77 mmol) were added to a solution of glycine ethyl ester hydrochloride (0.999 g, 7.16 mmol) in ethanol (50 mL). The orange solution was heated at reflux under a dinitrogen atmosphere for 12 h, resulting in the formation of a precipitate. The reaction solution was then cooled, and the solvent was removed *in vacuo*. The solid was then extracted into dichloromethane and washed with 0.1 M HCl (3 × 20 mL) and water (3 × 20 mL). The organic phase was then dried over $MgSO_4$, filtered, and reduced to a minimal volume. Precipitation with diethyl ether and subsequent filtration and drying afforded **Cl1** as an orange solid. Yield: 0.931 g, 2.93 mmol, 61 %. ^{1}H NMR (400 MHz, $CDCl_3$): δ_H = 8.43 (d, 1H, $^{3}J_{HH}$ = 7.0 Hz, nap), 8.33 (d, 1H, $^{3}J_{HH}$ = 8.5 Hz, nap), 8.28 (d, 1H, $^{3}J_{HH}$ = 8.0 Hz, nap), 7.64 (dd, 2H, J_{HH} = 8.0 Hz, 7.5 Hz, nap), 4.81 (s, 2H, NCH_2), 4.17 (q, 2H, $^{3}J_{HH}$ = 7.0 Hz, OCH_2CH$_3$),

1.22 (t, 3H, $^3J_{HH}$ = 7.0 Hz, OCH_2CH_3) ppm.

*Synthesis of 4–ethylenediamine–(N–glycine ethyl ester)–1,8–naphthalimide (**N1**)*[27]

Cl1 (0.630 g, 1.98 mmol) and *N–tert*–Boc–ethylenediamine (0.953 g, 5.95 mmol) were heated in dimethylsulfoxide (3 mL) at 70 °C under a nitrogen atmosphere for 12 h. The solution was then allowed to cool and was neutralised with 0.1 M HCl, which induced precipitation of a yellow solid. The crude product was extracted into dichloromethane, washed with water, dried over $MgSO_4$, and filtered. The solvent was reduced to a minimal volume, and precipitation was induced with petroleum ether, allowing subsequent filtration and drying to afford the intermediate product as an orange solid. Yield: 0.521 g, 1.18 mmol, 60 %. ^{1}H NMR (400 MHz, $CDCl_3$): δ_H = 8.38 (d, 1H, $^3J_{HH}$ = 8.0 Hz, nap), 8.29 (d, 1H, $^3J_{HH}$ = 8.0 Hz, nap), 8.17 (d, 1H, $^3J_{HH}$ = 8.5 Hz, nap), 7.42 (t, 1H, $^3J_{HH}$ = 8.0 Hz, N*H*), 6.95 (s, 1H, nap), 6.44 (d, 1H, $^3J_{HH}$ = 8.0 Hz, nap), 5.30 (t, 1H, $^3J_{HH}$ = 7.5 Hz, CON*H*), 4.87 (s, 2H, NCH_2), 4.20 (q, 2H, $^3J_{HH}$ = 7.0 Hz, $COCH_2CH_3$), 3.53 (broad app. quin, 2H, $NHCH_2$), 3.36 (broad t, 2H, CH_2CH_2), 1.42 (s, 9H, Bu), 1.25 (t, 3H, $^3J_{HH}$ = 7.0 Hz, OCH_2CH_3) ppm; ^{13}C{^{1}H} NMR (75 MHz, CDCl3): δ_C = 169.4 (*C*O), 164.3 (*C*O), 163.7 (*C*O), 157.9, 150.8, 135.0, 131.3, 127.6, 124.6, 122.1, 120.3, 108.7, 103.5, 99.6, 80.4, 61.7, 46.0, 41.3, 39.6, 31.0, 14.3 ppm; LRMS (ES^-) found *m/z* = 440.2 for $[M-H]^-$ and 476.2 for $[M+Cl]^-$.

Trifluoroacetic acid (TFA) (2 mL) was then added dropwise to a solution of the Boc–protected intermediate (0.495 g, 1.12 mmol) in dichloromethane (5 mL) under a nitrogen atmosphere and stirred for 24 h. The solvents were removed under vacuum, with further drying over 30 min. The residue was dissolved in methanol (20 mL) and then dried *in vacuo*, a process that was repeated in triplicate, to finally afford **N1** as a hygroscopic yellow solid. ^{1}H NMR (400 MHz, CD_3OD): δ_H = 8.40 (d, 1H, $^3J_{HH}$ = 8.0 Hz, nap), 8.36 (d, 1H, $^3J_{HH}$ = 7.0 Hz, nap), 8.23 (d, 1H, $^3J_{HH}$ = 8.0 Hz, nap), 7.57 (app. t, 1H, $^3J_{HH}$ = 7.5 Hz, nap), 6.76 (d, 1H, $^3J_{HH}$ = 8.0 Hz, nap), 4.83 (s, 2H, NCH_2), 4.26 (q, 2H, $^3J_{HH}$ = 7.0 Hz, OCH_2CH_3), 3.76 (t, 2H, $^3J_{HH}$ = 5.5 Hz, $NHCH_2$), 3.30–3.37 (m, 4H, $NHCH_2CH_2$), 1.32 (t, 3H, $^3J_{HH}$ = 7.0 Hz, OCH_2CH_3) ppm; ^{13}C{^{1}H} NMR (75 MHz, CD_3OD): δ_C = 169.3 (*C*O), 164.0 (*C*O), 163.5 (*C*O) 150.3, 134.2, 130.9, 129.2, 128.0, 124.4, 121.1, 120.3, 108.6, 103.8, 61.4, 40.8, 40.1, 38.2, 13.1 ppm; LRMS (ES^+) found *m/z* 342.2 for $[M+H]^+$ and 383.2 for $[M+MeCN]^+$.

*Synthesis of 4–chloro–(N–3'–aminopropanol)–1,8–naphthalimide (**Cl2**)*

Prepared as for **Cl1** but using 3–aminopropanol (0.48 mL, 6.13 mmol) and 4–chloro–1,8–naphthalic anhydride (0.713 g, 3.06 mmol) to give **Cl2** as an orange solid. Yield: 0.662 g, 2.29 mmol, 75 %. ^{1}H NMR (250 MHz, $CDCl_3$): δ_H = 8.61 (d, 1H, $^3J_{HH}$ = 7.5 Hz, nap), 8.56 (d, 1H, $^3J_{HH}$ = 8.5 Hz, nap), 8.45 (d, 1H, $^3J_{HH}$ = 8.0 Hz, nap), 7.83–7.76 (m, 2H, nap), 4.27 (t, 2H, $^3J_{HH}$ =

6.0 Hz, C*H*$_2$OH), 3.53 (broad t, 2H, NC*H*$_2$CH$_2$), 3.04 (broad s, 1H, O*H*), 1.92 (app. quin, 2H, $^3J_{HH}$ = 6.0 Hz, NCH$_2$C*H*$_2$) ppm.

*Synthesis of 4–ethylenediamine)–(N–3'–aminopropanol)–1,8–naphthalimide (**N2**)*

Prepared as for **N1** but using **Cl2** (0.510 g, 1.76 mmol) and *N–tert*–Boc–ethylenediamine (0.841 g, 5.25 mmol), giving the intermediate as an orange oil. Yield: 0.649 g, 1.57 mmol, 89 %. ^{1}H NMR (400 MHz, CDCl$_3$): δ_H = 8.35 (d, 1H, $^3J_{HH}$ = 7.0 Hz, nap), 8.18 (d, 1H, $^3J_{HH}$ = 8.5 Hz, nap), 8.14 (d, 1H, $^3J_{HH}$ = 8.5 Hz), 7.43 (app. t, 1H, $^3J_{HH}$ = 7.5 Hz, nap), 7.15 (broad s, 1H, N*H*), 6.38 (d, 1H, $^3J_{HH}$ = 8.5 Hz, nap), 5.97 (broad s, 1H, N*H*CO), 4.21 (t, 2H, $^3J_{HH}$ = 6.0 Hz, C*H*$_2$OH), 3.93 (broad s, 1H, O*H*), 3.58–3.52 (broad m, 2H, nap-NHC*H*$_2$), 3.52 (t, 2H, $^3J_{HH}$ = 5.5 Hz, NC*H*$_2$), 3.37 (app. broad s, 2H, C*H*$_2$NHCO), 1.91 (app. quin, 2H, $^3J_{HH}$ = 6.0 Hz, C*H*$_2$CH$_2$OH), 1.42 (s, 9H, Bu) ppm.

Deprotection of the intermediate with TFA in dichloromethane yielded **N2** as a hygroscopic yellow solid. ^{1}H NMR (400 MHz, CD$_3$OD): δ_H = 8.52 (app. t, 2H, $^3J_{HH}$ = 8.0 Hz, nap), 8.38 (d, 1H, $^3J_{HH}$ = 8.5 Hz, nap), 7.69 (app t, 1H, $^3J_{HH}$ = 7.5 Hz, nap), 6.89 (d, 1H, $^3J_{HH}$ = 8.5 Hz, nap), 4.48 (t, 2H, $^3J_{HH}$ = 6.0 Hz, NHC*H*$_2$), 4.28 (t, 2H, $^3J_{HH}$ = 7.0 Hz, C*H*$_2$OH), 3.81 (t, 2H, $^3J_{HH}$ = 6.5 Hz, NC*H*$_2$), 3.36 (t, 2H, $^3J_{HH}$ = 6.5 Hz, C*H*$_2$NH$_2$), 2.20 (app. quin, 2H, $^3J_{HH}$ = 6.5 Hz, C*H*$_2$CH$_2$OH) ppm.

*Synthesis of 4–chloro–(N–2(2'–aminoethoxy)ethanol)–1,8–naphthalimide (**Cl3**)*

Prepared as for **Cl1**, using 2–(2–aminoethyl)ethanol (0.80 mL, 8.04 mmol) and 4–chloro–1,8–naphthalic anhydride (0.935 g, 4.02 mmol) to give **Cl3** as an orange solid. Yield: 1.065 g, 3.33 mmol, 83 %. ^{1}H NMR (250 MHz, CDCl$_3$): δ_H = 8.53 (d, 1H, $^3J_{HH}$ = 8.5 Hz, nap), 8.45 (d, 1H, $^3J_{HH}$ = 9.5 Hz, nap), 8.37 (d, 1H, $^3J_{HH}$ = 8.0 Hz, nap), 7.72 (app. t, 1H, $^3J_{HH}$ = 7.5 Hz, nap), 7.69 (d, 1H, $^3J_{HH}$ = 8.0 Hz, nap), 4.34 (t, 2H, $^3J_{HH}$ = 5.5 Hz, NC*H*$_2$), 3.77 (t, 2H, $^3J_{HH}$ = 5.5 Hz, C*H*$_2$OH), 3.62–3.55 (m, 4H, C*H*$_2$OC*H*$_2$), 2.56 (s, 1H, O*H*) ppm.

*Synthesis of 4–ethylenediamine–(N–2(2'–aminoethoxy)ethanol)–1,8–naphthalimide (**N3**)*

Prepared as for **N1**, but using **Cl3** (0.401 g, 1.25 mmol) and *N–tert*–Boc–ethylenediamine (0.601 g, 3.75 mmol), affording the intermediate as a solid. Yield: 0.492 g, 1.11 mmol, 89 %. ^{1}H NMR (400 MHz, CDCl$_3$): δ_H = 8.00 (d, 1H, $^3J_{HH}$ = 8.0 Hz, nap), 7.90 (d, 1H, $^3J_{HH}$ = 7.0 Hz, nap), 7.84 (d, 1H, $^3J_{HH}$ = 8.0 Hz), 7.12 (app. t, 1H, $^3J_{HH}$ = 7.0 Hz, N*H*), 6.79 (s, 1H, nap), 6.24 (app. s, 1H, N*H*CO), 6.11 (d, 1H, $^3J_{HH}$ = 8.0 Hz, nap), 4.20 (app. br s, 2H, C*H*$_2$), 3.73 (br t, 2H, C*H*$_2$), 3.66 (app. br s, 2H, C*H*$_2$), 3.59 (app. br s, 2H, C*H*$_2$), 3.42 (app. br s, 2H, C*H*$_2$), 3.19 (app. br s, 2H, C*H*$_2$), 1.36 (s, 9H, Bu) ppm.

Deprotection of the intermediate with TFA, followed by work up yielded **N3** as a hygroscopic orange solid. ^{1}H NMR (400 MHz, CD_3OD): δ_H = 8.51 (d, 1H, $^{3}J_{HH}$ = 8.0 Hz, nap), 8.45 (d, 1H, $^{3}J_{HH}$ = 8.0 Hz, nap), 8.26 (d, 1H, $^{3}J_{HH}$ = 8.5 Hz, nap), 7.59 (app. t, 1H, $^{3}J_{HH}$ = 8.0 Hz, nap), 6.80 (d, 1H, $^{3}J_{HH}$ = 8.5 Hz, nap), 4.47 (app. t, 2H, $^{3}J_{HH}$ = 4.5 Hz, CH_2), 4.32–4.28 (m, 4H, CH_2), 3.84–3.77 (m, 4H, CH_2), 3.36 (t, 2H, $^{3}J_{HH}$ = 7.5 Hz, CH_2) ppm; ^{13}C{^{1}H} NMR (75 MHz, CD_3OD): δ_C = 164.7 (*C*O), 164.2 (*C*O), 150.2 (*C*O), 134.2, 130.9,127.9, 124.5, 122.0, 120.6, 109.4, 108.0, 104.1, 103.9, 84.1, 72.1, 67.9, 60.9, 39.8, 38.2, 37.6 ppm; LRMS (ES^+) found *m/z* 344.3 for $[M+H]^+$, 366.3 for $[M+Na]^+$ and 407.3 for $[M+MeCN+Na]^+$.

*Synthesis of 4–chloro–(N–3'–aminobenzyl alcohol)–1,8–naphthalimide (**Cl4**)*

Prepared similarly to **Cl1** using 4–chloro–1,8–naphthalic anhydride (0.144 g, 0.62 mmol) and 3–aminobenzyl alcohol (0.304 g, 2.47 mmol) with the addition of triethylamine (0.14 mL, 0.926 mmol) to afford **Cl4** as a yellow solid. Yield: 132 mg, 0.39 mmol, 63 %. ^{1}H NMR (250 MHz, $CDCl_3$): δ_H = 8.69 (d, 1H, $^{3}J_{HH}$ = 7.5 Hz, nap), 8.60 (d, 1H, $^{3}J_{HH}$ = 7.5 Hz, nap), 8.44 (d, 1H, $^{3}J_{HH}$ = 8.0 Hz, nap), 7.90–7.76 (m, 2H, Ph), 7.51–7.35 (m, 2H, nap, Ph), 7.26 (s, 1H, Ph), 7.20–7.08 (d, 1H, nap), 4.68 (s, 2H, CH_2OH) ppm.

*Synthesis of 4–ethylenediamine–(N–3'–aminobenzyl alcohol)–1,8–naphthalimide (**N4**)*

Prepared as for **N1** using **Cl4** (0.619 g, 1.83 mmol) and *N–tert*–Boc-ethylenediamine (0.881 g, 5.50 mmol). The intermediate was isolated as a sticky orange solid. Yield: 0.810 g, 1.76 mmol, 96 %. ^{1}H NMR (250 MHz, $CDCl_3$): δ_H = 8.59 (d, 1H, $^{3}J_{HH}$ = 7.0 Hz, nap), 8.46 (d, 1H, $^{3}J_{HH}$ = 8.5 Hz, nap), 8.33 (d, 1H, $^{3}J_{HH}$ = 8.5 Hz, nap), 7.61 (app. t, 1H, $^{3}J_{HH}$ = 8.0 Hz, nap), 7.52–7.40 (m, 2H, Ph), 7.35 (s, 1H, Ph), 7.28 (d, 1H, $^{3}J_{HH}$ = 8.0 Hz, Ph), 7.22 (br t, 1H, N*H*), 6.59 (d, 1H, $^{3}J_{HH}$ = 8.5 Hz, nap), 5.23 (t, 1H, $^{3}J_{HH}$ = 6.5 Hz, N*H*CO), 4.77 (s, 2H, CH_2OH), 3.73–3.63 (br m, 2H, NHCH_2), 3.50–3.46 (br m, 2H, CH_2NHCO), 2.27 (br s, 1H, O*H*), 1.51 (s, 9H, Bu) ppm.

Deprotection of the intermediate with TFA, followed by work up yielded **N4** as a hygroscopic yellow oil. ^{1}H NMR (400 MHz, CD_3OD): δ_H = 8.27 (d, 1H, $^{3}J_{HH}$ = 8.5 Hz, nap), 8.18 (d, 1H, $^{3}J_{HH}$ = 8.0 Hz, nap), 8.09 (d, 1H, $^{3}J_{HH}$ = 8.5 Hz, nap), 7.48–7.23 (m, 3H, nap, Ph), 7.17 (s, 1H, Ph), 7.05 (d, 1H, $^{3}J_{HH}$ = 7.0 Hz, Ph), 6.60 (d, 1H, $^{3}J_{HH}$ = 9.0 Hz, nap), 4.55 (s, 2H, CH_2OH), 3.62 (t, 2H, $^{3}J_{HH}$ = 6.0 Hz, CH_2CH_2), 3.19 (br s, 2H) ppm.

3.5.5 Ligand Synthesis

*Synthesis of 4-(N',N'–bis(pyridin–2–ylmethyl) ethylenediamine–(N–glycine ethyl ester)–1,8–naphthalimide (**L1**)*

N1 (0.176 g, 0.51 mmol) was added to a solution of 2–pyridinecarboxaldehyde (0.1 mL, 1.05 mmol) in 1,2–dichloroethane (15 mL) and stirred for 2 hours at room temperature

under a nitrogen atmosphere. Sodium triacetoxyborohydride (0.327 g, 1.54 mmol) was then added, and the mixture was stirred for a further 16 h. The solution was then neutralised with saturated aq. $NaHCO_3$, and the product was extracted using $CHCl_3$. The organic layer was washed with water (3 × 25 mL) and brine (2 × 25 mL) and then dried over $MgSO_4$. Following filtration, the solvent was removed *in vacuo* to afford **L1** as a yellow solid. Yield: 0.133 g, 2.55 mmol, 50%. ^{1}H NMR (400 MHz, $CDCl_3$): δ_H = 8.79 (d, 1H, $^3J_{HH}$ = 8.5 Hz, nap), 8.56 (d, 1H, $^3J_{HH}$ = 7.0 Hz, nap), 8.51 (d, 2H, $^3J_{HH}$ = 4.5 Hz, pyr), 8.35 (d, 1H, $^3J_{HH}$ = 8.5 Hz, nap), 7.93 (br t, 1H, N*H*), 7.63 (app. t, 1H, $^3J_{HH}$ = 8.0 Hz), 7.50 (app. t, 2H, $^3J_{HH}$ = 8.0 Hz, pyr), 7.31 (d, 2H, $^3J_{HH}$ = 8.0 Hz, pyr), 7.09 (app. t, 2H, $^3J_{HH}$ = 5.5 Hz, pyr), 6.47 (d, 1H, $^3J_{HH}$ = 8.5 Hz, nap), 4.87 (s, 2H, NCH_2), 4.17 (q, 2H, $^3J_{HH}$ = 7.0 Hz, OCH_2CH$_3$), 3.95 (s, 4H, NCH_2), 3.38–3.30 (broad m, 2H, HNCH_2), 3.00 (t, 2H, $^3J_{HH}$ = 5.0 Hz, HNCH$_2$CH_2), 1.22 (t, 3H, $^3J_{HH}$ = 7.0 Hz, OCH$_2$CH_3) ppm; ^{13}C{^{1}H} NMR (75 MHz, $CDCl_3$): δ_C = 199.3 (*C*O), 164.7 (*C*O), 163.8 (*C*O), 150.9, 149.3, 139.5, 136.8, 135.4, 131.5, 130.5, 128.2, 124.4, 123.5, 122.5, 117.3, 108.0, 104.1, 63.9, 61.4, 60.1, 59.8, 41.3, 41.0, 14.3 ppm; LRMS (ES$^+$) found *m/z* 524.5 for [M+H]$^+$, 546.5 for [M+Na]$^+$ and 587.6 for [M+MeCN+Na]$^+$. HRMS (ES$^+$) found *m/z* 524.2285 for $[C_{30}H_{30}O_4N_5]^+$, calculated at 524.2292 for $[C_{30}H_{30}O_4N_5]^+$; IR (solid) ν_{max} (±2 cm^{-1}) = 3302, 2987, 2899, 2848, 1737, 1685, 1641, 1586, 1568, 1549, 1471, 1427, 1400, 1371, 1321, 1302, 1236, 1209, 1136, 1112, 1010, 995, 952, 772, 752 cm^{-1}; UV–vis (MeCN): λ_{max} (ε/M^{-1} cm^{-1}) = 439 (13500), 340 (1100), 324 (1600), 282 (16000), 269 (15100), 256 (18000), 228 (21500) nm; UV–vis (MeOH): λ_{max} (ε/M^{-1}cm^{-1}) = 445 (13800), 338 (700), 324 (1600), 282 (18200), 268 (18600), 257 (20700), 228 (16000), 205 (40000) nm.

*Synthesis of 4–(N',N'–bis(pyridin–2–ylmethyl) ethylenediamine)–(N–3'aminopropanol)–1,8–naphthalimide (**L2**)*

Prepared as for **L1** but using 2–pyridinecarboxaldehyde (0.39 mL, 4.05 mmol), **N2** (0.605 g, 1.94 mmol), and sodium triacetoxyborohydride (1.23 g, 5.82 mmol), yielding a crude product. The product was extracted into 0.1 M HCl, washed with dichloromethane (20 mL), neutralised, and then re–extracted into dichloromethane, which was removed under vacuum to give **L2** as an orange oil. Yield: 366 mg, 0.74 mmol, 38%. ^{1}H NMR (400 MHz, $CDCl_3$): δ_H = 8.73 (d, 1H, $^3J_{HH}$ = 8.5 Hz), 8.48–8.44 (m, 3H, nap, pyr), 8.23 (d, 1H, $^3J_{HH}$ = 8.5 Hz, nap), 7.92 (s, 1H, N*H*), 7.57 (app. t, 1H, $^3J_{HH}$ = 7.5 Hz, nap), 7.45 (app. t, 2H, $^3J_{HH}$ = 7.5 Hz, pyr), 7.26 (d, 2H, $^3J_{HH}$ = 8.0 Hz, pyr), 7.03 (app. t, 2H, $^3J_{HH}$ = 5.5 Hz, pyr), 6.37 (d, 1H, $^3J_{HH}$ = 8.5 Hz, nap), 4.20 (t, 2H, $^3J_{HH}$ = 5.5 Hz, CH_2OH), 3.88 (s, 4H, CH_2), 3.47 (t, 2H, $^3J_{HH}$ = 5.5 Hz), 3.30–3.25 (broad m, 2H, CH_2), 2.92 (t, 2H, $^3J_{HH}$ = 5.0 Hz, CH_2), 1.86 (app. quin, 2H, $^3J_{HH}$ = 5.5 Hz, CH_2CH$_2$OH) ppm; ^{13}C{^{1}H} NMR (75 MHz, $CDCl_3$): δ_C = 165.3 (*C*O), 164.7 (*C*O), 159.5, 158.7, 150.8, 149.1, 149.0, 136.7, 135.1, 131.3, 128.1, 124.3, 123.4, 122.4, 122.3, 120.7,

108.3, 104.0, 59.6, 58.9, 51.0, 41.0, 36.5, 31.1 ppm; LRMS (ES^+) found *m/z* 495.2 for $[M]^+$; HRMS (ES^+) found *m/z* = 496.2335 for $[C_{29}H_{29}N_5O_3+H]^+$, calculated at 496.2343 for $[C_{29}H_{29}N_5O_3+H]^+$; IR (solid) ν_{max} (±2 cm^{-1}) = 3267 (br), 2852, 1680, 1641, 1584, 1549, 1476, 1429, 1395, 1331, 1259, 1242, 1140, 1115, 1049, 995, 922, 772, 750 cm^{-1}; UV–vis (MeCN): λ_{max} ($\varepsilon/M^{-1}cm^{-1}$) 437 (13100), 339 (700), 324 (1300), 281 (17200), 260 (22500), 228 (18200) nm; UV–vis (MeOH): λ_{max} ($\varepsilon/M^{-1}cm^{-1}$) = 431 (12900), 339 (1000), 323 (1400), 277 (13100), 257 (21600), 226 (16000), 203 (46800) nm.

*Synthesis of 4–(N',N'–bis(pyridin–2–ylmethyl)–ethylenediamine–(N–2(2'–aminoethoxy) ethanol)–1,8–naphthalimide (**L3**)*

Prepared as for **L1** using 2–pyridinecarboxaldehyde (70 μL, 0.76 mmol), **N3** (0.128 g, 0.37 mmol), and sodium triacetoxyborohydride (0.237 g, 1.12 mmol) to give **L3** as an orange solid. Yield: 35.6 mg, 67.5 μmol, 18 %. ^1H NMR (400 MHz, $CDCl_3$): δ_H = 8.77 (d, 1H, $^3J_{HH}$ = 8.5 Hz, nap), 8.56 (d, 1H, $^3J_{HH}$ = 6.5 Hz, nap), 8.51 (d, 2H, $^3J_{HH}$ = 4.0 Hz, pyr), 8.34 (d, 1H, $^3J_{HH}$ = 8.5 Hz, nap), 7.88 (s, 1H, N*H*), 7.62 (app. t, 1H, $^3J_{HH}$ = 8.0 Hz, nap), 7.50 (app. t, 2H, $^3J_{HH}$ = 8.5 Hz, pyr), 7.31 (d, 2H, $^3J_{HH}$ = 8.0 Hz, pyr), 7.09 (app. t, 2H, $^3J_{HH}$ = 6.0 Hz, pyr), 6.47 (d, 1H, $^3J_{HH}$ = 8.5 Hz, nap), 4.37 (t, 2H, $^3J_{HH}$ = 5.5 Hz, NCH_2), 3.95 (s, 4H, NCH_2), 3.79 (t, 2H, $^3J_{HH}$ = 5.5 Hz), 3.65–3.61 (m, 4H, CH_2), 3.40–3.30 (broad m, 2H, CH_2), 2.99 (t, 2H, $^3J_{HH}$ = 5.5 Hz, CH_2) ppm; $^{13}C\{^1H\}$ NMR (75 MHz, $CDCl_3$): δ_C = 187.6, 167.6 (*C*O), 164.2 (*C*O), 158.8, 151.5, 149.3, 143.9, 139.8, 137.3, 136.8, 135.7, 128.1, 123.4, 122.5, 107.5, 104.1, 81.3, 59.8, 23.0, 21.9, 20.5, 17.4, 13.8, 5.9 ppm; LRMS (ES^+) found *m/z* 526.2 for $[M+H]^+$ and 548.2 for $[M+Na]^+$; HRMS (ES^-) found *m/z* 560.2053 for $[C_{30}H_{31}O_4N_5 + Cl]^-$, calculated at 560.2047 for $[C_{30}H_{31}O_4N_5 + Cl]^-$; IR (solid) ν_{max} (±2 cm^{-1}) = 3208 (br), 2893, 2864, 1684, 1641, 1589, 1556, 1476, 1429, 1368, 1327, 1304, 1234, 1117, 1051, 1003, 885, 772, 756 cm^{-1}; UV–vis (MeCN): λ_{max} ($\varepsilon/M^{-1}cm^{-1}$) 437 (14400), 340 (1000), 324 (1500), 280 (20800), 260 (24400), 228 (18700) nm.

*Synthesis of 4–(N',N'–bis(pyridin–2–ylmethyl)ethylenediamine)–(N–3'–aminobenzyl alcohol)–1,8–naphthalimide (**L4**)*

Prepared as for **L1** using 2-pyridinecarboxaldehyde (0.32 mL, 3.35 mmol), **N4** (0.590 g, 1.63 mmol), and sodium triacetoxyborohydride (1.13 g, 4.85 mmol) to give crude **L4** as an orange oil. The product was purified *via* column chromatography, first eluting with dichloromethane and then collecting the product by eluting with 3% MeOH in dichloromethane. Yield: 149 mg, 0.74 mmol, 17 %. ^1H NMR (400 MHz, $CDCl_3$): δ_H = 8.77 (d, 1H, $^3J_{HH}$ = 8.5 Hz, nap), 8.53 (d, 1H, $^3J_{HH}$ = 7.0 Hz, nap), 8.46 (d, 2H, $^3J_{HH}$ = 4.5 Hz, pyr), 8.30 (d, 1H, $^3J_{HH}$ = 8.5 Hz, nap), 7.89 (br s, 1H, N*H*), 7.61 (app. t, 1H, $^3J_{HH}$ = 8.0 Hz, nap), 7.50–7.31 (m, 4H, nap, Ph, pyr), 7.29 (d, 2H, $^3J_{HH}$ = 8.0 Hz, pyr), 7.25 (s, 1H, Ph), 7.15 (d, 1H, $^3J_{HH}$ = 7.5 Hz,

nap), 7.05 (app. t, 2H, $^3J_{HH}$ = 6.5 Hz, pyr), 6.44 (d, 1H, $^3J_{HH}$ = 8.5 Hz, nap), 4.66 (s, 2H, HOCH_2), 3.89 (s, 4H, NCH_2), 3.40–3.25 (broad m, 2H, CH_2), 2.93 (t, 2H, $^3J_{HH}$ = 5.0 Hz, CH_2), 2.61 (broad s, 1H, OH) ppm; $^{13}C\{^1H\}$ NMR (75 MHz, $CDCl_3$): δ_C = 165.2, 164.4, 158.8, 150.9, 149.2, 142.8, 136.8, 135.3, 131.5, 129.4, 128.3, 127.9, 127.4, 126.9, 124.4, 123.5, 122.9, 122.5, 121.0, 108.7, 104.1, 64.7, 59.8, 51.2, 41.0 ppm; LRMS (ES^+) found m/z 526.2 for $[M+H]^+$ and 548.2 for $[M+Na]^+$; HRMS (ES^+) found *m/z* = 544.2338 for $[C_{33}H_{29}N_5O_3+H]^+$, calculated at 544.2343 for $[C_{33}H_{29}N_5O_3+H]^+$; IR (solid) ν_{max} (±2 cm^{-1}) = 3260 (br), 2830, 1688, 1641, 1576, 1539, 1433, 1358, 1260, 1240, 1146, 1003, 766, 754 cm^{-1}; UV–vis (MeCN): λ_{max} ($\varepsilon/M^{-1}cm^{-1}$) 436 (14900), 341 (1000), 325 (1700), 282 (18100), 265 (19500), 226 (22200) nm; UV–vis (MeOH): λ_{max} ($\varepsilon/M^{-1}cm^{-1}$) 445 (14200), 339 (900), 323 (2000), 282 (16200), 268 (17800), 261 (18000), 227 (20300), 203 (61500) nm.

3.5.6 Complex Synthesis

*Synthesis of fac–[Re(CO)$_3$(**L1**)]BF$_4$ (**ReL1**)*

L1 (57 mg, 0.11 mmol) and *fac*–$[Re(CO)_3(MeCN)_3]BF_4$ (50 mg, 0.10 mmol) were dissolved in $CHCl_3$ (10 mL) and heated at reflux under a nitrogen atmosphere for 18 hours. The reaction mixture was allowed to cool, the solvent was reduced to 1–2 mL, and precipitation was induced with the addition of diethyl ether. The product was collected by filtration and washed with diethyl ether, to give **ReL1** as a yellow solid. Yield: 16.7 mg, 19.0 μmol, 18 %. ^1H NMR (400 MHz, $(CD_3)_2CO$): δ_H = 8.86 (d, 2H, $^3J_{HH}$ = 8.0 Hz, pyr), 8.52 (d, 1H, $^3J_{HH}$ = 8.0 Hz, nap), 8.40 (d, 1H, $^3J_{HH}$ = 8.0 Hz, nap), 8.28 (d, 1H, $^3J_{HH}$ = 7.5 Hz, nap), 7.95–7.85 (m, 2H, nap, pyr), 7.60 (app. t, 1H, $^3J_{HH}$ = 8.5 Hz, nap), 7.56 (d, 2H, $^3J_{HH}$ = 8.0 Hz, pyr), 7.36 (app. t, 2H, $^3J_{HH}$ = 8.0 Hz, pyr), 7.19 (br t, 1H, $^3J_{HH}$ = 4.5 Hz, NH), 7.02 (d, 1H, $^3J_{HH}$ = 8.0 Hz, nap), 5.36 (d, 2H, $^2J_{HH}$ = 16.5 Hz, 1/2 × 2CH_2), 5.18 (d, 2H, $^2J_{HH}$ = 16.5 Hz, 1/2 × 2CH_2), 4.71 (s, 2H, NCH_2CO), 4.40 (t, 2H, $^3J_{HH}$ = 8.0 Hz, NCH_2), 4.20–4.10 (broad m, 2H, NCH_2), 4.07 (q, 2H, $^3J_{HH}$ = 8.5 Hz, OCH_2CH$_3$), 1.13 (t, 3H, $^3J_{HH}$ = 8.5 Hz, OCH$_2$CH_3) ppm; LRMS (ES^+) found *m/z* 792.2 for $[M]^+$; HRMS (ES^+) found *m/z* 792.1587; calculated 792.1591 for $[C_{33}H_{29}N_5O_7Re]^+$; IR (solid) ν_{max} (±2 cm^{-1}) = 2031, 1930, 1903, 1676, 1639, 1587 cm^{-1}; UV–vis (MeCN): λ_{max} ($\varepsilon/M^{-1}cm^{-1}$) 421 (12800), 338 (2300), 321 (4100), 277 (26300), 255 (23700), 228 (24600) nm; UV–vis (MeOH): λ_{max} ($\varepsilon/M^{-1}cm^{-1}$) 427 (13100), 339 (2500), 322 (4400), 277 (25900), 255 (24200), 228 (24100), 203 (55900) nm.

*Synthesis of fac–[Re(CO)$_3$(**L2**)]BF$_4$ (**ReL2**)*

Prepared as for **ReL2** using compound **L2** (53.6 mg, 0.11 mmol) and *fac*–$[Re(CO)_3(MeCN)_3]BF_4$ (48.0 mg, 0.10 mmol) to give **ReL2** as a yellow solid. Yield: 61.9 mg, 72.6 μmol, 73 %. ^1H NMR (400 MHz, CD_3CN): δ_H = 8.82 (d, 2H, $^3J_{HH}$ = 5.5 Hz, pyr), 8.53 (d, 1H, $^3J_{HH}$ = 7.5 Hz, nap), 8.42 (app. d, 2H, $^3J_{HH}$ = 8.5 Hz, nap), 7.92 (app. t, 2H, $^3J_{HH}$ = 8.0 Hz, pyr),

7.73 (app. t, 1H, $^3J_{HH}$ = 7.5 Hz, nap), 7.49 (d, 2H, $^3J_{HH}$ = 8.0 Hz, pyr), 7.34 (app. t, 2H, $^3J_{HH}$ = 6.5 Hz, pyr), 6.95 (d, 1H, $^3J_{HH}$ = 8.5 Hz, nap), 6.37 (br t, 1H, N*H*), 4.99 (d, 2H, $^2J_{HH}$ = 16.5 Hz, 1/2 × 2C*H*$_2$), 4.90 (d, 2H, $^2J_{HH}$ = 16.5 Hz, 1/2 × 2C*H*$_2$), 4.25 (t, 2H, $^3J_{HH}$ = 7.5 Hz, C*H*$_2$), 4.19 (t, 2H, $^3J_{HH}$ = 5.5 Hz, C*H*$_2$), 4.01 (app. q, 2H, C*H*$_2$), 3.55 (t, 2H, $^3J_{HH}$ = 6.0 Hz), 1.87 (app. quin, 2H, $^3J_{HH}$ = 6.0 Hz, C*H*$_2$CH$_2$OH) ppm; LRMS (ES$^+$) found *m/z* 766.1 for [M]$^+$; HRMS (ES$^+$) found *m/z* 764.1639 for [C$_{32}$H$_{29}$N$_5$O$_6$Re]$^+$; calculated 764.1642 for [C$_{32}$H$_{29}$N$_5$O$_6$Re]$^+$; IR (solid) ν_{max} (±2 cm^{-1}) = 2025, 1921, 1898, 1690, 1629 cm^{-1}; UV–vis (MeCN): λ_{max} (ε/M^{-1}cm^{-1}) = 421 (13800), 338 (4400), 323 (6100), 272 (35600), 258 (35600); UV–vis (MeOH): λ_{max} (ε/M^{-1}cm^{-1}) 427 (13000), 337 (3300), 324 (4800), 272 (29700), 258 (30900), 227 (26200), 203 (59200) nm.

*Synthesis of fac–[Re(CO)$_3$(**L3**)]BF$_4$ (**ReL3**)*

Prepared as for **ReL1** using **L3** (16.8 mg, 32.0 μmol) and *fac*–[Re(CO)$_3$(MeCN)$_3$]BF$_4$ (14.6 mg, 30.4 μmol) to give **ReL3** as a yellow solid. Yield: 15.5 mg, 17.6 μmol, 58 %. ^{1}H NMR (400 MHz, CDCl$_3$): δ_H = 8.59 (d, 2H, $^3J_{HH}$ = 5.5 Hz, pyr), 8.36–8.30 (m, 3H, nap, pyr), 7.79–7.69 (m, 2H, nap), 7.66 (d, 2H, $^3J_{HH}$ = 8.0 Hz, pyr), 7.49 (app. t, 1H, $^3J_{HH}$ = 8.0 Hz, nap), 7.14 (app. t, 2H, $^3J_{HH}$ = 6.0 Hz, pyr), 6.78 (br t, 1H, $^3J_{HH}$ = 8.5 Hz, N*H*), 6.67 (d, 1H, $^3J_{HH}$ = 8.0 Hz, nap), 5.53 (d, 2H, $^2J_{HH}$ = 16.5 Hz, 1/2 × 2C*H*$_2$), 4.58 (d, 2H, $^2J_{HH}$ = 16.5 Hz, 1/2 × 2C*H*$_2$), 4.34 (t, 2H, $^3J_{HH}$ = 5.0 Hz, NC*H*$_2$), 4.18 (t, 2H, $^3J_{HH}$ = 5.0 Hz, C*H*$_2$), 4.10–4.02 (m, 2H, C*H*$_2$), 3.83 (t, 2H, $^3J_{HH}$ = 5.5 Hz, NC*H*$_2$), 3.70–3.48 (m, 4H, OC*H*$_2$) ppm; LRMS (ES$^+$) found *m/z* 796.4 for [M]$^+$; HRMS (ES$^+$) found *m/z* 794.1741 for [C$_{33}$H$_{31}$N$_5$O$_7$Re]$^+$, calculated at 794.1748 for [C$_{33}$H$_{31}$N$_5$O$_7$Re]$^+$; IR (solid) ν_{max} (±2 cm^{-1}) = 2031, 1910 (br), 1690, 1643 cm^{-1}; UV–vis (MeCN): λ_{max} (ε/M^{-1}cm^{-1}) = 421 (12800), 338 (2300), 321 (4100), 277 (26300), 255 (23700), 228 (24600) nm; UV–vis (MeOH): λ_{max} (ε/M^{-1}cm^{-1}) = 427 (15200), 338 (5000), 323 (6600), 277 (28000), 258 (29600), 227 (28000), 203 (62300) nm.

*Synthesis of fac–[Re(CO)$_3$(**L4**)]BF$_4$ (**ReL4**)*

Prepared as for **ReL1** using **L4** (30.2 mg, 55.6 μmol) and *fac*–[Re(CO)$_3$(MeCN)$_3$]BF$_4$ (25.9 mg, 54.0 μmol) to give **ReL4** as a yellow solid. Yield: 33.4 mg, 37.1 μmol, 69 %. ^{1}H NMR (400 MHz, CD$_3$CN): δ_H = 8.82 (d, 2H, $^3J_{HH}$ = 5.5 Hz, pyr), 8.56 (d, 1H, $^3J_{HH}$ = 8.0 Hz, nap), 8.49 (d, 1H, $^3J_{HH}$ = 8.5 Hz, nap), 8.45 (d, 1H, $^3J_{HH}$ = 8.0 Hz, nap), 7.92 (app. t, 2H, $^3J_{HH}$ = 8.0 Hz, pyr), 7.78 (app. t, 1H, $^3J_{HH}$ = 7.5 Hz, nap), 7.55–7.40 (m, 4H, nap, Ph), 7.38–7.32 (m, 3H, pyr, Ph), 7.23 (d, 1H, $^3J_{HH}$ = 8.0 Hz, Ph), 7.01 (d, 1H, $^3J_{HH}$ = 8.5 Hz, nap), 6.42 (t, 1H, $^3J_{HH}$ = 8.0 Hz, N*H*), 4.98 (d, 2H, $^2J_{HH}$ = 17.0 Hz, 1/2 × 2C*H*$_2$), 4.90 (d, 2H, $^2J_{HH}$ = 17.0 Hz, 1/2 × 2C*H*$_2$), 4.68 (s, 2H), 4.26 (t, 2H, $^3J_{HH}$ = 6.0 Hz, C*H*$_2$), 4.10–4.02 (m, 2H, C*H*$_2$) ppm; LRMS (ES$^+$) found: *m/z* 766.1 for [M]$^+$; HRMS (ES$^+$) found *m/z* 812.1642 for [C$_{36}$H$_{29}$O$_6$N$_5$Re]$^+$, calculated at 812.1642 for [C$_{36}$H$_{29}$O$_6$N$_5$Re]$^+$; IR (solid) ν_{max} (±2 cm^{-1}) = 2029, 1906, 1682, 1640 cm^{-1};

UV–vis (MeCN): λ_{max} (ε/$M^{-1}cm^{-1}$) 420 (15200), 338 (3200), 321 (4800), 312 (4600), 276 (11100), 256 (13400), 226 (33500) nm; UV–vis (MeOH): λ_{max} (ε/$M^{-1}cm^{-1}$) 427 (17900), 336 (4100), 322 (6100), 270 (32600), 205 (81400).

3.6 References

1. S. Lee and X. Chen, *Molecular Imaging*, 2009, **8**, 87-100.
2. F. L. Thorp-Greenwood and M. P. Coogan, *Dalton Trans.*, 2011, 6129-6143.
3. J. Dilworth and S. I. Pascu, in *The Chemistry of Molecular Imaging*, eds. N. Long and W. T. Wong, John Wiley and Sons Inc., New Jersey, 1st edn., 2015, ch. 6, pp. 137-164.
4. W. Cai, S. S. Gambhir and X. Chen, *Molecular Imaging*, 2005, **39**, 14-25.
5. C. Spagnul, R. Alberto, G. Gasser, S. Ferrari, V. Pierroz, A. Bergamo, T. Gianferrara and E. Alessio, *J. Inorg. Biochem.*, 2013, **122**, 57-65.
6. P. J. Cassidy and G. K. Radda, *J. R. Soc. Interface*, 2005, **2**, 133-144.
7. A. François, C. Auzanneau, V. Le Morvan, C. Galaup, H. S. Godfrey, L. Marty, A. Boulay, M. Artigau, B. Mestre-Voegtlé, N. Leygue, C. Picard, Y. Coulais, J. Robert and E. Benoist, *Dalton Trans.*, 2014, **43**, 439-450.
8. N. N. Greenwood and A. Earnshaw, in *Chemistry of the Elements* ed. B.-H. Ltd, Butterworth-Heinemann Ltd, Oxford, UK, 2nd edn., 1997, ch. 24, pp. 1040-1062.
9. L. H. Davies, B. B. Kasten, P. D. Benny, R. L. Arrowsmith, H. Ge, S. I. Pascu, S. W. Botchway, W. Clegg, R. W. Harrington and L. J. Higham, *Chem. Commun.*, 2014, **50**, 15503-15505.
10. C. A. Kluba and T. L. Mindt, *Molecules*, 2013, **18**, 3206-3226.
11. L. A. Mullice, R. H. Laye, L. P. Harding, N. J. Buurma and S. J. A. Pope, *New J. Chem.*, 2008, **32**, 2140-2149.
12. R. Alberto, R. Schibli, A. Egli, A. P. Schubiger, U. Abram and T. A. Kaden, *J. Am. Chem. Soc.*, 1998, **120**, 7987-7988.
13. A. Boulay, M. Artigau, Y. Coulais, C. Picard, B. Mestre-Voegtlé and E. Benoist, *Dalton Trans.*, 2011, **40**, 6206-6209.
14. K. A. Stephenson, S. R. Banerjee, T. Besanger, O. O. Sogbein, M. K. Levadala, N. McFarlane, J. A. Lemon, D. R. Boreham, K. P. Maresca, J. D. Brennan, J. W. Babich, J. Zubieta and J. F. Valliant, *J. Am. Chem. Soc.*, 2004, **126**, 8589-8599.
15. L. Wei, J. W. Babich, W. Ouellette and J. Zubieta, *Inorg. Chem.*, 2006, **45**, 3057-3066.
16. S. Tzanopoulou, M. Sagnou, M. Paravatou-Petsotas, E. Gourni, G. Loudos, S. Xanthopoulos, D. Lafkas, H. Kiaris, A. Varvarigou, I. C. Pirmettis, M. Papadopoulos and M. Pelecanou, *J. Med. Chem.*, 2010, **53**, 4633-4641.
17. N. Agorastos, L. Borsig, A. Renard, P. Antoni, G. Viola, B. Spingler, P. Kurz and R. Alberto, *Chem. Eur. J.*, 2007, **13**, 3842-3852.
18. Y. Yang, L. Zhu, M. Cui, R. Tang and H. Zhang, *Bioorg. Med. Chem. Lett.*, 2010, **20**, 5337-5344.
19. Y. Yang, H. Song, H. Song, W. Zhao and M. Pu, *J. Porphyrins Phthalocyanines*, 2011, **15**, 271-276.
20. K. de Oliveira, P. Costa, J. Santin, L. Mazzambani, C. Burger, C. Mora, R. Nunes and M. de Souza, *Bioorg. Med. Chem.*, 2011, **19**, 4295-4306.
21. B. Dana, C. McAdam, B. Robinson, J. Simpson and H. Wang, *J. Inorg. Organomet. Polym. Mater.*, 2007, **17**, 547-559.
22. P. Nandhikonda, M. Begaye, Z. Cao and M. Heagy, *Org. Biomol. Chem.*, 2010, **8**, 3195-3201.
23. J. A. Riddick, W. B. Bunger and T. K. Sakano, *Techniques of Chemistry*, John Wiley and Sons, New York, 4th edn., 1985.
24. *Scifinder - Calculated using Advanced Chemistry Development (ACD/Labs) Software V11.02 (© 1994-2015 ACD/Labs)*.
25. E. P. Serjeant and D. B., *Ionisation constants of inorganic acids and bases in aqueous solution*, Pergamon Press, 2nd edn., 1979.
26. T. Gunnlaugsson, C. McCoy, R. Morrow, C. Phelan and F. Stomeo, *Arkivoc*, 2003, 216-228.
27. R. Stolarski, *Fibres & Textiles in Eastern Europe*, 2009, **17**, 91-95.

28. L. A. Mullice and S. J. A. Pope, *Dalton Trans.*, 2010, **39**, 5908-5917.
29. C. Zhang, Z. Liu, Y. Li, W. He, X. Gaod and Z. Guo, *Chem. Commun.*, 2013, **49**, 11430–11432.
30. H. Wang, L. Yang, W. Zhang, Y. Zhou, B. Zhao and X. Li, *Inorg. Chim. Acta*, 2012, **381**, 111-116.
31. Z. Y. Wu, J. N. Cui, X. H. Qian and T. Y. Liu, *Chin. Chem. Lett.*, 2013, **24**, 359-361.
32. G. R. C. Hamilton, Y. Sheng, B. Callan, R. F. Donnelly and J. F. Callan, *New J. Chem.*, 2015, **39**, 3461-3466.
33. J. V. Casper and T. J. Meyer, *J. Phys. Chem.*, 1983, **87**, 952-957.
34. L. A. Mullice, *PhD Thesis*, 2010, **Chapter 4**, 142.
35. G. A. Jeffery, *An Introduction to Hydrogen Bonding*, Oxford University Press, 1997.
36. D. E. Lewis, *Organic Biomolecular Chemistry*, 2013, **11**, 4390-4396.
37. E. E. Langdon-Jones, N. O. Symonds, S. E. Yates, A. J. Hayes, D. Lloyd, R. Williams, S. J. Coles, P. N. Horton and S. J. A. Pope, *Inorg. Chem.*, 2014, **53**, 3788-3797.
38. H. Xia and F. Zhao, *Applied Mechanics and Materials*, 2013, **252**, 306-309.
39. L. Chen, W. Sun, W. Li, J. Li, L. Du, W. Xu, H. Fang and M. Li, *Analytical Methods*, 2012, **4**, 2661-2663.
40. J. Zhang, M. Park, W. Ren, Y. Kim, S. Kim, J. Jung and J. Kim, *Chem. Commun.*, 2011, **47**, 3568-3570.
41. J. Yarnell, J. Deaton, C. McCusker and F. Castellano, *Inorg. Chem.*, 2011, **50**, 7820-7830.
42. S. S. Bag, M. K. Pradhan, R. Kundu and S. Jana, *Bioorg. Med. Chem.*, 2013, **23**, 96-101.
43. M. Shahid, P. Srivastava and A. Misra, *New J. Chem.*, 2011, **35**, 1690-1700.
44. S. Banerjee, E. B. Veale, C. M. Phelan, S. A. Murphy, G. M. Tocci, L. J. Gillespie, D. O. Frimannsson, J. M. Kelly and T. Gunnlaugsson, *Chem. Soc. Rev.*, 2013, **42**, 1601-1618.
45. Y. Dai, B.-K. Lv, X.-F. Zhang and Y. Xiao, *Chin. Chem. Lett.*, 2014, **25**, 1001-1005.
46. M. Wrighton and D. L. Morse, *J. Am. Chem. Soc.*, 1974, **96**, 998-1003.
47. V. Bojinov, N. Georgiev and P. Bosch, *J. Fluoresc.*, 2009, **19**, 127-139.
48. V. Bojinov and I. Panova, *Dyes Pigm.*, 2009, **80**, 61-66.
49. J. Gan, K. Chen, C. Chang and H. Tian, *Dyes Pigm.*, 2003, **57**, 21-38.
50. R. Parkesh, T. C. Lee and T. Gunnlaugsson, *Org. Biomol. Chem.*, 2007, **5**, 310-317.
51. E. B. Veale, J. A. Kitchen and T. Gunnlaugsson, *Supramol. Chem.*, 2013, **25**, 101-108.
52. M. Pluth, E. Tomat, S. Lippard, R. Kornberg, C. Raetz, J. Rothman and J. Thorner, *Annual Review of Biochemistry, Vol 80*, 2011, **80**, 333-355.
53. E. Hao, T. Meng, M. Zhang, W. Pang, Y. Zhou and L. Jiao, *J. Phys. Chem. A*, 2011, **115**, 8234-8241.
54. S. Huang, R. Han, Q. Zhuang, L. Du, H. Jia, Y. Liu and Y. Liu, *Biosens. Bioelectron.*, 2015, **71**, 313-321.
55. E. J. New and D. Parker, *Org. Biomol. Chem.*, 2009, **7**, 851-855.
56. T. Jia, C. Fu, C. Huang, H. Yang and N. Jia, *ACS Appl. Mater. Interfaces*, 2015, **7**, 10013-10021.
57. V. Fernández-Moreira, F. L. Thorp-Greenwood, A. J. Amoroso, J. Cable, J. B. Court, V. Gray, A. J. Hayes, R. L. Jenkins, B. M. Kariuki, D. Lloyd, C. O. Millet, C. F. Williams and M. P. Coogan, *Org. Biomol. Chem.*, 2010, **8**, 3888-3901.
58. F. Kielar, G.-L. Law, E. J. New and D. Parker, *Org. Biomol. Chem.*, 2008, **6**, 2256-2258.
59. S. J. Coles and P. A. Gale, *Chemical Science*, 2012, **3**, 683-689.
60. G. M. Sheldrick, *Acta crystallographica. Section A, Foundations of crystallography*, 2008, **64**, 112-122.
61. L. J. Farrugia, *J. Appl. Crystallogr.*, 1997, 565.
62. M. Frank, M. Nieger, F. Vogtle, P. Belser, A. von Zelewsky, L. D. Cola, V. Balzani, F. Barigelletti and L. Flamigni, *Inorg. Chim. Acta*, 1996, **242**, 281-291.

63. A. Juris, F. Barigelletti, S. Campagna, P. Belser and A. von Zelewsky, *Coord. Chem. Rev.*, 1988, **84**, 85-277.
64. S. R. Chhabra, A. Mahajan and W. C. Chan, *J. Org. Chem.*, 2002, **67**, 4017-4029.

3.7 Appendix

3.7.1 Crystallographic data for L3

Table S3. 1: Crystal Data and Structure Determination Refinement for L3

Identification code	2013ncs0294 / ELJ219	
Empirical formula	$C_{30}H_{29}N_5O_4$	
Formula weight	523.58	
Temperature	100(2) K	
Wavelength	0.71075 Å	
Crystal system	Monoclinic	
Space group	$P2_1/n$	
Unit cell dimensions	a = 4.8867(2) Å	α = 90°
	b = 33.784(2) Å	β = 92.598(2)°
	c = 14.9055(10) Å	γ = 90°
Volume	2458.3(2) Å^3	
Z	4	
Density (calculated)	1.415 Mg / m^3	
Absorption coefficient	0.096 mm^{-1}	
F(000)	1104	
Crystal	Plate; yellow	
Crystal size	0.220 × 0.130 × 0.020 mm^3	
θ range for data collection	2.990 – 27.482°	
Index ranges	$-5 \le h \le 6$, $-43 \le k \le 43$, $-19 \le l \le 19$	
Reflections collected	27085	
Independent reflections	5588 [R_{int} = 0.0527]	
Completeness to θ = 25.242°	98.6 %	
Absorption correction	Semi–empirical from equivalents	
Max. and min. transmission	1.000 and 0.706	
Refinement method	Full-matrix least-squares on F^2	
Data / restraints / parameters	5588 / 0 / 353	
Goodness-of-fit on F^2	1.027	
Final R indices [$F^2 > 2\sigma(F^2)$]	*R1* = 0.0417, *wR2* = 0.1108	
R indices (all data)	*R1* = 0.0534, *wR2* = 0.1196	
Extinction coefficient	n/a	
Largest diff. peak and hole	0.340 and –0.216 e Å^{-3}	

Diffractometer: *Rigaku AFC12* goniometer equipped with an enhanced sensitivity (HG) *Saturn724+* detector mounted at the window of an *FR-E+ SuperBright* molybdenum rotating anode generator with HF *Varimax* optics (100μm focus). **Cell determination and data collection**: *CrystalClear-SM Expert 3.1 b26* (Rigaku, 2013). **Data reduction, cell refinement and absorption correction**: *CrystalClear-SM Expert 3.1 b26* (Rigaku, 2013). **Structure solution**: *SHELXS97* (Sheldrick, G.M. (2008). Acta Cryst. A64, 112-122). **Structure refinement**: *SHELXL97* (Sheldrick, G.M. (2008). Acta Cryst. A64, 112-122). **Graphics:** *ORTEP3 for Windows* (L. J. Farrugia, J. Appl. Crystallogr. 1997, 30, 565).

3.7.2 Autofluorescence Assessment of Human Osteoarthritic Cells

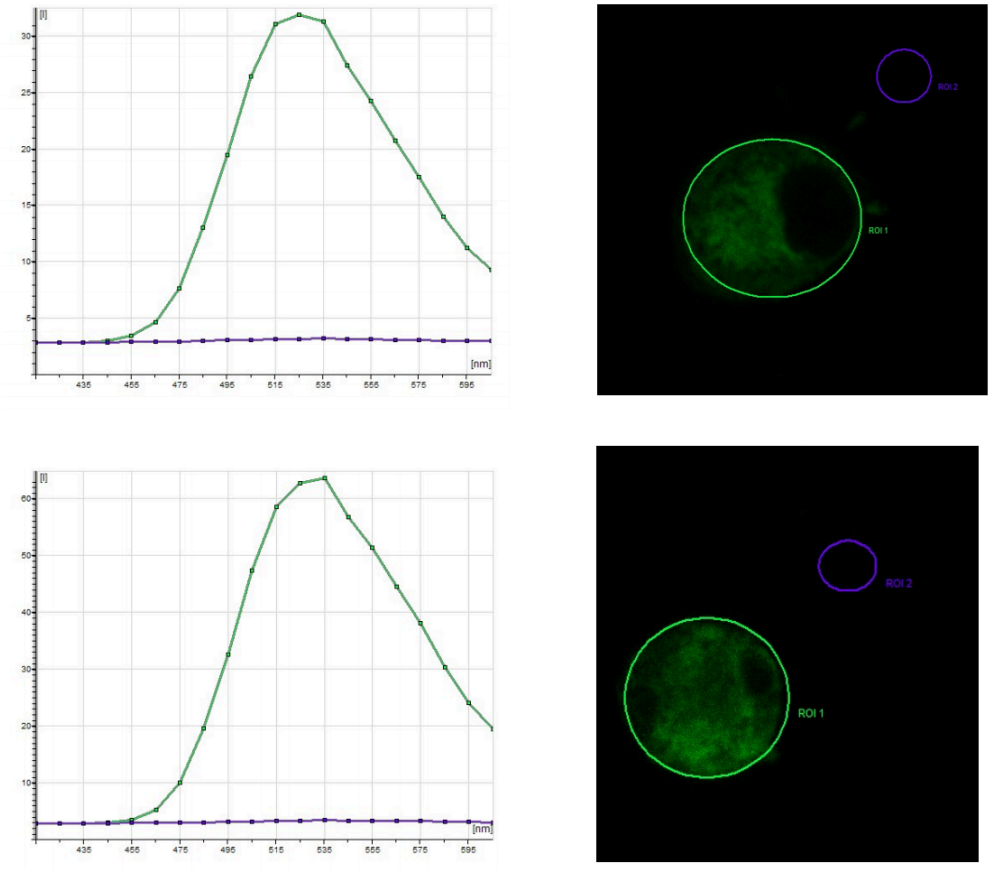

Figure S3. 1: Confocal fluorescence microscopy showing spectra profile of the labelled cell *versus* background signal for ReL2 (top) and ReL4 (bottom).

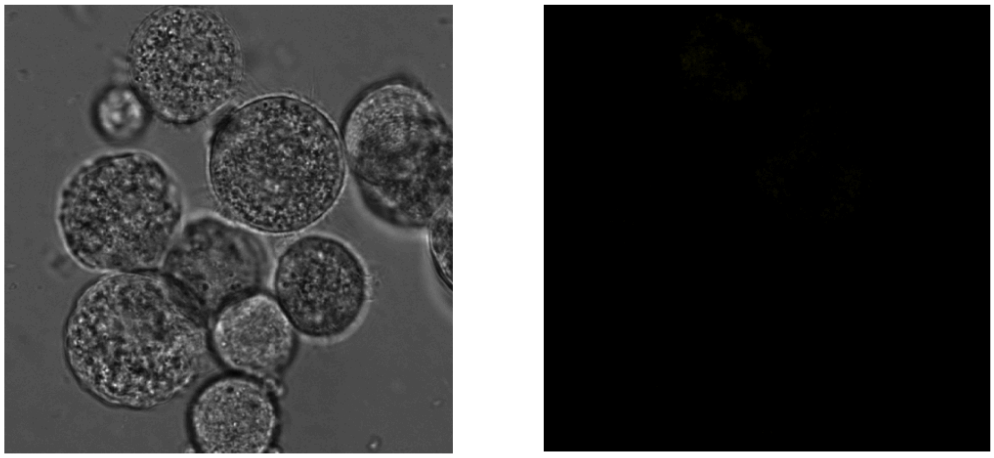

Figure S3. 2: Microscopy showing minimal autofluorescence in a group of unlabeled osteoarthritic cells using transmission (left) and fluorescence modes (right)

Chapter 4

Alkynyl–Naphthalimide Fluorophores: Gold Coordination Chemistry and Cellular Imaging Applications

4.1 Introduction

The synthesis and characterisation of seven new alkynyl–derived 1,8–naphthalimide fluorophores together with their linear two–coordinate Au(I) complexes is described herein. These new compounds were assessed for imaging capabilities, *via* the fluorescent naphthalimide ligand. In addition their inherent toxicity from the Au(I) core was assessed. The results show that the specific functionalisation of the 1,8–naphthalimide core determines the cellular uptake and distribution, with selected examples showing some outstanding imaging characteristics as potential bimodal optical/therapeutic agents.

4.1.1 Chemical Properties of Gold

Gold was the first metal known to early civilisations (40000 BC)[1] and today it is still known for its beauty and is associated with wealth and power.[2] In a chemical context gold has the lowest electrochemical potential of any metal,[1] resulting in its noble character. It is also the most electronegative of all metals[2] and transforming Au(0) to Au(–I) has been known since 1930.[1]

Gold(I) has a $5d^{10}6s^{0}$ electron configuration resulting in the relative stability of gold(I) compounds, with a closed set of *5d* orbitals. Post–lanthanide elements experience 'relativistic effects' that are most pronounced for gold. Gold possesses a large atomic number resulting in a very high effective nuclear charge and subsequently the electrons travel at velocities approaching the speed of light. The effect on the electrons (particularly *6s*) causes the orbital radius to be contracted and the distance from the nucleus to be reduced. This results in a number of effects in gold chemistry: i) the colour of gold arising from a transition from the filled *5d* band to the Fermi level (2.4 eV); ii) shorter covalent bond lengths involving gold atoms; and iii) the closed $5d^{10}$ shell is no longer chemically inert and can interact with other gold atoms in molecules or clusters.[1]

4.1.2 Au(I) Coordination Chemistry and Ligand Design

The chemistry of Au(I) compounds is by far the most developed and many mononuclear, dinuclear or polynuclear derivatives have been reported with interesting photophysical and photochemical properties.[3] Linear, two–coordinate Au(I) complexes dominate due to the small difference in energy between the *s, p* and *d* orbitals.[1] It is noteworthy that the destabilisation of the *5d* orbitals allows the easy formation of square planar Au(III) complexes.[2] The soft, electrophilic Au(I) ion has a high affinity for sulfur, phosphine, arsenic, alkynyl and selenium donors[2,4] and consequently many Au(I) complexes exist with such ligands. For example even though alkyne ligands (good σ and π donors)[5]

possess no lone pair, and therefore cannot be considered to form classical Werner coordination complexes, many stable Au(I) alkyne complexes have been synthesised due to the low oxidation state of Au(I).[5] This is often from metal halides in the presence of an alkali metal alkylating agent.[3] In such Au(I) complexes of terminal alkyne ligands the alkyne is isoelectronic with CN^- and CO ligands but can also be thought of as a pseudohalide.[3]

The d^{10} configuration of Au(I) complexes results in kinetically stable complexes. However ligand exchange is a fundamental contributory factor to the biological activity and behaviour of Au(I) coordination complexes. Solution calorimetry studies on a [Au(L)Cl] system (where L = phosphine or phosphite) showed that the electronic parameters of the phosphorus ligand dominate: typical bond dissociation enthalpies for tertiary phosphines from Au(I) were estimated at 58–65±5 $kcalmol^{-1}$.[6] In addition, tuning the amphiphilic nature of the ligands can modulate other important factors such as protein binding, excretion pathways and overall toxicity of Au(I) complexes.[7,8]

4.1.3 Therapeutic Activity of Gold (Crysotherapy)

The use of gold–based compounds in medicinal chemistry is known as chrysotherapy.[9-11] In this context, the most common class of gold coordination complex that has been used in a clinical setting are species incorporating Au(I) and thiolate ligands. For example, compounds sodium aurothiomalate and auranofin have been successfully used to treat inflammatory autoimmune conditions like rheumatoid arthritis (Figure 4.1).[12,13]

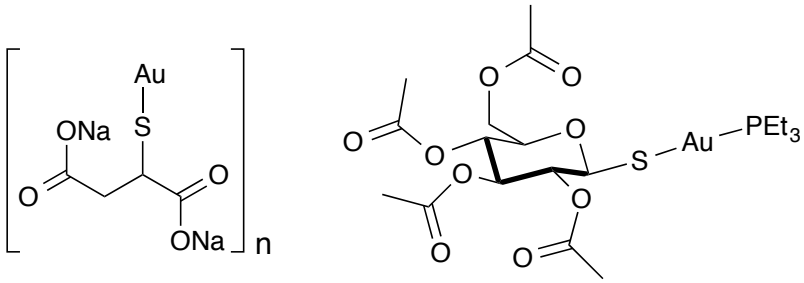

Figure 4.1: Examples of clinical Au(I) drugs. (left) Sodium aurothiolmalate, (right) auranofin.

Unravelling the biological action of such species is very challenging.[14,15] The mode of action of Au(I) drugs is believed to be related to the inhibition of cathepsin B activity (*via* targeting of lysosomal cysteine proteases),[16] and the interruption of oxidative stress regulation in cells through the inhibition of the enzyme Thioredoxin Reductase (TrxR).[17-19] More recently, the inhibition of selenium–glutathione peroxidase, emphasising the thio–

and selenophilic nature of Au(I), has also been described.[20,21] Research has focused upon the inhibitive character against TrxR that contains a selenocysteine residue in its active site.[22] TrxR is involved in several metabolic pathways, but it is the antioxidant capability of TrxR that is thought to protect cells from oxidative stress.[23] Elevated levels of TrxR have been noted in a variety of cancer cell lines.[24]

In addition to the focused studies on developing treatments for rheumatoid arthritis, a wide range of Au(I) complexes have been assessed for their anti–tumour properties[25,26] but the antitumour activity is also not well understood.[27] Auranofin and its structural analogues have displayed significant cytotoxicity against B16 melanoma and P388 leukaemia cell lines.[28] A key outcome of the work was the importance of the ancillary tertiary phosphine which induced additional potency, possibly through modulating lipophilicity which has been shown as an important factor in cellular uptake and anti–tumour activity.[29]

Unfortunately the toxicity from many Au(I) complexes, and the unclear biological mode of action[30] still detract from the established medical benefits.[31] Also many linear Au(I) undergo ligand exchange reactions and are very reactive with thiols which limits their potential as anticancer agents.[32]

4.1.4 Cytotoxic Au(I) Complexes

Antiproliferative effects of many Au(I) complexes have been investigated by microculture tetrazolium (MTT) assay. Common ligand types for such applications include: N–heterocyclic carbenes (NHCs), alkynyl–derived ligands and other biologically relevant organic structures (Figure 4.2).

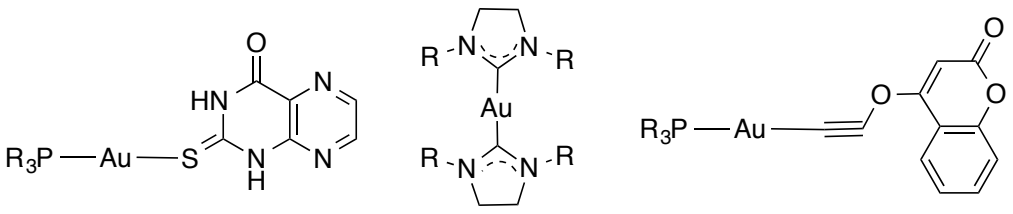

Figure 4.2: Examples of cytotoxic linear Au(I) complexes.

The use of NHCs as ligands for Au(I) has rapidly developed over the past decade with pioneering work by the groups of Baker and Berners–Price demonstrating comparable IC_{50} values to cisplatin. Supporting fluorescence microscopy imaging work indicated fragmented nuclei and other indicators of apoptosis (cell death). Furthermore, NHC complexes of Au(I) have shown anti-tumour activity,[33] TrxR inhibition[34] and more focused

studies have proposed that mitochondria are targeted.[35]

Biological evaluation of water–soluble alkynyl–derived Au(I) complexes has also been investigated. Complexes of the general form [Au(C≡CR′)(PR_3)] incorporated a wide variety of alkyl– and aryl–substituted alkynes (for example, where R′ = benzyl, pyridyl, thiazolyl) and were assessed from a cytotoxic perspective using human ovarian cancer cells, with comparison against cisplatin and auranofin. Under biological conditions, the alkyne ligands were prone to substitution reactions with cysteines; incubation with DNA showed no notable interactions or induced damage.[36]

Furthermore a series of bio–inspired mercapto–pteridine appended Au(I) complexes were investigated. Cytotoxic evaluation revealed strong anti-proliferative effects that were comparable to cisplatin. For a given pteridine ligand, the complexes incorporating PPh_3 were most active.[37]

4.1.5 Luminescent Monometallic Au(I) Complexes

The development of organometallic Au(I) species has afforded opportunities in the pursuit of luminescent complexes. The nature of the coordinated ligands dictates the luminescence properties of d^{10} Au(I) complexes. The *5d* frontier orbitals are full and therefore no ligand field excited states are available, however low energy metal centred (MC) transitions (*5d–6s/6p* at *ca.* 250 nm) are accessible.[38] Au(I) can furthermore be both reducing and oxidising and consequently LMCT transitions can also be accessed, commonly with π–acceptor ligands, such as phosphines. These transitions (π_l^*–p_{Au}) are observed at *ca.* 250 nm.[38] Also the propensity of a coordinatively unsaturated Au(I) complex to aggregate through metallophilic interactions can perturb excited states with ligand–centred and/or CT parentage, as well as produce new excited states due to aurophilic interactions.[4]

Supramolecular Au(I) architectures have been generated using 2–pyridineformamide thiosemicarbazone ligands, resulting in a luminescent species (Figure 4.3).[39] The absorption spectra were dominated by ligand–centred n–π^* transitions *ca*. 392 nm. Corresponding solid–state emission spectra were attributed to ligand–centred fluorescence in all cases, which were perturbed to varying degrees by the presence of Au(I) and the existence of any weak Au···Au interactions. This is also true for related thiocarbamoyl–pyrazoline ligands which also showed absorption at 300–350 nm due to a LMCT transition. The series of cytotoxic mercapto–pteridine ligands (Figure 4.2) also

show overlapping ligand–centred and S–to–Au LMCT transitions. The complexes were emissive in solution, displaying visible luminescence assigned to the fluorophore.[37]

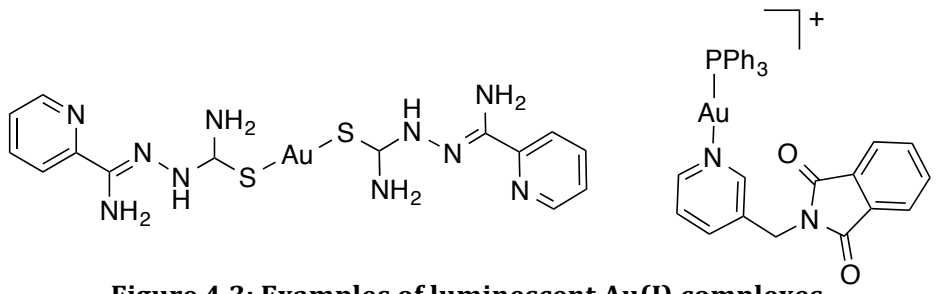

Figure 4.3: Examples of luminescent Au(I) complexes.

Isocyanide Au(I) complexes have been reported using a coordinative tetrafluorophenyl donor that is conjugated to a perylene fluorophore.[40] The emission from the complexes was attributed to the perylene unit in all cases. Short lifetimes typical of perylene–centred fluorescence and notable quantum yields (up to 96%) were observed, suggesting that heavy atom assisted quenching was not evident.

Despite their extensive application in transition metal coordination chemistry, the number of N–heterocycle complexes of Au(I) are relatively few. The simple heteroleptic species $[Au(PPh_3)(C_5H_5N)]^+$ was first reported by Schmidbaur as recently as 2004.[41] A range of homoleptic species $[Au(Py)_2]^+$ (where Py = a 4–substituted pyridine) were reported in 2008, with solid–state luminescent properties strongly dependent upon the nature of the intermolecular Au(I)···Au(I) interactions.[42] Since then (na)phthalimide–derived ligands have been investigated to form complexes of the type $[Au(PR_3)(L)]^+$ (Figure 4.3).[43,44] The emission data generally revealed metal–perturbed ligand–centred fluorescence in all cases, as suggested by literature precedent.

4.1.6 Fluorescence Bioimaging of Au(I) Complexes in Cells

A detailed understanding into the mechanisms of biological action informs the rational design of new therapeutics.[32] However, elucidating the cellular uptake and intracellular distribution of Au(I) complexes is challenging. The developments in the cellular imaging of Au(I) complexes can be embodied in two strategies: i) the functionalisation of Au(I) complexes with fluorescent labels compatible with confocal fluorescence microscopy; and ii) the use of analytical techniques that allow elemental isotopic (*e.g.* ^{197}Au) composition to be mapped. The latter involves destructive methods such as ICP–MS and SR–XRF and has low resolution. [32] It is important to note that the known therapeutic gold complexes sodium aurothiomalate and auranofin do not possess the necessary luminescence

properties to allow confocal fluorescence microscopy. In this context, and in contrast to better known d^6 [45,46] (*e.g.* based on Ru(II),[47] Re(I),[48] Ir(III)[49]) and d^8 (predominantly Pt(II))[50] lumophores which have been more widely applied to cellular imaging, only a small handful of studies have explored the cellular uptake and distribution of various (d^{10}) Au(I) complexes using confocal fluorescence microscopy.

Linear Au(I) complexes incorporating an ancillary phosphine (with varying alkyl/aryl groups) and a thiolated fluorophoric ligand, giving [Au(PR_3)(S-Nap)] (where S–Nap = 4–mercapto–1,8–naphthalic anhydride or N–(N′,N′–dimethylaminoethyl)–1,8–naphthalimide–4–sulfide) have been reported by the Ott Group[51] and confocal fluorescence microscopy imaging of MCF7 cells showed localisation in cell nuclei (Figure 4.4). Supporting cytotoxicity studies showed IC_{50} values of 1.1–3.7 μM for MCF7 cells, which were comparable to those of auranofin (IC_{50} = 1.1 μM) and cisplatin (IC_{50} = 2.0 μM); the free 1,8–naphthalimide ligands were also cytotoxic (IC_{50} = 1.9–4.6 μM).[52]

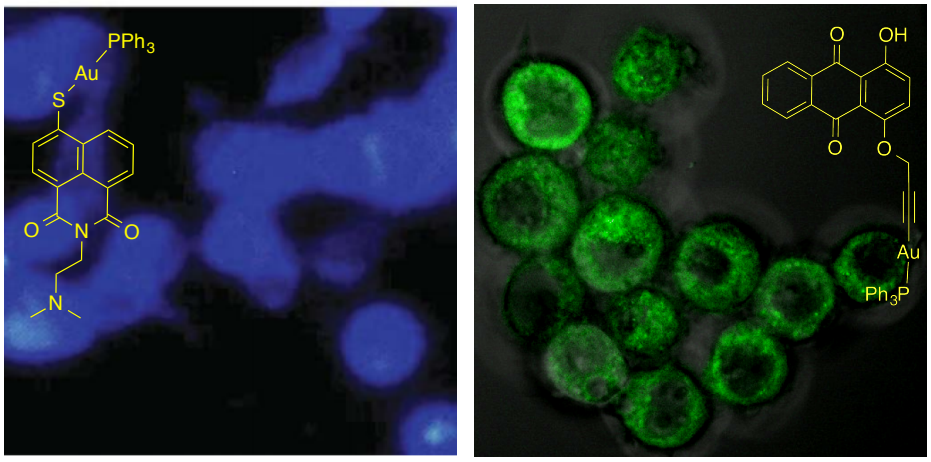

Figure 4.4: Examples of CFM of MCF7 cells using luminescence Au(I) complexes. Cells incubated with; (left) NI species by Bagowski *et al.*[51] and (right) anthraquinone species by Balasingham *et al.*[53]

Water–soluble cyclophane–bridged N–heterocyclic carbene complexes of Au(I) have also found applicability to confocal fluorescence microscopy.[35] The emission properties of the dimetallic Au(I) complexes were biocompatible and cell imaging with RAW264.8 cells revealed good uptake and lysosomal localisation with a mild cytotoxicity (IC_{50} = 52 μM). Recently, alkyne–coordinated Au(I) complexes have been shown to selectively target TrxR.[44] Previously, fluorescent alkynyl–functionalised anthraquinone ligands and their corresponding mono– and dimetallic Au(I) complexes have been applied to cellular studies (Figure 4.4).[53] Confocal fluorescence microscopy revealed that all complexes

showed good uptake (>80 %) with MCF7 cells, showing general cytoplasmic staining but limited evidence for any specific organelle localisation.

With appropriate design, Au(I) complexes have much to offer in the realm of cellular imaging, with the dual opportunities for therapeutic action.[4] Fluorescent Au(I) complexes that are based upon anthracenyl NHC ligands have been shown to lead to oxidation of the thioredoxin system, whilst the anthracene fluorophore enables visualisation of cellular distribution using fluorescence microscopy.[54] In related work, attachment of coumarin fluorophores to the NHC framework also allowed the study of the resultant Au(I) complexes, showing that they inhibit TrxR; fluorescence microscopy showed that the complexes can target the nuclear compartment in tumor cells.[55] Alkynyl derivatives of coumarin have also been described but may not possess the requisite luminescence properties for confocal fluorescence microscopy.[56] On the other hand pairing Au(I) alkyne moieties with luminescent Re(I) can facilitate imaging whilst suggesting cooperative behaviour with respect to biological action.[57]

4.2 Aims

The use of gold-based compounds in medicinal chemistry, known as chrysotherapy,[9-11] has been successfully used to treat inflammatory autoimmune conditions like rheumatoid arthritis.[12,13] A detailed understanding into the mechanisms of biological action informs the rational design of new therapeutics[32] however unravelling the biological action of such species is very challenging.[14] One such approach involves the functionalisation of Au(I) complexes with fluorescent labels compatible with confocal fluorescence microscopy.

This chapter aimed to develop the synthetic chemistry of a range of alkynyl functionalised–naphthalimide ligands highly suited for coordination to Au(I). Once synthesised, all ligands and complexes were spectroscopically and analytically characterised. The species were investigated for their biocompatibility and cytotoxicity against a range of cell lines. This provided data indicating their synthesis, with spectroscopic studies being particularly important for assessing their feasibility towards cell imaging applications. Ultimately the aim was to develop a range of imaging agents highly suited to confocal fluorescence microscopy with potential therapeutic action. The ease at which the naphthalimide ligand can be tuned gave excellent control over the physical and photophysical properties.

4.3 Results and Discussion

4.3.1 Ligand Synthesis and Characterisation

The ligands (**L1–L8**) were synthesised from 4–chloro–1,8–naphthalic anhydride in a one (**L1**) or two step process (Scheme 4.1). Firstly, reaction with propargyl amine in ethanol[58] efficiently yielded the corresponding 4–chloro–1,8–naphthalimide species, **L1**, with consistently high yields (80–90 %). Further functionalisation of this pro–ligand, allowing the tuning of physical and electronic properties, was achieved by heating **L1** with a selection of different amines in DMSO[59] to yield **L2–L8**. The yields obtained for this step were again advantageous (50–80 %), with the exception of **L8** containing the propyl alcohol substituent for which a lower yield was witnessed (35 %).[60] All 4–amino functionalised ligands were bright yellow/orange to the naked eye with **L6** and **L7** appearing fluorescent in the solid form. All ligands were found to be spectroscopically pure after precipitation with diethyl ether or hexane. An attempt was also made to synthesise a ketone variant using 4–piperidone hydrochloride. The reaction was successful once adding stoichiometric base (NEt_3) however this product could not be cleanly isolated. This variant was not further pursued due to the range of amphiphilic nature for **L1–8**.

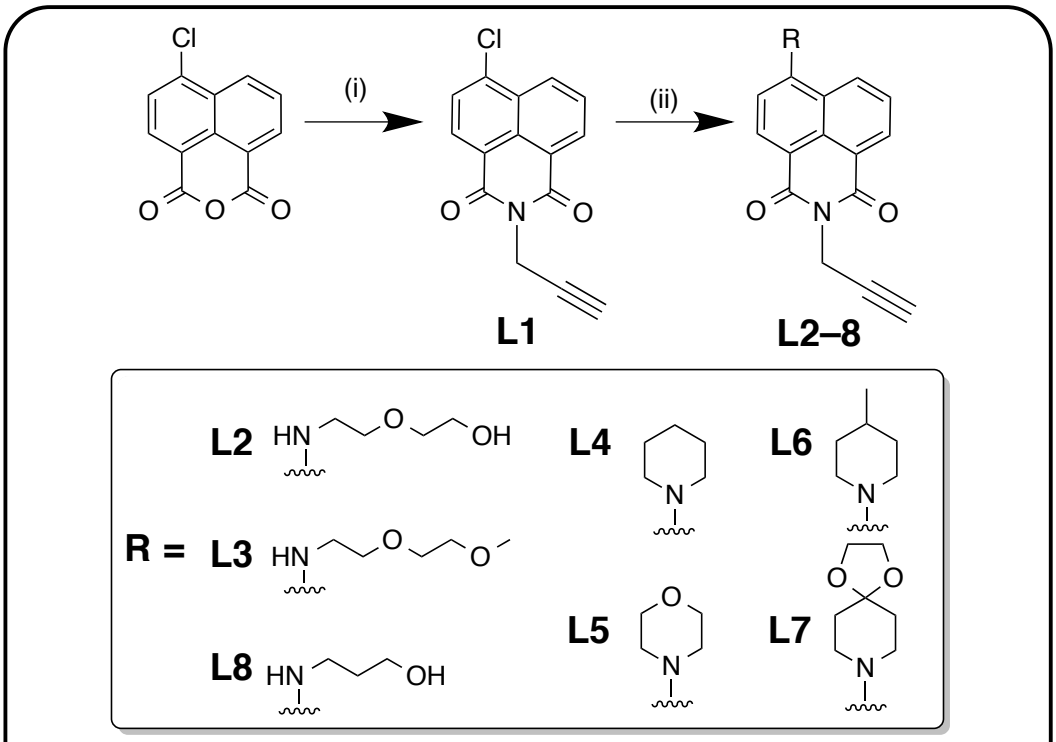

[a](i) propargyl amine, EtOH; (ii) appropriate amine, DMSO.

Scheme 4.1: Synthetic route to the ligands[a].

Ligands **L1** and **L4–5** had been previously reported in the literature however had been synthesised using different techniques, either from the 4–bromo[61] or 4–nitro[62] reagents. Furthermore 4–amino functionalisation was also carried out in different solvents (DMF,[62] 2–methoxyethanol).[61] Data collected for these ligands correlated well with previous reports.

The eight ligands were characterised by ^{1}H NMR spectroscopy (Figure 4.5) and high resolution mass spectrometry (HRMS) studies. Interestingly the methylene group adjacent to the alkyne (δ_H *ca*. 4.95 ppm) showed a $^{4}J_{HH}$ of *ca.* 2.5 Hz caused by coupling to the terminal alkyne proton. The alkyne proton was observed as the corresponding triplet at *ca*. 2.1 ppm. As for Chapters Two and Three, upon 4–amino functionalisation (**L2–8**), there was a significant change in the resonance of the C3–proton.

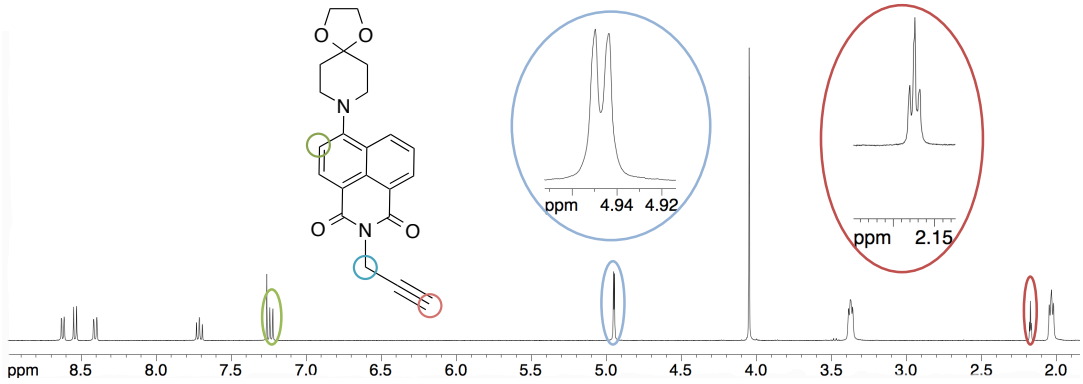

Figure 4.5: ^{1}H NMR spectra ($CDCl_3$, 400 MHz) of L7. Insets of magnified peaks showing the $^{4}J_{HH}$ coupling.

IR spectroscopy was used to distinguish differences in the carbonyl regions and spectra showed two distinct carbonyl peaks at *ca.* 1680 and 1640 cm^{-1}.[63,64] In addition the terminal alkyne C–H bond was observed at 3260–3280 cm^{-1} in all cases.[62] HRMS (ES^{+}) was performed on all novel ligands (**L2–3** and **L6–8**). In all cases the proposed molecular formula was supported, showing the $[M+H]^{+}$ cation peak and also commonly a peak for $[M+MeCN+H]^{+}$.

4.3.2 Complex Synthesis and Characterisation

Firstly the gold precursor complex [AuCl(PPh_3)] was obtained using well established methods from the literature.[65] The first coordination attempt using literature methods[53] (1.1 equivalents of KO^{t}Bu) applied to **L4** was successful. Despite this, subsequent analogous reactions with the other ligand variants proved ineffective. Extensive experimentation was then conducted, varying aspects such as: i) the solvent system to enhance ligand solubility (THF, MeOH[44]); ii) the strength of base in order to remove the

alkyne proton (0.2 M NaOH, 2M KOH[44]); and iii) the reaction time. All such reactions resulted in ligand scrambling with little evidence of successful binding of Au(I) to the alkyne moiety. This was even true when applying conditions from the literature[44] used to form an almost identical complex (Figure 4.6).

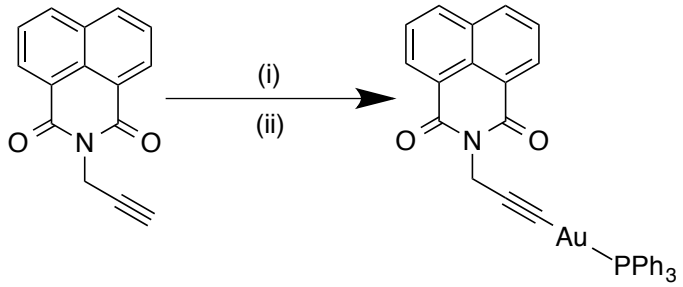

[a](i) 2–4 equiv 2M KOH in MeOH, RT, N_2, 5 mins;
(ii) 1 equiv [AuCl(PPh_3)], RT, N_2, 3 days.

Figure 4.6: Literature synthesis by Ott and co–workers[44] for related NI-Au(I) complex.[a]

At this point it was decided to return to the literature method previously used within the group,[53] however using a fresh batch of KO^{t}Bu. Eventually successful reaction conditions were found for **L1–7** (Scheme 4.2). To generate the corresponding Au(I) complexes an excess of base, added in two aliquots over a period of 48 hours, was generally required for the reaction to proceed to completion. Successful reaction conditions could not be found for **L8** that gave no indication of reaction progression by ^{1}H and ^{31}P NMR spectroscopy. No further work was conducted on **AuL8**.

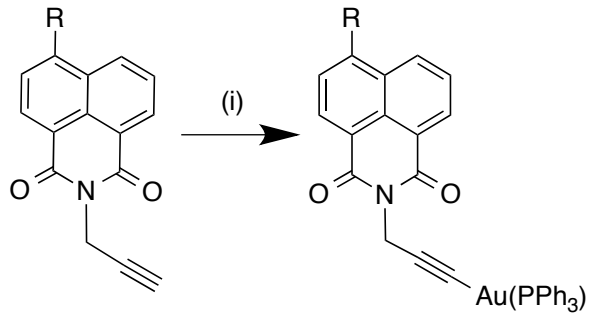

[a](i) [AuCl(PPh_3)], EtOH, 2 x 2 equiv KO^{t}Bu, 48 hrs.

Scheme 4.2: Synthetic route to the complexes.[a]

AuL1–7 were isolated as air stable, light sensitive yellow powders through precipitation with diethyl ether, resulting in yields between 82–100 % with the exception of **AuL4**. **AuL4** was synthesised without the optimised conditions and therefore the observed yield was much lower at 45 %.

The complexes were fully characterised using multinuclear NMR spectroscopy, HRMS and IR studies. $^{31}P\{^{1}H\}$ NMR was particularly useful in confirming the coordination of the alkyne moiety to Au(I), which induced *ca.* +12 ppm shift (relative to $[AuCl(PPh_3)]$) of the single phosphine resonance to around +42 ppm, consistent with related reports on two-coordinate Au(I) species involving alkyne/phosphine donors.[66] Further evidence of σ–bonded terminal Au(I) alkyne coordination came from the ^{1}H NMR spectra that showed an absence of the alkyne proton, and subsequent decoupling of the methylene resonance at *ca.* 5.1 ppm. This latter signal was split into a doublet, apparently attributed to a $^{5}J_{HP}$ coupling of *ca.* 1.5 Hz, providing categorical evidence of the proposed binding mode (Figure 4.7).

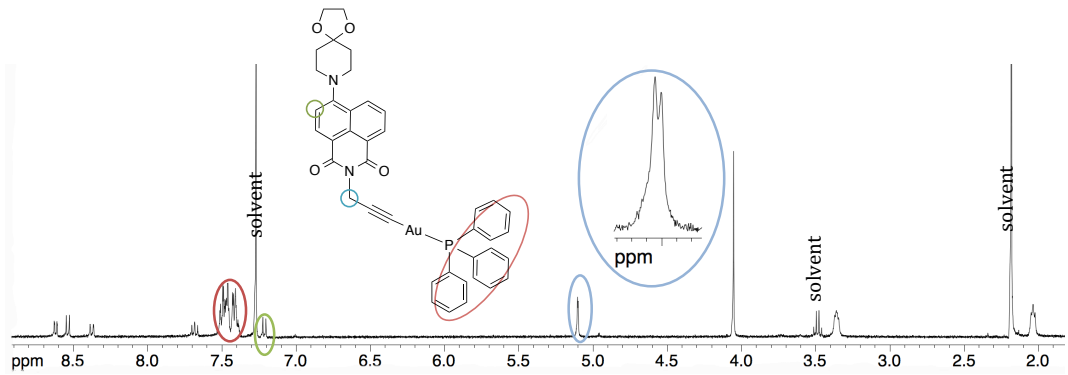

Figure 4.7: ^{1}H NMR spectra ($CDCl_3$, 400 MHz) of AuL7. Insets of magnified peaks showing the $^{5}J_{HP}$ coupling.

Mass spectrometry also proved useful in confirming the proposed structure, as each of the complexes gave peaks for $[M+H]^+$ and also commonly for $[M+Au(PPh_3)]^+$ due to ligand dissociation and recombination. This phenomenon has been seen for other examples in the literature, however for these cases mass spectrometry was not useful because only a peak with m/z = 721 for $[Au(PPh_3)_2]^+$ was observed with the parent ion not being present.[41,43,53]

After the successful formation of **AuL1–7**, that contain triphenylphosphine as the co–ligand, attempts were also made to react the set of ligands to a $[AuCl(P(OPh)_3)]$ precursor. Although these reactions were successful it quickly became apparent that the phosphite analogues were much less stable than their phosphine counterparts. Often after filtration or ^{1}H NMR spectroscopy experiments, grey powders formed indicating the photo–decomposition of AuCl that subsequently disproportionates to elemental, colloidal gold.[38] Henceforth, investigations with the Au(I) phosphite complexes were not continued.

4.3.3 Single Crystal X-ray Diffraction Studies

In addition to the solution–state characterisation, two single crystal structure determinations (Figure 4.8 and Table 4.1) were obtained for **L6** and the corresponding complex, **AuL6**. The crystals were grown from the slow evaporation of a chloroform/hexane solution and a chloroform/acetonitrile solution for **L6** and **AuL6**, respectively. The data collection parameters are shown in Appendix 4.7.1.

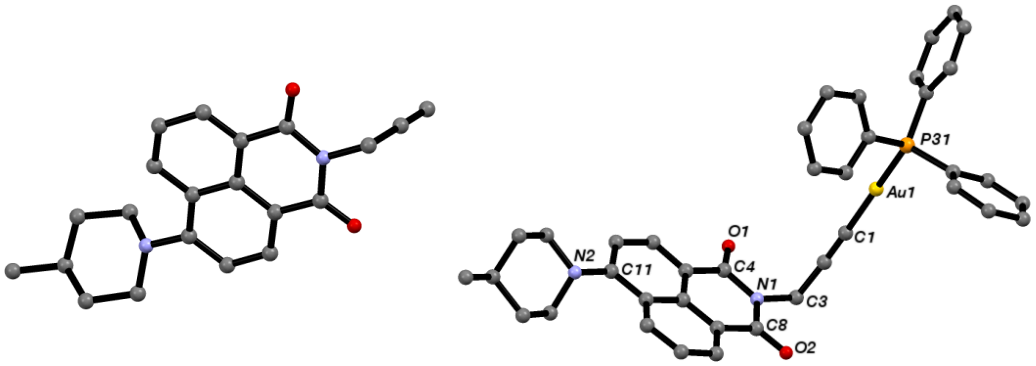

Figure 4.8: X-ray crystal structure of L6 (left) and AuL6 (right) with ellipsoids at 50 % occupancy. Hydrogen atoms omitted for clarity.

Table 4.1: Table of selected bond lengths and bond angles for L1.

Compound	L6	AuL6
Bond Lengths / Å		
C1–H1	0.9500	–
C1–C2	1.183(3)	1.207(4)
C1–Au1	–	1.995(3)
C3–N1	1.4754(19)	1.483(3)
C4–O1	1.222(2)	1.222(3)
C8–O2	1.220(2)	1.220(3)
C11–N2	1.399(2)	1.398(3)
C31–P31	–	1.824(2)
Au1–P31	–	2.2758(7)
Bond Angles / º		
C1–C2–C3	178.4(2)	175.6(3)
C1–Au1–P31	–	169.80(7)
C2–C3–N1	112.62(15)	111.0(2)
C2–C1–Au1	–	167.7(2)

The structure of the ligand showed the anticipated configuration with the piperidine unit twisted out of the plane of the NI core (Figure 4.8).

For the complex, the structure showed the expected two-coordinated Au(I) centre with *d*(Au–C) and *d*(Au–P) at 1.995(3) and 2.2758(7) Å, respectively.[67-70] A notable deviation from ideal linearity was observed across the four–centre C≡C–Au–P moiety, with corresponding bond angles of 169.80(7)° and 167.7(2)° for angles C1–Au1–P31 and C2--C1–Au1, respectively (Table 4.1). Comparison between **L6** and **AuL6** showed that upon coordination the alkyne C≡C bond length increases by *ca.* 0.025 Å, corresponding to a weakening of this bond induced by electron donation to Au(I) for bond formation. In addition the coordination event resulted in an obvious further move away from linearity (*ca.* 3°) of C1–C2–C3. Bond lengths away from the primary coordination sphere (*i.e.* past N1) were not affected by coordination of **L6** to Au(I). For example no difference was witnessed for the carbonyl bond lengths or 4–amino bond.

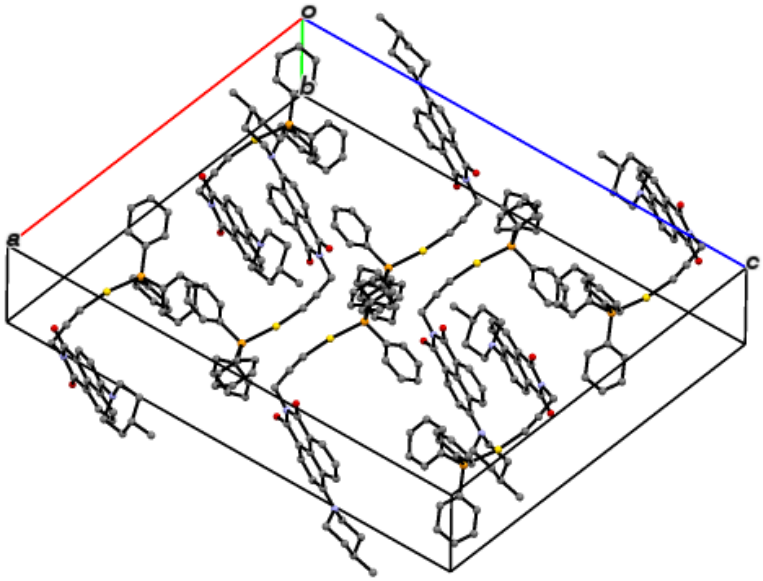

Figure 4.9: X–ray crystallographic packing diagram for AuL6.

In the crystal **AuL6** packed in a tail-to-tail arrangement (Figure 4.9) that allowed neighbouring NI cores to interact through intermolecular π-π stacking with C_{naph}–C_{phen} distances of approximately 3.34-3.57 Å (expected at 3.3–3.8 Å for true π-π stacking).[71,72] This arrangement , however, is not necessarily driven by the stacking but could instead be an artefact of the steric demands of the large Au(I) core and triphenylphosphine co–ligand.

4.3.4 UV–Vis Absorption Spectroscopy

Ligand Properties

The solution absorption spectra of **L1–8** (Table 4.2 and Figure 4.10) were composed of two sets of IL π-π^* transitions between 240-300 nm, associated with both the polyaromatic and alkynyl moiety.[40,53] The lowest energy π-π^* transition possessed strong vibronic structure, demonstrating particularly effective coupling between the vibronic mode of the polyaromatic system and the excited state.[40] A second dominant component was also seen for all ligands, with the exception of **L1**, observed as a broad band centred at 400–430 nm.[73-75] This peak was attributed to ICT character (arising from the electron donating character of the amino substituent and the electron accepting ability of the NI core).[75-79] The tuneability (*ca.* 30 nm) of the ICT peak was found to be dependent on the availability of the lone pair of the 4–amino group. The variable electron donating character of the 4–amino groups modulated the absorption energy of the ICT band. This is a crucial consideration for applications such as cell imaging in that subtle changes in the structure of the amine substituent can induce a shift in the position of the ICT band. For **L2–3** and **L8**, containing aliphatic amino substituents, this resulted in the most bathochromically shifted ICT absorption, which also correlated with the greatest upfield shift of the aromatic proton at the 3–position (*i.e.* adjacent to the amine substituent). **L1** displayed significantly different UV absorption properties, notably the lack of the ICT band and a large bathochromic shift of the π-π^* bands.

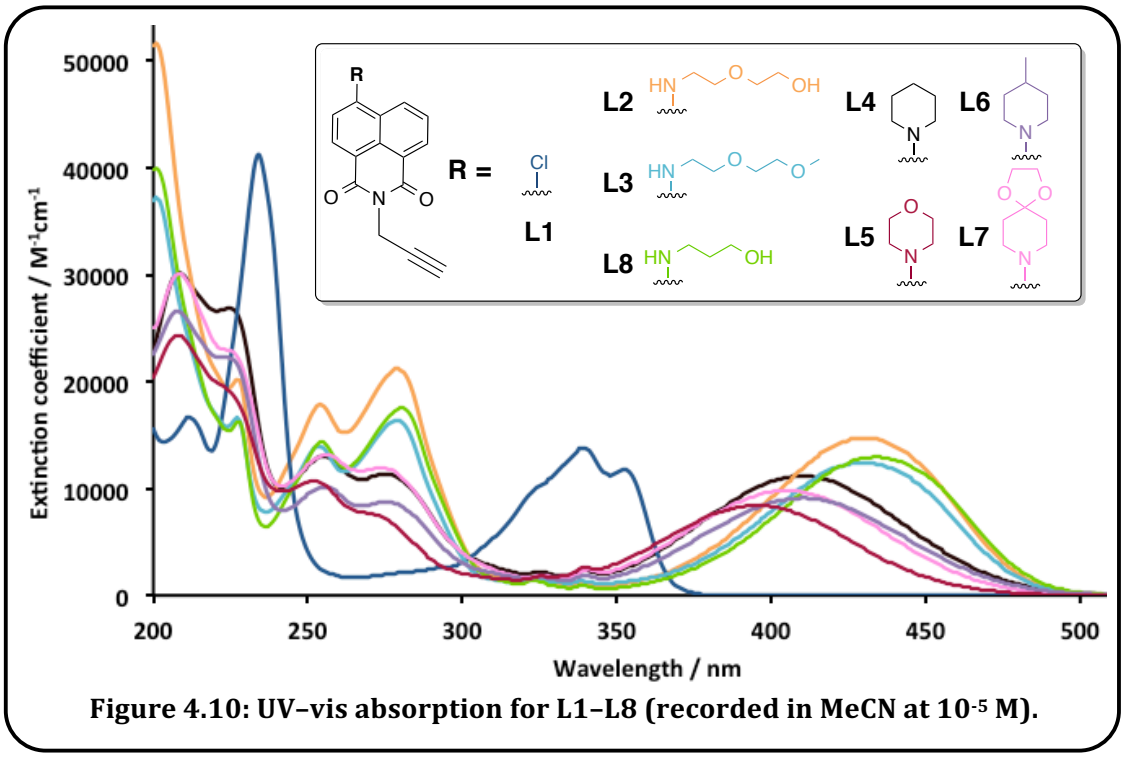

Figure 4.10: UV–vis absorption for L1–L8 (recorded in MeCN at 10^{-5} M).

Complex Properties

The absorption spectra of **AuL1–7** were dominated by ligand character (Table 4.2).[40,53] This was particularly true when considering the ICT transition which showed only a slight hypsochromic shift (0–3 nm) upon coordination[60] to Au(I). All Au(I) complexes experienced larger extinction coefficients for the π–π^* transitions <300 nm when compared to the free ligands due to the presence of multiple phenyl chromophores associated with the Au(PPh_3) unit.[53] Au–alkynyl species have previously shown metal–to–alkynyl MLCT transitions centred around 300–400 nm,[80] however in the case of **AuL1-7**, these transitions do not appear to be present. This is not surprising when considering the d^{10} configuration of Au(I). π_l^*–p_{Au} and MC transitions, which would overlap the ligand based π–π^* transitions,[38] could offer further reason for the larger extinction coefficients of the Au(I) complexes <300 nm, when compared to the free ligands.

Table 4.2: Absorption properties of the ligands and complexes.

Structure	λ_{max} / nm (ε / $M^{-1}cm^{-1}$)[a]	
	Ligand	**Complex**
L1	353 (11600)	353 (7600)
L2	429 (14400)	429 (5400)
L3	430 (12400)	428 (8700)
L4	410 (11100)	408 (8300)
L5	396 (8300)	393 (8900)
L6	410 (9000)	407 (5300)
L7	403 (9700)	400 (8500)
L8	434 (12900)	–

[a] 10^{-5} M MeCN.

4.3.5 Luminescence Spectroscopy

Ligand Properties

Solutions of **L2–8** were also found to be highly fluorescent (Table 4.3). When using an excitation wavelength of 385–430 nm on aerated MeCN solutions of the ligands, a visible broad emission band at *ca.* 520 nm was observed[51] (Figure 4.11), typical of ICT NI fluorophores. The advantageous Stokes' shifts were greatest for the piperidine and morpholine substituted ligands/complexes (up to 77000 cm^{-1}) and consistent with an excited state dominated by ICT character. It is notable that very subtle changes in the substituted amine (*e.g.* **L4** *versus* **L5**) induced measureable changes in emission maxima. **L2–8** showed moderate tuneability of the emission (*ca.* 15 nm), agreeing well with related

studies by Bagowski *et al*.[51] Their studies revealed that the luminescence was not affected by the phosphine substituents, but instead only by variation of the NI substituent.

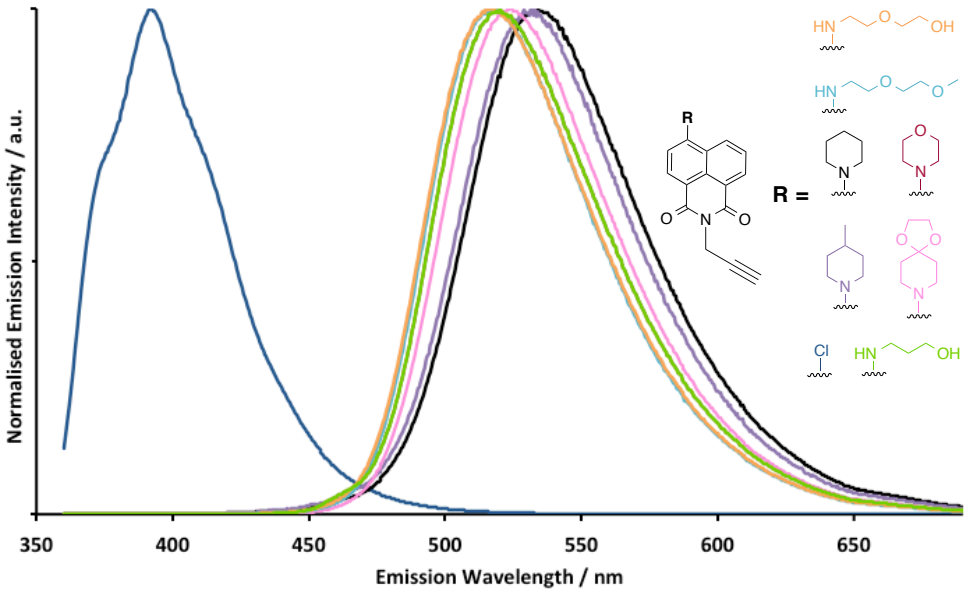

Figure 4.11: Emission profiles for the ligands recorded in MeCN (using λ_{exc} = 415 nm).

Supporting time–resolved measurements revealed lifetimes <11 ns that were indicative of fluorescence (Table 4.3). These observations are also consistent with previous work on this class of chromophore[60] reported in Chapter 3 and by others,[81] showing that the ICT fluorescent character is imparted by the presence of a donor group at the NI core.

Further studies on the solvent dependence of the emission properties were investigated using the most hydrophilic derivative, **L2**, which facilitated comparative studies across a range of solvents, including water. Both steady state and lifetime measurements were obtained in a range of solvents (ethyl acetate, dichloromethane, chloroform, acetone, ethanol, methanol, dimethyl sulfoxide, water) of varying polarity. The results showed a highly solvent–dependent[51] 50 nm shift in the emission maximum across the solvent range (Figure 4.12). The most polar solvent induced the largest bathochromic shift of the fluorescence, thus indicating a positive solvatochromism associated with the ICT state. The lifetimes also showed considerable variation across the solvent range (2.8 ns in water *versus* 8.2 ns in ethylacetate), suggestive that such chromophores may be applicable to fluorescence lifetime imaging microscopy (FLIM) when regarding localisation in lipo–*versus* hydrophilic cellular compartments. It is also important to note that **L2** retained its advantageous fluorescence properties in aqueous solution, suggesting good compatibility with biological environments and amenability with further confocal microscopy studies.

Overall it appears that PeT, which can account for significant quenching in amino–substituted NI chromophores,[82-84] is not problematic in these systems.

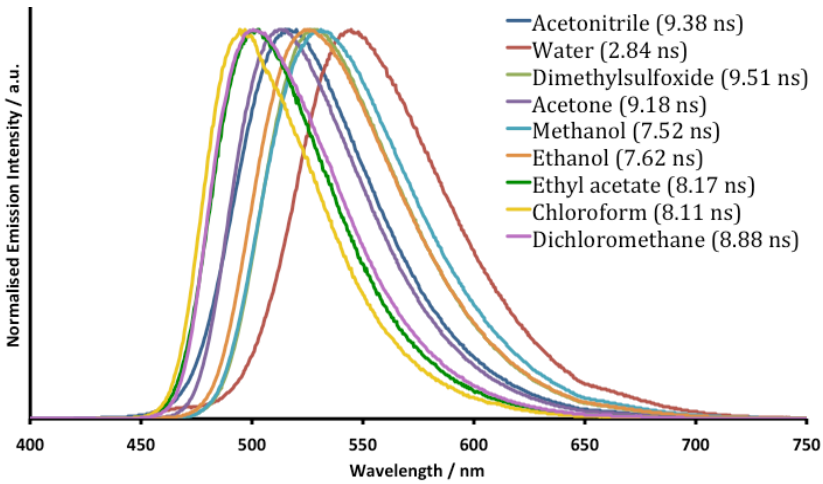

Figure 4.12: Emission data for L2 in different solvents (λ_{exc} = 415 nm) with corresponding lifetimes (λ_{exc} = 372 nm) in parentheses.

Complex Properties

Table 4.3: Emission properties of the complexes (ligand values in parentheses).

Complex	λ_{em} / nm[a,b]	τ / ns[a,c]	Φ [d]
Au-L1	391 (392)	-[e] (3.0)	< 0.01
Au-L2	514 (517)	10.1 (9.4)	0.50
Au-L3	515 (518)	10.0 (10.4)	0.60
Au-L4	532 (535)	1.2 (0.7)	0.06
Au-L5	523 (526)	5.7 (3.8)	0.60
Au-L6	530 (531)	1.2, 2.6 (0.6, 3.7)	0.11
Au-L7	521 (524)	4.7 (2.3, 3.5)	0.22

[a] 10^{-5} M MeCN; [b] λ_{ex} = 415 nm; [c] λ_{ex} = 295 nm or 372 nm; [d] in aerated MeCN; [e] too weak.

Upon coordination to Au(I), each of the ligands retained their characteristic luminescence properties[43] (Table 4.3 and Figure 4.13) with a slight hypsochromic shift (*ca.* 3 nm) for the emission maxima. Therefore the emission characteristics were highly ligand dominated as seen for other Au(I) species with appended chromophores.[40,53] Relative to the free ligands, fluorescence lifetimes were generally extended for the complexes, whilst the quantum yields were wide–ranging in aerated solution, but up to *ca*. 60% for the most emissive examples. The data suggests that a bathochromic shift in λ_{em} was generally accompanied by a significant reduction in quantum yield and lifetime. Furthermore no evidence of Au(I)

heavy atom assisted long–lived $M_{Au}L_{alkynyl}CT$ phosphoresence[38] was observed in either the steady state or time dependent luminescence studies.[53]

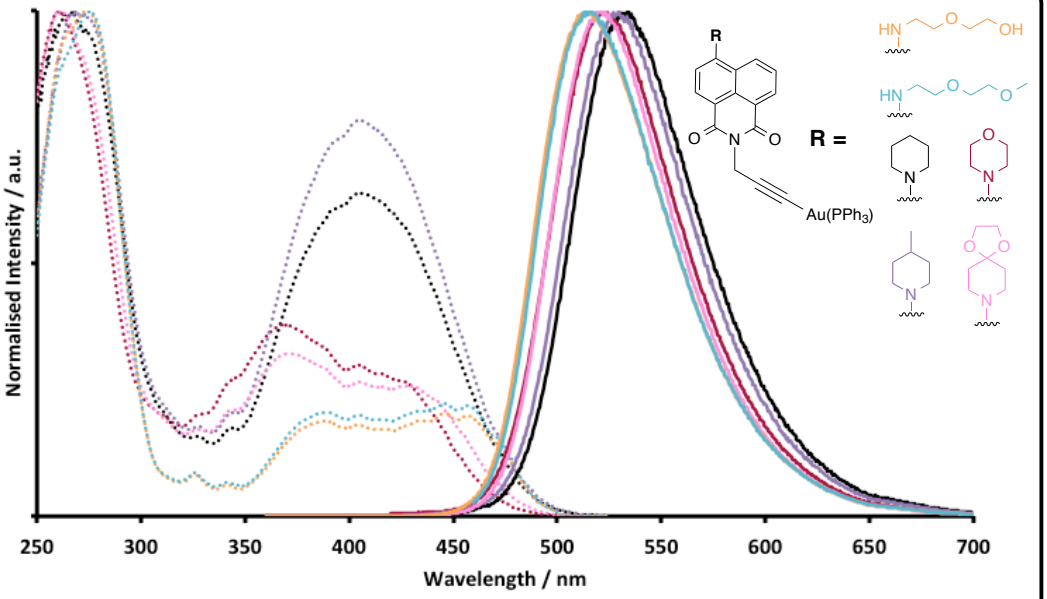

Figure 4.13: Excitation (dashed) and emission (solid) profiles for selected complexes (recorded in MeCN using λ_{exc} = 415 nm, λ_{em} = 535 nm).

4.3.6 Cytotoxicity Studies

Prior to microscopy studies, the ligands and complexes were assessed for cytotoxicity effects using the standard MTT assay against MCF7 (breast adenocarcinoma), A549 (lung adenocarcinoma), PC3 (prostate adenocarcinoma), LOVO (colon adenocarcinoma) and HEK cell lines. IC_{50} values for these compounds are shown in Table 4.4 and graphically represented for **AuL1–7** in Figure 4.14. The compounds were initially dissolved in DMSO and doses of 0.1, 1, 10 and 100 μM were tested to screen the activity of different concentrations whilst comparing to a control medium with no treatment.

Firstly, it was clear that the Au(I) complexes were significantly more toxic than the corresponding free ligands, an observation previously noted with Au(I) complexes of alkynyl–anthraquinone ligands[53] and other alkynyl containing species.[44] This also correlated with the relatively enhanced lipophilicities of the complexes (presumably *via* the coordinated PPh_3 ligand), which was supported by calculated partition coefficient $logP_{calc}$ values (see Section 4.3.7: Confocal Fluorescence Microscopy). Secondly, all compounds were more toxic to HEK cells than the cancer cell lines. However the cytotoxicity values of **AuL1–7** were not particularly low (*e.g.* $AuCl(PPh_3)$ IC_{50} = 2.6 μM,[53] cisplatin = 2.0 μM[85] in MCF7 cells).

Table 4.4: Cytotoxicity IC_{50} (μM) values of the ligands and complexes.[a]

	LOVO	A549	PC3	MCF7	HEK
L1	76.21 (8.36)	>100	>100	>100	22.68 (7.51)
L2	57.56 (1.91)	>100	>100	66.16 (1.19)	35.25 (1.52)
L3	>100	>100	>100	>100	28.42 (6.95)
L4	>100	>100	>100	>100	7.11 (1.75)
L5	>100	>100	>100	>100	>100
L6	>100	>100	>100	>100	3.14 (0.75)
L7	>100	>100	>100	>100	6.61 (0.63)
AuL1	>100	>100	>100	>100	8.02 (1.03)
AuL2	5.88 (0.72)	41.84 (6.57)	6.76 (0.88)	6.85 (0.75)	4.41 (0.55)
AuL3	5.12 (0.62)	51.96 (5.77)	8.26 (1.07)	6.23 (0.55)	0.77 (0.07)
AuL4	39.73 (5.92)	>100	45.35 (12.19)	59.02 (1.64)	6.65 (1.04)
AuL5	10.32 (1.00)	>100	39.86 (9.58)	49.41 (8.51)	3.87 (0.77)
AuL6	>100	>100	>100	68.34 (4.96)	9.53 (3.13)
AuL7	34.47 (5.16)	89.92 (5.72)	69.26 (4.91)	8.88 (0.14)	3.56 (0.25)

[a] using MTT assay; standard deviation given in parentheses.

For the ligands, chloro–derived **L1** showed some selectivity for LOVO among the cancer cell lines, whilst the glycol variant **L2** was also inhibitive to MCF7. In general the ligands only possessed low cytotoxicity. This correlates well with literature compounds where moderate or high cytotoxicity of NI based ligands (1.9–4.6 μM) is generally only observed when the fluorophore contains a sulfur residue[51,85] or pharmacore for proper DNA interaction.[61]

The complexes possessing the glycol appended substituted amine, **AuL2** and **AuL3**, appeared most potent, whilst **AuL6** showed some selectivity for MCF7 (cell line with higher mitochondrial mass[53]) over the other cancer cell lines as seen for other related examples in the literature[44,53] (Figure 4.14). The majority of cytotoxicity values for the range of Au(I) complexes across the cell lines falls within the region of established related drugs, such as auranofin (2.6 and 1.1 μM to HT27 and MCF7 cells, respectively)[51] and amonafide (4.7 and 1.1 μM to HT27 and MCF7 cells, respectively).[85] Importantly, the stability of the Au(I) complexes in d_6-DMSO was determined using ^{31}P NMR spectroscopy, which showed (for 96 hours at 37°C) only trace levels of either Ph_3P or Ph_3PO, suggesting that ligand displacement is not problematic under such conditions and complexes remain intact. The improved cytotoxicity of the complexes over the free ligands showed that the

cytotoxicity is due to the introduction of the Au(I)–alkynyl unit rather than the inherent biological activity of the NI ligands. However the appended ligand is still key in delivering the photophysical, uptake and localisation characteristics of the complexes.

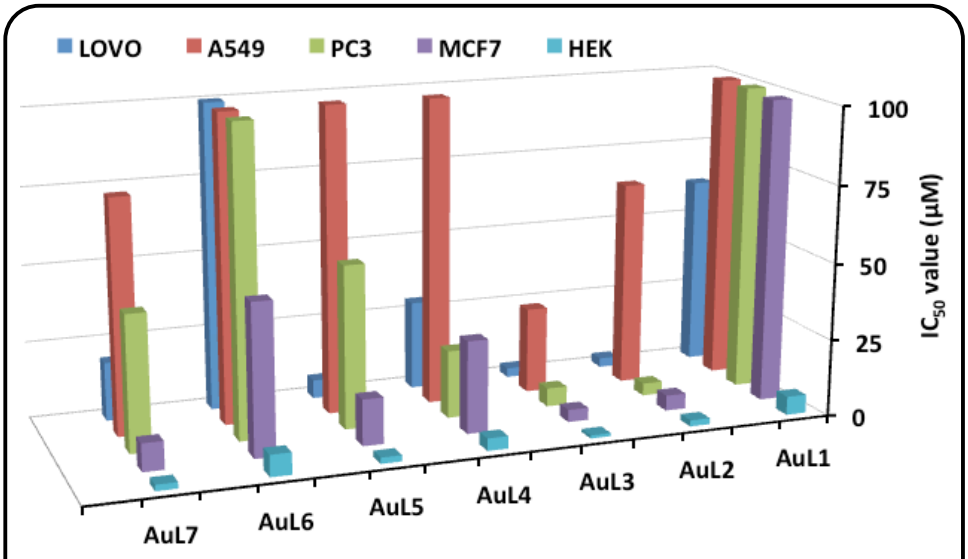

Figure 4.14: Graphical representation of the cytotoxicity of AuL1–7 to various cell lines.

4.3.7 Confocal Fluorescence Microscopy

Confocal fluorescence microscopy was performed using both HEK cells and the protistan fish parasite *Spironucleus vortens* (*S. vortens*). The fluorescent compounds used for imaging studies were added as 3–10 mM solutions in DMSO, with the final concentration on the slide reduced 10–fold. Imaging work showed that the NI ligands were capable of providing bright fluorescence signals even in polar solvent environments, as evidenced by the spectroscopic studies. In all cases an excitation wavelength of 405 nm was used together with a detection wavelength between 530-580 nm. Ligands **L2** ($logP_{calc}$ = 1.285), **L3** ($logP_{calc}$ = 1.807), **L5** ($logP_{calc}$ = 2.117) and **L7** ($logP_{calc}$ = 2.549) and their corresponding complexes **AuL2** ($logP_{calc}$ = 3.757), **AuL3** ($logP_{calc}$ = 4.280), **AuL5** ($logP_{calc}$ = 4.590) and **AuL7** ($logP_{calc}$ = 5.022),[86] which possess structural variance and increasing lipophilicities across the range, were selected for imaging studies.

Ligand Properties

In general, uptake into HEK cells was slow, and in a number of cases insufficient to allow quality images to be obtained. The morpholine derivative, **L5**, gave the brightest images with clear staining of both the plasma and nuclear membranes, including some background nuclear fluorescence (Figure 4.15). **L5** also showed very distinct localisation with high intensity punctate fluorescence suggestive of organelle staining/uptake,

suggestive of mitochondria.[87] The ligands, **L2**, **L3** and **L7** showed varied uptake for the HEK cells with relatively only weak fluorescent signals (Figure 4.15).

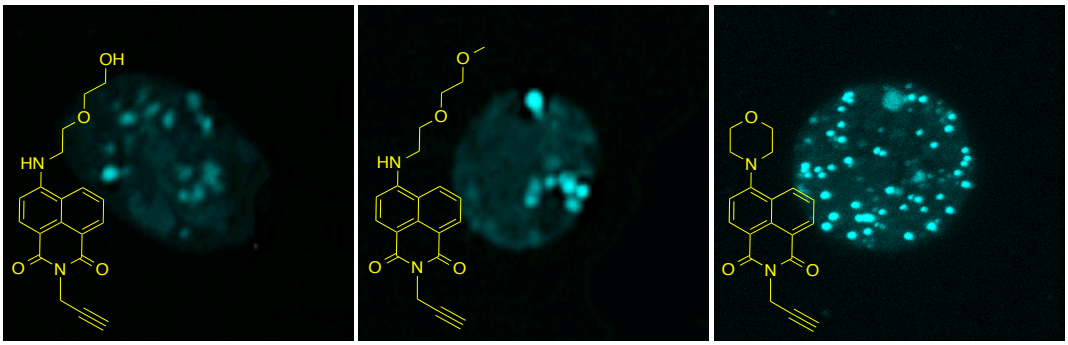

Figure 4.15: Fluorescence microscopy of HEK cells imaged with (left to right): L2 then L3, both showing relatively weak uptake and signal, and L5, showing localised signals (λ_{exc} = 405 nm, λ_{em} = 535 nm). Cells incubated with 100 μgmL^{-1} of lumophore.

Imaging experiments were also undertaken with the fish parasite, *S. vortens*[88] using the same selection of probes (Figure 4.16). Firstly, much better uptake was generally observed compared to the HEK cell work, and no evidence of compound toxicity was witnessed throughout the duration of the studies on *S. vortens* (2-3 hour period).[89,89]

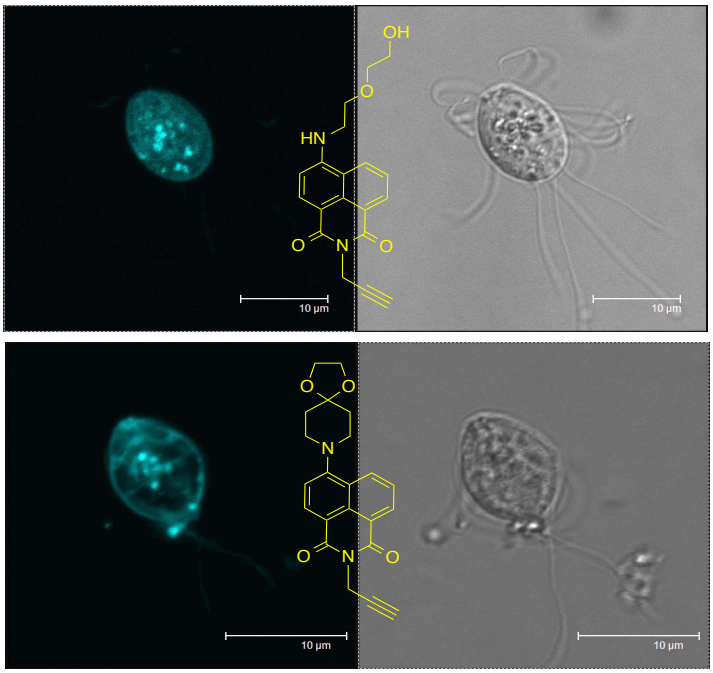

Figure 4.16: Microscope images of *S. vortens* imaged with (top): fluorescence from L2 (cytosol and hydrogenosomal staining) and transmitted light, (bottom): fluorescence of L7 (hydrogensomal and faint nuclear staining) and transmitted light. (λ_{exc} = 405 nm, λ_{em} = 535 nm). Cells incubated with 100 μgmL^{-1} of lumophore.

L2 showed specific hydrogenosome (organelles related to mitochondria[90-92]) staining and faint nuclear fluorescence, albeit with a stronger background of cytosol staining[73] than the other free ligands. The ketal derivative, **L7**, produced excellent images at significantly reduced (60-75%) laser power, staining the plasma and nuclear membrane, with very bright hydrogenosomes and larger lipid droplets, as well as some faint flagella staining (Figure 4.16). Lastly, **L5** again very specifically stained hydrogenosomes, with significantly reduced cytosol staining compared to **L2**.

Complex properties

The complexes **AuL2** and **AuL7** showed very limited uptake, even after 30 minutes. Uptake into HEK cells was best demonstrated using **AuL5**; the imaged cells showed staining of filapodia (fine protuberances from the cell surface) and various internal organelles and glycogen vacuoles (Figure 4.17).

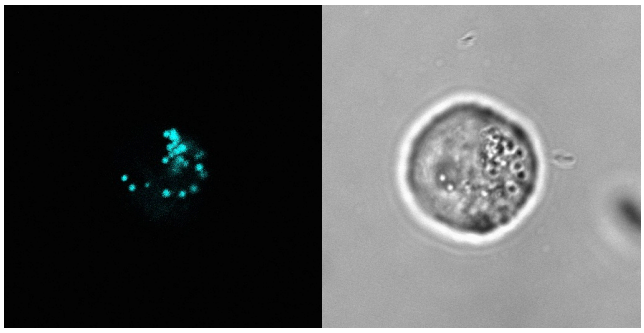

Figure 4.17: Microscopy of HEK cell imaged with AuL5 using fluorescence (left; = λ_{exc} 405 nm, λ_{em} = 535 nm) and transmitted light (right).

The methoxy glycol derivative, **AuL3**, showed slow uptake, but still produced good quality images after 55 mins. The fluorochrome was incorporated within ring shaped structures at the cell surface (possibly indicative of an apoptotic event, membrane blebs or autophagosomes), as well as general membrane structures and lipid rich areas (Figure 4.18). Comparative images using the commercial stain TMRE, which selectively targets mitochondria, showed excellent separation of the fluorophore signals (TMRE *vs.* **AuL3**) and a clear area of co–localisation (Figure 4.18) suggesting **AuL3** has some affinity for mitochondrial rich environments. This contrasts with the biodistribution into the nuclei of MCF7 cells demonstrated by the Au(I) complexes[93] of sulfur–substituted naphthalimide ligands by Ott and co–workers.[51,52,85] Many of the examples by Ott and co–workers also had a significant degree of photobleaching that resulted in signal loss after 2–4 minutes of irradiation.[85] This was not experienced for **AuL1–7**.

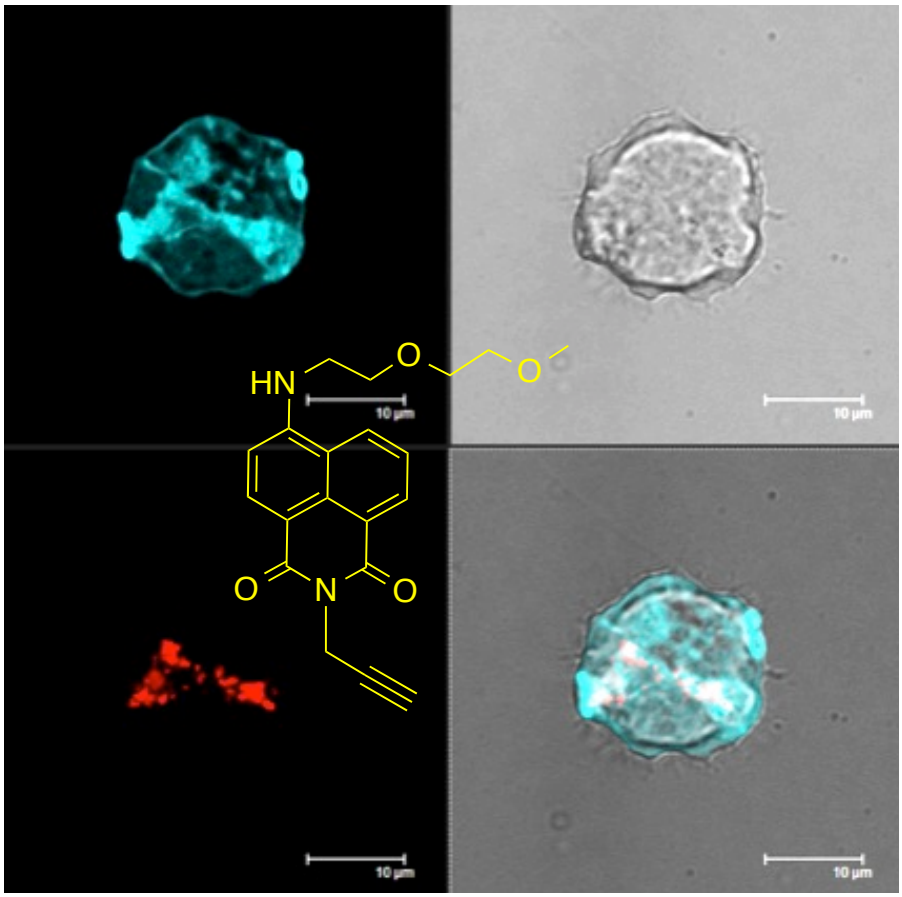

Figure 4.18: Microscope images of HEK cells incubated with AuL3 and TMRE showing (clockwise from top left): fluorescence from AuL3 (λ_{exc} = 488 nm, λ_{em} = 535 nm), transmitted light image, overlaid images showing degree of co–localisation, fluorescence from TMRE (λ_{exc} = 543 nm, λ_{em} = 600 nm. Cells incubated with 100µgmL^{-1} of lumophore.

Interestingly, despite the excellent results obtained with **L5**, **AuL5** showed very limited uptake into *S. vortens*; this observation also contrasts with the favourable uptake of **AuL5** by HEK cells. Conversely, **AuL7**, which showed poor uptake in HEK cells, showed excellent uptake by *S. vortens*. The images obtained with **AuL7** showed very brightly localised spots (Figure 4.19) of fluorescence consistent with hydrogenosome staining together with labelling of larger lipid droplets. **AuL2** again showed limited uptake, whilst **AuL3** produced good quality images (Figure 4.19) which facilitated further co–localisation analyses using TMRE and CTC (5-cyano-2,3-ditolyltetrazolium chloride).

The imaging results presented clear evidence of the biocompatible utility of the substituted naphthalimide fluorophores towards cell imaging using confocal fluorescence microscopy. For the ligands the morpholine substituent (**L5**) imparted very favourable characteristics, enhancing uptake and enabling some distinct localisation patterns. It was

evident that incorporating these ligands into the gold complexes enhanced their lipophilicity, but also led to very different behaviour (both for imaging and cytotoxicity). The uptake of the complexes into HEK cells seemed to correlate with the predicted lipophilicities *i.e.* the more lipophilic species (*e.g.* **L5**, **AuL5**) showed the best uptake; however, this does not seem to be the case with the *S. vortens* studies. Importantly, it appeared that the specific nature of the amine substituent could be used to tune the imaging capability, specifically uptake and localisation, of the probes. Very basic changes to the ligand structure (*e.g.* **L2** *versus* **L3**) had a profound influence upon the imaging capability of a given probe.

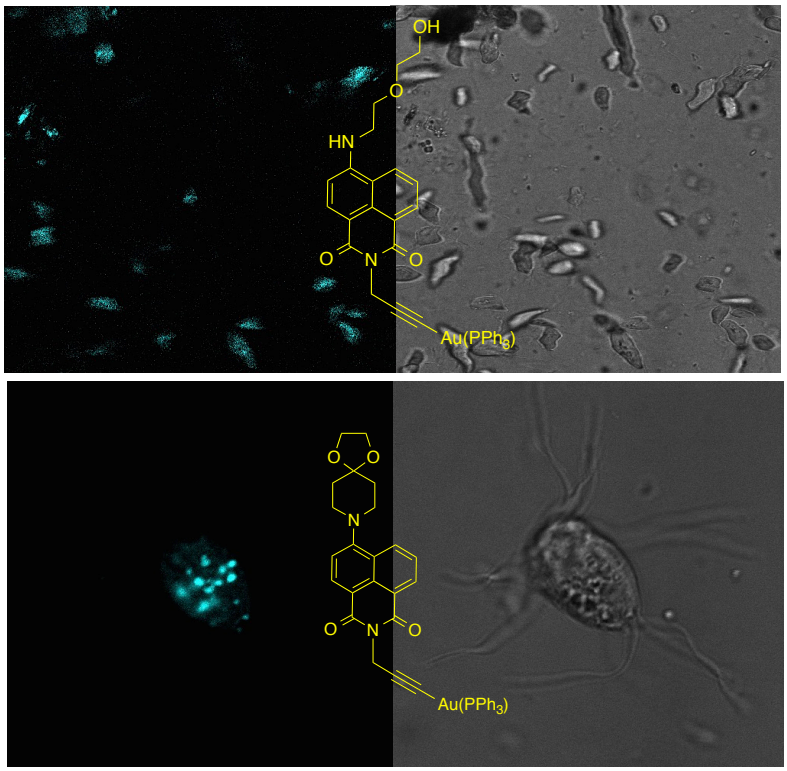

Figure 4.19: Microscope images of *S. vortens* imaged with (top): fluorescence from AuL3 and transmitted light in wide field view; (bottom): fluorescence of AuL7 (hydrogensomal and lipid droplet staining) and transmitted light. (λ_{exc} = 405 nm, λ_{em} = 535 nm). Cells incubated with 100 μgmL^{-1} of lumophore.

4.4 Conclusion

This chapter has described the synthetic development of an alkynyl-derived series of 1,8–NI fluorophores, generating eight new ligands that were successfully utilised for Au(I) coordination chemistry, with the exception of **L8**. The structural variants seek to address the balance between hydro– and lipophilic character.

The optical properties of the fluorophores were dictated by ligand-centred, ICT-dominated transitions that provide visible absorption and emission characteristics, the latter often associated with lifetimes up to *ca.* 10 ns and quantum yields in excess of 50 %.

Cytotoxicity assessments revealed that all compounds were more toxic to the HEK cells than a variety of cancer cell lines, and that the Au(I) complexes were generally more toxic than the corresponding ligands.

Cellular imaging studies were conducted on both HEK cells and *Spironucleus vortens* and showed the comparative imaging capabilities of selected ligands and complexes. The specific cellular uptake and localisation characteristics were seen to be controlled by the nature of the molecular structure, with remarkably contrasting uptake behaviour between ligand/complex pairs. The more lipophilic fluorophores (*e.g.* **L5**) showed a tendency for localisation in subcellular environments such as mitochondria (HEK) and hydrogenosomes (*S. vortens*).

4.5 Experimental Section

4.5.1 Diffraction Data Collection, Processing, Structure Analysis and Refinement

Data collection, refinement and structure solution was conducted by Dr Peter Horton at the UK National Crystallography Service, Southampton.

Suitable crystals were selected and measured following a standard method[94] on a *Rigaku AFC12* goniometer equipped with an enhanced sensitivity (HG) *Saturn724+* detector mounted at the window of a *FR-E+ SuperBright* molybdenum rotating anode generator with VHF *Varimax* optics (70μm focus) at 100K. Cell determination, data collection, reduction, cell refinement and absorption correction carried out using *CrystalClear-SM Expert 3.1b27* (Rigaku, 2013). Structures solved using *SUPERFLIP*[95] and refined using *SHELXL-2013*.[96] CCDC reference numbers 1056114 **L6** and 1056115 **AuL6**, contains the supplementary crystallographic data for this chapter. These data can be obtained free of charge from the Cambridge Crystallographic Data Centre.

4.5.2 Cell incubation and confocal microscopy

Undertaken by collaborators within the Lloyd and Hayes groups in BIOSCI at Cardiff University.

The human embryonic kidney cell line HEK293–EBNA (Invitrogen) were maintained in Dulbecco's Modification of Eagle Medium (DMEM) supplemented with 10% Foetal bovine serum, penicillin, streptomycin and 250 μg mL^{-1} G418. Cells were detached by tapping the side of the tissue culture flasks. The homogenous cell suspension was then distributed into 1 mL aliquots with each aliquot being subject to incubation with a different lumophore. Lumophores were initially dissolved in DMSO (5 $mgmL^{-1}$) before being added to the cell suspensions, final concentration 100 μg mL^{-1}, before incubation at 20° C for 30 min. Cells were finally washed in phosphate buffer saline (PBS, pH 7.2) removing lumophore from the medium then harvested by centrifugation (5 min, 800 g) and mounted on a slide for imaging. *S. vortens*, ATCC 50386, trophozoites were maintained in Keister's modified TYI–S–33 medium without bile supplement as described previously.[97] Trophozoites were incubated at 23–24 °C and routinely subcultured at 24–48 h intervals by transferring 500 μL of an inverted log-phase culture into 10 mL of culture medium, leaving a 5 mL head space in 15 mL screw capped Falcon tubes (Greiner Bio-one). Parasite viability was monitored according to cell motility and visual estimation of cell density by phase contrast microscopy. When accurate cell counts were necessary, trophozoites were fixed in 1.5 % formaldehyde and counted using an Improved Neubauer haemocytometer (Weber

Scientific International). To ensure axenic maintenance, cultures were regularly monitored for microbial contamination by plating-out 100 µL of an exponentially growing culture on TYI–S–33 agar (0.5%, w/v) and incubating under the above conditions for 5 days. Cell preparations were viewed by epifluorescence and transmitted light (Nomarski differential interference contrast optics) using a Leica TCS SP2 AOBS confocal laser microscope (Leica, Germany) using ×63 or ×100 objectives. Excitation of the lumophore was at 405 nm and detection between 530 and 580 nm.

4.5.3 Cytotoxicity assessment *via* MTT assay

Undertaken by Mr Huw Mottram in Pharmacy at Cardiff University.

The cytotoxicity of the complexes was assessed using the colourimetic and quantitative MTT [3–(4,5–dimethylthiazol–2–yl)–2,5–diphenyltetrazolium bromide] assay, first reported by Mosmann.[98] Quantification was achieved using a multi-well scanning spectrophotometer and reported as an IC_{50} value.

4.5.4 Method for cytotoxicity analysis

Anti-tumour evaluation in MCF7, LOVO, A549 and PC3 cell lines was performed by MTT assay. Compounds were prepared as 0.1–100 mM stock solutions dissolved in DMSO and stored at –20 °C. Cells were seeded into 96–well microtitre plates at a density of 5×10^3 cells per well and allowed 24 hours to adhere. Decimal compound dilutions were prepared in medium immediately prior to each assay (final concentration 0.1–100 µM). Experimental medium was DMEM +10 % FCS (PC3 and Lovo) or RPMI +10 % heat inactivated FCS (A549 and MCF7). Following 96 hours compound exposure at 37 °C, 5 % CO_2, MTT reagent (Sigma Aldrich) was added to each well (final concentration 0.5 $mgmL^{-1}$). Incubation at 37 °C for 4 hours allowed reduction of MTT by viable cells to an insoluble formazan product. MTT was removed and formazan solubilised by addition of 10 % Triton X-100 in PBS. Absorbance was read on a Tecan Sunrise spectrophotometer at 540 nm as a measure of cell viability; thus inhibition relative to control was determined (IC_{50}) from four independent sets of data.

4.5.5 General

^1H, $^{13}C\{^1H\}$ and $^{31}P\{^1H\}$ NMR spectra were recorded on an NMR-FT Bruker 400 MHz or Jeol Eclipse 300 MHz spectrometer and recorded in $CDCl_3$. ^1H, $^{13}C\{^1H\}$ and $^{31}P\{^1H\}$ NMR chemical shifts (δ) were determined relative to residual solvent peaks with digital locking and are given in ppm. Low-resolution mass spectra were obtained by the staff at Cardiff University using a Waters LCT Premier XE mass spectrometer. High-resolution mass

spectra were carried out at the EPSRC National Mass Spectrometry Facility at Swansea University. UV–Vis studies were performed on a Jasco V-570 spectrophotometer as MeCN solutions (2.5 or 5 × 10^{-5} M). Photophysical data were obtained on a JobinYvon–Horiba Fluorolog spectrometer fitted with a JY TBX picoseconds photodetection module as MeCN solutions. Emission spectra were uncorrected and excitation spectra were instrument corrected. Quantum yields using $[Ru(bpy)_3](PF_6)_2$ in aerated MeCN as a standard (Φ_{em} = 0.016).[99,100] The pulsed source was a Nano–LED configured for 295 or 372 nm output operating at 1 MHz. Luminescence lifetime profiles were obtained using the JobinYvon–Horiba FluoroHub single photon counting module and the data fits yielded the lifetime values using the provided DAS6 deconvolution software.

All reactions were performed with the use of vacuum line and Schlenk techniques. Reagents were commercial grade and were used without further purification. 2-(2-methoxyethoxy)ethanamine was synthesised from commercially available 2-(2-methoxyethoxy)ethanol according to literature methods.[101,102] The $[AuCl(PPh_3)]$ precursor was obtained using well established methods from the literature.[65]

4.5.6 Ligand synthesis

*Synthesis of 4–chloro–(N–(2–propyn–1–yl))–1,8-naphthalimide (**L1**)*[103]

Propargyl amine (0.33 mL, 5.22 mmol) was added to a solution of 4–chloro–1,8–naphthalic anhydride (608 mg, 2.61 mmol) in EtOH (30 mL) and heated to just below reflux, under a nitrogen atmosphere for 8 hours, followed by reduced heating at 50 ºC for 16 hours. Upon cooling the product was collected by filtration. Washing with EtOH (2 × 20 mL) and subsequent drying gave **L1** as an off-white solid. Yield: 634 mg, 2.35 mmol, 90 %. ^{1}H NMR (400 MHz, $CDCl_3$): δ_H = 8.72 (d, 1H, $^3J_{HH}$ = 7.3 Hz), 8.64 (d, 1H, $^3J_{HH}$ = 8.5 Hz), 8.55 (d, 1H, $^3J_{HH}$ = 7.9 Hz), 7.90-7.84 (m, 2H), 4.95 (d, 2H, $^4J_{HH}$ = 2.5 Hz, CH_2), 2.20 (t, 1H, $^4J_{HH}$ = 2.5 Hz, C≡C*H*) ppm; UV-Vis (MeCN): λ_{max} (ε/$M^{-1}cm^{-1}$) = 353 (11600), 339 (13700), 325(s) (10100), 233 (41100), 211 (16500) nm.

*Synthesis of 4–2–(2–aminoethoxy)ethanol)–(N–(2–propyn–1–yl))–1,8–naphthalic anhydride (**L2**)*

L1 (168 mg, 0.62 mmol) and 2–(2–aminoethoxy)ethanol (0.25 mL, 2.49 mmol) were stirred in DMSO (3 mL) at 90 ºC under a nitrogen atmosphere for 16 hours. The solution was then allowed to cool and water (10 mL) was added which induced precipitation of a yellow solid. The reaction mixture was then neutralized with 0.1 M HCl and the crude product extracted into dichloromethane, washed with water, dried over $MgSO_4$, and filtered. The solvent was reduced to a minimal volume, and precipitation was induced with

diethyl ether, allowing subsequent filtration and drying to afford **L2** as an orange solid. Yield: 156 mg, 0.46 mmol, 74 %. ^{1}H NMR (400 MHz, $CDCl_3$): δ_H = 8.71 (d, 1H, $^{3}J_{HH}$ = 6.4 Hz), 8.59 (d, 1H, $^{3}J_{HH}$ = 8.0 Hz), 8.27 (d, 1H, $^{3}J_{HH}$ = 7.6 Hz), 7.73 (app t, 1H, $^{3}J_{HH}$ = 7.6 Hz), 6.82 (d, 1H, $^{3}J_{HH}$ = 8.8 Hz), 6.00-5.94 (broad t, 1H, N*H*), 5.05 (d, 2H, $^{4}J_{HH}$ = 2.4 Hz, NCH_2), 4.02 (t, 2H, $^{3}J_{HH}$ = 5.6 Hz), 4.00-3.92 (broad m, 2H), 3.83-3.80 (m, 2H), 3.71 (app q, 2H, $^{3}J_{HH}$ = 5.2 Hz), 2.28 (t, 1H, $^{4}J_{HH}$ = 2.8 Hz, C≡C*H*) ppm; HRMS (ES+) found *m/z* 339.1343 for $[C_{19}H_{18}N_2O_4+H]^+$, calculated at 339.1345 for $[C_{19}H_{18}N_2O_4+H]^+$; IR (solid) ν_{max} (±2 cm^{-1}) = 3360, 3261, 2356, 1742, 1680, 1629, 1580, 1398, 1377, 1343, 1234, 1231, 1194, 1146, 1127, 1119, 1068, 995, 831, 757 cm^{-1}; UV-Vis (MeCN): λ_{max} (ε/$M^{-1}cm^{-1}$) = 429 (14400), 338 (900), 323 (1400), 279 (20900), 254 (17500), 227 (19900) nm.

*Synthesis of 4–(2–(2–methoxyethoxy)ethylamino)–(N–(2-propyn–1–yl))–1,8–naphthalic anhydride (**L3**)*

Synthesised as for **L2** using **L1** (150 mg, 0.56 mmol) and 2-(2-methoxyethoxy)ethanamine (265 mg, 2.23 mmol) to afford **L3** as a yellow solid. Yield: 94 mg, 0.27 mmol, 48 %. ^{1}H NMR (400 MHz, $CDCl_3$): δ_H = 8.64 (d, 1H, $^{3}J_{HH}$ = 8.4 Hz), 8.50 (d, 1H, $^{3}J_{HH}$ = 8.4 Hz), 8.21 (d, 1H, $^{3}J_{HH}$ = 8.4 Hz), 7.64 (app t, 1H, $^{3}J_{HH}$ = 7.2 Hz), 6.71 (d, 1H, $^{3}J_{HH}$ = 8.5 Hz), 6.02-5.96 (broad t, 1H, N*H*), 4.95 (d, 2H, $^{4}J_{HH}$ = 2.5 Hz, CH_2), 3.91 (t, 2H, $^{3}J_{HH}$ = 5.4 Hz), 3.77-3.73 (m, 2H), 3.64-3.60 (m, 2H), 3.60 (app q, 2H, $^{3}J_{HH}$ = 4.8 Hz, CH_2), 3.44 (s, 3H, CH_3), 2.10 (t, 1H, $^{4}J_{HH}$ = 2.4 Hz, C≡C*H*) ppm; LRMS (ES^+) found *m/z* 353.1 for $[M+H]^+$; HRMS (ES+) found *m/z* 353.1499 for $[C_{20}H_{20}N_2O_4+H]^+$, calculated at 353.1496 for $[C_{20}H_{20}N_2O_4+H]^+$; IR (solid) ν_{max} (±2 cm^{-1}) = 3279, 2893, 2372, 1682, 1647, 1587, 1549, 1456, 1402, 1373, 1337, 1296, 1246, 1192, 1169, 1143, 1093, 995, 947, 837, 778 cm^{-1}; UV-Vis (MeCN): λ_{max} (ε/$M^{-1}cm^{-1}$) = 430 (12400), 339 (1300), 324 (1600), 279 (16400), 254 (13600), 227 (16600) nm.

*Synthesis of 4–piperidinyl–(N–(2–propyn–1–yl))–1,8–naphthalic anhydride (**L4**)*[62]

Synthesised as for **L2** using **L1** (170 mg, 0.63 mmol) and piperidine (0.25 mL, 2.52 mmol) to afford **L4** as an orange solid. Yield: 133 mg, 0.42 mmol, 66.0 %. ^{1}H NMR (400 MHz, $CDCl_3$): δ_H = 8.59 (d, 1H, $^{3}J_{HH}$ = 7.3 Hz), 8.52 (d, 1H, $^{3}J_{HH}$ = 8.1 Hz), 8.39 (d, 1H, $^{3}J_{HH}$ = 8.4 Hz), 7.67 (app t, 1H, $^{3}J_{HH}$ = 7.9 Hz), 7.16 (d, 1H, $^{3}J_{HH}$ = 8.1 Hz), 4.94 (d, 2H, $^{4}J_{HH}$ = 2.3 Hz), 3.42-3.27 (broad m, 4H), 2.16 (t, 1H, $^{4}J_{HH}$ = 2.3 Hz, C≡C*H*), 1.88 (app t, 4H, $^{3}J_{HH}$ = 4.9 Hz), 1.72 (app d, 2H, $^{3}J_{HH}$ = 4.8 Hz) ppm; LRMS (ES+) found *m/z* 319.2 for $[M+H]^+$ and 382.2 for $[M+H+MeCN]^+$; UV-Vis (MeCN): λ_{max} (ε/$M^{-1}cm^{-1}$) = 410 (11100), 340 (2400), 324 (2100), 275 (11300), 255 (12900), 224 (26800), 208 (30100) nm.

*Synthesis of 4–morpholinyl–(N–(2–propyn–1–yl))–1,8–naphthalic anhydride (**L5**)*[61]

Synthesised as for **L2** using **L1** (180 mg, 0.67 mmol) and morpholine (0.23 mL, 2.67 mmol) to afford **L5** as a bright yellow solid. Yield: 178 mg, 0.56 mmol, 83 %. ^{1}H NMR (400 MHz, $CDCl_3$): δ_H = 8.63 (d, 1H, $^{3}J_{HH}$ = 7.3 Hz), 8.58 (d, 1H, $^{3}J_{HH}$ = 8.0 Hz), 8.40 (d, 1H, $^{3}J_{HH}$ = 8.4 Hz), 7.73 (app t, 1H, $^{3}J_{HH}$ = 7.7 Hz), 7.24 (d, 1H, $^{3}J_{HH}$ = 9.7 Hz), 4.95 (d, 2H, $^{4}J_{HH}$ = 1.9 Hz), 4.02 (t, 4H, $^{3}J_{HH}$ = 4.4 Hz), 3.27 (t, 4H, $^{3}J_{HH}$ = 4.5 Hz), 2.17 (t, 1H, $^{4}J_{HH}$ = 1.8 Hz, C≡C*H*) ppm; UV-Vis (MeCN): λ_{max} (ε/$M^{-1}cm^{-1}$) = 396 (8300), 340 (2500), 325 (1600), 271(s) (7300), 252 (10600), 222(s) (19600), 208 (24200) nm.

*Synthesis of 4–(4–methylpiperidinyl–(N–(2–propyn–1–yl))–1,8–naphthalic anhydride (**L6**)*

Synthesised as for **L2** using **L1** (169 mg, 0.63 mmol) and 4-methylpiperidine (0.30 mL, 2.51 mmol) to afford **L6** as an orange solid. Yield: 178 mg, 0.53 mmol, 84 %. ^{1}H NMR (400 MHz, $CDCl_3$): δ_H = 8.60 (d, 1H, $^{3}J_{HH}$ = 7.2 Hz), 8.52 (d, 1H, $^{3}J_{HH}$ = 8.1 Hz), 8.39 (d, 1H, $^{3}J_{HH}$ = 8.4 Hz), 7.67 (app t, 1H, $^{3}J_{HH}$ = 8.0 Hz), 7.18 (d, 1H, $^{3}J_{HH}$ = 8.1 Hz), 4.94 (d, 2H, $^{4}J_{HH}$ = 2.1 Hz), 3.58 (broad d, 2H, $^{3}J_{HH}$ = 12.2 Hz), 2.91 (app broad t, 2H, $^{3}J_{HH}$ = 11.8 Hz), 2.16 (t, 1H, $^{4}J_{HH}$ = 2.3 Hz, C≡C*H*), 1.86 (broad d, 2H, $^{3}J_{HH}$ = 11.2 Hz), 1.60-1.56 (m, 3H), 1.07 (d, 3H, $^{3}J_{HH}$ = 6.0 Hz) ppm; LRMS (ES^+) found *m/z* 333.1 for $[M+H]^+$; HRMS (ES+) found *m/z* 333.1599 for $[C_{21}H_{20}N_2O_2+H]^+$, calculated at 333.1603 for $[C_{21}H_{20}N_2O_2+H]^+$; IR (solid) ν_{max} (±2 cm^{-1}) = 3267, 2920, 2806, 1689, 1644, 1584, 1569, 1514, 1456, 1436, 1410, 1393, 1316, 1214, 1179, 1132, 1010, 951, 840 cm^{-1}; UV-Vis (MeCN): λ_{max} (ε/$M^{-1}cm^{-1}$) = 410 (9000), 340 (1800), 325 (1600), 275 (8600), 255 (10000) nm.

*Synthesis of 4–(4–ethylene ketal piperidinyl–(N–(2–propyn–1–yl)–1,8–naphthalic anhydride (**L7**)*

Synthesised as for **L2** using **L1** (181 mg, 0.67 mmol) and 4-piperidone ethylene ketal (0.34 mL, 2.68 mmol) to afford **L7** as a bright yellow solid. Yield: 190 mg, 0.51 mmol, 75 %. ^{1}H NMR (400 MHz, $CDCl_3$): δ_H = 8.62 (d, 1H, $^{3}J_{HH}$ = 7.2 Hz), 8.53 (d, 1H, $^{3}J_{HH}$ = 8.1 Hz), 8.40 (d, 1H, $^{3}J_{HH}$ = 8.4 Hz), 7.71 (app t, 1H, $^{3}J_{HH}$ = 8.1 Hz), 7.21 (d, 1H, $^{3}J_{HH}$ = 8.1 Hz), 4.94 (d, 2H, $^{4}J_{HH}$ = 2.4 Hz), 4.04 (s, 4H), 3.37 (t, 4H, $^{3}J_{HH}$ = 5.9 Hz), 2.17 (t, 1H, $^{4}J_{HH}$ = 2.3 Hz, C≡C*H*), 2.03 (t, 4H, $^{3}J_{HH}$ = 5.5 Hz) ppm; LRMS (ES^+) found *m/z* 377.1 for $[M+H]^+$; HRMS (ES+) found *m/z* 377.1496 for $[C_{22}H_{20}N_2O_4+H]^+$, calculated at 377.1502 for $[C_{22}H_{20}N_2O_4+H]^+$; IR (solid) ν_{max} (±2 cm^{-1}) = 2359, 1690, 1654, 1588, 1557, 1471, 1458, 1382, 1360, 1340, 1316, 1231, 1105, 1073, 1029, 945, 932, 781, 757 cm^{-1}; UV-Vis (MeCN): λ_{max} (ε/$M^{-1}cm^{-1}$) = 403 (9700), 340 (2300), 325 (1800), 273 (11800), 255 (13100) nm.

*Synthesis of 4–(3'–aminopropanol)–(N–(2–propyn–1–yl))–1,8–naphthalic anhydride (**L8**)*

Synthesised as for **L2** using **L1**(199 mg, 0.74 mmol) and 3–aminopropanol (0.23 mL, 2.95 mmol) to afford **L8** as an orange solid. Yield: 81 mg, 0.26 mmol, 36 %. ^{1}H NMR (400 MHz,

$CDCl_3$): δ_H = 8.56 (d, 1H, $^3J_{HH}$ = 6.9 Hz), 8.45 (d, 1H, $^3J_{HH}$ = 8.4 Hz), 8.06 (d, 1H, $^3J_{HH}$ = 8.9 Hz), 7.57 (app t, 1H, $^3J_{HH}$ = 8.2 Hz), 6.64 (d, 1H, $^3J_{HH}$ = 8.5 Hz, HNCC*H*), 4.94 (d, 2H, $^4J_{HH}$ = 2.4 Hz, NCH_2), 3.56 (t, 2H, $^3J_{HH}$ = 6.1 Hz, CH_2OH), 4.04 (t, 2H, $^3J_{HH}$ = 5.3 Hz, NHCH_2), 2.18 (t, 1H, $^4J_{HH}$ = 2.5 Hz, C≡C*H*), 2.09 (app quin, 2H, $^3J_{HH}$ = 6.0 Hz, NHCH$_2$CH_2) ppm; LRMS (ES+) found *m/z* 309.1 for $[M+H]^+$ and 372.1 for $[M+Na+MeCN]^+$; HRMS (ES+) found *m/z* 309.1237 for $[C_{18}H_{16}N_2O_3+H]^+$, calculated at 309.1234 for $[C_{18}H_{16}N_2O_3+H]^+$; IR (solid) ν_{max} (±2 cm^{-1}) = 3330, 3250, 2356, 1679, 1642, 1627, 1618, 1574, 1552, 1395, 1369, 1333, 1324, 1302, 1243, 1144, 1170, 1108, 1054, 1008, 947, 820, 774, 756 cm^{-1}; UV-Vis (MeCN): λ_{max} ($\varepsilon/M^{-1}cm^{-1}$) = 434 (12900), 339 (900), 323 (1400), 280 (17500), 254 (14300), 228 (16200), 202 (39600) nm.

4.5.7 Complex synthesis

*Synthesis of [Au(**L1**)(PPh_3)] (**AuL1**)*

L1 (18.2 mg, 67.5 μmol), [AuCl(PPh_3)] (37.1 mg, 75.0 μmol) and KO^{t}Bu (15.0 mg, 0.14 mmol) were stirred in EtOH (2 mL) in a foil-covered round-bottomed flask, under a nitrogen atmosphere for 24 hours at room temperature. 2 equivalents of KO^{t}Bu (15.0 mg, 0.14 mmol) were then added to the reaction mixture with stirring for a further 24 hours. The ethanol was then reduced in volume and the residue dissolved in minimal $CHCl_3$. Precipitation was induced with the addition of Et_2O allowing subsequent filtration and drying to afford **AuL1** as an off-white solid. Yield: 47.5 mg, 65.2 μmol, 97 %. ^{1}H NMR (400 MHz, $CDCl_3$): δ_H = 8.69 (d, 1H, $^3J_{HH}$ = 7.3 Hz), 8.58 (d, 1H, $^3J_{HH}$ = 8.5 Hz), 8.53 (d, 1H, $^3J_{HH}$ = 7.9 Hz), 7.85-7.78 (m, 2H), 7.53-7.30 (m, 15H), 5.10 (s, 2H, CH_2) ppm; ^{31}P{^{1}H} NMR (121 MHz, $CDCl_3$): δ_P = +41.9 ppm; LRMS (ES^+) found *m/z* 728.1 for $[M+H]^+$; HRMS (ES+) found *m/z* 728.0814 for $[C_{33}H_{22}AuClNO_2P+H]^+$, calculated at 728.0821 for $[C_{33}H_{22}AuClNO_2P+H]^+$; IR (solid) ν_{max} (±2 cm^{-1}) = 1744, 1667, 1632, 1587, 1479, 1433, 1329, 1234, 1099, 1049, 989, 779 cm^{-1}; UV-Vis (MeCN): λ_{max} ($\varepsilon/M^{-1}cm^{-1}$) = 353 (7600), 338 (8900), 322 (6600), 277 (7200) nm.

*Synthesis of [Au(**L2**)(PPh_3)] (**AuL2**)*

Synthesised as for **AuL1**, but using **L2** (28.8 mg, 85.1 μmol), [AuCl(PPh_3)] (46.3 mg, 93.6 μmol) and KO^{t}Bu (36.0 mg, 0.36 mmol) to afford **AuL2** as an orange solid. Yield: 55.8 mg, 70.0 μmol, 82 %. ^{1}H NMR (400 MHz, $CDCl_3$): δ_H = 8.39 (d, 1H, $^3J_{HH}$ = 7.3 Hz), 8.33 (d, 1H, $^3J_{HH}$ = 8.4 Hz), 8.21 (d, 1H, $^3J_{HH}$ = 8.4 Hz), 7.56-7.32 (m, 15H), 6.96 (app t, 1H, $^3J_{HH}$ = 8.1 Hz), 6.56 (d, 1H, $^3J_{HH}$ = 8.4 Hz), 5.99 (t, 1H, $^3J_{HH}$ = 4.7 Hz), 5.07 (s, 2H, CH_2), 3.92 (t, 2H, $^3J_{HH}$ = 5.1 Hz), 3.89 (broad t, 2H), 3.62-3.56 (m, 2H), 3.56 (app q, 2H, $^3J_{HH}$ = 4.8 Hz), 2.36 (broad s, 1H, O*H*) ppm; ^{31}P{^{1}H} NMR (121 MHz, $CDCl_3$): δ_P = +42.6 ppm; LRMS (ES^+) found *m/z* 797.2 for

[M+H]$^+$; HRMS (ES+) found *m/z* 797.1835 for [$C_{37}H_{32}AuN_2O_4P$+H]$^+$, calculated at 797.1838 for [$C_{37}H_{32}AuN_2O_4P$+H]$^+$; IR (solid) ν_{max} (±2 cm^{-1}) = 3300, 2877, 2359, 2029, 1736, 1683, 1627, 1610, 1572, 1437, 1364, 1323, 1296, 1230, 1099, 1045, 1001, 966, 744 cm^{-1}; UV-Vis (MeCN): λ_{max} (ε/M^{-1}cm^{-1}) = 429 (5400), 340 (700), 323 (1100), 275 (11400), 260 (11600) nm.

*Synthesis of [Au(**L3**)(PPh$_3$)] (**AuL3**)*

Synthesised as for **AuL1** but using **L3** (26.9 mg, 76.3 μmol), [AuCl(PPh$_3$)] (41.5 mg, 84.0 μmol) and KO^{t}Bu (32.0 mg, 0.31 mmol) to afford **AuL3** as an orange solid. Yield: 62.0 mg, 76.4 μmol, 100 %. ^{1}H NMR (400 MHz, $CDCl_3$): δ_H = 8.53 (d, 1H, $^3J_{HH}$ = 7.2 Hz), 8.42 (d, 1H, $^3J_{HH}$ = 8.4 Hz), 8.12 (d, 1H, $^3J_{HH}$ = 8.5 Hz), 7.53 (app t, 1H, $^3J_{HH}$ = 7.4 Hz), 7.49-7.33 (m, 15H), 6.63 (d, 1H, $^3J_{HH}$ = 8.4 Hz), 5.04 (s, 2H), 3.86 (t, 2H, $^3J_{HH}$ = 4.9 Hz, CH_2), 3.69 (t, 2H, $^3J_{HH}$ = 4.1 Hz, CH_2), 3.58-3.44 (m, 4H), 3.38 (s, 3H, CH_3) ppm; ^{31}P{^{1}H} NMR (121 MHz, $CDCl_3$): δ_P = +42.1 ppm; LRMS (ES$^+$) found *m/z* 811.2 for [M+H]$^+$; HRMS (ES+) found *m/z* 811.1993 for [$C_{38}H_{34}AuN_2O_4P$+H]$^+$, calculated at 811.2000 for [$C_{38}H_{34}AuN_2O_4P$+H]$^+$; IR (solid) ν_{max} (±2 cm^{-1}) = 2918, 2858, 2164, 2019, 1969, 1629, 1579, 1537, 1470, 1433, 1393, 1373, 1337, 1246, 1198, 1146, 1096, 831, 756 cm^{-1}; UV-Vis (MeCN): λ_{max} (ε/M^{-1}cm^{-1}) = 428 (8700), 339 (900), 324 (1300), 276 (16500), 258 (17100) nm.

*Synthesis of [Au(**L4**)(PPh$_3$)] (**AuL4**)*

Synthesised as for **AuL1**, but using **L4** (30.8 mg, 96.7 μmol), [AuCl(PPh$_3$)] (52.7 mg, 0.11 mmol) and KO^{t}Bu (12.0 mg, 0.11 mmol) to afford **AuL4** as a yellow solid. Yield: 33.9 mg, 43.6 μmol, 45 %. ^{1}H NMR (400 MHz, $CDCl_3$): δ_H = 8.59 (d, 1H, $^3J_{HH}$ = 7.2 Hz), 8.51 (d, 1H, $^3J_{HH}$ = 8.1 Hz), 8.36 (d, 1H, $^3J_{HH}$ = 8.4 Hz), 7.64 (app t, 1H, $^3J_{HH}$ = 7.3 Hz), 7.56-7.34 (m, 15H), 7.14 (d, 1H, $^3J_{HH}$ = 8.1 Hz), 5.09 (s, 2H), 3.26-3.11 (broad t, 4H), 1.91-1.81 (broad m, 4H), 1.66-1.76 (broad quin, 2H) ppm; ^{31}P{^{1}H} NMR (121 MHz, $CDCl_3$): δ_P = +41.2 ppm; LRMS (ES$^+$) found *m/z* 777.2 for [M+H]$^+$; HRMS (ES+) found *m/z* 777.1938 for [$C_{38}H_{32}AuN_2O_2P$+H]$^+$, calculated at 777.1945 for [$C_{38}H_{32}AuN_2O_2P$+H]$^+$; IR (solid) ν_{max} (±2 cm^{-1}) = 2927, 1740, 1689, 1655, 1583, 1477, 1435, 1377, 1316, 1246, 1233, 1177, 1155, 1099, 1128, 1074, 941, 755, 690 cm^{-1}; UV-Vis (MeCN): λ_{max} (ε/M^{-1}cm^{-1}) = 408 (8300), 340 (1400), 325 (1500), 273 (11900), 252 (17800) nm.

*Synthesis of [Au(**L5**)(PPh$_3$)] (**AuL5**)*

Synthesised as for **AuL1**, but using **L5** (28.0 mg, 87.5 μmol), [AuCl(PPh$_3$)] (47.6 mg, 86.2 μmol) and KO^{t}Bu (37.0 mg, 0.36 mmol) to afford **AuL5** as a yellow solid. Yield: 59.5 mg, 76.4 μmol, 87 %. ^{1}H NMR (400 MHz, $CDCl_3$): δ_H = 8.62 (d, 1H, $^3J_{HH}$ = 7.3 Hz), 8.56 (d, 1H, $^3J_{HH}$ = 8.0 Hz), 8.40 (d, 1H, $^3J_{HH}$ = 7.9 Hz), 7.68 (app t, 1H, $^3J_{HH}$ = 7.9 Hz), 7.51-7.34 (m, 15H), 7.21

(d, 1H, $^{3}J_{HH}$ = 8.1 Hz), 5.09 (d, 2H, $^{5}J_{HP}$ = 1.5 Hz, NCH_2), 4.01 (t, 4H, $^{3}J_{HH}$ = 4.6 Hz), 3.25 (t, 4H, $^{3}J_{HH}$ = 4.5 Hz) ppm; $^{31}P\{^{1}H\}$ NMR (121 MHz, $CDCl_3$): δ_P = +42.6 ppm; HRMS (ES+) found *m/z* 1237.2237 for $[C_{37}H_{30}AuN_2O_3P+AuPPh_3]$, calculated at 1237.2237 for $[C_{37}H_{30}AuN_2O_3P+AuPPh_3]$; IR (solid) ν_{max} (±2 cm^{-1}) = 1842, 1822, 1736, 1688, 1645, 1576, 1512, 1435, 1379, 1244, 1234, 1174, 1112, 1095, 1008, 935, 868, 779, 702 cm^{-1}; UV-Vis (MeCN): λ_{max} (ε/$M^{-1}cm^{-1}$) = 393 (6900), 340 (2800), 272 (13100), 255 (16600) nm.

*Synthesis of [Au(**L6**)(PPh_3)] (**AuL6**)*

Synthesised as for **AuL1**, but using **L6** (30.5 mg, 91.8 μmol), [AuCl(PPh_3)] (50.0 mg, 101.0 μmol) and KO^{t}Bu (39.0 mg, 0.38 mmol) to afford **AuL6** as an orange solid. Yield: 59.6 mg, 75.4 μmol, 82 %. ^{1}H NMR (400 MHz, $CDCl_3$): δ_H = 8.59 (d, 1H, $^{3}J_{HH}$ = 7.3 Hz), 8.51 (d, 1H, $^{3}J_{HH}$ = 8.1 Hz), 8.35 (d, 1H, $^{3}J_{HH}$ = 7.9 Hz), 7.63 (app t, 1H, $^{3}J_{HH}$ = 7.9 Hz), 7.52-7.44 (m, 15H), 7.15 (d, 1H, $^{3}J_{HH}$ = 8.1 Hz), 5.09 (d, 2H, $^{5}J_{HP}$ = 1.6 Hz), 3.56 (app broad d, 2H, $^{3}J_{HH}$ = 11.8 Hz), 2.89 (broad t, 2H, $^{3}J_{HH}$ = 11.5 Hz), 1.85 (app broad d, 2H, $^{3}J_{HH}$ = 9.5 Hz), 1.62 (app broad d, 1H, $^{3}J_{HH}$ = 7.3 Hz), 1.58 (app s, 2H, CH_2), 1.07 (d, 3H, $^{3}J_{HH}$ = 5.9 Hz, CH_3) ppm; $^{31}P\{^{1}H\}$ NMR (121 MHz, $CDCl_3$): δ_P = +42.6 ppm; LRMS (ES^+) found *m/z* 791.2 for $[M+H]^+$; HRMS (ES+) found *m/z* 791.2092 for $[C_{39}H_{34}AuN_2O_2P+H]^+$, calculated at 791.2096 for $[C_{39}H_{34}AuN_2O_2P+H]^+$; IR (solid) ν_{max} (±2 cm^{-1}) = 1734, 1688, 1647, 1583, 1516, 1481, 1456, 1435, 1412, 1377, 1336, 1244, 1226, 1174, 1153, 1130, 1076, 966, 792, 751 cm^{-1}; UV-Vis (MeCN): λ_{max} (ε/$M^{-1}cm^{-1}$) = 407 (5300), 339 (1300), 326 (1500), 277(s) (10900), 259 (13500), 245 (13300) nm.

*Synthesis of [Au(**L7**)(PPh_3)] (**AuL7**)*

Synthesised as for **AuL1**, but using **L7** (34.1 mg, 90.6 μmol), [AuCl(PPh_3)] (49.3 mg, 99.6 μmol) and KO^{t}Bu (38.0 mg, 0.37 mmol) to afford **AuL7** as a bright yellow solid. Yield: 70.3 mg, 84.2 μmol, 93 %. ^{1}H NMR (400 MHz, $CDCl_3$): δ_H = 8.61 (d, 1H, $^{3}J_{HH}$ = 7.6 Hz), 8.53 (d, 1H, $^{3}J_{HH}$ = 8.4 Hz), 8.37 (d, 1H, $^{3}J_{HH}$ = 9.6 Hz), 7.67 (app t, 1H, $^{3}J_{HH}$ = 8.4 Hz), 7.52-7.37 (m, 15H), 7.20 (d, 1H, $^{3}J_{HH}$ = 8.0 Hz), 5.09 (d, 2H, $^{5}J_{HP}$ = 1.6 Hz), 4.04 (s, 4H), 3.35 (broad t, 4H, $^{3}J_{HH}$ = 6.0 Hz), 2.03 (broad t, 4H, $^{3}J_{HH}$ = 6.0 Hz) ppm; $^{31}P\{^{1}H\}$ NMR (121 MHz, $CDCl_3$): δ_P = +42.1 ppm; LRMS (ES^+) found *m/z* 835.2 for $[M+H]^+$; HRMS (ES+) found *m/z* 835.1993 for $[C_{40}H_{34}AuN_2O_4P+H]^+$, calculated at 835.1994 for $[C_{40}H_{34}AuN_2O_4P+H]^+$; IR (solid) ν_{max} (±2 cm^{-1}) = 2847, 1736, 1695, 1655, 1589, 1481, 1462, 1437, 1411, 1383, 1336, 1315, 1232, 1172, 1141, 1101, 1076, 1028, 947, 914, 887, 842, 781, 753, 692 cm^{-1}; UV-Vis (MeCN): λ_{max} (ε/$M^{-1}cm^{-1}$) = 400 (8500), 340 (1900), 325 (1600), 274(s) (12700), 254 (18000) nm.

4.6 References

1. M. Concepción Gimeno, in *Modern Supramolecular Gold Chemistry: Gold-Metal Interactions and Applications*, ed. A. Laguna, Wiley VCH, Weinheim, 1st edn., 2008, ch. 1, pp. 1-63.
2. N. N. Greenwood and A. Earnshaw, in *Chemistry of the Elements*, ed. B.-H. Ltd, Butterworth-Heinemann Ltd., Oxford, UK, 2nd edn., 1997, ch. 28, pp. 1173-1200.
3. N. J. Long and C. W. Williams, *Angew. Chem. Int. Ed.*, 2003, **42**, 2586-2617.
4. E. Langdon-Jones and S. J. A. Pope, *Chem. Commun.*, 2014, **50**, 10343-10354.
5. D. M. P. Mingos, *Essentials of Inorganic Chemistry*, Oxford University Press, New York, 2nd edn., 2007.
6. G. C. Fortman and S. P. Nolan, *Organometallics*, 2010, **29**, 4579-4583.
7. M. J. McKeage, L. Maharaj and S. J. Berners-Price, *Coord. Chem. Rev.*, 2002, **232**, 127-135.
8. G. D. Hoke, G. F. Rush, G. E. Bossard, J. V. McArdle, B. D. Jensen and C. K. Mirabelli, *J. Biol. Chem.*, 1988, **262**, 11203-11210.
9. G. J. Higby, *Gold Bull.*, 1982, **15**, 130-140.
10. C. F. Shaw III, *Chem. Rev.*, 1999, **99**, 2589-2600.
11. P. J. Sadler, *Struct. Bonding (Berlin)*, 1976, **29**, 171-219.
12. K. D. Mjos and C. Orvig, *Chem. Rev.*, 2014, **114**, 4540-4563.
13. W. F. Kean, F. Forestier, Y. Kassam, W. W. Buchanan and P. J. Rooney, *Semin. Arthritis Rheum.*, 1985, **14**, 180-186.
14. E. R. T. Tiekink, *Oncol. Hematol.*, 2002, **42**, 225-248.
15. A. J. Lewis and D. T. Walz, *Prog. Med. Chem.*, 1982, **19**, 1-58.
16. S. S. Gunatilleke and A. M. Barrios, *J. Med. Chem.*, 2006, **49**, 3933-3937.
17. B. A. Stanley, V. Sivakumaran, S. Shi, I. McDonald, D. Lloyd, W. H. Watson, M. A. Aon and N. Paolocci, *J. Biol. Chem.*, 2011, **286**, 33669-33677.
18. C. F. Williams, N. Yarlett, M. A. Aon and L. D., *Mol. Biochem. Parasitol.*, 2014, **196**, 45-52.
19. T. V. Serebryanskaya, A. S. Lyakhov, L. S. Ivashkevich, J. Schur, C. Frias, A. Prokop and I. Ott, *Dalton Trans.*, 2015, **44**, 1161-1169.
20. J. R. Roberts and C. F. Shaw, *Biochem. Pharmacol.*, 1998, **55**, 1291-1299.
21. J. Chaudiere and A. L. Tappel, *J. Inorg. Biochem.*, 1984, **20**, 313-325.
22. R. P. Hirt, S. Müller, T. M. Embley and G. H. Coombs, *Trends Parasitol.*, 2002, **18**, 302-308.
23. K. Becker, S. Gromer, R. H. Schirmer and S. Müller, *Eur. J. Biochem.*, 2000, **267**, 6118-6125.
24. R. A. Rader, D. R. McMillin, M. T. Buckner, T. G. Matthews, D. J. Casadonte, R. K. Lengel, S. B. Whittaker, L. M. Darmon and F. E. Lytle, *J. Am. Chem. Soc.*, 1981, **102**, 5906-5912.
25. O. M. N. Dhubhghaill and P. J. Sadler, in *Metal complexes in cancer chemotherapy*, ed. B. K. Keppler, VCH, Weinheim, 1993, pp. 221-248.
26. P. J. Sadler and Z. Guo, *Pure Appl. Chem.*, 1998, **70**, 863-871.
27. I. Ott, *Coord. Chem. Rev.*, 2009, **253**, 1670-1681.
28. C. K. Mirabelli, R. K. Johnson, D. T. Hill, L. F. Faucette, G. R. Girard, G. Y. Kuo, C. M. Sung and S. T. Crooke, *J. Med. Chem.*, 2002, **29**, 218-223.
29. M. J. McKeage, S. J. Berners-Price, P. Galettis, R. J. Bowen, W. Brouwer, L. Ding, L. Zhuang and B. C. Baguley, *Cancer Chemotherapy and Pharmacology*, 2000, **46**, 343-350.
30. L. Messori and G. Marcon, 2004, vol. 41 : Metal Ions and Their Complexes in Medication, ch. 9.
31. T. R. C. o. t. E. R. Council, *Ann. Rheum. Dis.*, 1960, **19**, 95-119.
32. S. J. Berners-Price and A. Filipovska, *Metallomics*, 2011, **3**, 863-873.

33. R. Rubbiani, S. Can, I. Kitanovic, H. Alborzinia, M. Stefanopoulou, M. Kokoschka, S. Monchgesang, W. S. Sheldrick, S. Wolfl and I. Ott, *J. Med. Chem.*, 2011, **54**, 8646-8657.
34. R. Rubbiani, E. Schuh, A. Meyer, J. Lemke, J. Wimberg, N. Metzler-Nolte, F. Meyer, F. Mohr and I. Ott, *MedChemComm*, 2013, **4**, 942-948.
35. M. V. Baker, P. J. Barnard, S. J. Berners-Price, S. K. Brayshw, J. L. Hickley, B. W. Skelton and A. H. White, *Dalton Trans.*, 2006, **30**, 3708-3715.
36. E. Vergara, E. Cerrada, A. Casini, O. Zava, M. Laguna and P. J. Dyson, *Organometallics*, 2010, **29**, 2596-2603.
37. L. A. Mullice, H. J. Mottram, A. J. Hallett and S. J. A. Pope, *Eur. J. Inorg. Chem.*, 2012, **2012**, 3054-3060.
38. A. Vogler and H. Kunkely, *Coord. Chem. Rev.*, 2001, **219-221**, 489-507.
39. A. Castineiras, N. Fernandez-Hermida, R. Fernandez-Rodriguez and I. Garcia-Santos, *Cryst. Growth Des.*, 2012, **12**, 1432-1442.
40. S. Lentijo, G. Aullón, J. A. Miguel and P. Espinet, *Dalton Trans.*, 2013, **42**, 6353-6365.
41. S. E. Thwaite, A. Schier and H. Schmidbaur, *Inorg. Chim. Acta.*, 2004, **357**, 1549-1557.
42. J. C. Y. Lin, S. S. Tang, C. S. Vasam, W. C. You, T. W. Ho, C. H. Huang, B. J. Sun, C. Y. Huang, C. S. Lee, W. S. Hwang, A. H. H. Chang and I. J. B. Lin, *Inorg. Chem.*, 2008, **47**, 2543-2551.
43. L. A. Mullice, F. L. Thorp-Greenwood, R. H. Laye, M. P. Coogan, B. M. Kariuki and S. J. A. Pope, *Dalton Trans.*, 2009, 6836-6842.
44. A. Meyer, C. P. Bagowski, M. Kokoschka, M. Stefanopoulou, H. Alborzinia, S. Can, D. H. Vlecken, W. S. Sheldrick, S. Wolfl and I. Ott, *Angew. Chem. Int. Ed.*, 2012, **51**, 8895-8899.
45. M. P. Coogan and S. J. A. Pope, in *The Chemistry of Molecular Imaging*, eds. N. Long and W. T. Wong, John Wiley and Sons Inc., New Jersey, 1st edn., 2015, ch. 12, pp. 275-298.
46. F. L. Thorp-Greenwood, R. G. Balasingham and M. P. Coogan, *J. Organomet. Chem.*, 2012, **714**, 12-21.
47. E. Baggaley, M. R. Gill, N. H. Green, D. Turton, I. V. Sazanovich, S. W. Botchway, C. Smythe, J. W. Haycock, J. A. Weinstein and J. A. Thomas, *Angew. Chem. Int. Ed.*, 2014, **53**, 3367-3371.
48. R. G. Balasingham, F. L. Thorp-Greenwood, C. F. Williams, M. P. Coogan and S. J. A. Pope, *Inorg. Chem.*, 2012, **51**, 1419-1426.
49. C. Li, M. Yu, Y. Sun, W. Yongquan, C. Huang and F. Li, *J. Am. Chem. Soc.*, 2011, **133**, 11231-11233.
50. S. W. Botchway, M. Charnley, J. W. Haycock, A. W. Parker, D. L. Rochester, J. A. Weinstein and J. A. G. Williams, *Proc. Natl. Acad. Sci. U. S. A.*, 2008, **105**, 16071-16076.
51. C. P. Bagowski, Y. You, H. Scheffler, D. H. Vlecken, D. J. Schmitz and I. Ott, *Dalton Trans.*, 2009, 10799-10805.
52. I. Ott, Y. Xu and X. Qian, *J. Photochem. Photobiol., A*, 2011, **105**, 75-80.
53. R. G. Balasingham, C. F. Williams, H. J. Mottram, M. P. Coogan and S. J. A. Pope, *Organometallics*, 2012, **31**, 5835-5843.
54. A. Citta, E. Schuh, F. Mohr, A. Folda, M. L. Massimino, A. Bindoli, A. Casini and M. P. Rigobello, *Metallomics*, 2013, **5**, 1006-1015.
55. B. Bertrand, A. de Almeida, E. P. M. van der Burgt, M. Picquet, A. Citta, A. Folda, M. P. Rigobello, P. Le Gendre, E. Bodio and A. Casini, *Eur. J. Inorg. Chem.*, 2014, 4523-4528.
56. J. Arcau, V. Andermark, E. Aguilo, A. Gandioso, A. Moro, M. Cetina, J. C. Lima, K. Rissanen, I. Ott and L. Rodriguez, *Dalton Trans.*, **43**, 4426-4436.

57. V. Fernandez-Moreira, I. Marzo and M. C. Gimeno, *Chemical Science*, 2014, **5**, 4434-4446.
58. K. de Oliveira, P. Costa, J. Santin, L. Mazzambani, C. Burger, C. Mora, R. Nunes and M. de Souza, *Bioorg. Med. Chem.*, 2011, **19**, 4295-4306.
59. R. Stolarski, *Fibres & Textiles in Eastern Europe*, 2009, **17**, 91-95.
60. E. E. Langdon-Jones, N. O. Symonds, S. E. Yates, A. J. Hayes, D. Lloyd, R. Williams, S. J. Coles, P. N. Horton and S. J. A. Pope, *Inorg. Chem.*, 2014, **53**, 3788-3797.
61. M. Berchel, J.-P. Haelters, H. Couthon-Gourvès, L. Deschamps, P. Midoux, P. Lehn and P.-A. Jaffrès, *Eur. J. Org. Chem.*, 2011, **2011**, 6294-6303.
62. R. Sivkova, J. Vohlídal, M. Bláha, J. Svoboda, J. Sedláček and J. Zedník, *Macromol. Chem. Phys.*, 2012, **213**, 411-424.
63. T. Gunnlaugsson, C. McCoy, R. Morrow, C. Phelan and F. Stomeo, *Arkivoc*, 2003, 216-228.
64. G. R. C. Hamilton, Y. Sheng, B. Callan, R. F. Donnelly and J. F. Callan, *New J. Chem.*, 2015, **39**, 3461-3466.
65. R. Uson, A. Laguna, M. Laguna, D. A. Briggs, H. H. Murray and J. P. Fackler, in *Inorg. Synth.*, John Wiley & Sons, Inc., 2007, DOI: 10.1002/9780470132579.ch17, pp. 85-91.
66. V. G. Albano, L. Busetto, M. C. Cassani, P. Sabatino, A. Schmitz and V. Zanotti, *J. Chem. Soc., Dalton Trans.*, 1995, 2087-2093.
67. V. W.-W. Yam and S. W.-K. Choi, *J. Chem. Soc. Dalton Trans.*, 1996, 4227-4232.
68. V. W.-W. Yam, K. K.-W. Lo and K. M.-C. Wong, *J. Organomet. Chem.*, 1999, **578**, 3-30.
69. M. Ferrer, L. Rodriguez, O. Rosell, F. Pina, J. C. Lima, M. F. Bardia and X. Solans, *J. Organomet. Chem.*, 2003, **678**, 82-89.
70. H. Riva, M. Nieuwhuyzen, C. M. Fierr, P. R. Raithby, L. Male and M. C. Lagunas, *Inorg. Chem.*, 2006, **45**, 1418-1420.
71. C. Janiack, *Dalton Trans.*, 2000, 3885-3896.
72. S. Alvarez, *Dalton Trans.*, 2013, **42**, 8617-8636.
73. L. Chen, W. Sun, W. Li, J. Li, L. Du, W. Xu, H. Fang and M. Li, *Analytical Methods*, 2012, **4**, 2661-2663.
74. J. Zhang, M. Park, W. Ren, Y. Kim, S. Kim, J. Jung and J. Kim, *Chem. Commun.*, 2011, **47**, 3568-3570.
75. H. Wang, L. Yang, W. Zhang, Y. Zhou, B. Zhao and X. Li, *Inorg. Chim. Acta*, 2012, **381**, 111-116.
76. J. Yarnell, J. Deaton, C. McCusker and F. Castellano, *Inorg. Chem.*, 2011, **50**, 7820-7830.
77. S. S. Bag, M. K. Pradhan, R. Kundu and S. Jana, *Bioorg. Med. Chem.*, 2013, **23**, 96-101.
78. M. Shahid, P. Srivastava and A. Misra, *New J. Chem.*, 2011, **35**, 1690-1700.
79. S. Banerjee, E. B. Veale, C. M. Phelan, S. A. Murphy, G. M. Tocci, L. J. Gillespie, D. O. Frimannsson, J. M. Kelly and T. Gunnlaugsson, *Chem. Soc. Rev.*, 2013, **42**, 1601-1618.
80. V. W.-W. Yam, K. L. Cheung, S. K. Yip and K. K. Cheung, *J. Organomet. Chem.*, 2003, **681**, 196-209.
81. J. Xie, Y. Chen, W. Yang, D. Xu and K. Zhang, *J. Photochem. Photobiol., A*, 2011, **223**, 111-118.
82. V. Bojinov and I. Panova, *Dyes Pigm.*, 2009, **80**, 61-66.
83. M. Pluth, E. Tomat, S. Lippard, R. Kornberg, C. Raetz, J. Rothman and J. Thorner, *Annual Review of Biochemistry, Vol 80*, 2011, **80**, 333-355.
84. E. Hao, T. Meng, M. Zhang, W. Pang, Y. Zhou and L. Jiao, *J. Phys. Chem. A*, 2011, **115**, 8234-8241.
85. I. Ott, Y. Xu, J. Liu, M. Kokoschka, M. Harlos, W. S. Sheldrick and X. H. Qian, *Bioorg. Med. Chem.*, 2008, **16**, 7107-7116.

86. C. u. http://www.molinspiration.com.
87. S. Huang, R. Han, Q. Zhuang, L. Du, H. Jia, Y. Liu and Y. Liu, *Biosens. Bioelectron.*, 2015, **71**, 313-321.
88. C. O. M. Millet, D. Lloyd, M. P. Coogan, J. Rumsey and J. Cable, *Exp. Parasitol.*, 2011, **129**, 17-26.
89. V. Fernández-Moreira, F. L. Thorp-Greenwood, A. J. Amoroso, J. Cable, J. B. Court, V. Gray, A. J. Hayes, R. L. Jenkins, B. M. Kariuki, D. Lloyd, C. O. Millet, C. F. Williams and M. P. Coogan, *Org. Biomol. Chem.*, 2010, **8**, 3888-3901.
90. D. Lloyd and C. F. Williams, *Mol. Biochem. Parasitol.*, 2014, **197**, 43-49.
91. C. O. M. Millet, C. F. Williams, A. J. Hayes, A. C. Hann, J. Cable and D. Lloyd, *Exp. Parasitol.*, 2013, **135**, 262-273.
92. C. F. Williams, C. O. M. Millet, A. J. Hayes, J. Cable and D. Lloyd, *Trends Parasitol.*, 2013, **29**, 311-312.
93. L. E. Wedlock, M. R. Kilburn, J. B. Cliff, L. Filgueira, M. Saunders and S. J. Berners-Price, *Metallomics*, 2011, **3**, 917-925.
94. S. J. Coles and P. A. Gale, *Chemical Science*, 2012, **3**, 683-689.
95. L. Palatinus and G. Chapuis, *J. Appl. Crystallogr.*, 2007, **40**, 786-790.
96. G. M. Sheldrick, *Acta crystallographica. Section A, Foundations of crystallography*, 2008, **64**, 112-122.
97. C. F. Williams, D. Lloyd, D. Kolarich, K. Alagesan, M. Duchene, J. Cable, D. Williams and D. Leitsch, *Vet. Parasitol.*, 2012, **190**, 62-73.
98. T. Mosmann, *J. Immunol. Methods*, 1983, **65**, 55-63.
99. M. Frank, M. Nieger, F. Vogtle, P. Belser, A. von Zelewsky, L. D. Cola, V. Balzani, F. Barigelletti and L. Flamigni, *Inorg. Chim. Acta*, 1996, **242**, 281-291.
100. A. Juris, F. Barigelletti, S. Campagna, P. Belser and A. von Zelewsky, *Coord. Chem. Rev.*, 1988, **84**, 85-277.
101. V. Gudipati, D. P. Curran and C. S. Wilcox, *J. Org. Chem.*, 2006, **71**, 3599-3607.
102. M. K. Thompson, D. M. J. Doble, L. S. Tso, S. Barra, M. Botta, S. Aime and K. N. Raymond, *Inorg. Chem.*, 2004, **43**, 8577-8586.
103. C. Steigers, B. Olah, U. Wuerfel, J. Hohl-Ebinger, A. Hinsch and R. Haag, *Sol. Energy Mater. Sol. Cells*, 2009, **93**, 552-563.

4.7 Appendix

4.7.1 Crystallographic data for L3

Table S4. 1: Crystal Data and Structure Determination Refinement for L6

Identification code	**2014ncs0392 / ELJ433**	
Empirical formula	$C_{21}H_{20}N_2O_2$	
Formula weight	332.39	
Temperature	100(2) K	
Wavelength	0.71075 Å	
Crystal system	Monoclinic	
Space group	$P2_1/n$	
Unit cell dimensions	a = 9.5575(7) Å	α = 90°
	b = 10.8540(8) Å	β = 91.460(2)°
	c = 16.2316(11) Å	γ = 90°
Volume	1683.3(2) Å^3	
Z	4	
Density (calculated)	1.312 Mg / m^3	
Absorption coefficient	0.085 mm^{-1}	
F(000)	704	
Crystal	Plate; Orange	
Crystal size	0.240 × 0.090 × 0.030 mm^3	
θ range for data collection	3.084 – 27.483°	
Index ranges	$-12 \le h \le 12$, $-14 \le k \le 14$, $-21 \le l \le 21$	
Reflections collected	17195	
Independent reflections	3857 [R_{int} = 0.0631]	
Completeness to θ = 25.242°	99.8 %	
Absorption correction	Semi–empirical from equivalents	
Max. and min. transmission	1.000 and 0.553	
Refinement method	Full-matrix least-squares on F^2	
Data / restraints / parameters	3857 / 0 / 227	
Goodness-of-fit on F^2	1.033	
Final R indices [$F^2 > 2\sigma(F^2)$]	*R1* = 0.0588, *wR2* = 0.1664	
R indices (all data)	*R1* = 0.0672, *wR2* = 0.1743	
Extinction coefficient	n/a	
Largest diff. peak and hole	0.467 and –0.188 e Å^{-3}	

Table S4. 2: Crystal Data and Structure Determination Refinement for AuL6

Crystal	**2014ncs0914 / ELJ443**	
Empirical formula	$C_{21}H_{20}N_2O_2$	
Formula weight	790.62	
Temperature	100(2) K	
Wavelength	0.71075 Å	
Crystal system	Monoclinic	
Space group	*C*2/*c*	
Unit cell dimensions	*a* = 22.8825(16) Å	α = 90°
	b = 9.2776(7) Å	β = 106.004(2)°
	c = 30.604(2) Å	γ = 90°
Volume	6245.3(8) Å^3	
Z	8	
Density (calculated)	1.682 Mg / m^3	
Absorption coefficient	4.802 mm^{-1}	
F(000)	3136	
Crystal	Blade; Orange	
Crystal size	0.160 × 0.060 × 0.020 mm^3	
θ range for data collection	1.983 – 27.500°	
Index ranges	$-28 \le h \le 29$, $-12 \le k \le 12$, $-38 \le l \le 39$	
Reflections collected	27469	
Independent reflections	7153 [R_{int} = 0.0388]	
Completeness to θ = 25.242°	99.8 %	
Absorption correction	Semi–empirical from equivalents	
Max. and min. transmission	1.000 and 0.697	
Refinement method	Full-matrix least-squares on F^2	
Data / restraints / parameters	7153 / 0 / 407	
Goodness-of-fit on F^2	1.016	
Final *R* indices [$F^2 > 2\sigma(F^2)$]	*R1* = 0.0226, *wR2* = 0.0536	
R indices (all data)	*R1* = 0.0275, *wR2* = 0.0554	
Extinction coefficient	n/a	
Largest diff. peak and hole	0.801 and –0.709 e Å^{-3}	

Diffractometer: *Rigaku AFC12* goniometer equipped with an enhanced sensitivity (HG) *Saturn724+* detector mounted at the window of an *FR-E+ SuperBright* molybdenum rotating anode generator with HF *Varimax* optics (100µm focus). **Cell determination and data collection**: *CrystalClear-SM Expert 3.1 b27* (Rigaku, 2013). **Data reduction, cell refinement and absorption correction**: *CrystalClear-SM Expert 3.1 b27* (Rigaku, 2012). S**tructure solution**: *SUPERFLIP* (Palatinus, L. & Chapuis, G. (2007). J. Appl. Cryst. 40, 786-790.) S**tructure refinement**: *SHELXL-2013* (G Sheldrick, G.M. (2008). Acta Cryst. A64, 112-122.). **Graphics:** *ORTEP3 for Windows* (L. J. Farrugia, J. Appl. Crystallogr. 1997, 30, 565.)

Chapter 5

Fluorescent Rhenium Anthracene–derived Conjugates as Cellular Imaging Agents

5.1 Introduction

Cancer is the leading cause of human mortality. Consequently there is a pressing requirement for the development and understanding of new anticancer agents,[1] for which anthracene derivatives are a promising avenue. The synthesis and characterisation of two new functionlised anthracene–1,9–dicarboximide fluorophores, together with their Re(I) complexes are described herein. These new compounds were assessed for cell imaging capabilities, *via* the fluorescent anthracene ligand. The results allowed the cellular uptake and distribution to be determined.

5.1.1 Biological Properties of Anthracene–1,9–Dicarboximide Derivatives

Anthracene derivatives are comprised of a large, planar, polyaromatic system. As with naphthalimide species discussed in earlier chapters, they are of key interest due to their potential as anticancer agents.[2-5] However, despite such anthracene species possessing interesting medicinal and photophysical properties, their poor solubility[2] and non–selective nature[5] has been a hindrance to their investigation and application.

Anthracene–1,9–dicarboximides offer a route to more soluble products. Importantly they are very similar in structure to the known anticancer drug Amonafide (Figure 5.1),[4-6] however the naphthalimide core is replaced by an anthracene unit. Such anthracene–1,9–dicarboximides were first developed in the 1980s,[1] derived from work by Braña *et al*. on DNA intercalators.[4,6] The parent drug is called Azonafide (Figure 5.1), although many variants have since been synthesised.[1,6,7] The potency of such species is proportional to the DNA binding strength,[1,4,6,8] however this is not true for all analogues and therefore a method of investigating their mode of action[4] and metabolic fate,[6] is key. The agents have been shown to induce both single and double strand DNA breaks in addition to DNA cross–links, typical of topoisomerase II inhibition.[4,6]

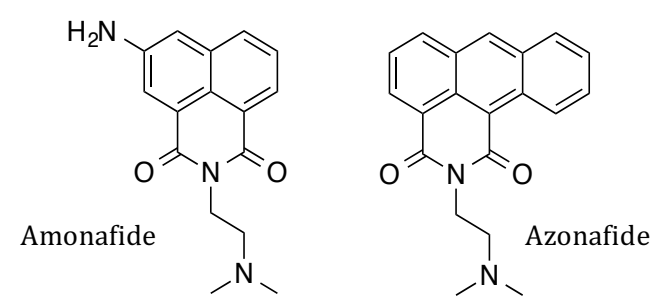

Figure 5.1: Structure of Amonafide and Azonafide, two related anticancer drugs.

Azonafide has shown enhanced potency when compared to Amonafide, its naphthalimide analogue.[3,6-9] For example in structures with three or more fused benzene rings only one amine chain is required to induce antitumour activity.[9] Structure–activity relationship correlations have suggested that substituent position and both the basicity and chain length of the amine group determine the potency of such anticancer agents.[1,9] Of these, the chemical properties of the amine are the most important factor. For example, the drug potency completely disappears upon replacing a tertiary amine with either a secondary or primary amine.[6] It is thought that the chain length is an important factor in positioning protonated amines close to hydrogen bonding sites in DNA. The basicity is important because it affects the ability of such drugs to pass through lipophilic membranes. The pKa of Amonafide and Azonafide is *ca*. 7.3 and therefore 67 % of the molecules are protonated at physiological pH.[9]

5.1.2 Photophysical Properties of Anthracene–1,9–Dicarboximide Derivatives

As well as rich biological properties, anthracene derivatives are known to possess strong photoluminescent, electroluminescent and electrochemical properties.[10] Consequently anthracene derivatives are used in the formation of many dyes (such as Alizarin red), photosensitisers for lanthanide complexes[11] and have also been investigated towards deep–blue OLEDs (Figure 5.2).[10]

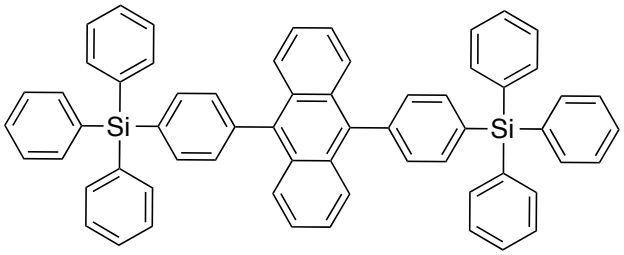

Figure 5.2: Anthracene based OLED by Kim *et al*.[10]

Specifically, anthracene–1,9–dicarboximides possess very interesting photophysical properties due to their strong emission and good photostabilty.[2] These properties have led to such derivatives being commonly used in the synthesis of emerald green dyes and pigments, such as Aceanthrene Green (Figure 5.3).[2] Anthracene–1,9–dicarboximide species are also light sensitive, which introduces many interesting properties. For example such products are known to photodimerise (4π + 4π cyclisation) in daylight, reversed by exposure to UV light[2,12] and have also been shown to form excimers at high concentration.[13,14] The photochromic and dimerisation properties of these species are the basis of many potential applications. Specifically the photodimerisation is key to

anticancer and DNA binding properties[2] and such dimeric species have been utilised as photosensitisers for photodynamic therapy due to absorption at therapeutic wavelengths (500–850 nm).[15] On the other hand, dimerisation needs to be avoided in order to improve solubility; excimer behaviour needs to be disrupted to allow for 'clean' OLED emission.[10]

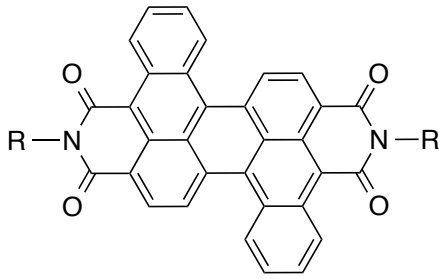

Figure 5.3: Core structure of Aceanthrene Green dyes.

The high degree of conjugation and electron fluidity in functionalised anthracene–1,9–dicarboximides results in relatively low energy emission (*ca*. 500 nm)[16,17] for an organic system, often structured due to the rigidity of the anthracene core. The energy is also slightly lower than for other anthracene species (*ca*. 430–460 nm).[13,14,16,18] Anthracene–1,9–dicarboximide species also possess the corresponding large Stokes' shift and long fluorescence lifetimes >10 ns, which are both favourable photophysical attributes in cell imaging.[14]

5.1.3 Fluorescent Anthracene Species as Biological Probes

The favourable photophysical properties of anthracene–1,9–dicarboximides are highly suited towards confocal fluorescence microscopy (CFM). Considering this alongside the desire for a better understanding of Azonafide's mode of action, it is surprising that, to my knowledge, there is only one reported example of cellular imaging with such species. In 1999, Mayr *et al*. reported CFM studies on Chinese hamster ovarian cells using a range of 6– and 7–substituted Azonafide derivatives, with the view to providing additional insight as to the drug's mode of action.[4] All derivatives showed rapid uptake into the cells with varied cytoplasmic, nuclear and perinuclear staining, depending on the nature of the substitution. Although the staining patterns were varied, all observations were consistent with DNA intercalators, such as Mitoxantrone and Doxorubicin, which are very similar in structure.

Other examples of anthracene derived biological probes include sensors by Chen *at al*.[19] and Guha *et al*.[20] for NaOCl and Cr(III) ions, respectively. Chen *et al*. developed ferrocene–anthracene conjugates that exploited ferrocene quenching *via* ICT. Upon exposure to

NaOCl incubated HeLa cells the strong, blue fluorescence was restored (Figure 5.4). Guha *et al*. reported an anthracene appended coumarin probe that similarly only fluoresced in cells with the presence of Cr(III). Anthracene functionalised nanoparticles have also been reported and used during cell imaging of HeLa cells.[21] Although CFM was conducted on these species, only uptake and emission was assessed towards 'on–off' *in vitro* sensors. Localisation was not described and therefore knowledge of the precise mode of action of Azonafide derivatives can be vastly improved with the development of new anthracene–1,9–dicarboximide cellular imaging agents.

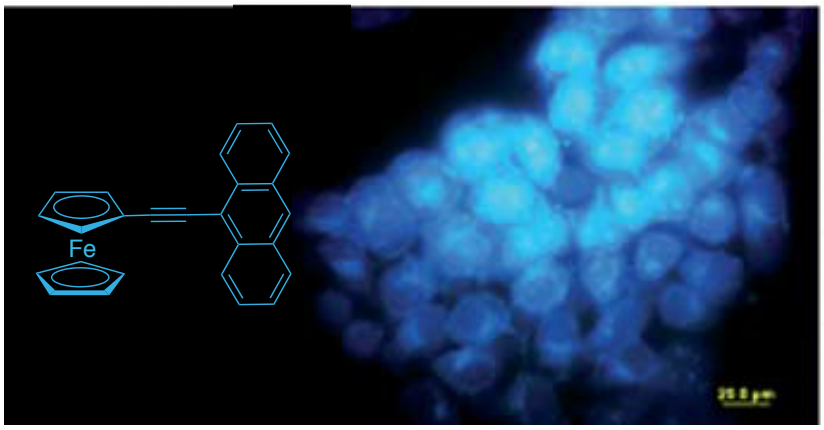

Figure 5.4: CFM image of NaOCl loaded HeLa cells by Chen *et al*.

5.1.4 Biological Probes that Exploit Excimer Behaviour

Excimers are dimers of molecules in the excited state. They are formed *via* collisions and therefore their creation is typically concentration dependent. Often luminescent compounds with strong π–π stacking, such as anthracene or pyrene species, lead to excimer formation. Excimers exhibit a bathochromic shift of the emission when compared to the monomer emission due to the energy of the excited states becoming delocalised over the two molecules, causing a decrease in energy and excimeric fluorescence. This favourable shift is useful for sensing applications. This is especially true for biological probes/imaging agents because the bathochromic shift results in more tissue friendly wavelengths and can easily be differentiated from autofluorescence.

The concentration dependent nature of excimer behaviour is a useful technique in cell imaging, especially to detect areas of localisation. All cell membranes possess a redox potential and therefore compounds can be actively taken into various organelles and concentrated, changing the emission wavelength *via* excimer formation in such organelles. This is especially true in the mitochondria for which compounds are found at *ca*. 1000

greater concentration than for outside the cell wall. The mitochondrial stain JC–1 (Figure 5.5) is an example of a molecular probe that uses this principle to determine membrane potential/polarisation (Section 5.3.5: Concentration dependent studies).

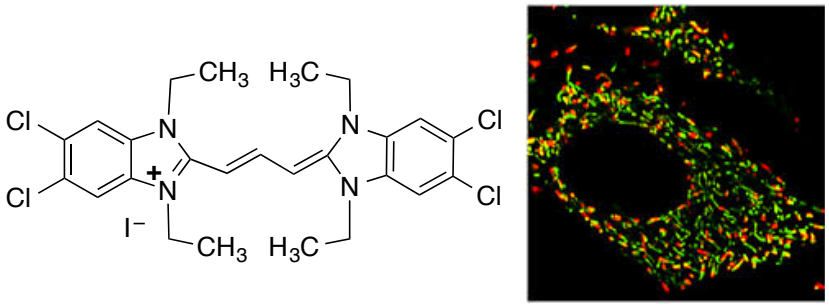

Figure 5.5: Mitochondrial potential stain, JC–1 in cellular imaging.

5.2 Aims

Work in this chapter aimed to further the research and development into novel luminescent rhenium (I) complexes based around anthracene derived ligand systems as potential anticancer cellular imaging agents.

This work aimed to fully characterise both spectroscopic and photophysical properties of the ligands and corresponding complexes. ^{1}H NMR and mass spectrometry data was collected to confirm the formation of the desired compound. UV-vis spectroscopy data was utilised to obtain information on the absorptivity of the compounds, which would then be used in conjugation with luminescent data to fully characterise the photophysics of the compounds.

Compounds synthesised will have the potential to be used for medical research *via* use in fluorescence imaging and with potential anticancer properties due to the high toxicity observed for many anthracene based ligands. Therefore the range of compounds herein were also subjected to confocal fluorescence microscopy and cellular studies to develop a preliminary understanding of the biological potential.

5.3 Results and Discussion

5.3.1 Ligand Synthesis and Characterisation

L1 and **L2** were both synthesised from anthracene–based precursors according to literature methods (Scheme 5.1), always taking into consideration the light sensitive nature of the products that photodimerise (4π + 4π cyclisation) in daylight.[2,12] Firstly a Friedel–Crafts reaction between anthracene and oxalyl chloride formed the diketone precursor, followed by oxidation to anthracene–1,10–dicarboxylic anhydride *via* the dicarboxylic acid intermediate.[2,22] **L1** and **L2** were then formed by reacting the anhydride precursor with the appropriate amine in ethanol.[23]

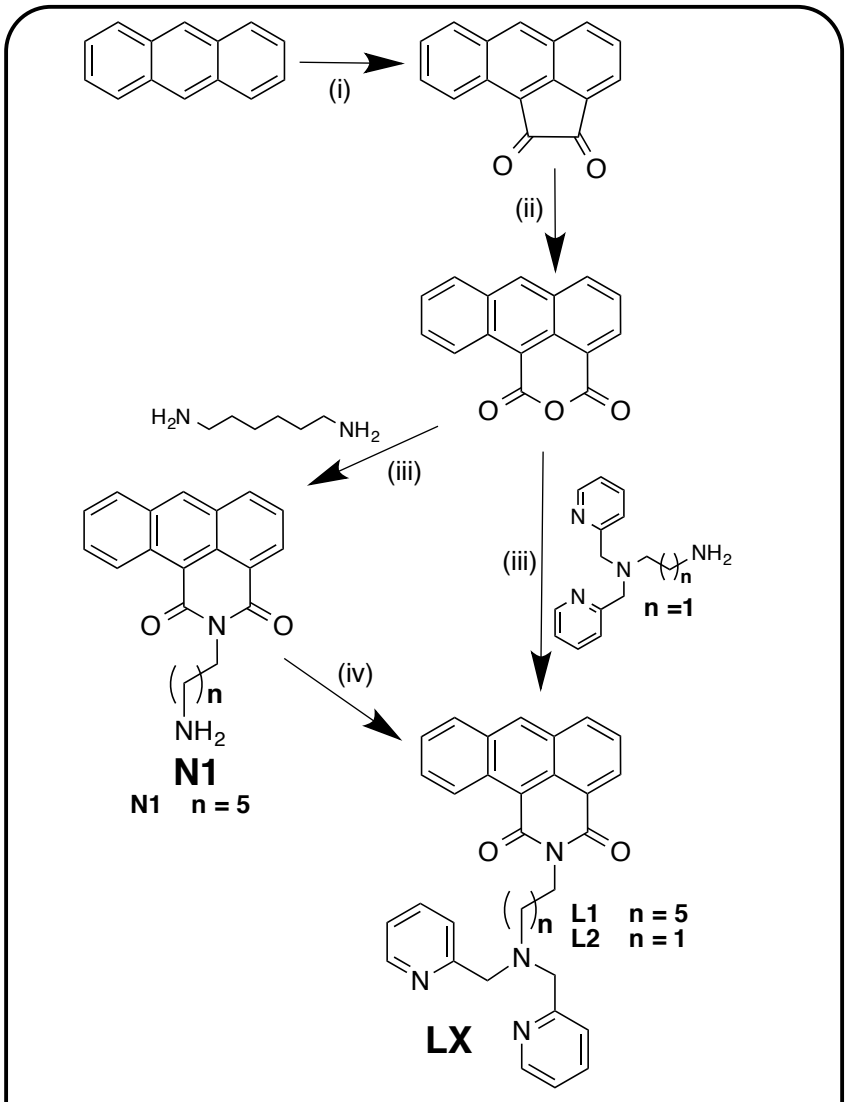

[a](i) oxalyl chloride, anhydrous $AlCl_3$, CS_2; (ii) NaOH, 30 % H_2O_2 solution, 1,4–dioxane, then H_2SO_4; (iii) depicted amine, EtOH; (iv) 2–pyridinecarboxaldehyde, $NaBH(OAc)_3$, 1,2–dichloroethane.

Scheme 5.1: Synthetic route to the ligands.[a]

For **L1** this was achieved *via* a reaction with 1,6–diaminohexane, added in 4–fold excess to avoid the formation of anthracene dimers. This proligand, **N1**, then underwent a one–pot reductive amination reaction using methods adapted from Chapter Three.[24] **N1** was stirred with 2–pyridinecarboxaldehyde in the presence of triacetoxyborohydride in 1,2–dichloroethane for a 4 day period, during which reaction progression was monitored by TLC (95:5 DCM:MeOH). This final reaction step to form **L1** was poor yielding (27 %), mostly due to a visible loss of product during purification *via* column chromatography. The above 2–step synthetic approach did not successfully yield **L2.** The successful synthesis of **L2** required the 2–dipicolylamine (2–DPA) binding site to be preformed on the ethylene linker, therefore requiring another multi–step synthesis. Firstly 1,2–ethylenediamine was mono–BOC–protected. The same reductive amination reaction as for **L1** was then applied to introduce the 2–DPA binding site to *N*–*tert*–Boc–ethylenediamine. Subsequent deprotection of the BOC–group with TFA yielded the appropriate amine to react with anthracene–1,10–dicarboxylic anhydride. All of the synthetic steps to form this amine were high yielding (65–84 %) resulting in a combined yield of 45 %. Fortunately the final synthetic step to form **L2**, reacting this amine with anthracene–1,10–dicarboxylic anhydride in ethanol, was very high yielding (98 %). Therefore the combined yield to form **L2**, including all the additional steps, was still higher than the yield of **L1**. This was partly explained by the hexyl linker of **L1** resulting in a highly soluble, oily product that made purification and isolation very difficult.

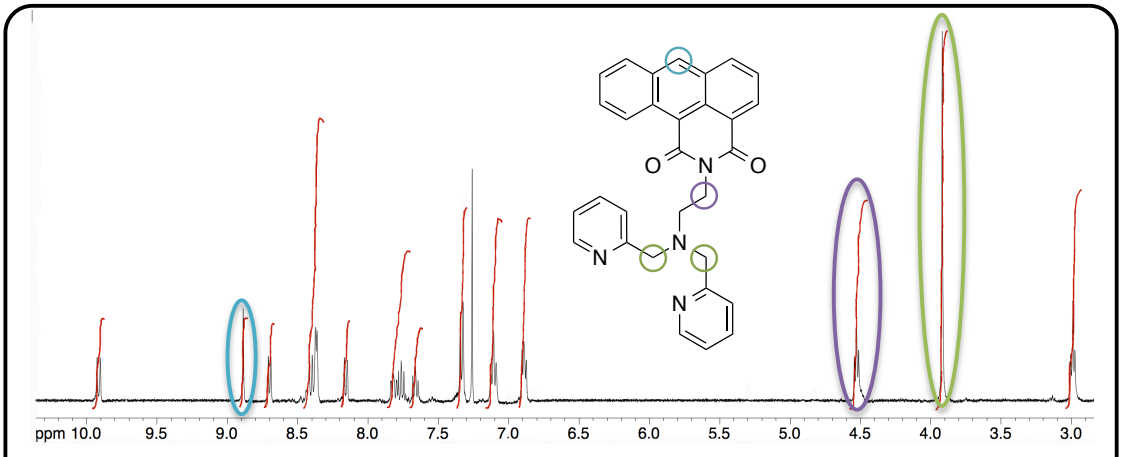

Figure 5.6: ^{1}H NMR spectra (400 MHz, $CDCl_3$) of L2 highlighting identifiable peaks.

Successful formation of both **L1** and **L2** was confirmed using ^{1}H and ^{13}C{^{1}H} NMR spectroscopies, IR spectroscopy and mass spectrometry. Upon hydrolysis of anthracene–1,10–dicarboxylic anhydride with an amine there was a general upfield shift of the aromatic protons, correlating well with previous naphthalimide analogues reported in

Chapter Three.[24] The aromatic resonances of anthracene–1,10–dicarboxylic anhydride were observed between 9.75–7.72 ppm whereas they were shifted to 9.79–7.50 ppm and 9.90–6.87 ppm, for **L1** and **L2** respectively (Figure 5.6). In addition the formation of **L2** also resulted in a marked shift of the aliphatic protons nearest the imide moiety, i.e. $N_{imide}CH_2$ (Figure 5.6); a downfield shift from 2.24 ppm (in bis(pyridin–2–ylmethyl)ethane–1,2–diamine) to 4.51 ppm in **L2** was observed due to an increase in deshielding from the electron withdrawing carbonyl groups. For **L1** this resonance was observed at 4.19 ppm and therefore both values were in good agreement with the literature precedent of *ca.* 4.35 ppm.[2,7-9] Both ligands showed the presence of peaks for pyridyl protons that overlapped with the anthryl resonances, and therefore assignments in the Experimental Section are tentative and mainly based on integration. The ^{1}H NMR spectra of each ligand also showed the methylene linker protons (4H), observed as a singlet at 3.78 ppm and 3.90 ppm for **L1** and **L2** respectively.[24,25] This corresponds with free rotation of the pyridyl units in solution.

$^{13}C\{^{1}H\}$ NMR spectroscopy showed the expected number of resonances for the proposed structures of **L1** and **L2**. This technique was particularly useful in determining the differences in the carbonyl environments, caused by the unsymmetrical substitution of the anthracene core.[24] Two peaks at *ca.* 165 ppm and 163.5 ppm were observed for both ligands.[2] The differences were more prominent in these anthracene–based ligands than for related naphthalimide structures, presumably due to a higher degree of assymmetry.[25-27] IR spectroscopy was also used to distinguish differences in the carbonyl regions and spectra show two distinct carbonyl peaks at *ca.* 1680 and 1650 cm^{-1}.[2,28] Finally positive mode high resolution mass spectrometry (HRMS) showed the $[M]^+$ cation for **L2** and $[M+H]^+$ and $[M+Na]^+$ cations for **L1**, supporting the formation of the desired products.

After the successful synthesis of **L1** and **L2**, that possessed vastly different linker lengths, it was attempted to formulate subtle variants. This included intermediate chain lengths and incorporating branched linkers with the hope to improve solubility. Imide formation was attempted with 3–aminopropanol, 1,4–diaminobutane and 1,3–diamino–2–propanol. These reagents would allow the subsequent reductive amination reaction to introduce the 2–DPA moiety. The exception to this was the 3–aminopropanol derivative that would need to undergo a nucleophilic substitution reaction after conversion to the corresponding chloro product. The amphiphilic nature of these products made product purification and isolation very difficult. In addition the product from 1,3–diamino–2–propanol formed a black sludge, indicating that photodimerisation had occurred, even though care was taken

to exclude light in the reaction vessel. This suggested that the electronic nature of the imide group greatly affects the photosensitivity of these compounds.

As a further attempt to introduce additional functionality to **L1** and **L2** it was attempted to form a 6–bromo–anthracene–1,10–dicarboxylic anhydride precursor from 9–bromoanthacene. Even though the synthesis of 6–bromo–anthracene–1,10–dicarboxylic anhydride and several corresponding imide derivatives have been reported in papers[22] or patents,[29,30] attempts at Cardiff to synthesise 6–bromo–anthracene–1,10–dicarboxylic anhydride were unsuccessful. This was possibly due to deviations from the stated conditions having to be employed. Neither variants were pursued any further.

5.3.2 Complex Synthesis and Characterisation

The preordered rhenium precursor complex *fac*–$[Re(CO)_3(MeCN)_3]BF_4$ was first synthesised[31] to be correctly designed for facile coordination to **L1** and **L2**, as for work within Chapter 3.[24] $[Re(CO)_3(\mathbf{LX})]BF_4$ (**ReL1** and **ReL2**) were formed *via* the reaction of each ligand with $[Re(CO)_3(MeCN)_3]BF_4$ in chloroform,[32] substituting the three facially arranged acetonitrile ligands with the 2–DPA binding group (Scheme 5.2). Reaction progression was monitored using TLC (14:2:1 mix of H_2O:MeCN:sat. aq. KNO_3), exploiting the charged and coloured nature of the product, until no free ligand was present in solution. The off–white to yellow powders were isolated by precipitation with diethyl ether. The lack of need for column chromatography resulted in relatively high yields *ca*. 65 %. The small scale of these reactions was most likely a large contributory factor to the loss of material; for example a small loss of solids on a sintered funnel results in a large drop in yield for such small scale reactions.

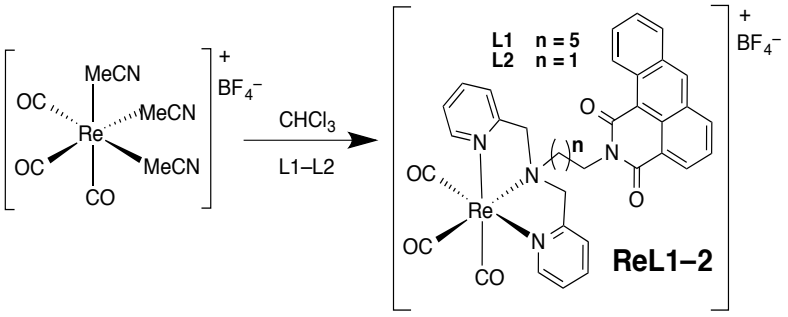

Scheme 5.2: Synthetic route to the complexes.

In order to confirm the proposed N_3 facially capped Re(I) complexes, **ReL1** and **ReL2** were fully characterised *via* NMR and IR spectroscopy. ^1H NMR spectroscopy (Figure 5.7) was used to confirm coordination of the ligand to Re(I) whereby upon coordination, the imide–CH_2 shifted by *ca*. 0.1 ppm, however the methylene linker shifted significantly compared to

the free ligands (*ca*. 3.8 ppm to *ca*. 5.3 and 4.4 ppm). Furthermore, akin to the related naphthalimide structures in Chapter Three,[24] coordination of **L1** and **L2** to Re(I) caused a splitting of the singlet resonance for the CH_2–pyr linker seen for the ligands. The resultant diastereotopic protons displayed a $^2J_{HH}$ geminal coupling[33] (16–17 Hz) in the ^{1}H NMR spectra of both complexes, confirming the proposed facial binding mode. This was crucial considering the lack of crystal structures of this set of compounds. In addition the pyridyl resonances shifted to a lower field upon coordination, consistent with the coordinative bonds influencing electron distribution across nearby bonds.[17]

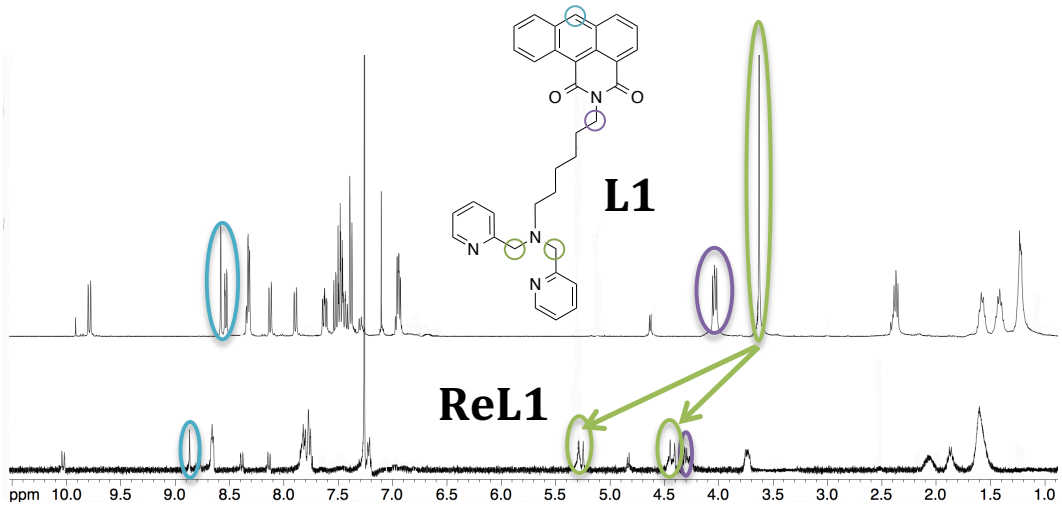

Figure 5.7: Comparison of the ^{1}H NMR spectra ($CDCl_3$, 400 MHz) of L1 (top) and ReL1 (bottom), highlighting significant resonances.

^{13}C{^{1}H} NMR spectroscopy was performed on **ReL2** however the spectra for **ReL1** was too weak to analyse. The two resonances for metal bound carbonyls were observed at a higher shift (*ca.* 195 ppm) than that for imide–carbonyls (*ca.* 165ppm). The observation of two carbonyl resonances in the ^{13}C{^{1}H} NMR spectra of **ReL2** and two metal bound CO stretching frequencies in the IR spectra of both complexes[33] (*ca*. 2030 and 1905 cm^{-1}) further supported the facially capped Re(I) geometry (pseudo C_{3v}). Furthermore, high resolution mass spectrometry confirmed the presence of Re(I), showing $[M]^+$ with the correct $^{185/187}$Re isotopic pattern[34] in all cases.

5.3.3 UV–vis Absorption Spectroscopy

The solution state absorption spectra of **L1** and **L2** (Figure 5.8) were recorded as MeCN solutions at 2.5 × 10^{-5} M and were closely comparable to related literature examples.[28] Both ligands showed three main absorption peaks, dominated by two strong (ε = 33,000–82,000[28] M^{-1}cm^{-1}) π–π* transitions at *ca*. 200 and 265 nm.[17,18,28,35] Of these, the lowest energy peak is known to originate from the anthracene core,[18] with the shoulder to 350

nm likely to have arisen from the 2–DPA moiety.[18] The ligands appear orange–brown in colour due to weaker (*ca*. ε = 8000 $M^{-1}cm^{-1}$),[2] broad and heavily structured[12,35] low energy π–π* transitions observed at 350–480 nm due to the extended conjugation, again well known for anthracene species.[17,18,35] The linker length seemed to have little effect on the absorption properties, however the extinction coefficients of **L2** were roughly a third larger than for **L1**.

Compared to the ligands and complexes reported in Chapter Three,[24] extending the π–system of the naphthalimide core to an anthracene unit in **L1** and **L2**, bathochromically shifted the absorption profiles to be highly compatible with confocal fluorescence microscopy, without the requirement of strong ICT bands providing good absorption at suitable wavelengths.

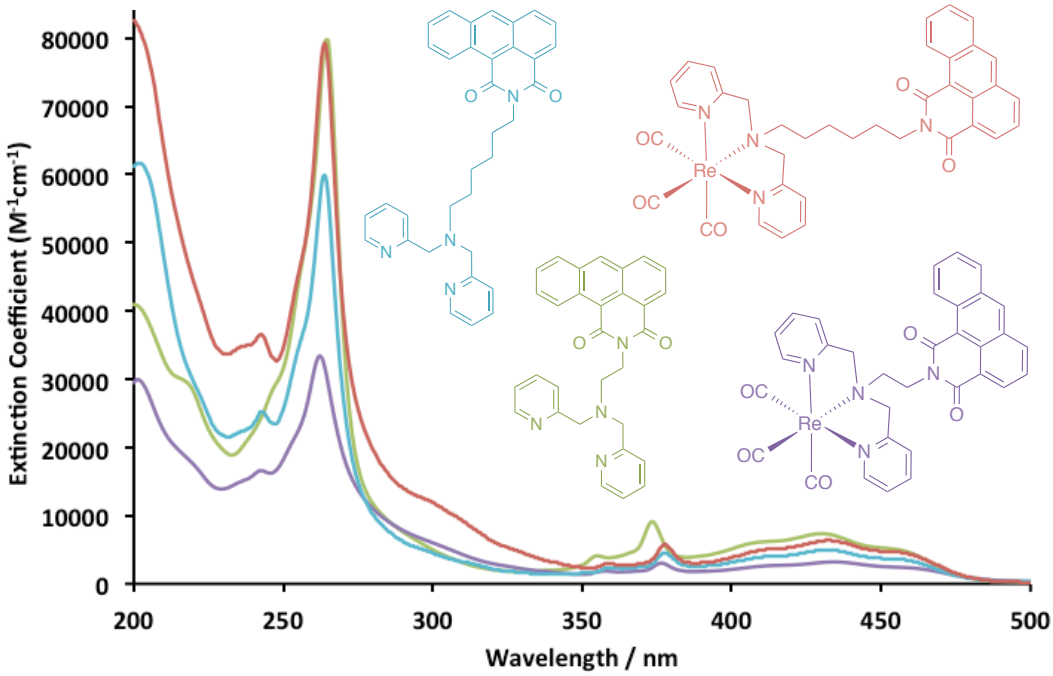

Figure 5.8: UV–vis absorption profiles of the ligands and complexes in MeCN at 2.5 × 10^{-5} M.

UV-vis spectroscopy was also conducted on the complexes (Figure 5.8). The absorption spectra of **ReL1** and **ReL2** were almost identical to the free ligands and therefore heavily ligand dominated.[35] Unlike the naphthalimide analogues reported in Chapter Three, upon coordination to Re(I) no obvious hypsochromic shift of the bands was observed.

5.3.4 Luminescence Spectroscopy

Ligand Properties

Solutions of **L1** and **L2** were found to be highly luminescent, as expected for anthracene–derived species (Figure 5.9 and Table 5.1). Steady state luminescence data showed that both ligands had very similar luminescent character. The strongest excitation peak was observed at 265 nm.[12] Comparison of the emission wavelength to the lowest energy absorption band revealed large Stokes' shifts for the ligands (*ca*. 170000 cm^{-1}), a favourable attribute for cell imaging applications. The large Stokes' shifts are thought to be caused by the pyridine groups acting as donor components to the anthracene ring and lowering its energy. In addition to the excitation peak at 265 nm, **L2** (with the shorter linker length) also possessed an additional, weaker, lower energy excitation band between 350–500 nm (Figure 5.9). This could be attributed to the extension of the conjugated system, lowering the energy of the excited state.

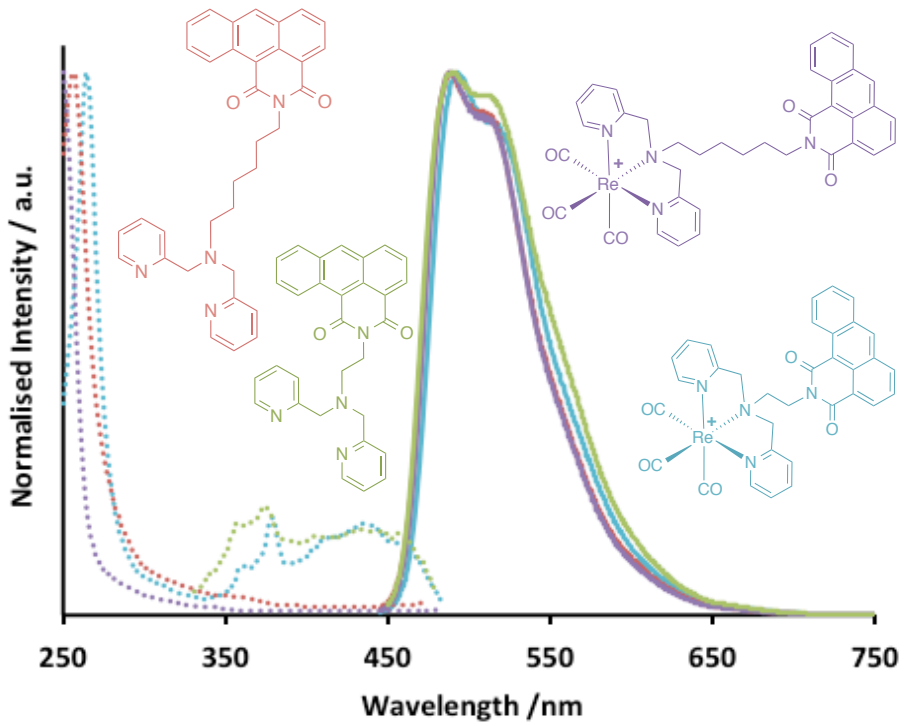

Figure 5.9: Excitation (dotted) and emission (solid) spectra of L1–2 and corresponding complexes in MeCN at 5 × 10^{-5} M.

Using an excitation wavelength of 345–425 nm on **L1–2** as aerated MeCN solutions revealed a visible emission band centred at 490 nm (10^{-5} M), with a lower energy shoulder at 510 nm[2] (Figure 5.9), both originating from the anthranyl luminophore.[16,17] This was almost identical to the naphthalimide analogues reported in Chapter Three.[24] The energy was slightly lower than typical for anthracene species (*ca*. 430–460 nm),[13,14,16,18] presumably due to the extension of the conjugated system *via* the imide unit. The emitting state of **L1–2** is likely to be mostly π–π* in character, with examples showing weak

vibronic structure, consistent with the rigid anthracene chromophore. This assignment was further supported by the chain length having little effect on emission properties.

In addition to steady state measurements, time resolved luminescence data was also collected in MeCN. Both ligands showed relatively long fluorescent lifetimes of approximately 3.3–16.0 ns (Table 5.1). The data for **L1** best fit to a bi–exponential decay with a minor quenched species (3.3 ns, 34 %) and major, longer component (10.6 ns, 66 %). On the other hand, the lifetime of **L2** was shown to be single component and extended compared to **L1**. Similar 9,10–bis(4–aminophenyl)anthracene examples by Sugino *et al*. best fit a tri component decay[14] with components <1 ns, *ca*. 3 ns and *ca*. 12 ns and therefore agree well with data in Table 5.1.

Complex Properties

Luminescence data was also collected for **ReL1** and **ReL2** as aerated MeCN solutions. A comparison of the ligands to their corresponding metal complexes yielded interesting results. As for the naphthalimide analogues reported in Chapter Three,[24] coordination of **L1** and **L2** to Re(I) had minimal effects on the excitation and emission profiles (Figure 5.9 and Table 5.1).

Table 5.1: Luminescent properties of the ligands and complexes.

Compound	λ_{em} / nm[a]	τ / ns[b]	ϕ[c]
L1	489, 509s	3.3 (67 %), 10.6 (33 %)	–
L2	490, 510 s	16.0	–
ReL1	489, 509s	6.7	0.36
ReL2	489, 510s	14.5	0.19

[a]MeCN, λ_{exc} = 425 nm, 5 × 10^{-5} M, [b]MeCN, λ_{exc} = 459 nm, [c]Aerated MeCN.

However, crucially upon coordination to Re(I) a shortening of the lifetimes was observed (Table 5.1), presumably due to an increase in non–radiative decay rates. On the other hand, both complexes displayed excellent quantum yields at 36 % and 19 % for **ReL1** and **ReL2**, respectively. Although favourable, the quantum yields of **ReL1–2** were found to be less than half those reported for the naphthalimide analogues in Chapter Three.[24]

5.3.5 Confocal Fluorescence Microscopy

Having recognised that the anthracene–based ligands and Re(I) complexes possessed favourable and attractive photophysical properties for fluorescence imaging (Stokes' shifts, intense emission *etc.*), CFM was conducted to assess the imaging capability of the series of compounds. The compounds were incubated with *Schizosaccharomyces pombe* (*S. Pombe*)

(fission yeast cells) due to their ease of culture and also MCF7 breast cancer cells due to their well understood ultrastructure. Following washing to remove the compounds from the culture medium, cells were imaged with λ_{exc} = 405 nm and detection between 480–540 nm (and 630–690 nm to probe red emission) with × 63 lens, × 4 zoom factor and 20% laser power.

Cell incubation with the compounds at a concentration of 10 μg mL^{-1} resulted in very poor uptake by the cells[36] however yeast cell walls are known to be relatively impermeable. To improve the cell uptake the concentration of the compounds was increased to 100 μg mL^{-1}. All compounds were found to photobleach (known as fading) quickly. Unstained controls of both cells showed completely negative autofluorescence signals at the detection wavelengths that were applied.

Ligand Properties

In general **L1** showed better results than **L2** due to enhanced solubility and uptake, showing that a slight structural variation of the linker length greatly affected the imaging capability of the free ligands. The uptake for **L1** and **L2** into *S. pombe* yeast cells was good once the higher incubation concentration was utilised, in both cases resulting in very bright emission.[21] **L1** had good uptake into all cells and revealed distinct foci of staining. **L2** showed a slightly weaker fluorescence in most cells.

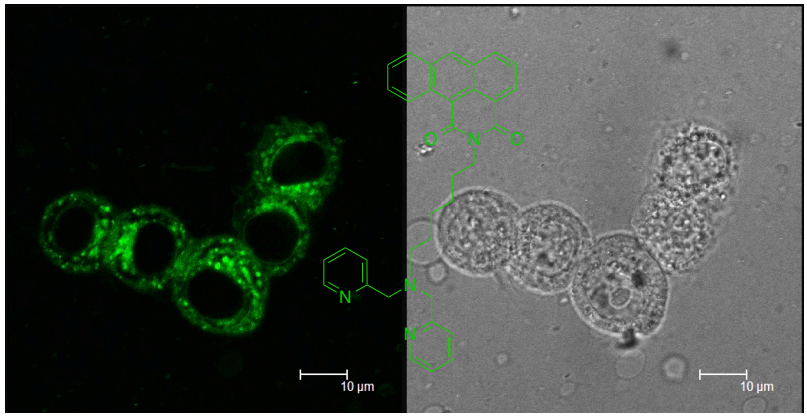

Figure 5.10: CFM images of MCF7 with L1 showing: (left) green fluorescence from L1 (λ_{exc} = 405 nm; λ_{em} = 480–560 nm) and (right) transmitted light image.

Uptake of **L1** and **L2** into MCF7 was better than for *S. Pombe* yeast cells, however the cells were tightly clustered which made imaging quite difficult. **L1** again revealed bright emission with a small amount of precipitate. General cytoplasmic labelling was observed with distinct foci of emission, possibly the mitochondria. This would correlate well with

related examples in Chapter Three.[24] In addition to the mitochondrial staining, **L1** also showed perinuclear staining,[4,37] possibly of the Golgi apparatus (Figure 5.10). No nuclear penetration was observed[24,37,38] but faint membrane staining revealed slight membrane blebbing, possibly indicating cell apoptosis. Imaging of MCF7 cells with **L2** as the probe was not as successful due to high amounts of precipitate, even visible by the naked eye. This resulted in no uptake into the cells, with the precipitate sitting around or on top of the cells. The aggregates possessed red emission, possibly due to π–stacking causing excimer behaviour (see 5.3.5 Concentration dependent studies).

Complex properties

CFM studies were also conducted on **ReL1** and **ReL2** with both *S. Pombe* yeast and MCF7 cells. Vast differences were observed for the imaging capability and cellular localisation of the free ligands and corresponding complexes. **ReL1** showed weaker emission in *S. Pombe* yeast cells than for **L1. ReL1** was taken into most of the cells however the faint emission revealed little detail. **ReL2** was only seen to label a subset of cells, possibly indictating uptake into dead or dying cells (Figure 5.11). This hypothesis was supported by the presence of ruffled membranes.

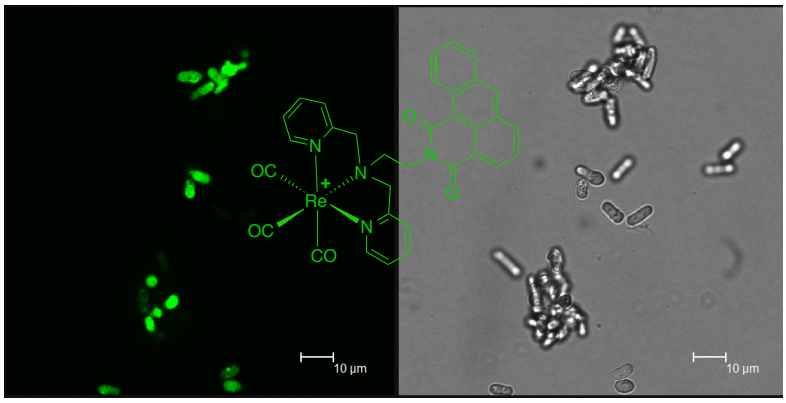

Figure 5.11: CFM images of *S. pombe* yeast cells with ReL2 showing: (left) green fluorescence from ReL2 (λ_{exc} = 405 nm; λ_{em} = 480–540 nm) and (right) transmitted light image.

ReL2 seemed to localise in the mitochondria[24] where a red signal was also detected by eye (see 5.3.5 Concentration dependent studies). Unfortunately, no image could be collected showing this phenomenon due to bleed through between the red and green channels. Preliminary cytotoxicity studies showed a viable population count of 84 % after imaging against the unstained control. Therefore **ReL2** showed slight cytotoxicity towards *S. pombe* yeast cells, almost identical in value to a related literature example.[21]

Imaging of MCF7 cells with **ReL1** and **ReL2** showed that all of the stained cells had an unhealthy 'foamy' appearance with some membrane blebbing, indicating apoptosis, akin to **L1** and related examples in Chapter Three.[24] **ReL1** again showed very bright green emission that revealed many round intracellular structures (negative signal)[4] with stained membranes, possibly correlating to natural lipid vacuoles[24,39] or artificial vesicles that can be induced upon cell stress or injury (Figure 5.12). This indicated that **ReL1** also possessed some cytotoxicity *via* the metal centre, as for **ReL2**. Uptake of **ReL2** into MCF7 was much improved when compared to **L2**, presumably due to the enhanced lipophilicity of the *fac*–$Re(CO)_3$ unit.[24] With MCF7 cells **ReL2** again showed a signal in both the red and green channel but channel bleedthrough indicated no differential colour staining in different areas of the cell. **ReL2** was seen to stain both the plasma and nuclear membranes,[4] nucleolous[40] and perinuclear area[37] (Golgi apparatus) (Figure 5.12) as seen for **L1** and related azathiaxanthone examples.[37,40]

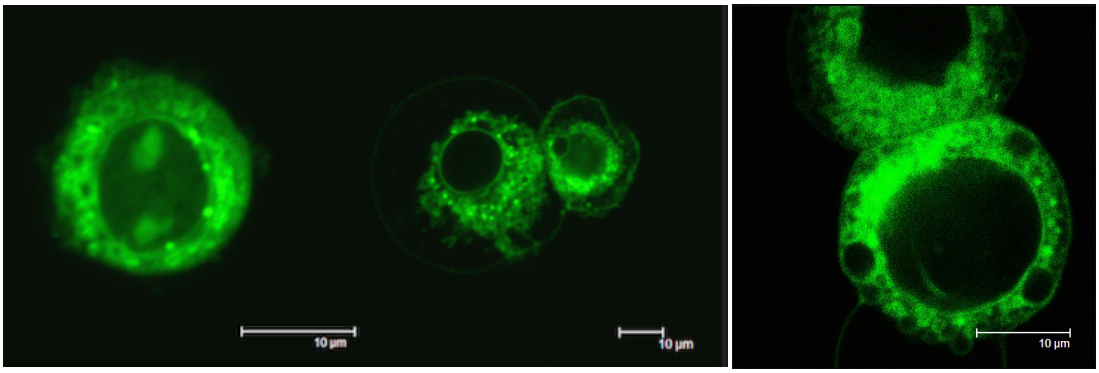

Figure 5.12: CFM images of MCF7 cells imaged using (left to right): ReL2 showing nucleolus; ReL2 showing Golgi and membrane staining; and ReL1 showing possible vacuoles or vesicles (λ_{exc} = 405 nm; λ_{em} = 480–540 nm).

Concentration dependent studies

As alluded to in the previous section, imaging of *S. Pombe* yeast cells using **ReL2** as the fluorophore showed localisation in mitochondria, as well an interesting dual signal containing both green and red wavelengths. The red emission of **ReL2** was visually seen in the mitochondria but unfortunately no images could be collected due to channel bleed through. It was noted that the images showed similarities to a known mitochondria stain, JC–1, which has been previously used for quantitation of membrane potentials.[41] It has been established that JC–1 produces green fluorescence as a monomer, and red fluorescence upon J–aggregate formation which occurs in high potential membranes (λ_{exc} = 590 nm).[41,42] Anthracene species have also been shown to exhibit excimer behaviour and therefore concentration dependent luminescence studies were conducted to probe this.

Mitochondria have a double membrane that consists of an inner and outer phospholipid bilayer. The inner membrane has a protein–to–lipid ratio of 80:20, whereas the outer membrane has a ratio of 50:50.[43] The ratios are important because the outer membrane is permeable to a wide range of ions and large molecules, whereas the inner membrane is more selective[44] and therefore acts as an electrical insulator and chemical barrier.[45] Because the potential of the membrane is transient the uptake of compounds will be affected by the metabolic processes occurring at that time.[46] Due to the double membrane potential (cell wall and mitochondrial wall) the concentration of **ReL2** would be expected at *ca*. 1000 times greater inside the mitochondria compared to outside the cell.[47]

Our hypothesis was that the concentration of **ReL2** enabled excimer formation, causing a bathochromic shift in emission due to the delocalisation of the excited state across the dimers, resulting in a decrease in energy. However, anthracene species are also known to easily photodimerise. This is more probable than excimer formation and would also result in a bathochromic shift in the emission profile.[14] Therefore concentration dependent luminescence studies, up to expected mitochondrial concentrations (× 10^{-2} M), were attempted on **L1**, **L2** and corresponding complexes in order to elucidate the cause of the dual emission.

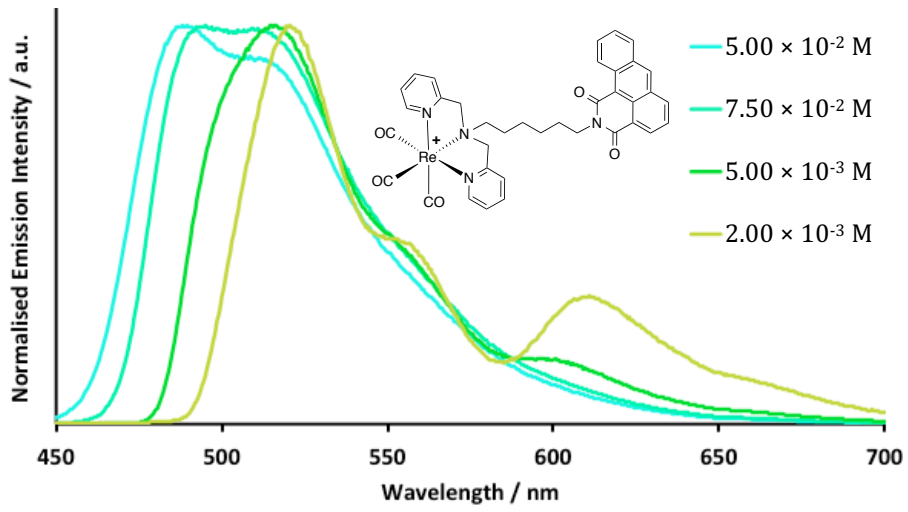

Figure 5.13: Concentration dependent emission of ReL1 in MeCN. λ_{exc} = 425 nm.

Luminescence data for aerated MeCN solutions was collected at six different concentrations between 5 × 10^{-5}–1 × 10^{-2} M for **ReL1–2** and 5 × 10^{-5}–1 × 10^{-3} M for the free ligands possesing lower solubility. All compounds showed a shift of emission wavelength upon increasing concentration. For **L1–2** and **ReL1** only a slight shift was witnessed from blue to green emission. In general, as the concentration was increased to × 10^{-4} M the

510 nm shoulder seen at lower concentrations (Figure 5.9 and Table 5.1) became of equal intensity, forming a wider plateaued emission profile (Figure 5.13). As the concentration increased again to × 10^{-3} M, the 510 nm peak became dominant with **L1** and **ReL1** possessing an additional shoulder at *ca*. 610 nm.

Excimer behaviour typically results in a broadening and bathochromic shift of the emission profile, accompanied by a loss of vibronic structure.[14] This is most widely known and understood for pyrene systems where the monomer structured emission profile typically sits between 375–410 nm; upon excimer formation the emission becomes broad and unstructured, centred ca. 480 nm. In addition a large extension of the lifetime, to *ca*. 50–90 ns, can be observed.[48,49] Reported examples of anthracene excimer behaviour are sparse however both report a shift of the emission to 513 nm[13] and 544 nm,[14] albeit in DMSO for the latter. Furthermore a general broadening of the emission peak was observed but the vibrational detail was maintained. Therefore observations for **L1**, **L2** and **ReL1** correlate well with these reported examples of anthracene excimer behaviour. However anthracene systems show photoreactivity and also allow photocyclisation that could also cause such observations. This hypothesis was negated by probing the reversibility of the observations; the strongest concentration was first prepared and other concentrations achieved by careful dilution. Therefore no structural photoinduced cycloaddition could have occurred due to the reversible trend upon dilution. In addition the photoreactions require basic conditions, long reaction time (days), high temperatures (*ca*. 230 ºC) and high flux photon source,[2] none of which are provided during CFM or luminescence studies.

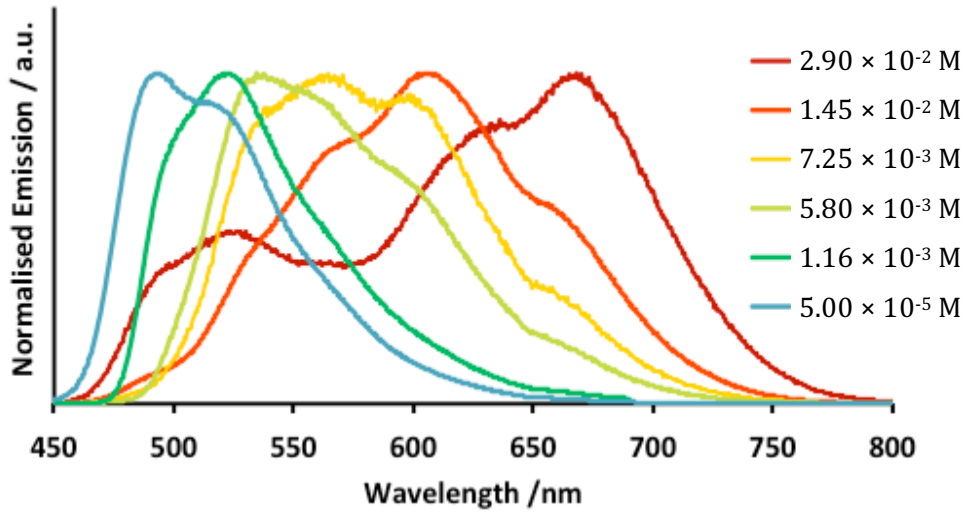

Figure 5.14: Concentration dependent emission of ReL2 in MeCN. λ_{exc} = 425 nm.

The concentration dependent luminescence behaviour of **ReL2** (Figure 5.14) was very different to the other compounds herein. A clear *ca*. 200 nm shift of emission wavelength upon increasing concentration was observed, from 490 nm (5.0×10^{-5} M) to *ca*. 680 nm (2.9×10^{-2} M). Therefore the emission profile for concentrations of $\times 10^{-2}$ M was in good agreement with the red emission observed in the mitochondria during the cell imaging studies. Clearly the linker length and incorporation of a metal greatly affected this behaviour.

The concentration dependent emission wavelengths supported the theory of excimer formation. Related examples by Sugino *et al*. showed the excimer to be extremely long lived with a lifetime of 29.2 ns.[14] This was not the case for **ReL2** that showed a lifetime of 7.4 ns when measured at 680 nm, compared to 6.7 ns at 490 nm. Detailed CFM studies showed extensive red/green channel bleedthrough and meant that the emission profiles were very broad and therefore did not allow determination of areas of different colour emission from the probe.

5.4 Conclusion

Two anthracene based ligands incorporating a facially capping 2–dipicolylamine unit were synthesised. The photophysical properties of **L1** and **L2** showed intense π–π* transitions at 200 and 265 nm with weaker π–π* transitions observed between 350–480 nm. This was replicated in the excitation spectra of the ligands. Both **L1** and **L2** were highly fluorescent with visible emission between 490–510 nm, with long fluorescence lifetimes ranging between 3–16 ns.

Each of the ligands were bound to Re(I), chosen due to the biological preference to d^6 kinetically inert metals and as a useful model for Tc(I). The photophysical properties of the **ReL1** and **ReL2** were highly ligand dominated. They possessed long ligand–based lifetimes between 6–15 ns and impressive quantum yields of 19 and 36 %.

Due to the favourable photophysical properties, cell imaging was undertaken on both the ligands and corresponding complexes. **L1** showed the most promising imaging capability of the free ligands and was seen to localise in the mitochondria and perinuclear region. Oppositely, of the complexes **ReL2** provided outstanding images and better results that **ReL1**. **ReL2** localised within mitochondria and penetrated the nuclear envelope to localise in the nucleolus (where ribosomes are synthesised after DNA transcription). Imaging with **ReL2** in yeast cells also yielded some interesting concentration dependent behaviour that was investigated and shown to be likely due to π–stacking effects and modulation of emission wavelength. The observed shift to red wavelengths at higher concentrations with **ReL2** should be highly beneficial because such wavelengths have a better depth of transmission in biological systems, and can be a clear marker for differentiating signals using optical filters.

5.5 Experimental Section

5.5.1 Cell incubation and confocal microscopy

Undertaken by collaborators within the Lloyd and Hayes groups in BIOSCI at Cardiff University.

Cell imaging was executed using *Schizosaccharomyces pombe* (*S. Pombe*) – fission yeast and MCF7 human breast adenocarcinoma cells.

The *S. Pombe* preparation used homogenous overnight cell suspension aliquots (1 mL), each being subject to incubation with a different lumophore (10 μL). Lumophores were initially dissolved in dimethylsulfoxide (DMSO) (5 $mgmL^{-1}$) to yield a concentration of $10\mu gmL^{-1}$. *S. pombe* yeast cells were then incubated at 35 °C (under 5 % CO_2 and 95 % air) and 20 °C, respectively, for 30 minutes. Cells were then twice washed in phosphate buffer saline (PBS, pH 7.2) removing the lumophore from the medium and finally *S. Pombe* cells 1 mL of PBS for imaging.

MCF7 cells were prepared by detachment from the culture flask using trypsin–EDTA, followed by re–suspention in an excess of Dulbecco's Modified Eagle's medium (DMEM), supplemented with 10v% fetal bovine serum, penicillin, and streptomycin, and concentrated by centrifugation. The MCF7 cells were re–suspended in 7 mL fresh of fresh DMEM, aliquoted into 1 mL volumes in Eppendorfs and incubated at 37 °C (under 5 % CO_2 and 95 % air) with 20 μL of each compound for 30 minutes (final concentration = 100 mg mL^{-1} for test compounds and 10 mg mL^{-1} for JC–1). Cells were finally washed in PBS (pH 7.2) and re–suspended in 100 μL DMEM for imaging.

Preparations were viewed by epifluorescence and transmitted light (Nomarski differential interference contrast optics) using a Leica TCS SP2 AOBS confocal laser microscope (Leica, Germany) using ×63 or ×100 objectives, ×4 zoom factor and laser power of 20 %. Excitation of the lumophore was at 405 nm using a diode laser, with detection between 480–540 nm (and 630–690 nm to probe red emission). Initial imaging yielded minimal fluorescence so the concentration of the lumophore was increased to 100 μg mL^{-1} final concentration, which was then incubated with the cells at room temperature for a further 30 minutes.

5.5.2 General

^{1}H and $^{13}C\{^{1}H\}$ NMR spectra were recorded on a NMR-FT Bruker 400 or 600 MHz or Jeol Eclipse 300 MHz spectrometer and recorded in a range of deuterated solvents. ^{1}H and

$^{13}C\{^{1}H\}$ NMR chemical shifts (δ) were determined relative to residual solvent peaks with digital locking and are given in ppm. Low-resolution mass spectra were obtained by the staff at Cardiff University using a Waters LCT Premier XE mass spectrometer. High-resolution mass spectra were carried out at the EPSRC National Mass Spectrometry Facility at Swansea University. UV–Vis studies were performed on a Jasco V-570 spectrophotometer as MeCN solutions (2.5×10^{-5} M). Photophysical data were obtained on a JobinYvon–Horiba Fluorolog spectrometer fitted with a JY TBX picoseconds photodetection module as MeCN solutions. Emission spectra were uncorrected and excitation spectra were instrument corrected. Quantum yields using $[Ru(bpy)_3](PF_6)_2$ in aerated MeCN as a standard (Φ_{em} = 0.016).[50,51] The pulsed source was a Nano–LED configured for 459 nm output operating at 1 MHz. Luminescence lifetime profiles were obtained using the JobinYvon–Horiba FluoroHub single photon counting module and the data fits yielded the lifetime values using the provided DAS6 deconvolution software.

All reactions were performed with the use of vacuum line and Schlenk techniques. Reagents were commercial grade and used without further purification. *fac*–$[Re(CO)_3(MeCN)_3]BF_4$[31] and *N*–*tert*–Boc–ethylenediamine[52] were prepared according to the literature. Anthracene–1,10–dicarboxylic anhydride was prepared from anthracene *via* aceanthrenequinone.[2] Bis(pyridin–2–ylmethyl)ethane–1,2–diamine was synthesised from *N*–*tert*–Boc–ethylenediamine according to previously used reductive amination techniques.[24]

5.5.3 Proligand synthesis

*Synthesis of (N–1',6'–diaminohexyl)–anthracene–1,10–dicarboxyimide (**N1**)*[23]

1,6–diaminohexane (0.61 mL, 4.66 mmol) was added to anthracene–1,10–dicarboxylic anhydride (289 mg, 1.16 mmol) in EtOH (10 mL) and heated at reflux, under a nitrogen atmosphere for 48 hours. After cooling the ethanol was removed *in vacuo* and the product dissolved in minimal chloroform. Water was added and the product neutralised with 1M HCl after which the mixture was paper filtered into a separating funnel. The crude product was washed with copious amounts of water, dried over $MgSO_4$ and filtered. The solvent was reduced to a minimal volume, and precipitation was induced with diethyl ether, allowing subsequent filtration and drying to afford the intermediate product **N1** as a brown solid. Yield: 153 mg, 0.48 mmol, 36 %. ^{1}H NMR (400 MHz, $CDCl_3$): δ_H = 9.79 (d, 1H, $^{3}J_{HH}$ = 9.1 Hz, an), 8.56 (d, 1H, $^{3}J_{HH}$ = 7.0 Hz, an), 8.53 (s, 1H, an), 8.12 (d, 1H, $^{3}J_{HH}$ = 8.4 Hz, an), 7.90 (d, 1H, $^{3}J_{HH}$ = 8.4 Hz, an), 7.69 (t, 1H, $^{3}J_{HH}$ = 7.0 Hz, an), 7.56 (dd, 1H, $^{4}J_{HH}$ = 8.5 Hz, $^{3}J_{HH}$ = 6.9 Hz, an), 7.50 (t, 1H, $^{3}J_{HH}$ = 7.9 Hz, an), 4.15 (t, 2H, $^{3}J_{HH}$ = 7.8 Hz, $N_{imide}CH_2$), 2.69–2.60 (broad m, 2H), 1.83–1.69 (broad m, 2H), 1.57–1.35 (broad m, 4H) ppm.

5.5.4 Ligand Synthesis

*Synthesis of (N',N'–bis(pyridin–2–ylmethyl) hexyldiamine)–anthracene–1,10–dicarboxyimide (**L1**)*

N1 (0.117 g, 0.34 mmol) was added to a solution of 2–pyridinecarboxaldehyde (0.1 mL, 0.98 mmol) in 1,2–dichloroethane (5 mL) and stirred for 2 hours at room temperature under a nitrogen atmosphere. Sodium triacetoxyborohydride (0.214 g, 1.01 mmol) was then added, and the mixture was stirred for a further 4 days. The solution was then neutralised with saturated aq. $NaHCO_3$, and the product was extracted using $CHCl_3$. The organic layer was washed with water (3 × 25 mL) and brine (2 × 25 mL) and then dried over $MgSO_4$. Following filtration, the solvent was reduced *in vacuo* and purified *via* column chromatography, washed with dichloromethane and eluted with a 95:5 mixture of DCM:MeOH. Removal of the solvent *in vacuo* afforded **L1** as a brown oil. Yield: 0.062 g, 0.12 mmol, 27 %. ^{1}H NMR (400 MHz, $CDCl_3$): δ_H = 9.94 (d, 1H, $^3J_{HH}$ = 9.1 Hz, an), 8.73 (s, 1H, an), 8.69 (dd, 1H, $^3J_{HH}$ = 7.1 Hz, $^3J_{HH}$ = 7.0 Hz, an), 8.52–8.47 (m, 2H, pyr), 8.28 (d, 1H, $^3J_{HH}$ = 7.8 Hz , an), 8.05 (d, 1H, $^3J_{HH}$ = 8.4 Hz, an), 7.79 (dd, 1H, $^3J_{HH}$ = 6.7 Hz, $^3J_{HH}$ = 6.6 Hz, an), 7.68–7.49 (m, 6H, pyr), 7.12–7.04 (m, 2H, pyr), 4.19 (t, 2H, $^3J_{HH}$ = 7.7 Hz, $N_{imide}CH_2$), 3.78 (s, 4H, pyr–CH_2), 2.56–2.48 (m, 2H), 1.80–1.65 (broad m, 2H), 1.65–1.51 (broad m, 2H), 1.44–1.32 (broad m, 4H) ppm; ^{13}C{^{1}H} NMR (75 MHz, $CDCl_3$): δ_C = 165.3 (*C*O), 163.8 (*C*O), 149.1, 136.6, 136.4, 134.9, 133.6, 133.5, 132.7, 131.4, 129.9, 129.0, 128.6, 127.8, 127.4, 127.3, 126.9, 126.6, 125.6, 123.1, 122.1 ppm; HRMS (ES$^+$) found *m/z* 529.2588 for $[C_{34}H_{32}N_4O_2+H]^+$ and 551.2400 for $[C_{34}H_{32}N_4O_2+Na]^+$, calculated at 529.2598 for $[C_{34}H_{32}N_4O_2+H]^+$; IR (solid) ν_{max} (±2 cm^{-1}) = 3057, 2927, 2854, 1685, 1647, 1589, 1562, 1433, 1352, 1311, 1149, 1114, 898, 794, 750, 736, 613, 518 cm^{-1}; UV–Vis (MeCN): λ_{max} (ε/M^{-1} cm^{-1}) = 457 (3100), 433 (4500), 406 (3300), 378 (4100), 360 (1900), 265 (56600), 244 (24400), 202 (61000) nm.

*Synthesis of (N',N'–bis(pyridin–2–ylmethyl) ethyldiamine)–anthracene–1,10–dicarboxyimide (**L2**)*

Prepared as for **N1** but using bis(pyridin–2–ylmethyl)ethane–1,2–diamine (106 mg, 0.50 mmol) and anthracene–1,10–dicarboxylic anhydride (122 mg, 0.50 mmol) with heating for 72 hours to afford **L2** as a dark orange powder. Yield = 123 mg, 0.49 mmol, 98 %. ^{1}H NMR (400 MHz, $CDCl_3$): δ_H = 9.90 (d, 1H, $^3J_{HH}$ = 9.9 Hz, an), 8.87 (s, 1H, an), 8.68 (d, 1H, d, $^3J_{HH}$ = 7.6 Hz, an), 8.39 (d, 1H, $^3J_{HH}$ = 9.3 Hz, an), 8.35 (d, 2H, $^3J_{HH}$ = 3.3 Hz, pyr), 8.14 (d, 1H, $^3J_{HH}$ = 7.7 Hz, an), 7.80 (t, 1H, $^3J_{HH}$ = 7.2 Hz, an), 7.75 (t, 1H, $^3J_{HH}$ = 7.8 Hz, an), 7.65 (t, 1H, $^3J_{HH}$ = 7.2 Hz, an), 7.22 (d, 2H, $^3J_{HH}$ = 9.3 Hz, pyr), 7.09 (t, 2H, $^3J_{HH}$ = 7.2 Hz, pyr), 6.87 (t, 2H, $^3J_{HH}$ = 6.0 Hz, pyr), 4.51 (t, 2H, $^3J_{HH}$ = 6.2 Hz, $N_{imide}CH_2$), 3.90 (s, 4H, CH_2), 2.97 (t, 2H, $^3J_{HH}$ =

6.2 Hz, C*H*$_2$) ppm; ^{13}C{^{1}H} NMR (75 MHz, $CDCl_3$) δ_C = 165.0 (CO), 163.6 (CO), 159.8, 148.8, 136.4, 136.2, 135.1, 133.7, 133.5, 132.6, 131.3, 129.8, 128.9, 128.4, 127.0, 126.6, 125.6, 122.9, 122.7, 77.6, 77.2, 76.7, 60.4, 52.0, 38.1 ppm; HRMS (EI$^+$) found *m/z* = 473.1967 for $[C_{38}H_{40}N_4O_2]^+$; calculated 473.1972 for $[C_{38}H_{40}N_4O_2]^+$; IR (solid) ν_{max} (±2 cm^{-1}) = 2959, 1680, 1680, 1560, 1082, 862 cm^{-1}; UV-vis (MeCN): λ_{max} (ε /M^{-1}cm^{-1}) = 428 (7300), 373 (9000), 360 (3800), 265 (79600), 219 (28900) nm.

5.5.5 Complex Synthesis

*Synthesis of fac–[Re(CO)$_3$(**L1**)]BF$_4$ (**ReL1**)*

L1 (63 mg, 0.12 mmol) and *fac*–[Re(CO)$_3$(MeCN)$_3$]BF$_4$ (54 mg, 0.14 mmol) were dissolved in $CHCl_3$ (10 mL) and heated at reflux under a nitrogen atmosphere for 12 hours. Reaction progression was monitored by a 14:2:1 mix of H_2O:MeCN:sat. KNO_3. Upon completion the reaction mixture was allowed to cool, the solvent was reduced to 1–2 mL, and precipitation was induced with the addition of diethyl ether. The product was collected by filtration and washed with diethyl ether, to give **ReL1** as a yellow solid. Yield: 61.0 mg, 68.9 μmol, 61 %. ^{1}H NMR (400 MHz, ($CDCl_3$): δ_H = 10.01 (d, 1H, $^3J_{HH}$ = 9.6 Hz, an), 8.87 (s, 1H, an), 8.78 (dd, 1H, $^3J_{HH}$ = 7.2 Hz, $^3J_{HH}$ = 7.1 Hz, an), 8.68–8.65 (m, 2H, pyr), 8.39 (d, 1H, $^3J_{HH}$ = 8.0 Hz, an), 8.14 (d, 1H, $^3J_{HH}$ = 8.0 Hz, an), 7.85–7.74 (m, 7H, an, pyr), 7.24–7.19 (m, 2H, pyr), 5.27 (d, 2H, $^2J_{HH}$ = 16.8 Hz, 1/2 × 2C*H*$_2$), 4.43 (d, 2H, $^2J_{HH}$ = 16.4 Hz, 1/2 × 2C*H*$_2$), 4.31 (t, 2H, $^3J_{HH}$ = 8.0 Hz, N_{imide}C*H*$_2$), 3.79–3.68 (broad m, 2H), 2.14–1.99 (broad m, 2H), 1.93–1.81 (broad m, 2H), 1.68–1.49 (broad m, 4H) ppm; HRMS (ES$^+$) found *m/z* 799.1917; calculated 799.1927 for $[C_{37}H_{32}N_4O_5Re]^+$; IR (solid) ν_{max} (±2 cm^{-1}) = 2978, 2027, 1904, 1645, 1610, 1533, 1485, 1435, 1280, 1247, 1053, 794, 763, 536 cm^{-1}; UV–Vis (MeCN): λ_{max} (ε/M^{-1}cm^{-1}) = 456 (4200), 432 (5900), 408 (4400), 377 (5200), 359 (2600), 264 (40000), 243 (36000), 236 (34300) nm.

*Synthesis of fac–[Re(CO)$_3$(**L2**)]BF$_4$ (**ReL2**)*

Prepared as for **ReL1** using [Re(CO)$_3$(MeCN)$_3$]BF$_4$ (83 mg, 0.17 mmol) and **L2** (82 mg, 0.17 mmol) to give **ReL2** as an off–white powder. Yield = 88 mg, 0.12 mmol, 67 %. ^{13}C{^{1}H} NMR (150 MHz, CD_3CN): δ_C = 196.1 (Re–*C*O), 194.8 (Re–*C*O), 165.2 (*C*O), 163.7 (*C*O), 160.2, 152.2, 140.5, 137.6, 136.0, 133.8, 133.3, 132.4, 131.8, 130.3, 129.0, 128.5, 126.6, 126.0, 125.8, 125.7, 123.7, 123.6, 122.2, 67.8, 66.7, 36.3 ppm; HRMS (EI$^+$) found *m/z* = 743.1290 for $[C_{41}H_{40}N_4O_5Re]^+$; calculated 743.1300 for $[C_{41}H_{40}N_4O_5Re]^+$; IR (solid) ν_{max} (±2 cm^{-1}) = 2033, 1906, 1719, 1690, 1458, 1433, 1259, 1161 cm^{-1}; UV-vis (MeCN): λ_{max} (ε /M^{-1}cm^{-1}) = 436 (3200), 202 (29800), 262 (33400), 355 (1700), 377 (3000) nm.

5.6 References

1. M. C. Sharma, S. Sharma, P. Sharma and A. Kumar, *Med. Chem. Res.*, 2013, **22**, 5772-5788.
2. H. Langhals, G. Schönmann and K. Polborn, *Chem. Eur. J.*, 2008, **14**, 5290-5303.
3. S. M. Sami, R. T. Dorr, D. S. Alberts, A. M. Sólyom and W. A. Remers, *J. Med. Chem.*, 2000, **43**, 3067-3073.
4. C. A. Mayr, S. M. Sami, W. A. Remers and R. T. Dorr, *Anti-Cancer Drugs*, 1999, **10**, 163-170.
5. A. Wu, P. Mei, Y. Xu and X. Qian, *Chem. Biol. Drug Des.*, 2011, **78**, 941-947.
6. C. A. Mayr, S. M. Sami, W. A. Remers and R. T. Dorr, *Drug Metab. Dispos.*, 1998, **26**, 105-109.
7. S. M. Sami, R. T. Dorr, A. M. Sólyom, D. S. Alberts and W. A. Remers, *J. Med. Chem.*, 1995, **38**, 983-993.
8. S. M. Sami, R. T. Dorr, D. S. Alberts, A. M. Sólyom and W. A. Remers, *J. Med. Chem.*, 1996, **39**, 4978-4987.
9. S. M. Sami, R. T. Dorr, D. S. Alberts and W. A. Remers, *J. Med. Chem.*, 1993, **36**, 765-770.
10. Y.-H. Kim, H.-C. Jeong, S.-H. Kim, K. Yang and S.-K. Kwon, *Adv. Funct. Mater.*, 2005, **15**, 1799-1805.
11. T. Lazarides, M. A. H. Alamiry, H. Adams, S. J. A. Pope, S. Faulkner, J. A. Weinstein and M. D. Ward, *Dalton Trans.*, 2007, 1484-1491.
12. A. Beyeler, P. Belser and L. De Cola, *Angew. Chem. Int. Ed.*, 1997, **36**, 2779-2781.
13. T. Seko, K. Ogura, Y. Kawakami, H. Sugino, H. Toyotama and J. Tanaka, *Chem. Phys. Lett.*, 1998, **291**, 438-444.
14. M. Sugino, Y. Araki, K. Hatanaka, I. Hisaki, M. Miyata and N. Tohnai, *Cryst. Growth Des.*, 2013, **13**, 4986-4922.
15. M. E. Alberto, C. Iuga, A. D. Quartarolo and N. Russo, *J. Chem. Inf. Model.*, 2013, **53**, 2334-2340.
16. J.-I. Jin, S.-J. Chung and S.-H. Yu, *Macromol. Symp.*, 1998, **128**, 79-87.
17. W. Liu, Y. Chen, R. Wang, X.-H. Zhou, J.-L. Zuo and X.-Z. You, *Organometallics*, 2008, **27**, 2990-2997.
18. R. Tan, Z.-B. Wang, Y. Li, D. J. Kozera, Z.-H. Lu and H. Song, *Inorg. Chem.*, 2012, **51**, 7039-7049.
19. S. Chen, J. Lu, C. Sun and H. Ma, *Analyst,* 2010, **135**, 577-582.
20. S. Guha, S. Lohar, A. Banerjee, A. Sahana, S. K. Mukhopadhyay, J. S. Matalobos and D. Das, *Anal. Methods*, 2012, **4**, 3163-3168.
21. X. Diao, W. Li, J. Yu, X. Wang, X. Zhang, Y. Yang, F. An, Z. Liu and X. Zhang, *Nanoscale*, 2012, **4**, 5373-5377.
22. J. H. Yao, C. Chi, J. Wu and K.-P. Loh, *Chem. Eur. J.*, 2009, **15**, 9299-9302.
23. R. Stolarski, *Fibres & Textiles in Eastern Europe*, 2009, **17**, 91-95.
24. E. E. Langdon-Jones, N. O. Symonds, S. E. Yates, A. J. Hayes, D. Lloyd, R. Williams, S. J. Coles, P. N. Horton and S. J. A. Pope, *Inorg. Chem.*, 2014, **53**, 3788-3797.
25. H. Wang, L. Yang, W. Zhang, Y. Zhou, B. Zhao and X. Li, *Inorg. Chim. Acta*, 2012, **381**, 111-116.
26. Z. Y. Wu, J. N. Cui, X. H. Qian and T. Y. Liu, *Chin. Chem. Lett.*, 2013, **24**, 359-361.
27. C. Zhang, Z. Liu, Y. Li, W. He, X. Gaod and Z. Guo, *Chem. Commun.*, 2013, **49**, 11430–11432.
28. J. Gawroński, K. Gawrońska, P. Skowronek and A. Holmén, *J. Org. Chem.*, 1999, **64**, 234-241.
29. *USA Pat.,* D. S. Alberts, R. T. Dorr, W. A. Remers and S. M. Sami, US 1993-142283, 1997.
30. *USA Pat.,* D. S. Alberts, R. T. Dorr, W. A. Remers and S. M. Sami, WO 9406771, 1994.
31. J. V. Casper and T. J. Meyer, *J. Phys. Chem.*, 1983, **87**, 952-957.

32. L. A. Mullice, *PhD Thesis*, 2010, **Chapter 4**, 142.
33. L. A. Mullice, R. H. Laye, L. P. Harding, N. J. Buurma and S. J. A. Pope, *New J. Chem.*, 2008, **32**, 2140-2149.
34. N. N. Greenwood and A. Earnshaw, in *Chemistry of the Elements* ed. B.-H. Ltd, Butterworth-Heinemann Ltd, Oxford, UK, 2nd edn., 1997, ch. 24, pp. 1040-1062.
35. M. E. Walther and O. S. Wenger, *Dalton Trans.*, 2008, 6311-6318.
36. V. Fernández-Moreira, M. L. Ortego, C. F. Williams, M. P. Coogan, M. D. Villacampa and M. C. Gimeno, *Organometallics*, 2012, **31**, 5950-5957.
37. B. S. Murray, E. J. New, R. Pal and D. Parker, *Org. Biomol. Chem.*, 2008, **6**, 2085-2094.
38. A. A. Nazarov, J. Risse, W. H. Ang, F. Schmitt, O. Zava, A. Ruggi, M. Groessl, R. Scopelitti, L. Juillerat-Jeanneret, C. G. G. Hartinger and P. J. Dyson, *Inorg. Chem.*, 2012, **51**, 3633-3639.
39. E. E. Langdon-Jones, D. Lloyd, A. J. Hayes, S. D. Wainwright, H. J. Mottram, S. J. Coles, P. N. Horton and S. J. A. Pope, *Inorg. Chem.*, 2015, **54**, 6606-6615.
40. S. Pandya, J. Yu and D. Parker, *Dalton Trans.*, 2006, 2757-2766.
41. in *The Molecular Probes Handbook: A Guide to Fluorescent Probes and Labeling Technologies*, ed. L. Technologies, Thermo Fisher Scientific Inc. , 11th edn., 2010, ch. 12.2.
42. S. T. Smiley, M. Reers, C. Mottola-Hartshorn, M. Lin, A. Chen, T. W. Smith, G. D. Steele Jr. and L. B. Chen, *Proc. Natl. Acad. Sci. U. S. A.*, 1991, **88**, 3671-3675.
43. E. Y. Kim, J. Y. Shin, Y.-J. Park and A. K. Kim, *Anticancer Res.*, 2014, **34**, 4895-4992.
44. Y. Liu, M. Du and G. Zhang, *Toxicology Reports*, 2014, **1**, 1076-1086.
45. A. Peeters, A. B. Shinde, R. Dirkx, J. Smet, K. De Bock, M. Espeel, I. Vanhorebeek, A. Vanlander, R. Van Coster, P. Carmeliet, M. Fransen, P. P. Van Veldhoven and M. Baes, *BBA Molecular Cell Research*, 2015, **1853**, 285-298.
46. Y. H. L. Zheng, J. Chen, Y. Wang, H. Yang, Y. Zhang and S. Xie, *Optics in Healthcare and Biomedicinal Optics*, 2012, **8553**, 855314-855317.
47. A. D. L. Martyn A. Sharpe, and David S. Baskin, *Journal of Toxicology*, 2012, **201**, 800-813.
48. G. K. Bains, S. Kim, H., E. J. Sorin and V. Narayanaswami, *Biochemistry*, 2012, **51**, 6207-6219.
49. J. B. Birks and L. G. Christophorou, *Spectrochim. Acta, Part A*, 1963, **19**, 401-410.
50. M. Frank, M. Nieger, F. Vogtle, P. Belser, A. von Zelewsky, L. D. Cola, V. Balzani, F. Barigelletti and L. Flamigni, *Inorg. Chim. Acta*, 1996, **242**, 281-291.
51. A. Juris, F. Barigelletti, S. Campagna, P. Belser and A. von Zelewsky, *Coord. Chem. Rev.*, 1988, **84**, 85-277.
52. S. R. Chhabra, A. Mahajan and W. C. Chan, *J. Org. Chem.*, 2002, **67**, 4017-4029.

Chapter 6

NO Responsive Luminescent Probes Based on Cyclometalated Iridium (III) Complexes

6.1 Introduction

Nitric oxide (NO), a reactive free radical, plays a vital role in many biological processes. There are currently many fluorescent, organic NO sensors however very few exploit the favourable attributes of metal phosphorescent probes. This chapter describes the synthesis of three novel cyclometalated Ir(III) complexes of the general form $[Ir(C^N)_2(N^N)]BF_4$, where N^N represents a novel, fluorescent phenylimidazo–phenanthroline based ligand, capable of binding NO. All precursors, ligands and complexes have been extensively characterised, with the complexes in particular showing promising sensing capability.

6.1.1 Biological Significance of Nitric Oxide

NO is an important biological signalling molecule[1,2] in many vertebrates.[3] The gaseous free radical is produced from arginine[3] by nitric oxide synthase[4-6] (Figure 6.1) and plays a role in both beneficial and detrimental biological processes.[7]

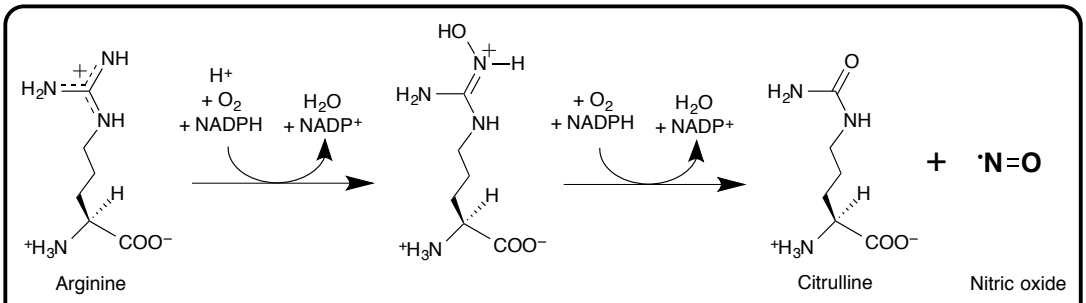

Figure 6.1: Synthesis of nitric oxide.[3]

At low concentrations, NO assists with biological functions such as neurotransmission, muscle relaxation and the regulation of vasodilation, immune response and potentiation in the brain.[4,6,8] However the presence of NO at higher concentrations leads to reactive nitrogen species and has been associated with carcinogenesis and neurodegenerative disorders[4,8] (such as Alzheimer's disease, multiple sclerosis and Huntington's disease).[6] More recently the misregulation of NO has also been associated with other health risks such as strokes, heart disease, hypertension and erectile dysfunction.[2]

More specifically the immune system contains cells known as macrophages, a type of white blood cell, which are known to produce NO in order to kill bacteria invading cells[9] or as a biological defence mechanism.[10] The role of NO in vasodilation works *via* the phosphorylation of several proteins that are involved in the relaxation of smooth muscles, blood pressure and blood flow.[11,12] Its role in neurotransmission involves the movement between nerve cells as a part of redox signalling; an example of this use is in the intestines

during the relaxation of the gastrointestinal muscle tract.[13] The explained roles and examples show the apparent importance of NO in metabolic processes. Further details about what function NO performs in these roles are poorly understood:[5] a method of quantitative detection of NO can evidently assist in developing knowledge of important metabolic processes.

6.1.2 Luminescent NO Sensors

A detailed understanding of the origin and biological function of NO is highly desired.[1,4] So far NO has proved challenging to track physiologically due to a number of exigent properties of NO: i) high diffusivity through tissue;[8,14] ii) high reactivity with other radicals and metal containing proteins;[14] and iii) a short half life *ca*. 5 seconds.[2,6] Nevertheless several techniques have been previously explored including chemiluminescence, colorimetry, EPR and amperometry. However these are high cost, time consuming and have poor resolution.[1,2,8] Commercially, colorimetry uses the Griess reagent to indirectly monitor NO *via* nitrate and nitrite species (Figure 6.2).[1] Luminescent probes are the ideal choice for NO sensing because fluorescence offers rapid intra– and extracellular detection, at high resolution, with good sensitivity.[6,8]

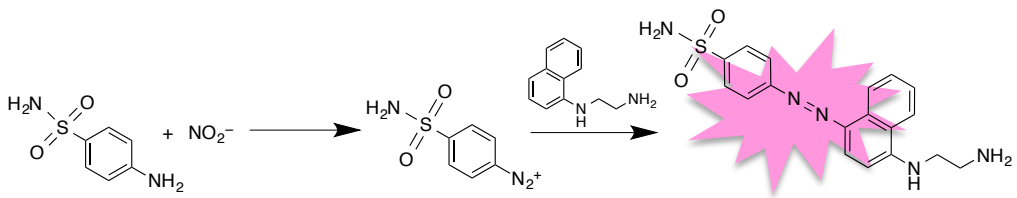

Figure 6.2: Mechanism of sensing NO_2^- using Griess reagent.

NO selective luminescent probes were first pioneered by the Nagano and Lippard groups. To date many luminescent probes for NO have been reported, typically falling into one of two categories. Most reports centre around organic species[5] containing the highly selective, electron rich *o*–phenylenediamine moiety, first developed by Nagano.[6] Before exposure to NO the luminescence of these species is highly quenched *via* PeT however upon binding to NO, and subsequent triazole formation, the luminescent properties are restored.[4,7] Commercial examples of this type of NO probe are *o*–diaminonaphthalene (DAN) and *o*–diaminofluoresceins (DAFs)[4,7,8] (Figure 6.3) with literature examples extending to rhodamine, BODIPY and cyanine.[6] *o*–Phenylenediamine species have a severe limitation in that they indirectly detect NO and instead react with oxidised species such as N_2O_3.[2,5,7] Therefore the detection of NO using these species, even with luminescence techniques, cannot truly be considered real–time. In addition the emission wavelength of

the benzotriazole species is pH dependent[2] which can reduce the sensitivity to NO.[4] Furthermore it is often difficult to achieve a high concentration in cells for biological NO detection[7] and ideally any binding event probe should be reversible, which triazole formation is not.

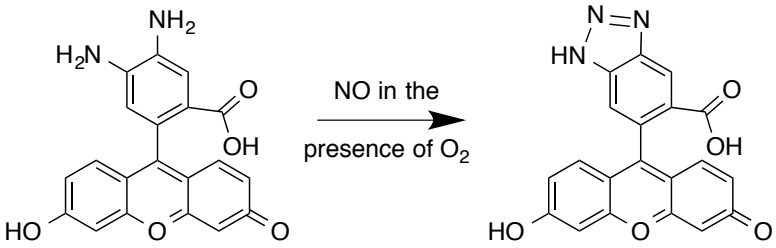

Figure 6.3: Structure of a DAF sensor and triazole formation with NO.

The second approach was pioneered by Lippard and involves the use of (paramagnetic) transition metal complexes (*e.g*. Cu(II), Fe(II), Ru(II) and Rh(III))[1,2] where direct coordination of NO restores the luminescence properties,[7] such as commercially available CuFL1 (Figure 6.4).[1] This occurs because any NO present reduces the metal. Subsequent displacement of the ligand then enhances emission.[6] These probes, although directly detecting NO, still have some limitations, for example the maximum response is slow (*ca*. 5 minutes).[4]

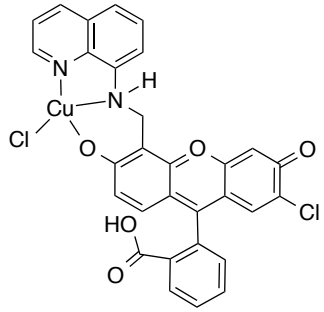

Figure 6.4: Commercially available NO probe, CuFL1.

Despite both of the above approaches being used, very few examples combining NO reactive diamine ligands with phosphorescent transition metal complexes have been reported.[6] Such species would offer favourable attributes such as intense and long lived emission with a high degree of photostability.[6] Recently Choi *et al*. developed a Re(I)-based example (Figure 6.5) where intense emission was observed after trizaole formation. Promisingly this was found to be independent of pH and NO sensitivity was dependent on the electron density of the diaminoaromatic moiety.[6] On the other hand, the irreversible nature of the binding event for these species by Choi *et al.* still poses a severe limitation.

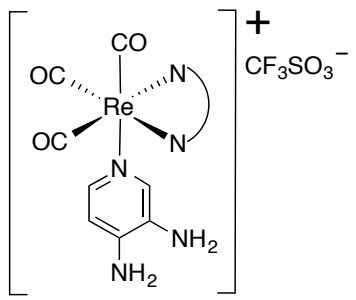

Figure 6.5: Example of a phosphorescent NO probe by Choi *et al*.

6.1.3 Properties of Phenylimidazo–Phenanthroline Ligands

Phenanthroline derivatives are a staple auxiliary, bidentate, bridging ligand for a range of transition metal ions, such as Ir(III), Ru(II) and Pt(II) systems.[15-17] In their own right phenylimidazo–phenanthroline ligands have attracted a lot of attention due their fully conjugated system and corresponding electron fluidity[15,18] that consequences in rich, unique photophysical properties.[16,19] Favourable properties include a high degree of photostability, efficient emission, strong absorption and good thermal stability.[16,19,20] More specifically phenylimidazo–phenanthroline ligands possess strong absorption below 350 nm due to intramolecular π–π* and n–π* imidazo based transitions.[17,20] Excitation at appropriate wavelengths results in efficient, environment sensitive (pH, polarity *etc*.) blue emission centred between 390–450 nm,[17,19] tuned by varying the imidazole substituents.[17] Certain phenylimidazo–phenanthroline ligands also display a secondary emission peak up to 580 nm[21] as a result of excited state electron transfer processes[20] or photo–induced excimer behaviour upon aggregate formation.[20] The charge transfer character results in relatively large Stokes' shifts (30–100 nm)[19,20] for organic molecules and helps to reduce self quenching of the fluorescent emission (τ < 5 ns).[17,19,21]

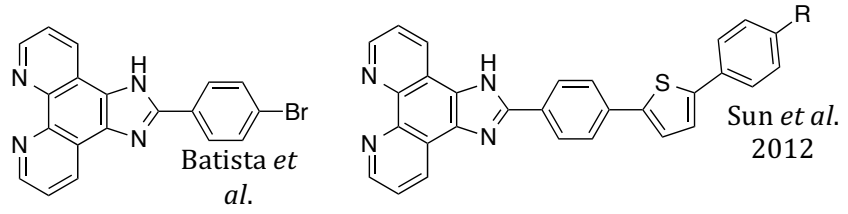

Figure 6.6: Examples of phenylimidazo–phenanthroline ligands towards anticancer and NLO applications, respectively.

In addition to these encouraging photophysical properties, imidazole derivatives are found in many biological systems.[18,19] Subsequently phenylimidazo–phenanthroline ligands have been employed in a wide range of analytical and biological applications

(Figure 6.6). Reported analytical applications include use in lasers, polymer stabilisers[19] and more widely as probes, due to their inherent fluorescence and chemiluminescence.[17,19] These species have also shown great promise as nonlinear optical materials.[16,21]

In addition phenylimidazo–phenanthroline ligands have been investigated towards various biological applications. They possess anticancer properties, due to their metal chelating and DNA binding properties resulting in inhibition of DNA synthesis, and have also demonstrated mitochondria mediated cell apoptosis.[18] Unfortunately the use of such ligands in biological applications has been limited due to their high planarity[16,20] resulting in intrinsically poor solubility, particularly in aqueous environments.[15] This can be improved by placing a phenyl substituent, sitting antiperiplanar to the phenylimidazo–phenanthroline core, on the N_{imiazo} atom. This helps to disrupt π–stacking interactions that cause aggregation in solution.[19]

6.1.4 Luminescent Iridium (III) Cyclometalated Complexes

Currently iridium(III) complexes are at the forefront of science because their luminescent properties show high phosphorescence quantum yields, with tunable and environment sensitive emission properties.[22-25] In addition they can be easily synthesised and purified at yields approaching theoretical.[26] Currently they are being employed for a range of sensing techniques, much of which arises from triplet states, such as oxygen, facilitating phosphorescence quenching.[27] Other uses include organic light–emitting diodes (OLEDs), light–emitting electrochemical cells (OLECs), photocatalysts for water splitting and dye sensitised solar cells (Figure 6.7).[22,25,28-30]

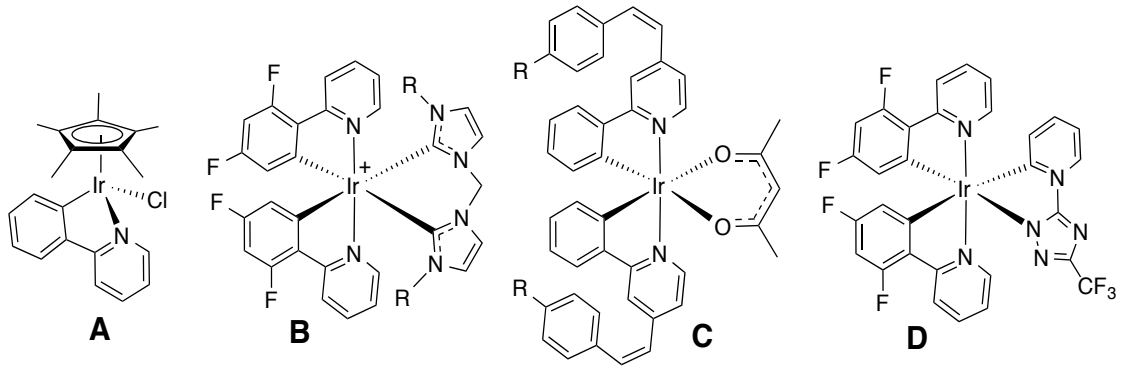

Figure 6.7: Examples of Ir(III) complexes for: a) water splitting;[31] b) OLEC;[32] c) NLO;[33] and d) OLED[34] applications.

In the past the poor water solubility of many Ir(III) complexes has overshadowed the potential biological applications but now, with the development of new water soluble

ligand systems, Ir(III) biological probes and imaging agents have been reported.[23] Nevertheless utilising Ir(III) complexes as molecular probes is in its early stages due to excitation wavelengths falling in the UV/blue region of the spectrum. These wavelengths can cause considerable cell photodamage and also have poor tissue depth penetration.[22,35] For example Ir(III) complexes containing phenylimidazo–phenanthroline ligands possess strong absorption bands below 350 nm, assigned to ligand based π–π* transitions. Weaker absorption bands are also observed up to 430 nm due to ^{1}MLCT ((Ir–phenyl)–to–imidazo)/^{1}LLCT, often seen with a weak shoulder near 500 nm due to spin forbidden ^{3}MLCT transitions.[22-24,26,28,29,35,36]

The emission of Ir(III) cyclometalated complexes is highly efficient for a number of reasons. Firstly the strong field cyclometalating ligands, such as phenylpyridine (ppy), cause a large ligand field splitting energy. This combined with a high oxidation state and presence of *5d* electrons results in a high crystal field and leads to efficient heavy atom assisted spin–orbit coupling (SOC) (ξ = 3909 cm^{-1}).[25,26,28] Consequently long–lived triplet states are accessible *via* efficient ISC.[30] Mixing of singlet and triplet states then allows phosphorescence relaxation that is normally regarded as Laporte forbidden. For example upon irradiation Ir(III) complexes containing phenylimidazo–phenanthroline ligands possess strong, efficient, orange–yellow phosphorescence (τ = 0.2–100 μs, ϕ = 1–50 %), centred between 540–600 nm. The excited states of these complexes have a high degree of charge transfer nature and hence they possess favourably large Stokes' shifts of *ca*. 210 nm which helps to reduce self–quenching.[22-26,28,29,35,36]

Ir(III), with an electron rich, low spin, d^6 configuration, is known for its inherent stability. This is a key advantage for biological applications. Ir(III) has strong preferences to cyclometalate and can be coordinated to a range of mono–, bi– or tri–dentate ligands.[37] Many of these are focused around polypyridine structures, such as phenanthroline derivatives.[28] Phenylimidazo–phenanthroline ligands are a good choice of such derivatives and are well suited due to their fully conjugated nature and incorporation of protic sites for pH dependance.[28]

6.1.5 Ir(III) Complexes as Probes

Applications of Ir(III) complexes as probes are very varied. Current research is focused on two–photon absorption techniques that provide high 3D resolution. This technique allows excitation in the near–IR region of the spectrum which reduces photodamage and improved tissue penetrability.[35]

Complexes containing an acidic or basic substituent, such as iridium (III) bis-terpyridine complexes reported by Licini and Williams,[38] can be utilised as pH sensors (Figure 6.8.A). Other ion sensors include those discovered by Ho *et al*.[39] (Figure 6.8.B) where the free nitrogen atoms cause a vast change in emission when in the presence of certain cations due to increased ^{3}MLCT character. Furthermore anion sensors exist, such as those created by Bian *et al*.[41] (Figure 6.8.C) that shows specific colour change for the cyanide anion, proposedly due to CN^- breaking conjugation in the molecule.[37]

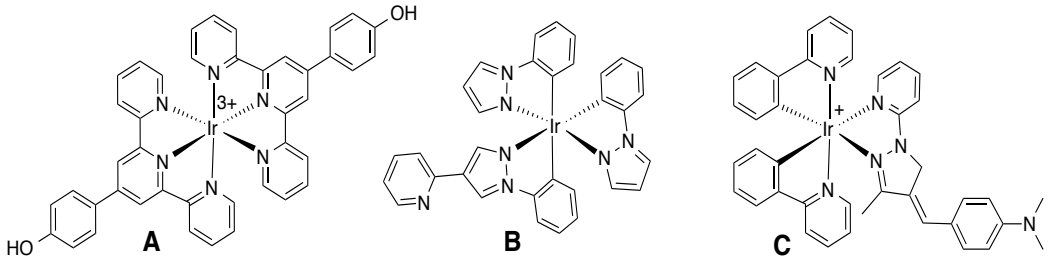

Figure 6.8: Examples of Ir(III) probes.

Small molecule probes also exist. Many achieve a sensing response when the phosphorescence of the complex is quenched by molecules with a triplet ground state, such as oxygen.[40] Other small molecule probes have been made by Sato *et al*. that exploit vapochromism.[41] Other types of probes are focused on biological aspects. DNA and nucleotide probes show more efficient energy transfer when bound to a nucleotide. Protein probes can either involve a mild reaction with the complex and amino acid residue, or like the infamous avidin–biotin system, use non-covalent interactions.[37] Such non–covalent probes have also been used in the sensing of oestrogen and human serum albumin.[37]

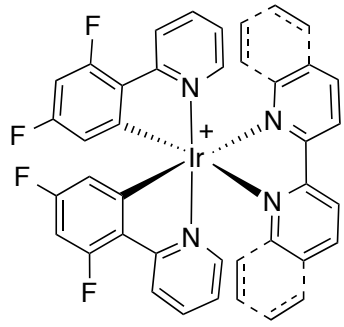

Figure 6.9: Example of Ir(III) cellular probes by Zhao *et al*.

The final type of Ir(III) probes are those used for cell imaging applications. Cellular imaging is a very fast growing area involving the development of biocompatible

luminescent dyes. Phosphorescence allows a longer time of study compared to fluorescent stains and improved differentiation of signals. Zhao *et al*.[42] have developed stains for live cell imaging that show intense red and green emissions, solely staining the cytoplasm. The essential factor in designing these types of probes is cellular uptake, and therefore the molecules need to be amphiphilic;[37] hydrophilic to ensure solubility in the aqueous systems such as blood and cytoplasm, yet lipophilic enough to be able to passively diffuse through the plasma membrane, *i.e*. for cell penetration.

6.2 Aims

The field of NO sensors requires investigation towards alternative metal centres, thus allowing the application of a variety of new ligand types. Cyclometalated iridium (III) complexes are widely utilised in a range of sensing applications and therefore, with careful design, should be well suited to NO sensing.

This chapter aimed to develop the synthetic chemistry of a range of novel, fluorescent functionalised phenylimidazo–phenanthroline based ligands containing an *o*–phenyldiamine unit commonly employed for NO sensing applications. Investigations were completed into the coordination chemistry of these ligands with Ir(III).

In order to assess the feasibility of these compounds towards NO sensors, an aliquot of each compound was reacted with gaseous NO in solvent and the resulting benzotriazole products isolated. These products were also fully characterised and assessing their photophysical properties furthermore revealed the feasibility of these ligands and complexes as luminescent NO probes. Additionally, theoretical studies were conducted in order to support spectral data and successful binding to NO.

6.3 Results and Discussion

6.3.1 Ligand Synthesis and Characterisation

The ligands (**L1–L2**) were synthesised from 1,10–phenanthroline–5,6–dione with good yields (60–90%) using methods from the literature (Scheme 6.1).[17,43] Firstly, a condensation reaction of 1,10–phenanthroline–5,6–dione with 4–chloro–3–nitrobenzaldehyde, in the presence of ammonium acetate in acetic acid, efficiently yielded the corresponding chloro pro–ligand species **ClA$_{NO2}$**.[36,44] Further functionalisation of this pro–ligand was attempted by heating **ClA$_{NO2}$** with different amines in DMSO,[43] allowing the tuning of physical and electronic properties. Successful reaction was indicated by TLC as well as a colour and solubility change during the reaction. However the products were very insoluble, presumably due to the highly planar nature of the core, and were consequently not suitable for: i) characterisation by NMR spectroscopy; or ii) further chemical reduction of the nitro group and/or reaction conditions for coordination to iridium.

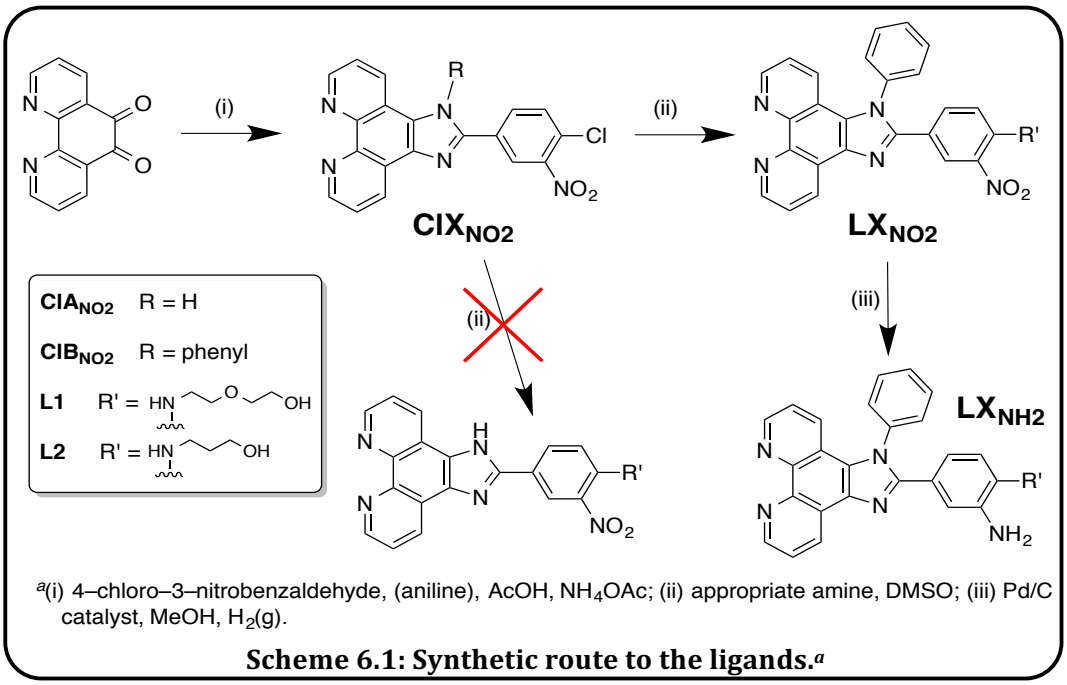

[a](i) 4–chloro–3–nitrobenzaldehyde, (aniline), AcOH, NH_4OAc; (ii) appropriate amine, DMSO; (iii) Pd/C catalyst, MeOH, H_2(g).

Scheme 6.1: Synthetic route to the ligands.[a]

To remedy the solubility problems associated with **ClA$_{NO2}$**, an attempt was made to disrupt any stacking interactions by alkylating the imidazo group with a phenyl ring that would sit perpendicular to the phenanthroline core. **ClB$_{NO2}$** was synthesised using similar conditions to **ClA$_{NO2}$**, however with the addition of aniline and a smaller excess of ammonium acetate.[17] Further functionalisation of **Cl2$_{NO2}$** was again achieved by heating **ClA$_{NO2}$** with different amines in DMSO,[43] however this time the solubility of the products, **L1$_{NO2}$/L2$_{NO2}$**, was greatly improved. Yields obtained for this step were advantageous (70–90 %),

assisted by both nitro ligands being found to be spectroscopically pure after precipitation and washing with water. Upon the S_NAr reaction, a large shift of the resonance for the proton on the adjacent carbon to the amino group (NHCC*H*) was witnessed. Typically this resonance shifts from part of an aromatic multiplet above 7.20 ppm to a doublet (split by the neighbouring CH group) at 6.6–6.8 ppm, depending on the nature of the amino substituent. $^{13}C\{^1H\}$ NMR spectra were also consistent with the proposed structure and HRMS (ES^+) showed the presence of $[M+H]^+$ in both cases. Furthermore broad NH stretch bands (*ca*. 3360 and 2920 cm^{-1}) and NO_2 bands (*ca*. 1560 and 1360 cm^{-1}) were observed in the IR spectra, again consistent with the proposed structure.

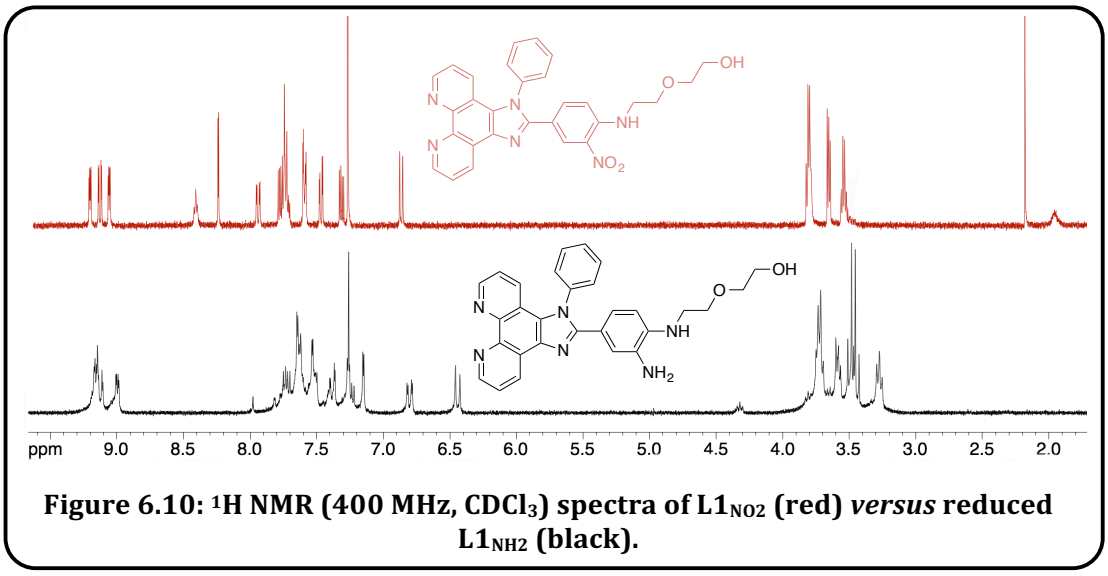

Figure 6.10: ^1H NMR (400 MHz, $CDCl_3$) spectra of $L1_{NO2}$ (red) *versus* reduced $L1_{NH2}$ (black).

In order to generate the NO binding motif the nitro moiety of **$L1_{NO2}$/$L2_{NO2}$** was reduced to form a 1,2–diamino structure using methods adapted from the literature.[45] High yields (65–80%) were achieved by stirring **$L1_{NO2}$/$L2_{NO2}$** and a Pd/C catalyst, in MeOH, with H_2(g) passed through the solvent for 16 hours. After filtering off the Pd/C through celite the reduced ligands were found to be spectroscopically pure by ^1H NMR spectroscopy. A large shift of the aromatic singlet, assigned to the proton of the adjacent carbon to the NO_2/NH_2 group, was witnessed. This resonance moved from being *ca.* 8.2 ppm in the **LX_{NO2}** species to around *ca.* 7.2 ppm for the reduced **LX_{NH2}** species, consistent with the electron withdrawing nature of the nitro group *versus* the electron donating character of amines (Figure 6.10). **LX_{NH2}** were further characterised by $^{13}C\{^1H\}$ NMR and IR spectroscopies and mass spectrometry. Again both LRMS and HRMS (ES^+) showed the presence of the $[M+H]^+$ peak in both cases and an additional NH stretch was observed in the IR spectra when compared to **LX_{NO2}**.

6.3.2 Complex Synthesis and Characterisation

Preliminary work was conducted on the $\mathbf{LX_{NO2}/LX_{NH2}}$ phenanthroline based ligands with coordination to Re(I), in the hope of forming $[Re(CO)_3(\mathbf{LX_Y})(X)]$ complexes, where; $\mathbf{LX_Y}$ = the synthesised ligand bound in a N^N mode, and X = an anionic ligand such as Br^-. Unfortunately coordination attempts to Re(I), using previously successful reaction conditions from the group used on very similar ligands,[17] proved ineffective: No data indicating the successful coordination to Re(I) could be obtained by ^1H NMR spectroscopy or mass spectrometry. However, phenanthroline based ligands are well–known to coordinate to range of metals and therefore a move to Ir(III) was made. Ir(III) would still allow for phosphorescent complexes to be synthesised and has a strong precedent in cellular imaging and sensing techniques.

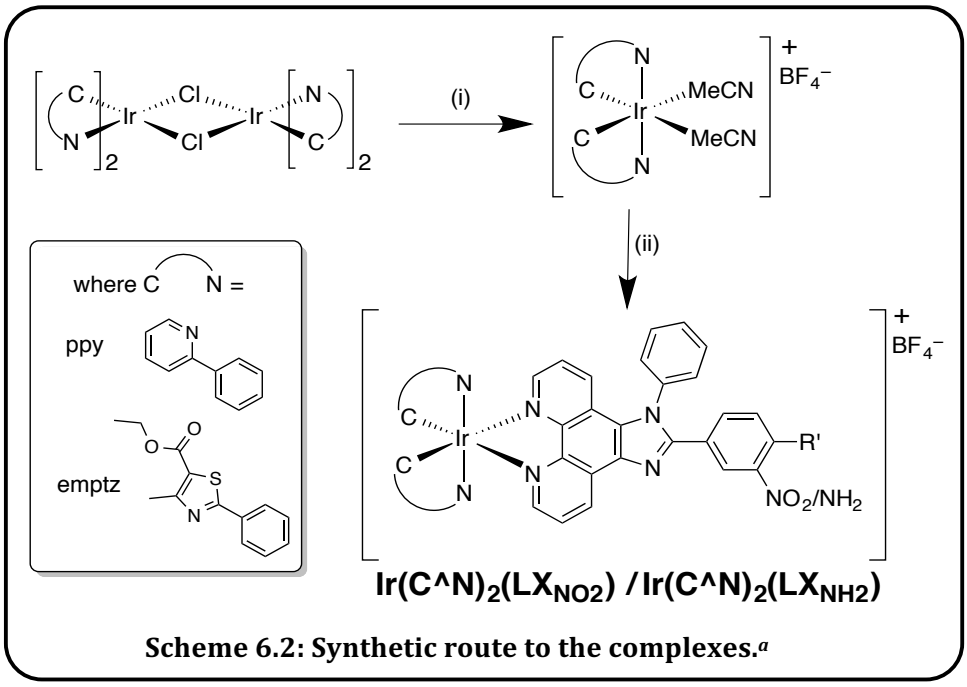

Scheme 6.2: Synthetic route to the complexes.[a]

The relatively good solubility of **L1–2** allowed facile coordination to the bis–acetonitrile iridium precursors (Scheme 6.2). Although first splitting the dimers with labile acetonitrile ligands induces an additional step to the synthesis, it importantly offers more gentle reaction conditions for coordination of $\mathbf{L1_X–2_X}$ (*i.e.* $CHCl_3$ at reflux[46] *versus* 2–methoxyethanol at 120 ^oC[47,48]). The set of $\mathbf{LX_{NO2}}$ and $\mathbf{LX_{NH2}}$ were all successfully coordinated to iridium with two phenylpyridine (ppy) co–ligands and also ethyl–4–methylphenylthiazole–5–carboxylate (emptz) co–ligands in the case of $\mathbf{L2_{NO2}}$ and $\mathbf{L2_{NH2}}$. The average combined yield for the two synthetic steps exceeded 70% and was therefore higher than typical coordination yields for related ligands directly with $[Ir(\mu–Cl)_2(C^N)_2]$ dimers (60–65 %).[24,36] This gave a set of six new monometallic cationic complexes of the general form $[Ir(C^N)_2(N^N)](BF_4)$, where varying the cyclometalating and di–imine unit

offers potential influence on the electronic and physical properties of the complexes, as well as providing opportunities for further chemistry. For example the enhanced amphiphilic nature of **L2$_X$,** combined with the protected carboxylic acid groups of ethyl–4–methylphenylthiazole–5–carboxylate (emptz) (Scheme 6.2), offers potential towards water–soluble iridium complexes.

All new complexes were characterised using a range of spectroscopic techniques. The ^{1}H NMR spectra of the complexes show aromatic regions with overlapping resonances associated with the cyclometalated and di–imine ligands (Figure 6.11). For complexes of the emptz co–ligand, retention of the ethyl ester functionality was observed in the aliphatic region in addition to the alkyl chains of the coordinated ligands.

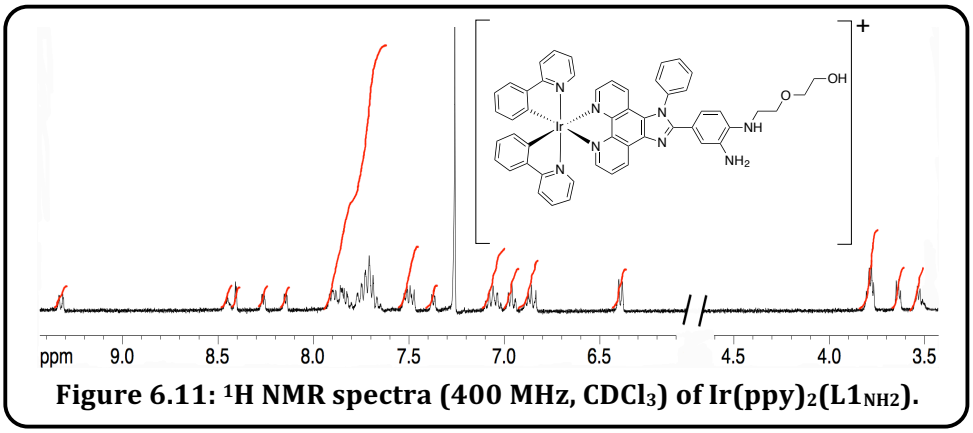

Figure 6.11: ^{1}H NMR spectra (400 MHz, $CDCl_3$) of Ir(ppy)$_2$(L1$_{NH2}$).

Solid state IR spectra and $^{13}C\{^1H\}$ NMR spectra were also obtained on all complexes, agreeing well with the proposed structures. Both techniques highlighted the ester functionality of emptz containing species (*ca*. 180 ppm and 1710 cm^{-1}) and IR spectroscopy also revealed the BF_4^- counter ion stretches at *ca.* 1160 and 1030 cm^{-1}. Importantly both low and high resolution mass spectra were obtained for the complexes revealing the parent cations of $[M - BF_4]^+$, with the appropriate isotopic distribution for iridium observed in each case (Figure 6.12).

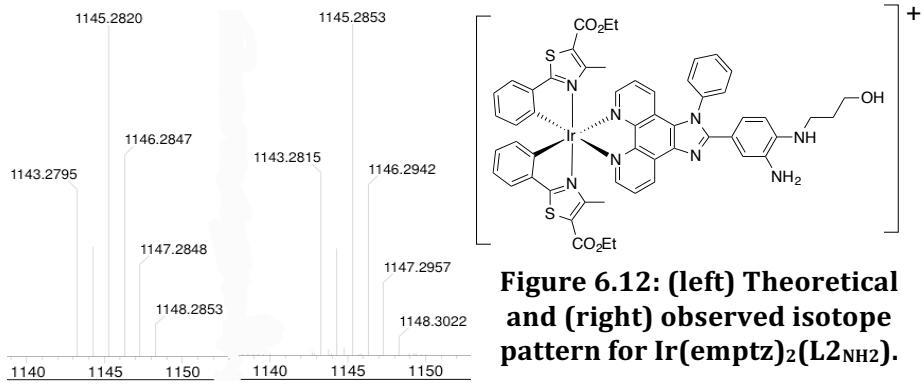

Figure 6.12: (left) Theoretical and (right) observed isotope pattern for Ir(emptz)$_2$(L2$_{NH2}$).

6.3.3 NO bound species: synthesis and characterisation

In order to identify successful binding of the 1,2–diamine species with NO, an aliquot of $\mathbf{L1_{NH2}}$, $\mathbf{L2_{NH2}}$ and their corresponding complexes was taken and reacted with NO(g) (Figure 6.13) in solvent. This was done by bubbling NO(g) through a degassed solution of the compounds for 5 minutes. NO(g) delivery was achieved using a needle inserted into the previously sealed, inert vessel. The latter prevented the oxidation of NO(g) to NO_2(g), until sufficient concentrations had been reached. After reprecipitation the triazole products were isolated in high yields (>80 % in all except one case). It was apparent that $\mathbf{LX_{NH2}}$ and corresponding complexes reacted rapidly, and under very mild conditions with NO(g) as with other NO sensors.[1,49] The first indication of successful binding was a slight colour change of the solution and the lower solubility observed for the products.

Due to the irreversible nature of the binding event, resulting in the formation of a benzotriazole species and overall loss of water, all of the NO reacted species ($\mathbf{LX_{NO}}$ and corresponding complexes) were fully characterised (Figure 6.13). Spectroscopic techniques were difficult in some cases due to the poor solubility of the NO bound species, related to the increased aromaticity, however importantly data from these techniques further supported the formation of benzotriazole moieties that could have only arisen from successful reaction with NO.

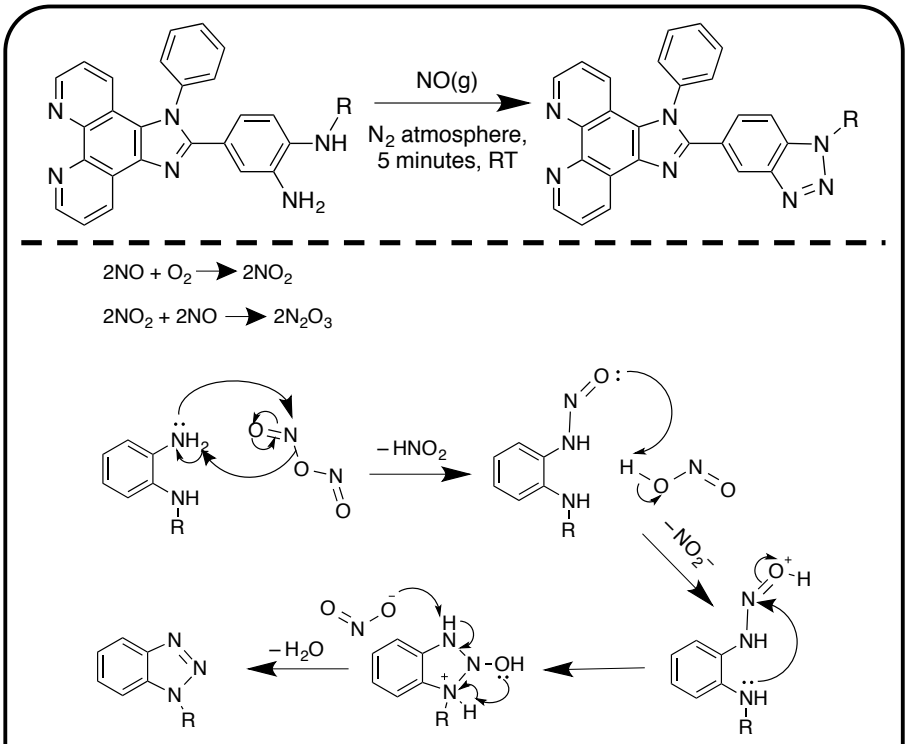

Figure 6.13: Benzotriazole formation upon successful binding of $\mathbf{LX_{NH2}}$ to NO(g) to form $\mathbf{LX_{NO}}$. Speculative mechanism inspired from the Graebe–Ullmann synthesis[50] and other sources.[51-53]

^{1}H NMR spectroscopy showed the loss of the N*H* resonance in all cases. In addition significant downfield shifts[49] (*ca*. 0.4–1.0 ppm) of the aromatic resonances were observed, associated with transformation of the electron rich *o*–phenylenediamine to the electron deficient benzotriazole group, containing two electron withdrawing nitrogen atoms. Due to the poor solubility, particularly of **Ir(ppy)$_2$(LX$_{NH2}$)**, mass spectrometry and solid state IR spectroscopy techniques were key in identifying successful binding to NO. Both low and high resolution mass spectra showed the presence of $[M–BF_4]^+$ in all cases.[6] IR studies of **LX$_{NO}$** and corresponding complexes showed the addition of a strong peak at *ca*. 1330 cm^{-1} when compared to the free ligand, presumably attributed to the triazole moiety.

6.3.4 Electrochemistry

The electrochemical characteristics of the complexes were studied in de-oxygenated acetonitrile (Table 6.1 and Figure 6.14). The cyclic voltammograms were measured at a platinum disc electrode (scan rate υ = 200 mVs^{-1}, 1×10^{-3} M solutions, 0.1 M $[NBu_4][PF_6]$ as a supporting electrolyte) using the couple of $FeCp_2^{0/1+}$ as an internal reference.

Table 6.1: Electrochemical properties of $[Ir(C^N)_2(LX_Y)]BF_4$ where C^N = ppy or emptz, X = 1–2 and Y = NO_2, NH_2 or NO.

Complex	E_{ox} / V[a]	E_{red} / V[a]
Ir(ppy)$_2$(L1$_{NO2}$)	+1.35	–1.13, –1.42
Ir(ppy)$_2$(L1$_{NH2}$)	+1.36	–1.42
Ir(ppy)$_2$(L1$_{NO}$)	+1.35	–1.42
Ir(ppy)$_2$(L2$_{NO2}$)	+1.36	–1.23, –1.47
Ir(ppy)$_2$(L2$_{NH2}$)	+0.76, +1.40	–1.38
Ir(ppy)$_2$(L2$_{NO}$)	+1.78	–1.30, –1.46
Ir(emptz)$_2$(L2$_{NH2}$)	+1.51	–1.37, –1.65
Ir(emptz)$_2$(L2$_{NO}$)	+1.42	–1.40

[a]Oxidation and reduction potentials measured in MeCN solutions at 200 mV s^{-1} with 0.1 M $[NBu_4][PF_6]$ as supporting electrolyte, calibrated with Fc/Fc^+.

Each complex showed one non–fully reversible oxidation, generally over the range +1.35 to +1.51 V, assigned to the $Ir^{3+/4+}$ couple.[23,24,47,48,54] However the value for **Ir(ppy)$_2$(L2$_{NO}$)** fell outside this narrow window and was instead observed at + 1.78 V, very close to the solvent window. **Ir(ppy)$_2$(L2$_{NH2}$)** also showed an additional oxidation potential at +0.76 V at a scan rate υ = 200 mVs^{-1}, however this was not observed at either 50 or 500 mVs^{-1}. The oxidation of the complexes containing the glycol appended ligands (**L1$_{NO2}$**, **L1$_{NH2}$** and **L1$_{NO}$**) showed no variation across the series. On the other hand the oxidation potential value for complexes of **L2** derived species were much more varied. For the **Ir(ppy)$_2$(L2$_X$)** species,

the least stable complex was found to incorporate the nitro ligand, **L2$_{NO2}$**, with the NO bound species observed as much more stable (+ 0.4 V compared to **Ir(ppy)$_2$(L2$_{NO2}$)**). On the other hand the **Ir(emptz)$_2$** species of **L2$_X$** showed the reverse trend where the di–amino species gave a higher oxidation potential than the NO bound species. The results clearly suggest that, with the exception of **Ir(ppy)$_2$(L2$_{NO}$)**, the Ir(III) ion of complexes that incorporate cyclometalated emptz ligands were relatively stabilised *versus* the ppy analogues.[54] Overall complexes of the di–amino ligands, **LX$_{NH2}$**, were seen to be most reversible, suggesting a large contribution to the HOMO from the cyclometalating ligand.[24] This correlated with the greater electron donating ability of the di–amino unit versus nitro and triazole moieties, affecting the electron density of the HOMO on the Ir(III) core.[47]

Each complex also showed one or two partially reversible or fully reversible reduction waves. These were mostly observed between the narrow range of –1.37 to –1.47 V and can be assigned to ligand–centred processes involving both the di–imine and cyclometalated ligands.[23,48] Similar imidazo–phenanthroline examples in the literature by Tordera *et al.* [36] and Jayabharathi *et al.*[24] showed reversible reduction waves at *ca.* –1.76 and –2.00 V, respectively. As for the oxidation waves, much greater variability was seen in the data for iridium complexes of **L2$_X$** variants.

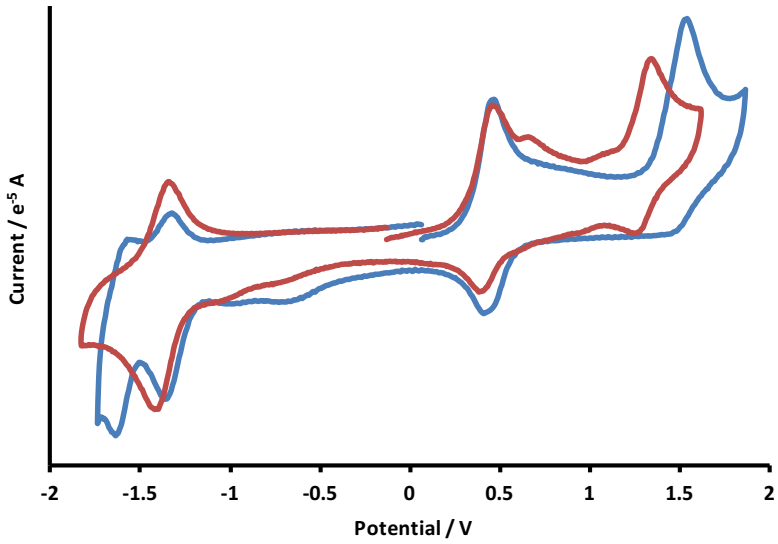

Figure 6.14: Cyclic voltammogram of Ir(ppy)$_2$(L2$_{NH2}$) and Ir(emptz)$_2$(L2$_{NH2}$) in MeCN solutions, at 200 mVs^{-1} with 0.1 M [NBu$_4$][PF$_6$] as supporting electrolyte, calibrated with FeCp$_2$.

6.3.5 UV–Vis Absorption Spectroscopy

Ligand Properties

The UV-vis absorption spectra of the ligands were recorded in aerated MeCN (2.5 × 10^{-5} M) (Figure 6.15). All ligands possessed strong absorption bands below 400 nm, assigned

to both spin allowed π–π* and imidazo–based n–π* transitions, as for related halogenated examples in the literature.[17,19,43,44] The lowest energy peak of $\mathbf{LX_{NH2}}$ was bathochromically shifted by 10 nm when compared to the corresponding $\mathbf{LX_{NO2}}$. In addition the spectra of $\mathbf{LX_{NO2}}$ species also possessed a weak, lower energy band centred at *ca*. 450 nm that could be a consequence of ICT between the amino (electron donating) and nitro (electron withdrawing) functional groups. Subtle variation of the R group was also shown to have a slight effect on $\boldsymbol{\lambda}_{abs}$ (*ca.* 5 nm).

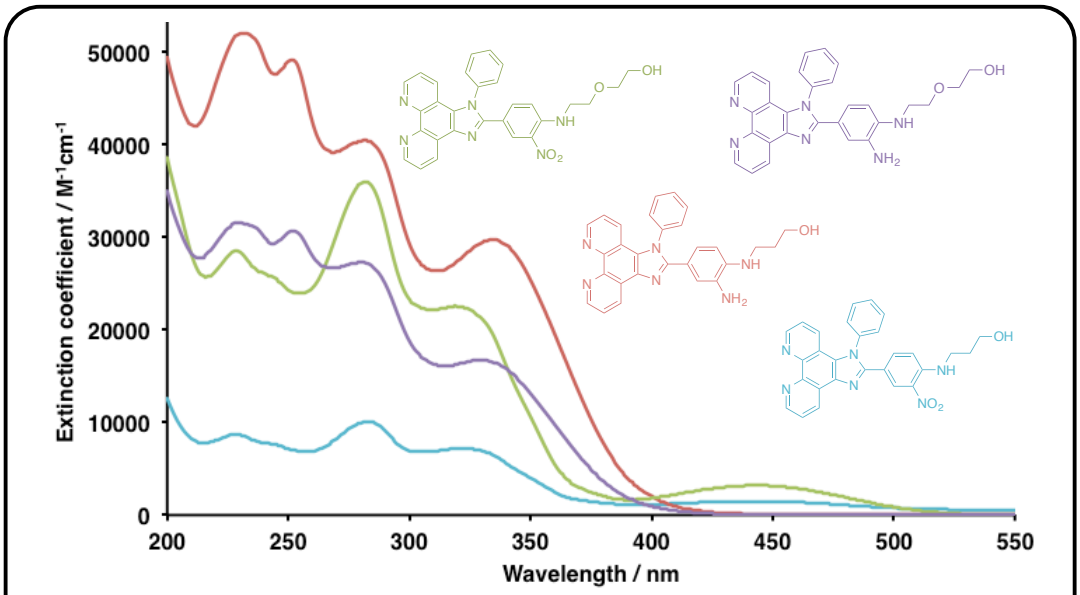

Figure 6.15: UV-vis absorption profile of the ligands in MeCN at 2.5 × 10^{-5} M.

Complex Properties

The UV-vis absorption spectra of the complexes were also obtained as aerated MeCN solutions (2.5 × 10^{-5} M) (Figure 6.16). The absorption properties of the complexes can largely be described as metal–perturbed ligand–centred[17] and consequently strong absorption bands were observed between 200–380 nm, akin to the free ligands.[22-24,26,35] However for the complexes the extinction coefficients were roughly double those of the free ligands due to spin allowed, π–π* ligand–centered transitions arising from both cyclometalated and di–imine ligands of each complex.[25,28,48] In addition to the ligand centred transitions, the set of complexes possessed weaker bands in the visible region at 350–450 nm. These were assigned to spin-allowed ^{1}MLCT (Ir(d)–π*) and ^{1}LLCT (π_{phenyl}–$\pi^*_{imidazo}$) transitions,[25,26,28,35,36] with the possibility of spin–forbidden ^{3}MLCT transitions contributing to the weaker low-energy shoulder at *ca*. 480 nm.[23-25,36] The latter suggests efficient ISC between the singlet and triplet states of iridium, facilitated by the heavy atom effect. Varying the coordinated di–imine ligand resulted in only minor tuning of the wavelength of the visible absorption bands. On the other hand vast differences were

observed in the absorption wavelengths (*ca*. 40 nm) between ppy and emptz complexes of the same di–imine ligand (Figure 6.16).

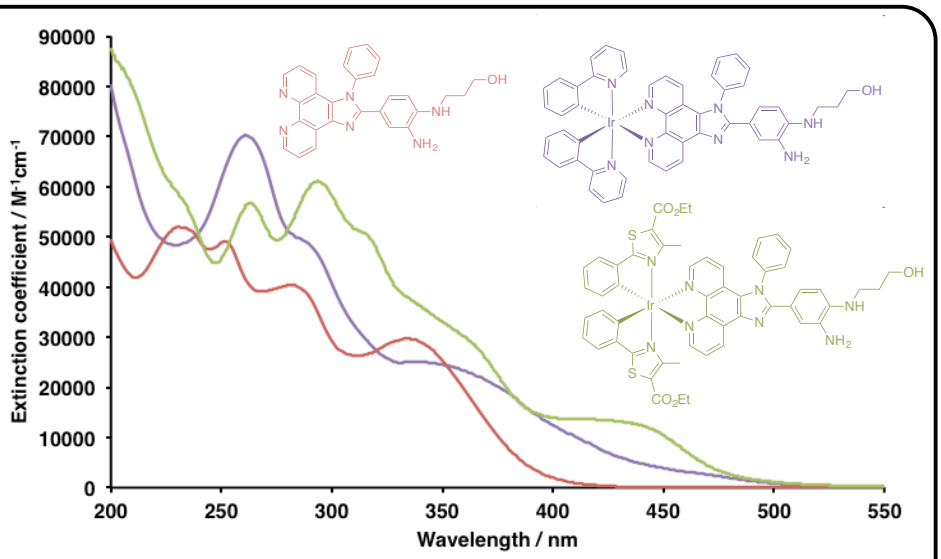

Figure 6.16: UV-vis absorption profile comparing $L2_{NH2}$ and corresponding complexes in MeCN at 2.5 × 10^{-5} M.

Triazole species (NO bound) properties

The electronic properties of the ligands and complexes should be greatly affected due to the formation of the benzotriazole moiety. Changes in the absorption properties after reaction with NO were first indicated by green to brown colour changes between the unbound and bound species.[1] The UV-vis spectra showed a *ca*. 5–20 nm hypsochromic shift of the transitions for the NO bound species (Figure 6.17).[55] The shift was most apparent for the lower energy transitions, particularly the MLCT peaks of the complexes.

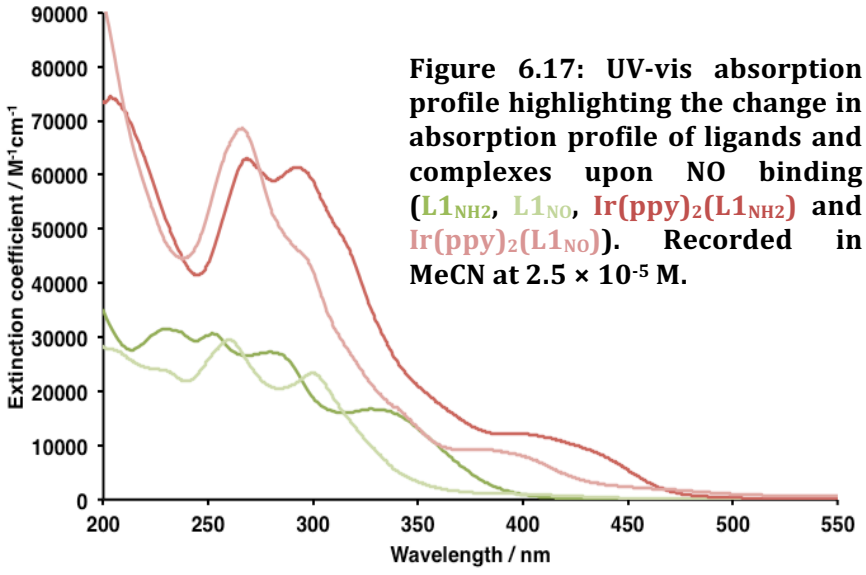

Figure 6.17: UV-vis absorption profile highlighting the change in absorption profile of ligands and complexes upon NO binding ($L1_{NH2}$, $L1_{NO}$, $Ir(ppy)_2(L1_{NH2})$ and $Ir(ppy)_2(L1_{NO})$). Recorded in MeCN at 2.5 × 10^{-5} M.

6.3.6 DFT

Charge transfer excited states play a key role in photophysical behaviour and therefore TD–DFT (Section 6.5.1), conducted by Dr Benjamin Ward, was used to investigate the charge transfer nature of **LX** and **Ir(ppy)$_2$(LX)** species by calculating the first fifty excited states. The calculations in simulated MeCN (Figure 6.18 and Figure 6.20) were performed in order to support electronic and spectral data, as well as provide additional evidence towards the successful binding to NO. Spin density isosurfaces were also calculated (Figure 6.18 and Figure 6.19) along with the main orbital calculations (appropriate excited state files provided on CD-ROM). The TD–DFT calculations were in much better agreement with the experimental data when the CAM–B3LYP functional, designed for molecules with a high degree of charge transfer, was used. After applying this functional the transition energies were underestimated by only *ca*. 30 nm.

Ligand Properties

The TD–DFT studies of the ligands (Figure 6.18) suggested the assignment of the lowest lying absorption bands dominated by π–π* transitions. For both **LX$_{NH2}$** and **LX$_{NO}$**, the first transition involved excitation from the HOMO to LUMO,[21] predicted at 305 nm (oscillator strength = 0.28 au) and 300 nm (oscillator strength = 0.17 au), respectively.

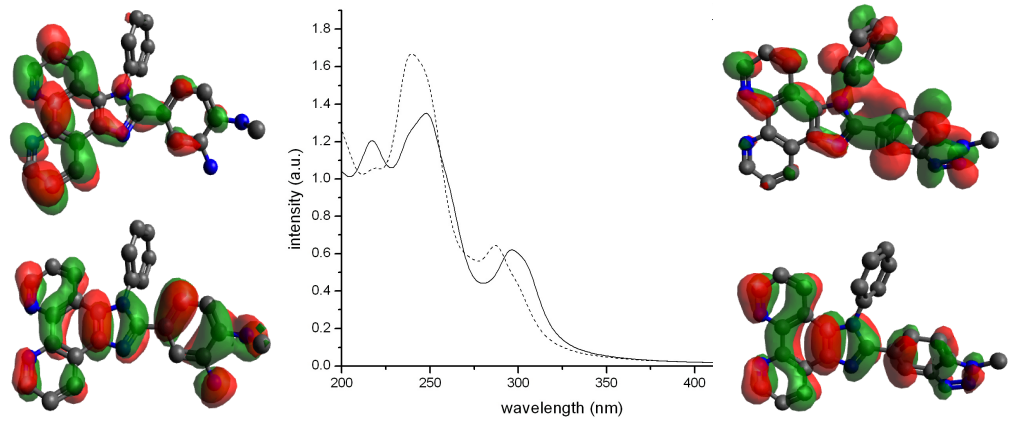

Figure 6.18: Electron density distribution of the frontier orbitals (LUMO, top; HOMO, bottom) for LX$_{NH2}$ (left) and LX$_{NO}$ (right) with hydrogen atoms omitted for clarity. Theoretical UV-vis spectra (centre) of LX$_{NH2}$ (solid) and LX$_{NO}$ (dotted) simulated in MeCN.

For **LX$_{NH2}$** the electron density for the HOMO was spread over the molecular axis whereas for the LUMO it sat mostly on imidazo–phenanthroline structure.[19,21] This was vastly different for NO bound **LX$_{NO}$** where the LUMO was mostly situated on N-phenylimidazo and benzotriazole moeities. For both **LX$_{NH2}$** and **LX$_{NO}$** a set of stronger bands centred between 240–290 nm (290, *ca* 0.37 au; 250 nm, 0.61 au; 236 nm, 0.31 or 0.85 au), was

also predicted, in good agreement with Figure 6.15. These bands were again dominated by varying π–π* transitions, as well as an ICT contribution. The predicted hypsochromic shift upon binding to NO and subsequent benzotriazole formation supports the experimental binding of NO by **L1$_{NH2}$**.

Complex Properties

The TD–DFT studies of the **Ir(ppy)$_2$(LX)** complexes (Figure 6.19) suggested the assignment of the lowest lying absorption bands as having substantial mixed MLCT and LLCT character.[22] For **Ir(ppy)$_2$(LX$_{NH2}$)** the lowest energy absorption involves excitation from HOMO–1 (Ir–5d + cyclometalating phenyl–π)[29] to LUMO (Ir–5d + phenanthroline–π*) and HOMO (phenylimidazo π*)[15,29] to LUMO.[28] It was predicted to lie at 350 nm (oscillator strength = 0.28 au) and was therefore in excellent agreement with the lowest energy shoulder feature seen in the experimental UV-vis spectra (Figure 6.16). The electron density maps for these transitions support the ^{3}MLCT and ^{3}LLCT assignment for these transitions. A set of stronger π–π* bands between 200–325 nm (313 nm, 0.30 au; 291 nm, 0.42 au; 254 nm, 0.43 au) was also predicted, again consistent with Figure 6.16.

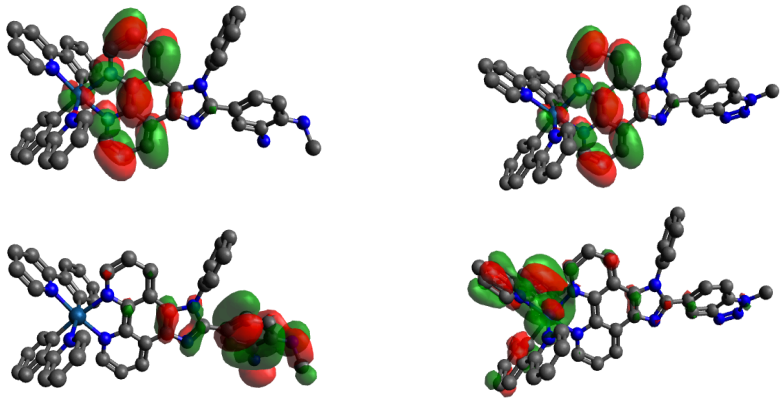

Figure 6.19: Electron density distribution of the frontier orbitals (HOMO, bottom; LUMO, top) of Ir(ppy)$_2$(LX$_{NH2}$) (left) and Ir(ppy)$_2$(LX$_{NO}$) (right) with hydrogen atoms omitted for clarity.

In comparison, TD–DFT simulation of NO bound **Ir(ppy)$_2$(LX$_{NO}$)** in MeCN suggested a very different nature to the LLCT the transition. The lowest lying absorption band is dominated by excitation from the HOMO (Ir–5d + cyclometalating phenyl–π) to LUMO (Ir–5d + phenanthroline–π*) as well as a small contribution from HOMO–4 (cyclometalating phenyl π* + benzotriazole π*) to LUMO, predicted at 347 nm (oscillator strength = 0.09 au).

Similarly to **Ir(ppy)$_2$(LX$_{NH2}$)**, it was also predicted that **Ir(ppy)$_2$(LX$_{NO}$)** possessed additional stronger π–π* bands >335 nm (334 nm, 0.19 au; 304, 0.12 au, 273 nm, 0.44 au; 253 nm, 0.47 au), again consistent with Figure 6.16 and are mostly π–π* in character. As

for the free ligands, comparisons between the simulated UV-vis spectra of **Ir(ppy)$_2$(LX$_{NH2}$)** and **Ir(ppy)$_2$(LX$_{NO}$)** in MeCN (Figure 2.20) predicted a *ca*. 15 nm hypsochromic shift upon binding to NO, in good agreement with experimental data (Figure 6.17).

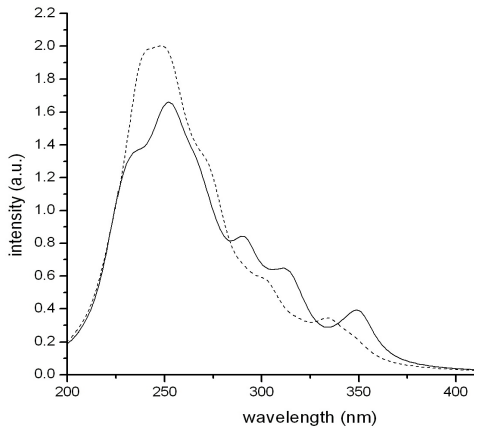

Figure 6.20: TD–DFT simulated UV-vis spectra of Ir(ppy)$_2$(LX$_{NH2}$) (solid line) and Ir(ppy)$_2$(LX$_{NO}$) (dotted line) in MeCN.

6.3.7 Luminescence Spectroscopy

The luminescence properties of all ligands and complexes were measured in aerated MeCN (Table 6.2).

Table 6.2: Photophysical properties of the complexes. Ligand values below in parenthesis.

Compound	λmax$_{exc}$ / nm[a,b,c]	λ$_{em}$ / nm[a,b,d]	τ / ns[a,e]	ϕ[a]
Ir(ppy)$_2$(L1$_{NO2}$)	281 (265)	522 (433)	6.6, 17.2 (80 %) (0.7, 2.6 (68 %)	0.000
Ir(ppy)$_2$(L1$_{NH2}$)	276 (257)	579 (431)	5.2, 65.1 (92 %) (5.1)	0.018
Ir(ppy)$_2$(L1$_{NO}$)	276 (271)	494 (418)	8.8, 69.7 (78 %) (4.0)	0.054
Ir(ppy)$_2$(L2$_{NO2}$)	282 (275)	517 (427)	4.1, 20.7 (97 %) (0.5, 2.6 (64 %))	0.006
Ir(ppy)$_2$(L2$_{NH2}$)	277 (273)	579 (435)	5.2, 62.7 (98 %) (1.0, 4.7 (89 %))	0.014
Ir(ppy)$_2$(L2$_{NO}$)	272 (269)	496 (416)	9.6, 320.3 (98 %) (0.4, 4.0 (94 %))	0.017
Ir(emptz)$_2$(L2$_{NH2}$)	276 (273)	548, 587s (435)	0.6, 239 (98 %) (1.0, 4.7 (89 %))	0.006
Ir(emptz)$_2$(L2$_{NO}$)	275 (269)	546, 580s (416)	13.5, 322 (99%) (0.4, 4.0 (94%))	0.107

[a]recorded in aerated MeCN solution, [b]ligand values below in parentheses, [c]λ_{em} = emission maxima value nm, [d]λ_{exc} = 355 nm, [e]λ_{exc} = 372 nm laser.

Ligand Properties

Room temperature solution state luminescence data showed all ligands to be emissive in aerated MeCN (5×10^{-5} M). Ligands possessed broad excitation bands centred around 270 nm, with the exception of $\mathbf{L2_{NH2}}$ that was centred at 257 nm (Figure 6.21). The excitation spectra of all ligands possessed a shoulder observed at 320–360 nm. Very little variation was seen in either the excitation or emission profiles of the ligands.

Upon irradiation at 355 nm all ligands produced a broad, blue emission band centered at *ca*. 430 nm for both $\mathbf{LX_{NO2}}$ and $\mathbf{LX_{NH2}}$, characteristic of phenylimidazo–phenanthroline ligands of this type.[17,22,44] The broad emission (370–600 nm) suggests an excited state of charge transfer nature. This assignment was again supported by the large Stokes' shifts observed for the ligands (*ca*. 125000 cm^{-1}) that were slightly extended for $\mathbf{LX_{NH2}}$ species compare to $\mathbf{LX_{NO2}}$. Previous related ligands by Jayabharathi *et al*. have also showed large Stokes shifts of *ca*. 66700 cm^{-1} in polar, protic solvents.[19]

The lifetimes (Table 6.2) of the ligands were indicative of fluorescence in all cases, with lifetimes <5 ns.[17,19,22] In most cases the lifetime data best fit a bi–exponential, indicating dual component emission. In each case one short (<1 ns) and heavily quenched (< 35 %) emissive state was observed in conjunction with a longer, dominant component.

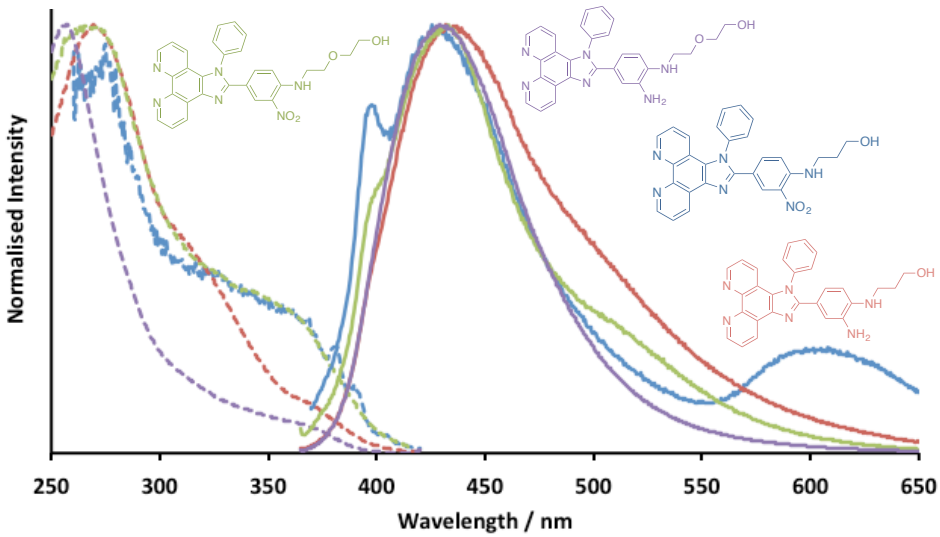

Figure 6.21: Excitation (dashed) and emission (solid) profiles of $\mathbf{LX_{NO2}}$ and $\mathbf{LX_{NH2}}$.

Complex Properties

Steady state, room temperature luminescence measurements were also conducted on aerated MeCN solutions of the complexes (Table 6.2 and Figure 6.22). The excitation properties for all complexes closely resembled those of the free ligands. The main

excitation peak experienced only a slight bathochromic shift (3–20 nm) upon coordination however the shoulders and tail were extended to 500 nm. All of the complexes showed visible green or orange emission centred between 495–575 nm.[22,23,25,26,35,36] Therefore bathochromic shifts of the emission peak, ranging between 90–150 nm, were observed upon coordination. This is likely due to the introduction of a ^{3}MLCT system which is favoured by complexes that possess large ligand field stabilisation energy, induced by the high oxidation state and ligand field splitting of the cyclometalating ligands, favouring ISC.[25] It is noteworthy that whilst differences in the emission wavelength were observed between **Ir(ppy)$_2$LX$_{NO2}$** (*ca*. 520 nm) and **Ir(ppy)$_2$LX$_{NH2}$** (*ca*. 580 nm), the nature of the R substituent had negligible affect on the photophysical properties. The emission maxima for the complexes were broad and featureless,[17,36] characteristic of MLCT based transitions.[36,56] This was further supported by the highly favourable Stokes' shifts of *ca*. 100000 cm^{-1} for **Ir(ppy)$_2$LX$_{NO2}$** and *ca*. 62500[35] cm^{-1} for **Ir(ppy)$_2$LX$_{NH2}$. Ir(emptz)$_2$(L2$_{NO2}$)** possessed different emission properties to **Ir(ppy)$_2$(LX)** species. Notably the emission wavelength was observed at 548 nm with an additional shoulder at 587 nm characteristic of a stronger vibronic component to the excited state.

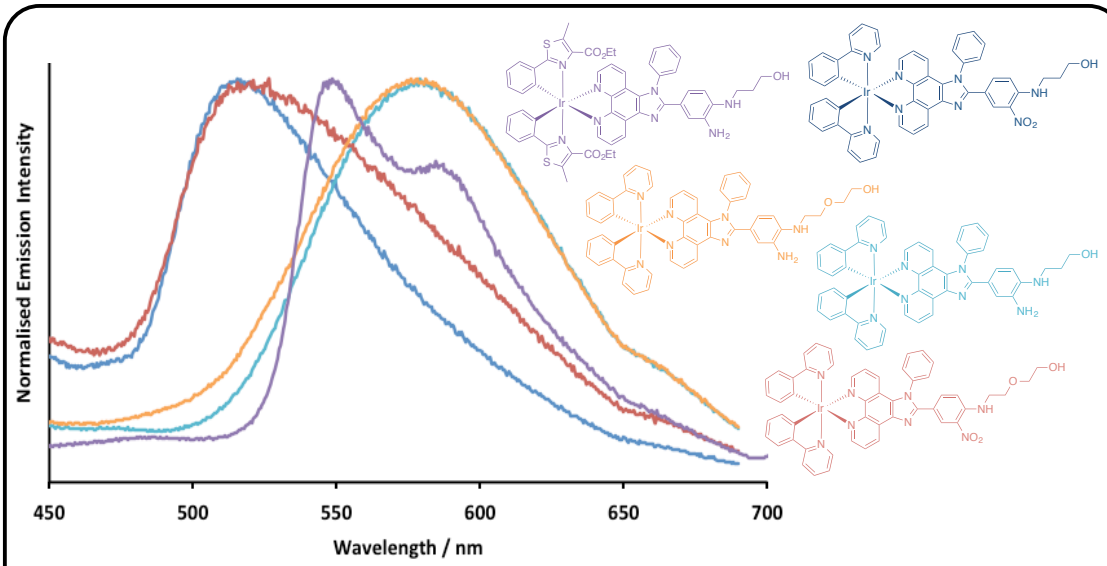

Figure 6.22: Emission properties of the non–NO bound complexes recorded in MeCN.

Time–resolved emission lifetime measurements revealed that the decays were bi–exponential and highly varied across the series. The phosphorescent lifetimes for **Ir(ppy)$_2$(LX)** species were observed between 20–65 ns, whereas the emptz species showed a much longer lifetime at 239 ns.[23] This value is more common for phenylimidazo–phenanthroline iridium complexes for which lifetimes in excess of 1 µs have been reported (albeit often in degassed solvent).[22,28] The shortest lifetimes were

observed for complexes of $\mathbf{LX_{NO2}}$ species (*ca*. 20 ns); nitro is well known quenching moiety. All lifetimes were shorter than expected based on similar literature examples that have shown lifetimes in the tens of microseconds range.[25,36] In addition these literature examples also showed much more favourable quantum yields, typically of *ca.* 40%. Complexes herein each exhibited modest quantum yields, typically between 1–5 %, comparable to similar cationic cinchophen Ir(III) complexes described in related studies.[48]

Triazole species (NO bound) properties

It is very important that a luminescent probe for NO shows measurable changes to the photophysical properties upon exposure and binding to NO. Assessing the photophysical properties of the NO bound species, $\mathbf{LX_{NO}}$ and corresponding complexes, allowed identification of these changes and the feasibility of this series of compounds as NO receptors/dosimeters.

Upon ligand binding to NO (Table 6.2), $\mathbf{LX_{NH2}}$ showed a 13–19 nm hypsochromic shift[1] that was most pronounced for $\mathbf{L2_{NH2}}$. The NO bound species possessed shorter emission wavelengths than both $\mathbf{LX_{NO2}}$ and $\mathbf{LX_{NH2}}$ species. Overall the photophysical properties of the NO bound species are closer to that of the NO_2 species, corresponding with the CV and UV-vis data. A *ca*. 1 ns shortening of lifetimes was also observed for the NO bound ligands.

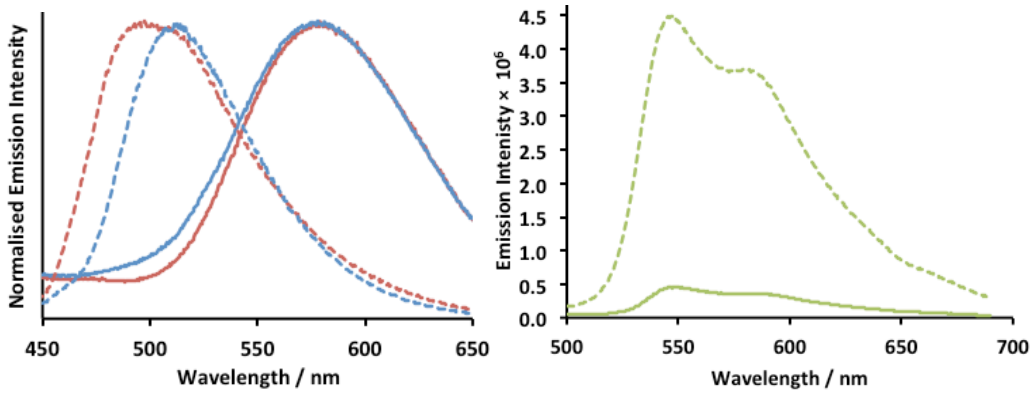

Figure 6.23: Changes to the photophysical properties of $Ir(ppy)_2(L1_{NH2})$ (blue), $Ir(ppy)_2(L2_{NH2})$ (red) and $Ir(emptz)_2(L2_{NH2})$ (green) upon NO binding (dashed).

The photophysical changes upon NO binding for the complexes were much more dramatic (Figure 6.23). Firstly $\mathbf{Ir(ppy)_2(LX_{NO})}$ species showed a *ca*. 83 nm hypsochromic shift of the emission wavelengths when compared to $\mathbf{Ir(ppy)_2(LX_{NH2})}$ species. Oppositely, a negligible shift of the emission wavelength was observed for $\mathbf{Ir(emptz)_2(L2_{NH2})}$, however data analysis showed a 10–fold enhancement of the emission intensity upon NO binding (Figure 6.23).[1,6] This also seems to be true for all other species although direct comparisons cannot be drawn due to different slit values having to be used for

luminescence measurements of the di–amino and triazole species. Further support for the luminescent enhancement of the complexes upon NO binding was seen in the quantum yield data that generally showed an increase in all cases. This was negligible for **Ir(ppy)$_2$(L2$_{NO}$)** whereas a 3–fold and 10–fold improvement in the quantum yields was observed for **Ir(ppy)$_2$(L1$_{NO}$)** and **Ir(emptz)$_2$(L2$_{NO}$)**, respectively. The latter agreed well with the observed 10–fold fluorescent enhancement of that species. Many other literature examples of fluorescent *o*–phenylenediamine appended NO probes have also shown large emission enhancement (up to 30 times) upon binding to NO.[5,14,57] It has been suggested that this enhancement is due to the disappearance of the electron rich *o*–phenylenediamine unit that quenches fluorescence *via* PeT.[6]

The other photophysical properties of the complexes also showed varied responses to NO binding (Table 6.2). All complexes showed a lengthening of lifetimes upon formation of the triazole species, **Ir(C^N)$_2$(LX$_{NO}$)**. This could in part be explained by the increased rigidity of triazole ring reducing vibrational deactivation pathways as well as the *o*–phenylenediamine PeT quenching mechanism being deactivated in the NO bound, triazole species. The lifetime extension was negligible for **Ir(ppy)$_2$(L1$_{NO}$)**, however substantial extensions were observed for the lifetimes of **Ir(ppy)$_2$(L2$_{NO}$)** (*ca*. 240 ns) and **Ir(emptz)$_2$(L1$_{NO}$)** (80 ns). Such an observation is important when considering the application of luminescent probes to fluorescence/phosphorescence lifetime imaging microscopy.

6.4 Conclusion

This chapter has described the synthesis, structural and spectroscopic properties of a range of cationic Ir(III) complexes that incorporate bi–dentate, substituted phenanthroline–imidazo ligands towards sensors for NO. Both ligands and complexes were extensively characterised through both experimental and theoretical studies. The ligands incorporating aliphatic alcohol chains resulted in good solubility properties for the complexes, as well as inducing subtle changes to the photophysical properties. The *o*–phenylenediamine variants all showed effective NO binding properties.

The emissive properties of the fluorophores were dictated by π–π* transitions, with lifetimes up to *ca.* 5 ns. DFT calculations support the assignment of predominantly π–π* transitions and that spectral changes are consistent with successful NO binding. The complexes were found to be phosphorescent with visible emission wavelengths and lifetimes of ^{3}MLCT and ICT character. The precise nature of the cyclometalating ligand influenced the observed emission profiles and lifetimes. This leads to possible further work with these complexes. Previous work has shown that the deprotection of ester groups in the emptz cyclometalated ligand is a viable route to water-soluble phosphorescent species.[54] In addition other C^N ligands and R/R' groups on the di–imine ligands could be investigated to further tune the photophysical properties. Furthermore these variants could improve physical properties to facilitate such species being used for NO detection in a biological context using fluorescence imaging.

NO responsive studies showed effective binding to NO, with the NO bound triazole species also being fully characterised. Within this small collection of compounds, a large range of different responses were observed upon binding to NO. Significant changes were seen in the photophysical properties, particularly of the complexes. Among the collection several of the compounds' responses showed great promise for potential application as NO probes. Notably **Ir(ppy)$_2$(L2$_{NH2}$)** showed an impressive *ca*. 240 ns extension to the phosphorescent lifetime and therefore has possible applications as a lifetime (imaging) probe for NO. Furthermore, **Ir(emptz)$_2$(L2$_{NH2}$)** was shown to have a 10–fold luminescence enhancement upon binding to NO and quantum yield data suggested this was also true for the other **Ir(C^N)$_2$(Lx$_{NH2}$)** complexes, albeit to a lesser extent. Importantly the route to a water soluble complex offered by **Ir(emptz)$_2$(L2$_{NH2}$)** presents the opportunity for NO sensing in biological conditions, for example using CFM on living cells.

6.5 Experimental Section

6.5.1 DFT Studies

DFT calculations were conducted by Dr Benjamin Ward at Cardiff University's School of Chemistry.

Scalar relativistic DFT calculations were carried out using the Gaussian 09 package,[58] with relativistic effects incorporated *via* the use of appropriate effective core potentials (ECPs). Geometry optimisations were performed without symmetry constraints at the CAM–B3LYP level,[59] which was developed specifically to improve the description of excited states involving substantial charge-transfer character. The D3 version of Grimme's dispersion correction was included in all calculations.[60] The calculations were undertaken with a basis set consisting of the Stuttgart-Dresden basis set plus ECP on Ir, and the cc–pVDZ double–ζ basis set on all remaining atoms.[61,62] Time-dependent DFT (TD–DFT) calculations also employed CAM–B3LYP; the first 50 excited states were calculated. Calculations employing the B3LYP[63,64] or M06[65] functionals substantially underestimated the excitation energies, by *ca.* 50 nm. As shown by Vlček *et al.*,[66] solvent effects can be crucial for obtaining satisfactory agreement between experiment and TD–DFT. Solvent was therefore modelled using the polarisable continuum model,[67] with the molecular cavity defined by a united atom model that incorporates hydrogen into the parent heavy atom, and included in both geometry optimisations and TD-DFT calculations.

6.5.2 Electrochemical studies

Electrochemical studies were carried out using a Parstat 2273 potentiostat in conjunction with a three-electrode cell. The auxiliary electrode was a platinum wire and the working electrode a platinum (1.0 mm diameter) disc. The reference was a silver wire separated from the test solution by a fine porosity frit and an agar bridge saturated with KCl. Solutions (10 mL MeCN) were 1.0×10^{-3} moldm^{-3} in the test compound and 0.1 moldm^{-3} in $[NBun_4][PF_6]$ as the supporting electrolyte. Under these conditions, $E^{0\prime}$ for the one electron oxidation of $[Fe(\eta\text{-}C_5H_5)_2]$, added to the test solutions as an internal calibrant, is 0.46 V.[68] Unless specified, all electrochemical values are at υ = 200 mV s^{-1}.

6.5.3 General

^{1}H and ^{13}C{^{1}H} NMR spectra were recorded on an NMR–FT Bruker 400 MHz or Jeol Eclipse 300 MHz spectrometer and recorded in $CDCl_3$, CD_3CN or DMSO–*d6*. ^{1}H and ^{13}C{^{1}H} NMR chemical shifts (δ) were determined relative to residual solvent peaks with digital locking and are given in ppm. Low–resolution mass spectra were obtained by the staff at Cardiff

University. High–resolution mass spectra were carried out at the EPSRC National Mass Spectrometry Service at Swansea University. UV–vis studies were performed on a Jasco V–570 spectrophotometer in MeCN solutions (2.5×10^{-5} M). IR spectra were recorded on a Thermo Scientific Nicolet iS5 spectrometer fitted with an iD3 ATR attachment. Photophysical data were obtained on a JobinYvon–Horiba Fluorolog spectrometer fitted with a JY TBX picoseconds photodetection module. Emission spectra were uncorrected, and excitation spectra were instrument corrected. The pulsed source was a Nano-LED configured for 372 nm output operating at 1 MHz. Luminescence lifetime profiles were obtained using the JobinYvon–Horiba FluoroHub single photon counting module and the data fits yielded the lifetime values using the provided DAS6 deconvolution software. Quantum yield measurements were obtained on aerated MeCN solutions of the complexes, using $[Ru(bpy)_3](PF_6)_2$ in aerated MeCN as a standard (Φ_{em} = 0.016). [69,70] Electrochemical studies were carried out using a Parstat 2273 potentiostat in conjunction with a three-electrode cell. The auxiliary electrode was a platinum wire and the working electrode a platinum (1.0 mm diameter) disc. The reference was a silver wire separated from the test solution by a fine porosity frit and an agar bridge saturated with KCl. Solutions (10 mL CH_2Cl_2) were 1.0×10^{-3} moldm^{-3} in the test compound and 0.1 moldm^{-3} in $[NBun_4][PF_6]$ as the supporting electrolyte. Under these conditions, E0′ for the one–electron oxidation of $[Fe(\eta\text{-}C_5H_5)_2]$, added to the test solutions as an internal calibrant, is 0.46 V. Unless specified, all electrochemical values are at υ = 200 mV s^{-1}.

All reactions were performed with the use of vacuum line and Schlenk techniques. Reagents were commercial grade and were used without further purification. **L1–2** were prepared according to the literature procedures.[17,43] 1,10–Phenanthroline–5,6–dione was firstly synthesised according to well known literature techniques.[17]

6.5.4 Proligand Synthesis

*Synthesis of 2–(3'–nitro–4'–chlorophenyl)–1H–imidazo[4,5-f][1, 10]–phenanthroline (**ClA$_{NO2}$**)*

4–chloro–3–nitrobenzaldehyde (263 mg, 1.42 mmol) in glacial AcOH (6 mL) was added to a heated solution of 1,2–phenanthroline–5,6–dione (298 mg, 1.42 mmol) and ammonium acetate (3.44 g, 44.7 mmol) in glacial AcOH (9 mL) at 70 ºC, and the heat was continued, with stirring, for 3 hours. The cooled solution was poured into ice cold water (200 mL) and neutralised with 1M NaOH solution. The yellow precipitate was filtered from the solution and washed with copious amounts of water. Drying in an oven then afforded **CLA$_{NO2}$** as a yellow powder. Yield = 476 mg, 1.27 mmol, 89 %. ^{1}H NMR (400 MHz, DMSO)

δ_H = 9.06 (dd, 2H, $^3J_{HH}$ = 4.3, 1.7 Hz), 8.88 (d, 2H, $^3J_{HH}$ = 2.1 Hz), 8.87 (broad s, 1H, N*H*), 8.54 (dd, 1H, $^3J_{HH}$ = 8.4, 2.1 Hz), 8.05 (d, 1H, $^3J_{HH}$ = 8.5 Hz), 7.90–7.82 (broad m, 2H) ppm.

*Synthesis of 2–(3'–nitro–4'–chlorophenyl)–1–phenyl–1H–imidazo[4,5-f][1, 10]–phenanthroline (**ClB$_{NO2}$**)*

1,2–phenanthroline–5,6–dione (450 mg, 2.14 mmol), aniline (0.20 mL, 2.14 mmol), 4–chloro–3–nitrobenzaldehyde (397 mg, 2.14 mmol) and ammonium acetate (1.65 g, 21.4 mmol) in glacial AcOH (9 mL) were heated at reflux for 3 hours. The cooled solution was poured into ice cold water (200 mL) and neutralised with 10 % NH_4OH solution. To this 1 drop of 50 % hypochlorite solution was added and the yellow precipitate them extracted into CH_2Cl_2 (2 x 200 mL) and washed with water (2 × 200 mL). The organic phase was dried over $MgSO_4$ and the volume reduced to allow precipitation induced by the addition of Et_2O. The precipitate was filtered and dried to give the product as a yellow powder. Yield = 787 mg, 1.74 mmol, 81 %. ^{1}H NMR (400 MHz, $CDCl_3$) δ_H = 9.16–9.12 (m, 1H), 9.07–9.01 (m, 2H), 8.04 (s, 1H, NO_2CCH), 7.74–7.62 (m, 5H, phenyl), 7.52 (d, 2H, $^3J_{HH}$ = 7.3 Hz), 7.49–7.37 (m, 2H), 7.27–7.20 (m, 1H) ppm.

6.5.5 Ligand Synthesis

*Synthesis of **L1$_{NO2}$***

2–(2–aminoethyl)ethanol (0.52 mL, 5.27 mmol) was added to **ClB$_{NO2}$** (426 mg, 1.05 mmol) stirred in DMSO (6mL) under a dinitrogen atmosphere. The slurry was heated at *ca.* 80 ºC for 48 hours and then cooled and the product precipitated by the addition of water (20 mL). The reaction mixture was then neutralised with 1M HCl and then the product filtered, washed with copious amounts of water and then oven dried to give **L1$_{NO2}$** as a fluorescent orange-red powder. Yield = 378 mg, 0.73 mmol, 69 %. ^{1}H NMR (400 MHz, $CDCl_3$) δ_H = 9.13–9.11 (m, 1H, arom), 9.06 (dd, 1H, $^3J_{HH}$ = 8.1 Hz, $^3J_{HH}$ = 8.3 Hz, arom), 9.00–8.97 (m, 1H, arom), 8.34 (broad t, 1H, $^3J_{HH}$ = 4.2 Hz, N*H*), 8.17 (s, 1H, NO_2CCH), 7.87 (dd, 1H, $^3J_{HH}$ = 9.0 Hz, $^3J_{HH}$ = Hz, arom), 7.72–7.63 (m, 4H, arom), 7.53 (d, 1H, $^3J_{HH}$ = 7.6 Hz, arom), 7.52 (d, 1H, $^3J_{HH}$ = 8.1 Hz, arom), 7.40 (dd, 1H, $^3J_{HH}$ = 8.4 Hz, $^3J_{HH}$ = 8.4 Hz, arom), 7.24 (dd, 1H, $^3J_{HH}$ = 8.4 Hz, $^3J_{HH}$ = 8.4 Hz, arom), 6.80 (d, 1H, $^3J_{HH}$ = 9.2 Hz, NHCC*H*), 3.76–3.70 (m, 4H, $NH_2CH_2CH_2$), 3.58 (t, 2H, $^3J_{HH}$ = 4.8 Hz, OCH_2CH_2), 3.47 (app quar, 2H, $^3J_{HH}$ = 5.3 Hz, OCH_2CH_2), 1.87 (broad s, 1H, O*H*) ppm; ^{13}C{^{1}H} NMR (151 MHz, $CDCl_3$): δ_C = 150.3, 148.7, 148.0, 145.4, 137.8, 136.5, 135.9, 131.5, 131.0, 130.8, 128.6, 128.1, 127.2, 127.0, 123.9, 123.6, 122.5, 119.8, 117.1, 114.0, 72.5, 68.9, 61.9, 42.7 ppm; LRMS (AP$^+$) found *m/z* 521.19 for $[M+H]^+$; HRMS (ES$^+$) found *m/z* 521.1923 for $[C_{29}H_{24}N_6O_4+H]^+$, calculated at 521.1932 for $[C_{29}H_{24}N_6O_4+H]^+$; IR (solid) ν_{max} (±2 cm^{-1}) = 3356, 2922, 2858, 1627, 1597, 1571, 1517, 1496, 1469, 1446, 1390, 1354, 1286, 1255, 1224, 1184, 1151, 1118, 1060, 1028, 987, 960,

929, 887, 823, 798, 783, 736, 711, 677, 653, 615, 529, 488, 457, 424, 416, 407 cm^{-1}; UV-Vis (MeCN): λ_{max} ($\varepsilon/M^{-1}cm^{-1}$) = 447 (3200), 322 (22400), 284 (35600), 245 (25400), 231 (28200) nm.

Synthesis of ***L1$_{NH2}$***

L1$_{NO2}$ (207 mg, 0.40 mmol) and a 10 % loaded Pd/C catalyst (42 mg, 40 μmol) were stirred in MeOH (15 mL) with H_2 gas delivered into the solvent, for 16 hrs, forming a green solution. The solution was filtered through celite to remove the Pd/C and the MeOH removed under *vacuo* to give **L1$_{NH2}$** as a green crystalline solid. Yield = 130 mg, 0.46 mmol, 67 %. ^{1}H NMR (250 MHz, $CDCl_3$) δ_H = 9.17–9.03 (m, 2H, arom), 9.01–8.90 (m, 1H, arom), 7.72–7.51(m, 5H, arom and N*H*/NH_2), 7.51–7.42 (m, 2H, arom), 7.40–7.27 (m, 2H, arom), 7.27–7.13 (m, 2H, arom), 7.09 (s, 1H, NH_2CCH), 6.74 (dd, 1H, $^3J_{HH}$ = 8.3 Hz, $^3J_{HH}$ = 8.2 Hz, arom), 6.38 (d, 1H, $^3J_{HH}$ = 8.3 Hz, NHCC*H*), 3.66 (app quin, 4H, $NH_2CH_2CH_2$), 3.64 (t, 2H, $^3J_{HH}$ = 5.6 Hz, OCH_2CH_2), 3.21 (app quar, 2H, $^3J_{HH}$ = 5.1 Hz, OCH_2CH_2) ppm; $^{13}C\{^1H\}$ NMR (75 MHz, $CDCl_3$): δ_C = 148.9, 139.2, 138.5, 133.6, 130.8, 130.5, 130.2, 129.2, 129.0, 128.0, 123.5, 122.3, 122.2, 119.9, 117.9, 110.7, 72.2, 69.2, 65.8, 61.8,43.6, 29.8, 27.4, 15.4 ppm; LRMS (AP^+) found *m/z* 491.22 for $[M+H]^+$; HRMS (ES^+) found *m/z* 491.2182 for $[C_{29}H_{26}N_6O_2+H]^+$, calculated at 491.2190 for $[C_{29}H_{26}N_6O_2+H]^+$; IR (solid) ν_{max} (±2 cm^{-1}) = 3334, 3234, 3062, 2926, 2864, 1598, 1562, 1543, 1494, 1469, 1446, 1392, 1377, 1338, 1327, 1296, 1276, 1238, 1163, 1118, 1064, 1033, 995, 927, 879, 802, 738, 707, 675, 621, 405 cm^{-1}; UV-Vis (MeCN): λ_{max} ($\varepsilon/M^{-1}cm^{-1}$) = 333 (16600), 284 (26900), 255 (30172), 232 (31400) nm.

Synthesis of ***L2$_{NO2}$***

Prepared as for **L1$_{NO2}$** but using 3–aminopropanol (0.31 mL, 3.98 mmol) and **ClB$_{NO2}$** (360 mg, 0.80 mmol) to give **L2$_{NO2}$** as a red solid. Yield = 349 mg, 0.71 mmol, 89 %. ^{1}H NMR (400 MHz, $CDCl_3$) δ_H = 9.13 (d, 1H, $^3J_{HH}$ = 1.6 Hz, arom), 9.05 (dd, 1H, $^3J_{HH}$ = 8.1 Hz, $^3J_{HH}$ = 8.0 Hz, arom), 9.00–8.97 (m, 1H, arom), 8.18 (broad t, 1H, $^3J_{HH}$ = 4.6 Hz, N*H*), 8.15 (d, 1H, $^3J_{HH}$ = 2.2 Hz, arom), 7.72–7.65 (m, 5H, arom), 7.62–7.58 (m, 2H), 7.37 (dd, 1H, $^3J_{HH}$ = 85 Hz, $^3J_{HH}$ = 8.4 Hz, arom), 7.27 (dd, 1H, $^3J_{HH}$ = 4.3 Hz, $^3J_{HH}$ = 4.3 Hz, arom), 6.58 (d, 1H, $^3J_{HH}$ = 9.2 Hz, NHCC*H*), 3.83 (t, 2H, $^3J_{HH}$ = 5.7 Hz, $OHCH_2$), 3.34 (app quar, 2H, $^3J_{HH}$ = 5.9 Hz, $NHCH_2$), 2.22 (broad s, 1H, O*H*), 1.91 (app quin, 2H, $^3J_{HH}$ = 6.4 Hz, $NHCH_2CH_2$) ppm; $^{13}C\{^1H\}$ NMR (75 MHz, $CDCl_3$): δ_C = too weak; HRMS (ES^+) found *m/z* 491.1821 for $[C_{28}H_{22}N_6O_3+H]^+$, calculated at 491.1826 for $[C_{28}H_{22}N_6O_3+H]^+$; IR (solid) ν_{max} (±2 cm^{-1}) = 3375, 2929, 2902, 2866, 1627, 1566, 1543, 1517, 1498, 1462, 1444, 1425, 1413, 1390, 1367, 1342, 1298, 1255, 1234, 1209, 1166, 1002, 912, 891, 866, 804, 83, 740, 704, 717, 671, 524, 408cm^{-1};

UV-Vis (MeCN): λ_{max} (ε/$M^{-1}cm^{-1}$) = 560 (3900), 446 (4800), 322 (10500), 282 (13400), 241 (11100), 228 (12100) nm.

Synthesis of ***L2$_{NH2}$***

Prepared as for **L1$_{NH2}$** but using **L2$_{NO2}$** (272 mg, 0.56 mmol) and a 10% loaded Pd/C

catalyst (59 mg, 56 μmol) to give **L2$_{NH2}$** as a green crystalline solid. Yield = 208 mg, 0.46 mmol, 81 %. ^{1}H NMR (400 MHz, $CDCl_3$) δ_H = 9.11–9.03 (m, 2H, arom), 8.97–8.92 (m, 1H, arom), 7.69–7.65 (m, 1H, arom), 7.62–7.54 (m, 3H, arom), 7.47 (d, 2H, $^3J_{HH}$ = 6.6 Hz, arom), 7.33 (dd, 1H $^3J_{HH}$ = 8.4 Hz, $^3J_{HH}$ = 8.1 Hz, arom), 7.22–7.16 (m, 1H), 7.23 (s, 1H, $NH_2CC\mathit{H}$), 6.74 (dd, 1H, $^3J_{HH}$ = 8.4Hz, $^3J_{HH}$ = 8.3 Hz, NHCCHC*H*), 6.35 (d, 1H, $^3J_{HH}$ = 6.44 Hz, NHCC*H*), 3.74 (t, 2H, $^3J_{HH}$ = 5.7 Hz, OHCH_2), 3.14 (t, 2H, $^3J_{HH}$ = 56.8 Hz, NHCH_2), 1.91 (app quin, 2H, $^3J_{HH}$ = 6.0 Hz, $NHCH_2C\mathit{H}_2$) ppm; $^{13}C\{^1H\}$ NMR (151 MHz, $CDCl_3$): δ_C = 153.0, 148.8, 147.6, 144.6, 144.2, 139.5, 138.5, 135.9, 133.3, 130.6, 130.4, 130.1, 129.0, 127.9, 126.6, 123.9, 123.4, 122.3, 122.1, 119.9, 119.1, 117.7, 111.3, 61.6, 41.9, 31.7 ppm; HRMS (ES^+) found *m/z* 461.2080 for $[C_{28}H_{24}N_6O+H]^+$, calculated at 461.2084 for $[C_{28}H_{24}N_6O+H]^+$; IR (solid) ν_{max} (±2 cm^{-1}) = 3242, 3051, 2947, 1637, 1593, 1564, 1537, 1514, 1494, 1485, 1467, 1442, 1421, 1350, 1294, 1267, 1157, 1047, 908, 812, 779, 740, 721, 711, 640, 621, 507, 405 cm^{-1}; UV-Vis (MeCN): λ_{max} (ε/$M^{-1}cm^{-1}$) = 334 (29300), 281 (40000), 252 (48700), 231 (51600) nm.

6.5.6 NO Bound Ligand Synthesis

Synthesis of ***L1$_{NO}$***

$NO_{(g)}$ was slowly bubbled through a degassed $CHCl_3$ solution of **L1$_{NH2}$** (21 mg, 43.8 μmol) for 30 seconds in a sealed vessel. $NO_{(g)}$ delivery was ceased and the solution stirred for 5 minutes. The vessel was then opened to air and stirred for 30 minutes during which excess $NO_{(g)}$ was removed as toxic, orange $NO_{2(g)}$. The solvent was then removed *in vacuo* and the sticky residue dissolved in minimal MeCN. Precipitation of the product was induced with the slow addition of diethyl ether and subsequent filtration and drying gave **L1$_{NO}$** as a yellow–orange solid. Yield = 16 mg, 31.9 μmol, 73 %. ^{1}H NMR (400 MHz, CD_3CN) δ_H = 9.72 (d, 1H, $^3J_{HH}$ = 7.0 Hz, arom), 9.27 (dd, 1H, $^3J_{HH}$ = 5.2 Hz, $^3J_{HH}$ = 5.1 Hz, arom), 9.14 (app t, 1H, arom), 8.41–8.36 (m, 1H, arom), 8.14 (s, 1H, arom), 8.01 (dd, 1H, $^3J_{HH}$ = 8.8 Hz, $^3J_{HH}$ = 8.7 Hz, arom), 7.95 (d, 1H, $^3J_{HH}$ = 9.1 Hz, arom), 7.88–7.76 (m, 7H, arom), 4.02 (t, 2H, $^3J_{HH}$ = 5.1 Hz, NCH_2), 3.66–3.31 (m, 4H, 2 × CH_2), 1.20 (t, 2H, $^3J_{HH}$ = 7.0 Hz, CH_2) ppm; LRMS (ES^+) found *m/z* 524.2 for $[M+Na]^+$; HRMS (ES^+) found *m/z* 502.1973 for $[C_{29}H_{23}N_7O_2+H]^+$, calculated at 502.1986 for $[C_{29}H_{23}N_7O_2+H]^+$; IR (solid) ν_{max} (±2 cm^{-1}) = 3344, 3062, 2924, 2873, 1612, 1577, 1543, 1496, 1477, 1442, 1338, 1315, 1242, 1172, 1126, 1060, 1041, 979,

864, 829, 806, 717, 621, 474, 412 cm^{-1}; UV-Vis (MeCN): λ_{max} ($\varepsilon/M^{-1}cm^{-1}$) = 393 (1100), 300 (23300), 260 (29600), 228 (24000) nm.

Synthesis of ***L2$_{NO}$***

Prepared as for **L1$_{NO}$** but using **L2$_{NH2}$** (28 mg, 60.8 μmol) to give **L2$_{NO}$** as a yellow–orange solid. Yield = 27 mg, 57.2 μmol, 95 %. ^{1}H NMR (400 MHz, DMSO–*d6*) δ_H = 9.65 (d, 1H, $^3J_{HH}$ = 8.1 Hz, arom), 9.31 (d, 1H, $^3J_{HH}$ = 4.9 Hz, arom), 9.18 (d, 1H, $^3J_{HH}$ = 4.2 Hz, arom), 8.43–8.35 (m, 1H, arom), 8.05 (s, 1H, arom), 8.00–7.75 (m, 8H, arom), 7.64 (d, 1H, $^3J_{HH}$ = 8.6 Hz, arom), 4.76 (t, 2H, $^3J_{HH}$ = 6.8 Hz, NCH_2), 2.05 (app quin, 2H, NCH_2CH_2) ppm N.B. one CH_2 resonance must sit under the solvent peak; $^{13}C\{^1H\}$ NMR (151 MHz, DMSO–*d6*): δ_C = 153.4, 147.2, 145.1, 137.1, 135.0, 133.8, 131.7, 131.5, 131.3, 129.3, 129.0, 128.0, 126.7, 126.1, 125.2, 125.1, 121.2, 120.6, 111.6, 71.5, 65.4, 58.0, 45.4, 45.0, 32.8, 31.2, 15.6 ppm; LRMS (ES^+) found *m/z* 472.3 for $[M+H]^+$ and 494.3 for $[M+Na]^+$; HRMS (ES^+) found *m/z* 472.1881 for $[C_{28}H_{21}N_7O+H]^+$, calculated at 472.1880 for $[C_{28}H_{21}N_7O+H]^+$; IR (solid) ν_{max} (±2 cm^{-1}) = 3394, 3074, 1603, 1577, 1543, 1496, 1473, 1438, 1384, 1315, 1280, 1242, 1165, 1126, 1072, 1037, 979, 945, 875, 829, 783, 717, 621, 540, 416 cm^{-1}; UV-Vis (MeCN): λ_{max} ($\varepsilon/M^{-1}cm^{-1}$) = 412 (500), 299 (7400), 261 (11100), 230 (8800) nm.

6.5.7 General Procedure for the Synthesis of Ir(III) μ-Chlorobridged Dimers

Emptz was firstly synthesised according to literature techniques.[67] $[(C\hat{}N)_2Ir(\mu\text{–}Cl)_2Ir(C\hat{}N)_2]$ where (C^N = ppy or epmtz) were synthesized according to the Nonoyama route[71] and used without further purification. $IrCl_3{\cdot}xH_2O$ (0.200 g, 0.68 mmol) and the appropriate ligand (2.5 equiv) in 2–methoxyethanol (6 mL) and distilled water (2 mL) were heated at 120 °C for 48 h. The mixture was allowed to cool, and the product precipitated by addition of distilled water (30 mL). The yellow (ppy) or red (emptz) solids were collected by filtration, washed with distilled water, and dried in an oven. The Ir(III) dimers was used in subsequent reactions without purification or characterization.

6.5.8 Synthesis of [Ir(III) $(C\hat{}N)_2(MeCN)_2]BF_4$ Precursors

$[Ir(III)(C\hat{}N)_2(MeCN)_2]BF_4$ and $[Ir(III)(C\hat{}N)_2(\mathbf{LX})]BF_4$ where (C^N = ppy and epmtz) were synthesised according to previously reported techniques.[46]

Synthesis of cyclometalated $[Ir(III)(ppy)_2(MeCN)_2]BF_4$

In a foil-wrapped flask $AgBF_4$ (71 mg, 0.36 mmol) in MeCN (15 mL) was added to a stirred solution of $[(ppy)_2Ir(\mu\text{–}Cl)_2Ir(ppy)_2]$ (195 mg, 0.18 mmol) in hot MeCN (20 mL), under a dinitrogen atmosphere. The solution was then heated at reflux for 2 hours and cooled. Precipitation of the product was assisted by the addition of diethyl ether and was subsequently filtered and dried to give $[Ir(III)(ppy)_2(MeCN)_2]BF_4$ as a yellow powder.

Yield = 231 mg, 0.16 mmol, 91 %. ^{1}H NMR (400 MHz, $CDCl_3$) δ_H = 9.02 (d, 2H, $^3J_{HH}$ = 5.8 Hz, arom), 7.87–7.83 (m, 4H, arom), 7.48 (d, 2H, $^3J_{HH}$ = 6.9 Hz, arom), 7.35 (app t, 2H, $^3J_{HH}$ = 6.2 Hz, arom), 6.84 (app t, 2H, $^3J_{HH}$ = 6.5 Hz, arom), 6.69 (app t, 2H, $^3J_{HH}$ = 6.9 Hz, arom), 6.02 (d, 2H, $^3J_{HH}$ = 7.6 Hz, IrNC*H*), 2.30 (s, 6H, *Me*CN) ppm.

Synthesis of cyclometalated [Ir(III)(emptz)$_2$(MeCN)$_2$]BF$_4$

Prepared as for [Ir(III)(ppy)$_2$(MeCN)$_2$]BF$_4$ but using $AgBF_4$ (71 mg, 0.36 mmol) and [(emptz)$_2$Ir(μ–Cl)$_2$Ir(emptz)$_2$] (149 mg, 0.11 mmol) to give [Ir(III)(emptz)$_2$(MeCN)$_2$]BF$_4$ as a yellow powder. Yield = 153 mg, 0.18 mmol, 87 %. ^{1}H NMR (400 MHz, $CDCl_3$) δ_H = 7.53 (d, 2H, $^3J_{HH}$ = 6.7 Hz, arom), 6.92 (dd, 4H, $^3J_{HH}$ = 7.5 Hz, $^3J_{HH}$ = 7.4 Hz, arom), 6.84 (dd, 2H, $^3J_{HH}$ = 7.5 Hz, $^3J_{HH}$ = 6.8 Hz, arom), 6.23 (d, 2H, $^3J_{HH}$ = 7.5 Hz, IrNC*H*), 4.46 (quar, 4H, $^3J_{HH}$ = 7.1 Hz, CO_2CH_2), 3.04 (s, 6H, arom–*Me*), 2.43 (s, 6H, *Me*CN), 1.47 (t, 6H, $^3J_{HH}$ = 6.4 Hz, $CO_2CH_2CH_3$) ppm.

6.5.9 Complex Synthesis

*Synthesis of [Ir(ppy)$_2$(**L1$_{NO2}$**)]BF$_4$ (**Ir(ppy)$_2$(L1$_{NO2}$)**)*

L1$_{NO2}$ (33.1 mg, 63.6 μmol) and [Ir(III)(ppy)$_2$(MeCN)$_2$]BF$_4$ (42.6 mg, 63.6 μmol) were heated at reflux in $CHCl_3$ (10 mL) for 48 hours during which reaction progression was monitored by TLC (95:5 DCM:MeOH). The solvent was then reduced to minimal *in vacuo* and precipitation of the product induced by the slow addition of diethyl ether. Subsequent filtration and drying gave **Ir(ppy)$_2$(L1$_{NO2}$)** as a orange powder. Yield = 57 mg, 51.1 μmol, 80 %. ^{1}H NMR (400 MHz, $CDCl_3$) δ_H = 9.32(d, 1H, $^3J_{HH}$ = 8.4 Hz, arom), 8.45 (broad t, 1H, $^3J_{HH}$ = 3.6 Hz, N*H*), 8.41 (d, 1H, $^3J_{HH}$ = 2.4 Hz, arom), 8.26 (d, 1H, $^3J_{HH}$ = 3.6 Hz, arom), 8.15 (d, 1H, $^3J_{HH}$ = 4.8 Hz, arom), 7.91–7.65 (m, 13H, arom), 7.53–7.47 (m, 2H, arom), 7.37 (d, 1H, $^3J_{HH}$ = 6.8 Hz, arom), 7.10–7.02 (m, 3H, arom), 6.96 (app t, 2H, arom), 6.89–6.84 (m, 2H, arom), 6.39 (d, 2H, $^3J_{HH}$ = 7.6 Hz, ppy), 3.79 (app quar, 4H, 2 × CH_2), 3.68–3.62 (m, 2H, CH_2), 3.55–3.50 (m, 2H, CH_2), 0.81 (broad s, 1H, O*H*) ppm; ^{13}C{^{1}H} NMR (151 MHz, $CDCl_3$): δ_C = 168.1, 167.3, 152.7, 150.5, 149.9, 149.5, 149.1, 148.7, 148.4, 145.8, 145.0, 144.9, 143.9, 143.4, 138.1, 138.0, 136.8, 136.7, 136.4, 132.9, 132.1, 131.8, 131.7, 131.6, 131.4, 131.0, 130.7, 130.6, 129.1, 128.6, 128.1, 128.0, 127.9, 126.6, 126.4, 126.2, 124.8, 124.7, 123.9, 123.1, 122.8, 12.7, 119.6, 119.4, 116.4, 114.3, 114.1 ppm; LRMS (ES$^+$) found *m/z* 1019.3 for [M]$^+$; HRMS (ES$^+$) found *m/z* 1019.2761 for [$C_{51}H_{40}N_8O_4Ir$]$^+$, calculated at 1019.2772 for [$C_{51}H_{40}N_8O_4Ir$]$^+$; IR (solid) ν_{max} (±2 cm^{-1}) = 3533, 3369, 3045, 2937, 2872, 1627, 1606, 1579, 1519, 1477, 1448, 1381, 1352, 1305, 1276, 1238, 1161, 1118, 1053, 1031, 829, 630, 759, 729, 669, 630, 540, 518, 415 cm^{-1}; UV-Vis (MeCN): λ_{max} (ε/M^{-1}cm^{-1}) = 455 (5900), 412 (10300), 318 (44500), 290 (59000), 270 (68100), 253 (58800) nm.

*Synthesis of [Ir(ppy)$_2$(**L1$_{NH2}$**)]BF$_4$ (**Ir(ppy)$_2$(L1$_{NH2}$)**)*

Prepared as for **Ir(ppy)$_2$(L1$_{NO2}$)** but using **L1$_{NH2}$** (29.4 mg, 59.9 μmol) and [Ir(III)(ppy)$_2$(MeCN)$_2$]BF$_4$ (40.1 mg, 59.9 μmol) to give **Ir(ppy)$_2$(L1$_{NH2}$)** as a pale green powder. Yield = 53 mg, 49.2 μmol, 82 %. ^{1}H NMR (400 MHz, $CDCl_3$) δ_H = 9.35 (d, 1H, $^3J_{HH}$ = 8.1 Hz, arom), 8.45 (broad t, 1H, $^3J_{HH}$ = 3.6 Hz, NH), 8.41 (s, 1H, arom), 8.25 (d, 1H, $^3J_{HH}$ = 4.3 Hz, arom), 8.14 (d, 1H, $^3J_{HH}$ = 4.1 Hz, arom), 7.92–7.65 (m, 13H, arom), 7.53–7.47 (m, 3H, arom), 7.37 (d, 1H, $^3J_{HH}$ = 5.1 Hz, arom), 7.11–6.81 (m, 7H, arom), 6.40 (d, 2H, $^3J_{HH}$ = 7.5 Hz, ppy), 3.76–3.69 (m, 4H, 2 × CH_2), 3.60 (t, 2H, $^3J_{HH}$ = 4.7 Hz, CH_2), 3.47 (t, 2H, $^3J_{HH}$ = 4.6 Hz, CH_2), 0.82 (broad s, 1H, O*H*) ppm; ^{13}C{^{1}H} NMR (151 MHz, CD_3CN): δ_C = 167.5, 155.6, 150.6, 150.3, 149.5, 149.3, 148.4, 144.8, 144.7, 144.2, 139.1, 138.5, 137.7, 136.8, 134.4, 132.4, 131.7, 130.9, 130.8, 130.7, 130.4, 129.9, 128.8, 128.7, 127.8, 127.0, 126.4, 125.9, 124.9, 123.4, 123.3, 122.6, 122.6, 121.2, 119.8, 119.8, 117.3, 109.5, 72.368.9, 61.0, 43.2, ppm; LRMS (ES$^+$) found *m/z* 989.3 for [M]$^+$; HRMS (ES$^+$) found *m/z* 989.3051 for $[C_{51}H_{42}N_8O_2Ir]^+$, calculated at 989.3037 for $[C_{51}H_{42}N_8O_2Ir]^+$; IR (solid) ν_{max} (±2 cm^{-1}) = 3369, 3062, 2960, 2924, 2363, 1606, 1581, 1477, 1419, 1381, 1352, 1338, 1303, 1261, 1226, 1161, 1030, 950, 883, 806, 758, 727, 669, 518, 415 cm^{-1}; UV-Vis (MeCN): λ_{max} (ε/M^{-1}cm^{-1}) = 455 (1400), 340 (11600), 289 (22900), 260 (30100) nm.

*Synthesis of [Ir(ppy)$_2$(**L2$_{NO2}$**)]BF$_4$ (**Ir(ppy)$_2$(L2$_{NO2}$)**)*

Prepared as for **Ir(ppy)$_2$(L1$_{NO2}$)** but using **L2$_{NO2}$** (36.5 mg, 74.4 μmol) and [Ir(III)(ppy)$_2$(MeCN)$_2$]BF$_4$ (49.8 mg, 74.4 μmol) to give **Ir(ppy)$_2$(L2$_{NO2}$)** as a yellow powder. Yield = 61.7 mg, 70.3 μmol, 57 %. ^{1}H NMR (400 MHz, $CDCl_3$) δ_H = 9.33 (d, 1H, $^3J_{HH}$ = 7.6 Hz, arom), 8.14–8.10 (m, 1H, arom), 7.91–7.12 (m, 13H, arom), 7.52–7.44 (m, 3H, arom), 7.35 (d, 1H, $^3J_{HH}$ = 6.7 Hz, arom), 7.06–6.78 (m, 7H, arom), 6.37 (d, 2H, $^3J_{HH}$ = 8.3 Hz, ppy), 3.77 (t, 2H, $^3J_{HH}$ = 5.7 Hz, NHCH_2), 2.11 (t, 2H, $^3J_{HH}$ = 4.2 Hz, CH_2OH), 1.96–1.88 (m, 2H, NHCH$_2$CH_2), 0.81 (broad s, 1H, O*H*) ppm; ^{13}C{^{1}H} NMR (151 MHz, $CDCl_3$): δ_C = 167.3, 152.8, 149.3, 148.4, 145.7, 143.8, 143.2, 138.1, 138.0, 136.7, 136.4, 132.1, 131.8, 131.7, 131.3, 131.2, 131.0, 129.1, 127.9, 126.4, 126.2, 124.8, 124.7, 123.9, 123.1, 122.7, 119.6, 119.4, 116.0, 114.3, 60.3, 40.5, 31.3, 29.7 ppm; LRMS (ES$^+$) found *m/z* 989.3 for [M]$^+$; HRMS (ES$^+$) found *m/z* 989.2673 for $[C_{50}H_{38}N_8O_3Ir]^+$, calculated at 989.2673 for $[C_{50}H_{38}N_8O_3Ir]^+$; IR (solid) ν_{max} (±2 cm^{-1}) = 3547, 3365, 3059, 2929, 2875, 1627, 1606, 1577, 1527, 1496, 1477, 1448, 1419, 1303, 1267, 1230, 1157, 1055, 1031, 894, 808, 758, 711, 669, 630, 518. 417 cm^{-1}; UV-Vis (MeCN): λ_{max} (ε/M^{-1}cm^{-1}) = 456 (5300), 414 (7800), 316 (37300), 293 (46400), 270 (54900), 250 (47900) nm.

*Synthesis of [Ir(ppy)$_2$(**L2$_{NH2}$**)]BF$_4$ (**Ir(ppy)$_2$(L2$_{NH2}$)**)*

Prepared as for **Ir(ppy)$_2$(L1$_{NO2}$)** but using **L2$_{NH2}$** (35.0 mg, 76.5 μmol) and [Ir(III)(ppy)$_2$(MeCN)$_2$]BF$_4$ (51.2 mg, 76.5 μmol) to give **Ir(ppy)$_2$(L2$_{NH2}$)** as a brown powder. Yield = 62 mg, 59.2 μmol, 77 %. ^{1}H NMR (400 MHz, $CDCl_3$) δ_H = 9.32 (d, 1H, $^3J_{HH}$ = 7.6 Hz, arom), 8.23 (d, 1H, $^3J_{HH}$ = 5.0 Hz, arom), 8.11 (d, 1H, $^3J_{HH}$ = 4.0 Hz, arom), 7.90 (d, 2H, $^3J_{HH}$ = 8.1 Hz, arom), 7.84–7.79 (m, 1H, arom), 7.77–7.56 (m, 10H, arom), 7.48–7.42 (m, 3H, arom), 7.34 (d, 1H, $^3J_{HH}$ = 5.2 Hz, arom), 7.10–6.84 (m, 6H, arom), 6.38 (d, 2H, $^3J_{HH}$ = 7.7 Hz, ppy), 3.72 (t, 2H, $^3J_{HH}$ = 5.8 Hz, NHCH_2), 3.22 (t, 2H, $^3J_{HH}$ = 6.4 Hz, CH_2OH), 1.82–1.80 (m, 2H, NHCH$_2$CH_2), 0.84 (broad s, 1H, O*H*) ppm; ^{13}C{^{1}H} NMR (151 MHz, CD_3CN): δ_C = 167.5, 156.1, 150.5, 150.2, 149.4, 149.3, 148.4, 144.8, 144.2, 139.3, 138.4, 134.2, 132.4, 131.7, 131.6, 131.4, 130.9, 130.4, 128.9, 128.8, 128.7, 126.9, 126.5, 125.9, 124.9, 123.4, 122.6, 121.2, 119.8, 115.9, 109.0, 59.7, 40.7, 31.7 ppm; LRMS (AP$^+$) found *m/z* 959.3 for [M]$^+$; HRMS (ES$^+$) found *m/z* 959.2928 for [$C_{50}H_{40}N_8OIr$]$^+$, calculated at 959.2931 for [$C_{50}H_{40}N_8OIr$]$^+$; IR (solid) ν_{max} (±2 cm^{-1}) = 3354, 3041, 2937, 2875, 1606, 1581, 1477, 1419, 1381, 1303, 1269, 1157, 1051, 1030, 808, 758, 727, 669, 630, 524, 403 cm^{-1}; UV-Vis (MeCN): λ_{max} (ε/M^{-1}cm^{-1}) = 466 (2900), 410 (10200), 344 (24900), 288 (49000), 264 (69600) nm.

*Synthesis of [Ir(emptz)$_2$(**L2$_{NH2}$**)]BF$_4$ (**Ir(emptz)$_2$(L2$_{NH2}$)**)*

Prepared as for **Ir(ppy)$_2$(L1$_{NO2}$)** but using **L2$_{NH2}$** (36.2 mg, 78.6 μmol) and [Ir(III)(emptz)$_2$(MeCN)$_2$]BF$_4$ (67.1 mg, 78.6 μmol) to give **Ir(emptz)$_2$(L2$_{NH2}$)** as an orange powder. Yield = 86 mg, 69.8 μmol, 89 %. ^{1}H NMR (400 MHz, $CDCl_3$) δ_H = 9.40 (d, 1H, $^3J_{HH}$ = 8.3 Hz, arom), 8.19 (d, 1H, $^3J_{HH}$ = 4.9 Hz, arom), 8.07 (d, 1H, $^3J_{HH}$ = 4.9 Hz, arom), 7.97–7.90 (m, 1H, arom), 7.80–7.51 (m, 9H, arom and NH), 7.14 (app quar, 2H, arom), 7.08 (app quar, 2H, arom), 6.92 (d, 1H, $^3J_{HH}$ = 9.9 Hz, arom), 6.52 (app t, 2H, arom), 6.43 (d, 1H, $^3J_{HH}$ = 8.6 Hz, arom), 4.29–4.21 (m, 4H, 2 × CO_2CH_2), 3.70 (t, 2H, $^3J_{HH}$ = 5.5 Hz, NHCH_2), 3.15 (t, 2H, CH_2OH), 1.79 (app t, 2H, NHCH$_2$CH_2), 1.58 (s, 6H, CCH_3), 1.29 (t, 6H, $^3J_{HH}$ = 7.1 Hz, $CO_2CH_2CH_3$) ppm; ^{13}C{^{1}H} NMR (151 MHz, $CDCl_3$): δ_C = 182.5, 160.3, 160.2, 158.5, 158.4, 156.2, 149.2, 149.1, 140.0, 144.7, 140.1, 140.0, 139.9, 136.9, 136.7, 133.4, 133.2, 132.5, 132.4, 131.3, 131.2, 130.8, 128.5, 128.5, 126.6, 126.4, 126.2, 123.8, 123.7, 120.2, 120.0, 62.3, 62.2, 61.2, 53.4, 41.7, 31.3, 14.6, 14.5, 14.1 ppm; LRMS (AP$^+$) found *m/z* 1143.3 for [M]$^+$; HRMS (ES$^+$) found *m/z* 1143.2815 for [$C_{54}H_{48}N_8O_5S_2Ir$]$^+$, calculated at 1143.2795 for [$C_{54}H_{48}N_8O_5S_2Ir$]$^+$; IR (solid) ν_{max} (±2 cm^{-1}) = 3379, 3061, 2931, 1710, 1598, 1583, 1552, 1496, 1440, 1373, 1327, 1288, 1257, 1159, 1128, 1097, 1055, 1004, 810, 761, 671, 543, 428 cm^{-1}; UV-Vis (MeCN): λ_{max} (ε/M^{-1}cm^{-1}) = 418 (13600), 355 (31800), 315 (50700), 294 (61100), 263 (56800), 232 (5800) nm.

6.5.10 NO Bound Complex Synthesis

*Synthesis of [Ir(ppy)$_2$(**L1$_{NO}$**)]BF$_4$ (**Ir(ppy)$_2$(L1$_{NO}$)**)*

Prepared as for **L1$_{NO}$** but using **Ir(ppy)$_2$(L1$_{NH2}$)** (25.1 mg, 23.2 μmol) to give **Ir(ppy)$_2$(L1$_{NO}$)** as a brown solid. Yield = 24.2 mg, 22.2 μmol, 96 %. ^{1}H NMR (400 MHz, CD_3CN) δ_H = 9.29 (d, 1H, $^3J_{HH}$ = 7.6 Hz, arom), 8.33 (d, 1H, $^3J_{HH}$ = 5.6 Hz, arom), 8.19 (d, 1H, $^3J_{HH}$ = 4.8 Hz, arom), 8.10–7.64 (m, 16H, arom), 7.53–7.47 (m, 3H, arom), 7.13–7.07 (m, 2H, arom), 7.01–6.87 (m, 4H, arom), 6.93 (app t, 2H, arom), 4.84 (t, 2H, $^3J_{HH}$ = 4.8 Hz, NCH_2), 3.96 (t, 2H, $^3J_{HH}$ = 4.8 Hz, CH_2), 3.47–3.42 (m, 4H, 2 × CH_2) ppm; HRMS (ES$^+$) found *m/z* 1000.2834 for $[C_{51}H_{39}N_9O_2Ir]^+$, calculated at 1000.2827 for $[C_{51}H_{39}N_9O_2Ir]^+$; IR (solid) ν_{max} (±2 cm^{-1}) = 3395, 3064, 1606, 1583, 1496, 1477, 1438, 1417, 1305, 1226, 1053, 1031, 885, 810, 759, 727, 669, 630, 460, 416, 408 cm^{-1}; UV-Vis (MeCN): λ_{max} (ε/M^{-1}cm^{-1}) = 453 (2200), 379 (9300), 341 (16700), 293 (46200), 267 (68500) nm.

*Synthesis of [Ir(ppy)$_2$(**L2$_{NO}$**)]BF$_4$ (**Ir(ppy)$_2$(L2$_{NO}$)**)*

Prepared as for **L1$_{NO}$** but using **Ir(ppy)$_2$(L2$_{NH2}$)** (21.5 mg, 20.5 μmol) to give **Ir(ppy)$_2$(L2$_{NO}$)** as a yellow–brown solid. Yield = 17.5 mg, 16.5 μmol, 81 %. ^{1}H NMR (400 MHz, CD_3CN) δ_H = 9.33 (d, 2H, $^3J_{HH}$ = 8.0 Hz, arom), 8.71 (dd, 2H, $^3J_{HH}$ = 13.0 Hz, $^3J_{HH}$ = 12.9 Hz, arom), 8.34 (app t, 2H, arom), 8.27 (d, 1H, $^3J_{HH}$ = 5.3 Hz, arom), 8.06–7.92 (m, 10H, arom), 7.84–7.67 (m, 4H, arom), 7.09–7.03 (m, 2H, arom), 6.66 (dd, 1H, $^3J_{HH}$ = 8.5 Hz, $^3J_{HH}$ = 8.4 Hz, arom), 4.76 (t, 2H, $^3J_{HH}$ = 7.3 Hz, NHCH_2), 3.51 (t, 2H, $^3J_{HH}$ = 6.0 Hz, CH_2OH), 2.46–2.37 (m, 2H, NCH_2CH_2) ppm; LRMS (ES$^+$) found *m/z* 973.4 for [M]$^+$ and 1060.4 for [M]BF_4; HRMS (ES$^+$) found *m/z* 973.1699 for $[C_{50}H_{37}N_9OIr+H]^+$, calculated at 973.2828 for $[C_{50}H_{37}N_9OIr+H]^+$; IR (solid) ν_{max} (±2 cm^{-1}) = 3456, 3114, 1612, 1589, 1573, 1504, 1481, 1454, 1334, 1284, 1226, 1165, 1107, 1056, 1034, 883, 783, 756, 740, 725, 648, 420 cm^{-1}; UV-Vis (MeCN): λ_{max} (ε/M^{-1}cm^{-1}) = 392 (9100), 342 (15500), 263 (44200), 232 (29800) nm.

*Synthesis of [Ir(emptz)$_2$(**L2$_{NO}$**)]BF$_4$ (**Ir(emptz)$_2$(L2$_{NO}$)**)*

Prepared as for **L1$_{NO}$** but using **Ir(emptz)$_2$(L2$_{NH2}$)** (34.5 mg, 28.0 μmol) to give **Ir(emptz)$_2$(L2$_{NO}$)** as a yellow solid. Yield = 29.4 mg, 23.6 μmol, 84 %. ^{1}H NMR (400 MHz, $CDCl_3$) δ_H = 9.48–9.39 (m, 1H, arom), 8.59 (d, 1H, $^3J_{HH}$ = 11.0 Hz, arom), 8.27–7.52 (m, 15H, arom), 7.23–7.10 (m, 2H, arom), 7.10–6.99 (m, 2H, arom), 6.52 (app t, 1H, arom), 4.82–4.79 (m, 2H, NHCH_2), 4.33–4.19 (m, 4H, CO_2CH_2), 3.60 (t, 2H, $^3J_{HH}$ = 5.2 Hz, CH_2OH), 2.26–2.16 (m, 2H, NCH_2CH_2), 1.60 (s, 6H, CCH_3), 1.29 (t, 6H, $^3J_{HH}$ = 6.8 Hz, $CO_2CH_2CH_3$) ppm; ^{13}C{^{1}H} NMR (151 MHz, $CDCl_3$): δ_C = aromatic too weak, 62.3, 62.2, 58.7, 44.9, 32.2, 30.9, 14.2 ppm; LRMS (ES$^+$) found *m/z* 1154.3 for [M]$^+$; HRMS (ES$^+$) found *m/z* 1154.2594 for $[C_{54}H_{45}N_9O_5S_2Ir]^+$, calculated at 1154.2585 for $[C_{54}H_{45}N_9O_5S_2Ir]^+$; IR (solid) ν_{max} (±2 cm^{-1}) =

3400, 3059, 2980, 1714, 1697, 1618, 1583, 1554, 1498, 1440, 1388, 1327, 1288, 1253, 1163, 1129, 1004, 875, 812, 761, 727, 547, 415 cm^{-1}; UV-Vis (MeCN): λ_{max} ($\varepsilon/M^{-1}cm^{-1}$) = 403 (12000), 293 (61400), 268 (63000), 204 (74600) nm.

6.6 References

1. E. Victor, S. Kim and S. Lippard, *Inorg. Chem.*, 2014, **53**, 12809-12821.
2. C.-B. Huang, J. Huang and L. Xu, *RSC Adv.*, 2015, **3**, 13307-13310.
3. J. M. Berg, J. L. Tymoczko and L. Stryer, in *Biochemistry*, eds. J. M. Berg, J. L. Tymoczko and L. Stryer, W. H. Freeman and `Company, New York, 5th edn., ch. 24.
4. Y.-Q. Sun, J. Liu, H. Zhang, Y. Huo, X. Lv, Y. Shi and W. Guo, *J. Am. Chem. Soc.*, 2014, **136**, 12520-12523.
5. M. H. Lim, B. A. Wong, W. H. Pitcock, D. Mokshagundam, M.-H. Baik and S. Lippard, *J. Am. Chem. Soc.*, 2006, **128**, 14364-14373.
6. A. W.-T. Choi, C.-S. Poon, H.-W. Liu, H.-K. Cheng and K. K.-W. Lo, *New J. Chem.*, 2013, **37**, 1711-1719.
7. X. Chen, X. Tian, I. Shin and J. Yoon, *Chem. Soc. Rev.*, 2011, **40**, 4783-4804.
8. M. H. Lim and S. Lippard, *Acc. Chem. Res.*, 2007, **40**, 41-51.
9. A. Beltra, M. I. Burguete, D. R. Abánades, D. Pérez-Sala, L. S. V. and F. Galindo, *Chem. Commun.*, 2014, **50**, 3579-3581.
10. D. A. Ovchinnikov, *Genesis*, 2008, **46**, 447-462.
11. H. L. J. Liu, Y. Li, X. Xu, Z. Chen, L. Liu, X. Yu, Y. Gao and D. Dou, *J. Cardiovasc. Pharmacol.*, 2014, **64**, 452-459.
12. C. Aicart-Ramos, L. Sánchez-Ruiloba, M. Gómez-Parrizas, C. Zaragoza, T. Iglesias and I. Rodríguez-Crespo, *J. Cell Sci.*, 2014, **127**, 3360-3372.
13. T. O Vilz, B. Stoffels, M. von Websky, J. Kalff and S. Wehner, *Journal of Visualised Experiments*, 2012, **408**, 172-179.
14. P. Wu, J. Wang, C. He, X. Zhang, Y. Wang, T. Y. Liu and C. Duan, *Adv. Funct. Mater.*, 2012, **22**, 1698-1703.
15. H. Tang, Y. Li, Q. Chen, B. Chen, Q. Qiao, W. Yang, H. Wu and Y. Cao, *Dyes Pigm.*, 2014, **100**, 79-86.
16. R. M. F. Batista, S. P. G. Costa, M. Belsley and M. M. M. Raposo, *Dyes Pigm.*, 2009, **80**, 329-336.
17. R. O. Bonello, I. R. Morgan, B. R. Yeo, L. E. J. Jones, B. M. Kariuki, I. A. Fallis and S. J. A. Pope, *J. Organomet. Chem.*, 2014, **749**, 150-156.
18. D.-D. Sun, W.-Z. Wang, J.-W. Mao, W.-J. Mei and J. Liu, *Bioorg. Med. Chem.*, 2012, **22**, 102-105.
19. J. Jayabharathi, V. Thanikachalam, M. V. Perumal and N. Srinivasan, *J. Fluoresc.*, 2012, **22**, 409-417.
20. A. O. Eseola, W. Li, W.-H. Sun, M. Zhang, L. Xiao and J. A. O. Woods, *Dyes Pigm.*, 2011, **88**, 262-273.
21. H.-G. Zhang, X.-T. Tao, K.-S. Chen, C.-X. Yuan and M.-H. Jiang, *Synth. Met.*, 2011, **161**, 354-359.
22. J. Sun, W. Wu, H. Guo and J. Zhao, *Eur. J. Inorg. Chem.*, 2011, 3165-3173.
23. K. J. Castor, K. L. Metera, U. M. Tefashe, C. J. Serpell, J. Mauzeroll and H. F. Sleiman, *Inorg. Chem.*, 2015, **54**, 6958-6967.
24. J. Jayabharathi, R. Sathishkumar, V. Thanikachalam and K. Jayamoorthy, *J. Fluoresc.*, 2014, **24**, 445-453.
25. S. Mandal, D. K. Poria, R. Ghosh, P. S. Ray and P. Gupta, *Dalton Trans.*, 2014, **43**, 17463-17474.
26. H. Tang, Y. Li, B. Zhao, W. Yang, H. Wu and Y. Cao, *Organic Electronics*, 2012, **13**, 3211-3219.
27. J. Kuli, P. Steunenberg, P. T. K. Chin, J. Oldenburg, K. Jalink, A. H. Velders and F. W. B. van Leeuwen, *ChemBioChem*, 2011, 1897-1903.
28. S. K. Seth, S. Mandal, P. Purkayastha and P. Gupta, *Polyhedron*, 2015, **95**, 14-23.
29. Q. Zhao, S. Liu, M. Shi, F. Li, H. Jing, T. Yi and C. Huang, *Organometallics*, 2007, **26**, 5922-5930.
30. M. S. Lowry and S. Bernhard, *Chem. Eur. J.*, 2006, **12**, 7970-7977.

31. J. D. Blakemore, N. D. Schley, D. Balcells, J. F. Hull, G. W. Olack, C. D. Incarvito, O. Eisenstein, G. W. Brudvig and R. H. Crabtree, *J. Am. Chem. Soc.*, 2010, **132**, 16017-16029.
32. C.-H. Yang, J. Beltran, V. Lemaur, J. Cornil, D. Hartmann, W. Sarfert, R. Frohlich, C. Bizzarri and L. De Cola, *Inorg. Chem.*, 2010, **49**, 9891-9901.
33. C. Dragonetti, A. Colombo, D. Marinotto, S. Righetto, D. Roberto, A. Valore, M. Escadeillas, V. Guerchais, H. Le Bozec, A. Boucekkine and C. Latouche, *J. Organomet. Chem.*, 2014, **751**, 568-572.
34. C.-H. Yang, Y.-M. Cheng, Y. Chi, C.-J. Hsu, F.-C. Fang, K.-T. Wong, P.-T. Chou, C.-H. Chang, M.-H. Tsai and C.-C. Wu, *Angew. Chem. Int. Ed.*, 2007, **119**, 2470 –2473.
35. C. Jin, J. Liu, Y. Chen, L. Zeng, R. Guan, C. Ouyang, L. Ji and H. Chao, *Chem. Eur. J.*, 2015, **21**, 12000-12010.
36. D. Tordera, A. Pertegas, N. M. Shavaleev, R. Scopelliti, E. Orti, H. J. Bolink, E. Baranoff, M. Gratzel and M. K. Nazeeruddin, *J. Mater. Chem.*, 2012, **22**, 19264-19268.
37. K. K.-W. Lo, S. P.-Y. Li and K. Y. Zhang, *New J. Chem.*, 2011, 265-287.
38. M. Licini and J. A. G. Williams, *Chem. Commun.*, 1999, 1943-1944.
39. M. L. Ho, Y. M. Cheng, G. H. Lee, Y. Chi, L. C. Wu, P. T. Chou and F. C. Hsu, *Polyhedron*, 2007, 4886-4892.
40. L. Huynh, Z. Wang, J. Yang, V. Stoeva, A. Lough, I. Manners and M. A. Winnick, *Chem. Mater.*, 2005, 4765-4773.
41. H. Sato, K. Tamura, M. Taniguchi and A. Yanagishi, *New J. Chem.*, 2010, 617-622.
42. M. Yu, Q. Zhao, L. Shi, F. Li, Z. Zhou, H. Yang, T. Yi and C. Huang, *Organometallics*, 2010, **29**, 1085-1091.
43. Q. Sun, R. Wu, S. Cai, Y. Lin, L. Sellers, K. Sakamoto, B. He and B. R. Peterson, *J. Med. Chem.*, 2011, **54**, 1126-1139.
44. N. N. Serveega, M. Donnier-Marechal, G. Vaz, A. M. Davies and M. O. Senge, *J. Inorg. Biochem.*, 2011, **105**, 1589-1595.
45. V. Peytou, R. Condom, N. Patino, R. Guedj, A.-M. Aubertin, N. Gelus, C. Bailly, R. Terreux and D. Cabrol-Bass, *J. Med. Chem.*, 1999, **42**, 4042-4053.
46. Y.-J. Yuan, Z.-T. Yu, H.-L. Gao, Z.-G. Zou, C. Zheng and W. Huang, *Chem. Eur. J.*, 2013, **19**, 6340-6349.
47. E. E. Langdon-Jones, A. J. Hallett, J. D. Routledge, D. A. Crole, B. D. Ward, J. A. Platts and S. J. A. Pope, *Inorg. Chem.*, 2013, **52**, 448-456.
48. R. Smith, E. Stokes, E. Langdon-Jones, J. Platts, B. Kariuki, A. Hallett and S. Pope, *Dalton Trans.*, 2013, **42**, 10347-10357.
49. J. Hu, M. R. Whittaker, H. Duong, Y. Li, C. Boyer and T. P. Davis, *Angew. Chem. Int. Ed.*, 2014, **53**, 7779-7784.
50. Z. Wang, *Comprehensive Organic Name Reactions and Reagents*, John Wiley & Sons, Hoboken, New Jersey, 2009.
51. D. Jourd'heuil, D. Kang and M. B. Grisham, *Frontiers in Bioscience 2*, 1997, 189-196.
52. M. M. Tarpey, D. A. Wink and M. B. Grisham, *Am. J. Physiol.*, 2004, **286**, 431-444.
53. N. Nakatsubo, H. Kojima, K. Sakurai, K. Kikuchi, H. Nagoshi, Y. Hirata, T. Akakie, H. Maeda, Y. Urano, T. Higuchi and T. Nagano, *Biol. Pharm. Bull.*, 1998, **21**, 1247-1250.
54. E. C. Stokes, E. E. Langdon-Jones, L. M. Groves, J. A. Platts, P. N. Horton, I. A. Fallis, S. J. Coles and S. J. A. Pope, *Dalton Trans.*, 2015, **44** 8488–8496.
55. V. F. Plyusnin, A. S. Kupryakov, V. P. Grivin, A. H. Shelton, I. V. Sazanovich, A. J. H. M. Meijer, J. A. Weinstein and M. D. Ward, *Photochemical and Photobiological Sciences*, 2013, **12**, 1666-1679.
56. J. E. Jones, R. L. Jenkins, R. S. Hicks, A. J. Hallett and S. J. A. Pope, *Dalton Trans.*, 2012, **41**, 10372-10381.
57. L. E. McQuade and S. Lippard, *Inorg. Chem.*, 2010, **49**, 7464-7471.

58. M. J. Frisch, G. W. Trucks, H. B. Schlegel, G. E. Scuseria, M. A. Robb, J. R. Cheeseman, G. Scalmani, V. Barone, B. Mennucci, G. A. Petersson, H. Nakatsuji, M. Caricato, X. Li, H. P. Hratchian, A. F. Izmaylov, J. Bloino, G. Zheng, J. L. Sonnenberg, M. Hada, E. Ehara, K. Toyota, R. Fukuda, J. Hasegawa, M. Ishida, T. Nakajima, Y. Honda, O. Kitao, H. Nakai, T. Vreven, J. A. Montgomery Jr, J. E. Peralta, F. Ogliaro, M. Bearpark, J. J. Heyd, E. Brothers, K. N. Kudin, V. N. Staroverov, T. Keith, R. Kobayashi, J. Normand, K. Raghavachari, A. Rendell, J. C. Burant, S. S. Lyengar, J. Tomasi, M. Cossi, N. Rega, J. M. Millam, M. Klene, J. E. Knox, J. B. Cross, V. Bakken, C. Adamo, J. Jaramillo, R. Gomperts, R. E. Stratmann, O. Yazyev, A. J. Austin, R. R. Cammi, C. Pomelli, J. W. Ochterski, R. L. Martin, K. Morokuma, V. G. Zakrzewski, G. A. Voth, P. Salvador, J. J. Dannenberg, S. Dapprich, A. D. Daniels, O. Farkas, J. B. Foresman, J. V. Ortiz, J. Cioslowski and D. J. Fox, *Gaussian 09*, Gaussian Inc., Wallingford CT, Revision D.01 edn., 2010.
59. T. Yanai, D. Tew and N. Handy, *Chem. Phys. Lett.*, 2004, **393**, 51-57.
60. S. Grimme, J. Antony, E. Ehrlich and H. Krieg, *J. Chem. Phys.*, 2010, **132**, 154104.
61. D. Andrae, U. Haussermann, M. Dolg, H. Stoll and H. Preuss, *Theor. Chim. Acta*, 1990, **77**, 123-141.
62. T. H. Dunning Jr., *J. Chem. Phys.*, 1989, **90**, 1007-1023.
63. A. D. Becke, *J. Chem. Phys.*, 1993, **98**, 5648-5652.
64. C. T. Lee, W. T. Yang and R. G. Parr, *Physical Reviews B*, 1988, **37**, 785-789.
65. Y. Zhao and D. G. Truhlar, *Theor. Chem. Acc.*, 2008, **120**, 215-241.
66. A. Vlček and S. Zalis, *Coord. Chem. Rev.*, 2007, **251**, 258-287.
67. J. Tomasi, B. Mennucci and R. Cammi, *Chem. Rev.*, 2005, **105**, 2999-3093 and references therein.
68. N. G. Connelly and W. E. Geiger, *Chem. Rev.*, 1996, **96**, 877−910.
69. M. Frank, M. Nieger, F. Vogtle, P. Belser, A. von Zelewsky, L. D. Cola, V. Balzani, F. Barigelletti and L. Flamigni, *Inorg. Chim. Acta*, 1996, **242**, 281-291.
70. A. Juris, F. Barigelletti, S. Campagna, P. Belser and A. von Zelewsky, *Coord. Chem. Rev.*, 1988, **84**, 85-277.
71. M. Nonoyama, *M. Bull. Chem. Soc. Jpn.*, 1974, **47**, 767-768.

Chapter 7

Summary and Future Work

7.1 Summary

The aim of this thesis has been to develop several collections of fluorescent, multimodal imaging agents, with particular focus on utilisation in CFM combined with other imaging modalities and/or therapeutic action. Work herein has shown that this can be achieved by, but not limited to; (i) utilising luminescent ligands possessing therapeutic potential, (ii) combining ligands of photophysical interest with metals to provide additional modality, or (iii) using the phosphorescent nature of many transition metal complexes towards CFM where the metal can also provide additional imaging modalities. In all cases the ligand can be used to tune both the photophysical and physical parameters (such as solubility and cell uptake and localisation).

Naphthalimide ligands were the main thread of a large section of the work herein. This was due to the favourable attributes offered by NI ligands such as stepwise functionalisation, allowing careful ligand design, and desirable photophysical properties such as strong and visible ICT emission. In Chapter Two it was demonstrated how NI ligands could be axially coordinated to Re(I) using a pyridine binding site situated off the imide. Both ligands and complexes possessed fantastic photophysical properties that were highly suited towards CFM. It was observed that subtle structural variation of the 4–amino group greatly tuned the imaging properties (localisation and capability). Unfortunately, poor cell uptake was experienced with these compounds so their application in CFM was limited. On the other hand, several compounds showed promising oxygen sensitivity which indicated their potential use towards PDT.

Chapter Three continued with developing NI ligands towards CFM, however investigated a different coordination mode to Re(I), this time synthesising the *fac*-$[Re(CO)_3(L)]^+$ complexes. This chapter allowed investigation into how varying the structure of the imide substituent affected the ligand properties. The tuning affects afforded by the imide group were shown to be much less profound than when varying the 4–amino substituent, as in Chapter Two. On the other hand, the amphiphilic groups incorporated into the ligand structure (*e.g.* glycol, propyl alcohol) greatly improved the cellular uptake of the species when compared to the more aromatic ligands in Chapter Two. In addition to the species within Chapter Three being proved as excellent cellular probes for CFM, the metal complexes also have potential use towards SPECT because the *fac*–$Re(CO)_3$ core is often used as a cold model for $^{99m}Tc(I)$, and furthermore Re(I) has radionuclides in its own right.

Chapter Four utilised knowledge obtained from work within Chapters Two and Three to progress the design of NI based bimodal imaging and/or therapeutic agents. It had become obvious from the previous chapters that the photophysical properties of the complexes were highly ligand dominated and that the properties were more greatly tuned *via* the 4–amino substituent. Therefore, Chapter Four moved towards Au(I), that is spectroscopically quiet but offers a strong precedent for therapeutic action. Coordination to Au(I) was achieved using a pendant alkyne moiety situated off the imide and the 4–amino groups were carefully selected to give a range of amphiphilic nature. This resulted in remarkably contrasting cellular uptake and localisation behavior and both ligands and complexes showed bright emission. Unfortunately toxicity studies revealed that, although the introduction of the Au(I) ion greatly increased the cytotoxic nature of the species, all compounds within Chapter Four were found to be more toxic to HEK cells than a variety of cancerous cell lines.

In a move to achieve a plausible tri–modal system, Chapter Five extended the NI core to an anthracene unit which has literature precedent of strong cytotoxic properties and the extended aromatic core provides visible emission without the requirement of ICT. The cytotoxic and photophysical properties towards CFM were provided by the ligand in Chapter Five. This then allowed the metal to be selected for an additional imaging modality. In this case the *fac*–$Re(CO)_3$ core was again selected due to the relevance to SPECT. Work herein revealed how the linker length between the anthracene core and metal binding site greatly affected the imaging capability of the species. The observed red shifts in emission wavelengths due to extended conjugation were highly beneficial because they offer a better depth of penetration and therefore differentiation from autofluorescence emission.

Chapter Six took a slightly different thread to the previous chapters and arose due to a conversation while conducting CFM on previous chapters, where the importance of nitric oxide to cells was discussed. Therefore this chapter aimed to develop a series of NO probes with potential use in CFM. The ligands and Ir(III) complexes within Chapter Six all showed profound photophysical changes upon irreversible binding to NO and therefore have the potential to act as rapid NO detectors. The photophysical parameters were again well suited to CFM and the complexes show particular promise as agents capable of tracing NO within cells.

Overall the work within this thesis presents a range of fluorescent probes that have been highly successful towards CFM, combined with the potential for use in other imaging or

therapeutic applications, in some cases requiring further tuning of the systems. Importantly the work offers many further avenues of investigation and the work related to NI ligands has vastly expanded the field of related cellular imaging agents for CFM.

7.2 Suggestions for future work

A number of open problems or continued research directions arose throughout the work herein and must be pursued in order to develop a truly feasible multi–modal system.

One such direction would be to investigate water soluble species related to Chapter Two, achieved by placing carboxylic acid groups on the di–imine, auxiliary ligand. This ligand could also be tuned to improve solubility in other solvents, for example by attaching long alkyl chains. In addition, longer lifetime species often show enhanced oxygen sensitivity and hence greater promise towards PDT. Therefore, it would be appropriate to test the oxygen sensitivity of the Re(I) complexes of the 4–chloro ligands that showed the longest phosphorescent lifetimes.

Most importantly the ligands in Chapters Three and Five would allow for facile coordination to ^{99m}Tc(I), a SPECT active ion. Therefore the ^{99m}Tc(I) complexes of these ligands should be synthesised and their application as SPECT agents tested. This is in fact currently underway through a collaboration with the University of Hull and the Tc(I) analogues of species detailed in Chapter Five have been synthesised. It is hoped that the SPECT imaging results will reveal a strong candidate for a multimodal radio–luminescent probe.

The CFM results from Chapter Five certainly merit further investigation and an obvious area of future work would be to develop a range of ligands with intermediate linker lengths between those of **L1** (hexyl) and **L2** (ethyl) reported in Chapter Five. It would be of further benefit to solve the synthesis of analogous ligands that are substituted on the anthracene ring in a similar fashion to the NI species in Chapters Two and Four. Conducting toxicity studies on a larger set of compounds would extend the knowledge of structure–activity relationships for related ligands and drugs, such as Azonafide. Toxicity studies have now been conducted for the compounds reported in Chapter Five and showed that **L2** had reduced toxicity compared to the other samples. **L1** was somewhat selective for MCF7 cells and interestingly was more toxic than the corresponding complex, the opposite trend to what was witnessed for species in Chapter Four. In addition, for publication purposes it may be beneficial to conduct 2D–NMR studies on the species within Chapter Five in order to confidently assign the anthracene and pyridyl NMR peaks.

Work related to Chapter Four is already being undertaken by the Pope group where students are attempting to bond a phosphine to the NI ring for direct coordination to Au(I). Coordination of the NI *via* a phosphine would leave a further coordination site on Au(I) to be used for a variety of purposes. A more obvious direction of further work derived from Chapter Four would be to solve the coordination issues that occurred for the series of ligands when a different phosphine co–ligand was used on Au(I).

Finally Chapter 6 also offers a range of potential routes for future work. The obvious investigation that needs to be conducted in order to round–off the work within this chapter is to conduct CFM studies to determine if the species are valid cellular NO probes. It would be important to assess whether the species within Chapter Six show different emission wavelengths in areas or cells of differing NO concentration. Furthermore for this application it would be highly beneficial to return to attempting coordination of the set of ligands to Re(I) which is known to show a greater degree of localisation within cells than Ir(III).